AN INVESTIGATION OF THE PLASMA FOCUS BY FARADAY ROTATION POLARIMETRY

by

DAVID GEORGE MUIR

Department of Physics
Royal Holloway College
University of London

This thesis is submitted for the
Degree of Doctor of Philosophy
in the University of London

February 1983

ABSTRACT

The azimuthal magnetic field and current density structure of a Plasma Focus device, have been investigated by the observation of the Faraday rotation of a ruby laser probe beam. The magnetic field and current distributions play important roles in plasma compression, heating, confinement, stability, and particle acceleration. However, in over two decades of research, no satisfactory experimental data on the field or the current have been produced. The results reported are of the first measurements of magnetic field and current distribution in the Plasma Focus, using a non perturbing diagnostic technique. A full description of the experimental apparatus and method, the physics of the differential polarimetry (with refraction effects included), and theoretical reviews of Faraday rotation, birefringence, dichroism, and refraction, are given. It was found that during the collapse phase of the discharge, times t = -10 ns to t = 0 ns (peak compression), the current and field are confined to the plasma skin. The penetration depth is 0.56 mm, and the resistivity is classical. During the dense pinch phase, between t = 0 ns and t = +10 ns, the plasma develops a turbulent core, of radius 2 mm, in which the resistivity is highly anomalous (by a factor $\sim$ 6000). This results in a rapid diffusion (lasting approximately 10 ns) of field and current (typically 20% of the total) into the core. Particle acceleration is suppressed at this stage because the ion Hall term, $\omega_{ci}\tau_{ii}$, is less than unity. Outside this core, the resistivity is classical, and the current is carried in the plasma skin. At times t = +10 ns to t = +15 ns, axial current filamentation was observed. These filaments last less than 2.5 ns, and carry in excess of 12% of the current. Future studies of the filamentation should lead to a better understanding of the intense neutron production observed in Plasma Focus devices.

Table of Contents

LIST OF FIGURES

LIST OF TABLES

ACKNOWLEDGEMENTS

I wish to express my thanks to my supervisors Dr. N.J. Peacock and Dr. E.R. Wooding, and to my colleagues R.E. Kirk and M.J. Forrest for their encouragement throughout this work and for their help in running and maintaining the Plasma Focus experiment. I also wish to thank C. Shepherd for typing the mathematics in this thesis.

I acknowledge the assistance given to me by R.E. Kirk in obtaining the holographic interferograms of the Plasma Focus discharge.

I am indebted to the U.K.A.E.A. Culham Laboratory for their financial assistance and generous provision of facilities during this work.

To Karen, for her patience.

INTRODUCTION

The internal magnetic fields of laboratory plasmas can be measured by a variety of techniques, such as Thomson scattering [1,2,3], and Zeeman splitting of line radiation from neutral lithium probe beams [4,5]. These techniques are reviewed by Peacock [6] and the TFR group [7]. However, this class of measurement has proved difficult, so that there is no single method which can be described as established or routine. In addition, because of the large variation in the basic parameters of the many laboratory plasmas in existence, e.g. in electron density, a measurement technique which can be applied to one type of plasma may not be feasible with another. One method which is becoming established, although far from being routine, and which is independent of plasma type, is Faraday rotation. This method has been applied to a variety of plasmas ranging from the smallest laser produced plasmas (radius $\sim$ 250 microns, magnetic field $\sim$ 200 Tesla, electron density $\sim 10^{27}$ m^{-3}) [8,9], to the largest Tokamak plasmas (radius $\sim$ 0.25 m, magnetic field $\sim$ 2 Tesla, electron density $\sim 10^{19}$ m^{-3}) [10,11,12]. This is the method which was chosen to measure the unknown azimuthal magnetic field structure of a Plasma Focus device, and it is this investigation which is the subject of this thesis.

The Plasma Focus [13,14] is a device in which a plasma sheath is formed across an insulator between and at one end of two concentric cylindrical electrodes. The current through the plasma forms a magnetic field within the volume between the electrodes and the insulator side of the plasma sheath. The result is that the magnetic pressure, or volume $\underline{J}x\underline{B}$ force, drives the plasma away from the insulator and down between the two electrodes 'snow-ploughing' the low

pressure gas ahead. The gas is normally deuterium at a pressure of approximately 2 torr. This phase is called the run-down phase. Eventually, the sheath reaches the open end of the electrodes and, as a result of the $\underline{J}x\underline{B}$ radial force component, pinches. This phase of the discharge is called the collapse phase. On the axis of the device used in this experiment [15], described in chapter 2, electron densities greater that 10^{25} m^{-3} have been observed at maximum compression of the pinch column, when the plasma radius is approximately 2mm, and the plasma current 340 kA, with an associated magnetic field strength $\lesssim$ 30 Tesla. All chronlogy is with reference to this time and is denoted t = 0. The phase commencing from peak compression, is called the dense pinch phase.

The magnetic field plays an important role in the dynamics of the Plasma Focus. Initially, it is the driving force which forms the plasma. Later, around the time of peak compression, it is an important source of ion heating. At peak compression of the pinch, the beta, or ratio of kinetic to magnetic pressure, is of order unity. As a result, the plasma can interact strongly with the magnetic field, modifying it. Current driven instabilities can be generated which lead to anomalous resistivity [16], and consequently enhanced Ohmic heating. In order to investigate and quantify these processes, the magnetic field structure must be measured.

Faraday rotation experiments on the Plasma Focus, have been attempted previously [17,18,19], but none have been totally successful. Other techniques have been employed to measure the internal magnetic field: by the spectroscopic observation of the Zeeman splitting of impurity ion line radiation from the plasma [20], and by the insertion of magnetic probes into the plasma volume to

measure the field locally [21,22]. The former measurement gave only an estimate of the field strength (50-100 Tesla), while the latter succeeded but only at the price of seriously perturbing the plasma. Therefore, the magnetic field of a Plasma Focus had not been determined experimentally with any precision or confidence. For this reason, it was decided to design a polarimeter, and measure the internal magnetic field structure using the Faraday rotation method.

In this method, a plane polarised electromagnetic probe beam is directed through the plasma in a direction parallel to a component of magnetic field, and the change in the plane of polarisation determined. The change is called Faraday rotation, and occurs because the plasma is birefringent to circularly polarised light. The angle of rotation is small, and depends upon the square of the probe beam's wavelength, and on the line integral $\int_L n_e B_{||} dl$, where n_e is the electron density, and $B_{||}$ is the parallel component of magnetic field. It is therefore a line integral measurement technique, with the inherent problem of unfolding the many measurements needed from different plasma chords to give the magnetic field profile. In addition, the electron density must also be known, and in the work described here, was determined using ruby laser 1.5 ns double exposure holographic interferometry. This measurement is itself a line integral measurement technique requiring unfolding, and is described in section 2.2.3.

Several methods exist by which small Faraday rotation angles can be measured. For example, if the probe beam's plane of polarisation is made to circularly rotate at a constant angular frequency, then the intensity detected through an analyser would be observed to vary as a sine squared curve at this angular frequency. Faraday rotation either advances or retards the probe beam's plane of polarisation, and results

in a phase shift of the transmitted signal [23]. The phase shift is exactly the Faraday rotation angle. This method is independent of the probe beam's intensity, so that variations in the illumination of the analyser cannot be misinterpreted as being due to Faraday rotation. Another method consists of using a probe beam with a plane of polarisation which oscillates through a small angle, larger than the Faraday rotation angle, at a constant frequency [24]. The intensity transmitted through a crossed analyser then varies at the oscillation frequency. Faraday rotation alters the amplitude of the signal observed at this frequency by lock-in techniques. Unlike the previous phase method, this amplitude method has the problem that variations in the analyser illumination may be interpreted as being due to Faraday rotation. However, by observing the signal amplitude at twice the fundamental oscillation frequency in addition, the illumination term can be removed to leave only information about the Faraday rotation angle [12].

Both these methods were devised for application on Tokamak plasmas, where the time scales involved are of the order of milliseconds, and the required oscillation frequencies in the range 10 - 100 MHz. For the Plasma Focus, the time scales are of the order of nanoseconds, which would require variations in the probe beam's plane of polarisation at GHz frequencies. This was considered to be too difficult to achieve with the ruby laser used in the experiment, because good spatial and temporal coherence were required along with high power operation. Therefore, both of these methods were rejected for use on the Plasma Focus.

The technique adopted is known as the differential half-shade method [25], and is described in chapter 3. The plane polarised probe

beam emerging from the plasma is divided into two equally intense beams, which are transmitted through two analysers. To achieve high sensitivity, these analysers are set at a small angle from the crossed position. This angle is called the half-shade angle, and was 2° in the experiment. The crossed positions were chosen so that with Faraday rotation, the transmittance of one analyser increases, while the other decreases. By detecting the intensities transmitted, and calculating the ratio of signal difference to signal sum, the direction and magnitude of the Faraday rotation angle can be determined. By taking this ratio, the effect of variations in the probe beam illumination is removed. A Q-switched ruby laser (694.3 nm, 0.5 J) of pulse length 30 ns was used as source. It was chosen for several reasons. At the laser's wavelength, the expected Faraday rotation angle $\lesssim 5^{\circ}$, was sufficiently large for accurate measurements, with minimal complications due to refraction and birefringence.

The experimental scheme adopted was to image a 250 micron diameter plasma chord onto a single detector, via two fibre optic links of different length. Many measurements were taken during a laser pulse, with a time resolution of 2.5 ns. The full spatial and temporal details of the Faraday rotation were built up on a shot to shot basis, at several viewing chord positions.

This scheme is different to that commonly employed in laser produced plasma diagnostics [8,9], where a very short laser pulse is used to 'freeze' the plasma, and in which the whole plasma is imaged onto photographic film via polarisation analysers. From the resulting optical density of the photographic images, the Faraday rotation angle is determined. This technique gives all the spatial information required to unfold the data, assuming cylindrical symmetry.

Interferometry can also be performed simultaneously along the same optical path, which is an advantage in plasmas where the parameters can vary considerably from shot to shot. In the Plasma Focus, the electron density distribution is reproducible during the collapse phase, afterwhich instabilities occur which break up the plasma column. A similar 'freeze' scheme was attempted on the Plasma Focus [26], but did not have sufficient sensitivity to observe the much smaller than anticipated actual Faraday rotation ($\lesssim 0.5°$). One disadvantage which has possibly been overlooked by experimentalists, is that the 'freeze' technique cannot observe very rapid changes in magnetic field. For example, the unique observations of the short-lived axial current filaments reported in this thesis, were seen as a very rapid change in the Faraday rotation angle in the neighbourhood of the magnetic axis. These filaments lasted for a time period $\lesssim 2.5$ ns, and if the 'freeze' technique had been employed, the probability of observing a filament would have been very small.

In any Faraday rotation experiment, there is an optimum choice of probe wavelength. It was stated that Faraday rotation scales as λ^2, so that as large a wavelength as is feasible would at first appear the best choice. However, there are several complicating factors which must be considered. The probe beam is refracted by the plasma, and the refraction angle, also scaling as λ^2, sets an upper limit to the wavelength, depending on what is acceptable. The perpendicular component of magnetic field in the plasma causes the plasma to be birefringent to linearly polarised light, with the consequence that the probe beam emerges elliptically polarised. This effect is known as the Cotton-Mouton effect [27], and scales as λ^3. It is polarisation sensitive and can be minimised, in addition to correctly choosing the wavelength, by the choice of initial plane of polarisation. Other

effects which must be considered are dichroism and birefringence, caused by electron collisionality and plasma density inhomogeneities respectively. All of these optical properties are examined in detail in chapter 1. The two final important factors are the availability of a suitable high power source (high power is required when analysers are used near the crossed position), and the sensitivity and speed of detectors at the optimum wavelength.

Complications in the measurement of Faraday rotation occur in practice due to the effect of optical elements on the probe beam's polarisation state. The curvature of lens surfaces with Fresnel reflection, can alter the polarisation planes spatially within the probe beam (see appendix B). Stress-birefringence within the elements can cause polarisation ellipticity. Dielectric beam-splitters have different reflection coefficients for s and p polarisation states. This latter property of beam-splitters has been turned to an advantage by using them to amplify Faraday rotation. All of these effects can change during a plasma shot due to the probe beam's optical path changing as a result of refraction. The angles of incidence, and therefore the values of reflection and transmission coefficients, as well as the points of reflection can change. This latter change can have the effect of altering the reflection plane of a beam-splitter, which consequently appears as a rotation of the probe beam's plane of polarisation.

A full theoretical analysis of the optical behaviour of the polarimeter developed for this measurement is given in chapter 3. The effect of plasma refraction on the measurement of Faraday rotation has been assessed It is shown that for this instrument, there is an optimum operating point where the effects of refraction are minimised.

This can and has been verified experimentally by simulating the effects of refraction. New criteria are presented for determining the optimum sensitivity when limited by either polarisation ellipticity, or by the analysers finite rejection ratio.

The results of the Faraday rotation experiment, together with the results from holographic interferometry, are given in chapter 4. Also discussed, is the analysis of these measurements, e.g. the Abel inversion, and the accuracy of the unfolded electron density and magnetic field. These magnetic field results are the first detailed measurements made on a Plasma Focus by a non-perturbing technique.

The interpretation of the results is also given in chapter 4. From the interferometry measurements, information on the temporal evolution of the plasma's axial length, plasma radius (at a variety of Z axis positions), and sheath velocities, is described. In addition, from the unfolded electron density distributions, the electron line density and average density, can be calculated. From these, the axial particle loss rate, and the focussing efficiency of the Plasma Focus, can be evaluated. The magnetic field measurements give directly the plasma current, and the current leakage across the insulator. Assuming pressure balance models, average temperature profiles are determined. In addition, the plasma resistivity can be estimated from the magnetic field diffusion rate. From Ampere's law, the axial current density profile is obtained. This gives the electron drift velocities, and the Ohmic heating deposition. The interpretation of the results for axial current filaments, are also discussed. The information presented on many of these topics are original, since they follow from the first accurate magnetic field measurements made on a Plasma Focus device.

Finally, in chapter 5, a summary of the results and conclusions from the investigation of the Plasma Focus is given. The new work presented in chapters 1 and 3 on polarisation effects, refraction, and polarimetry, are discussed. Suggestions for improving the experimental technique and for future research are given.

CHAPTER 1 A REVIEW OF FARADAY ROTATION AND OTHER OPTICAL PROPERTIES OF PLASMA

1.1 INTRODUCTION

A plasma permeated by a magnetic field has optical properties which are similar to those of crystals. It is birefringent, optically active, and dichroic. In addition, because of gradients in electron density, they are refractive. Starting from the theory of electromagnetic wave propagation in magnetised plasma, the theories of Faraday rotation, birefringence, and dichroism, are reviewed. The coupling of these effects is also examined, and the manner in which the effects of birefringence can be minimised discussed. The theory is applied to a simple cylindrical plasma model, for which the method of extracting the magnetic field profile from Faraday rotation measurements is considered. Useful analytical expressions are derived which quantify these effects. Refraction by cylindrical plasmas is also reviewed.

1.2 WAVE PROPAGATION IN A HOMOGENEOUS MAGNETISED PLASMA

In this section, the theory of electromagnetic wave propagation in an infinite homogeneous Lorentz plasma will be considered. A Lorentz plasma is a simple plasma model in which the ions are at rest, acting as a continuous stationary fluid, through which the electrons

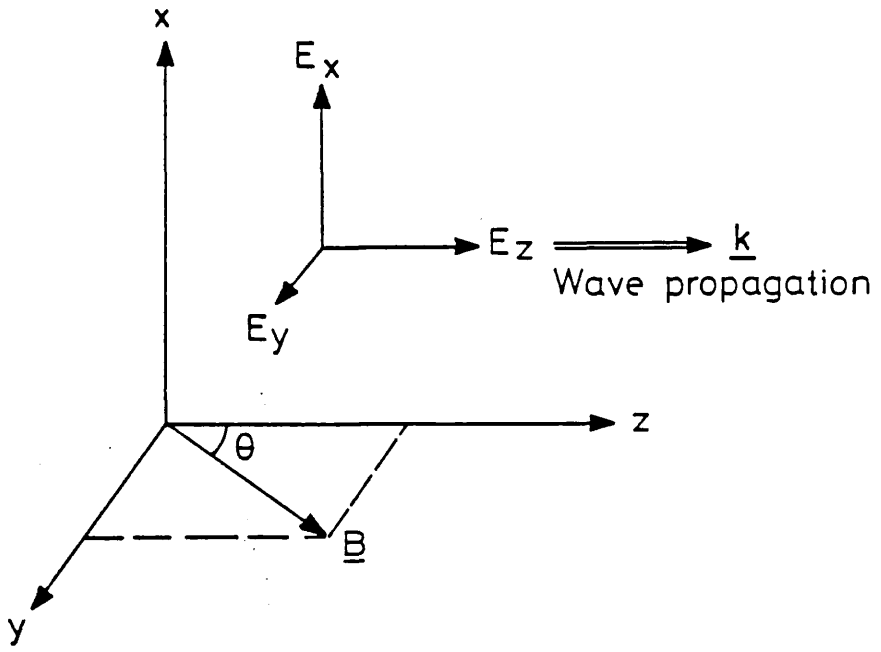

Figure 1.1

Coordinate frame for wave propagation in an arbitrary direction to the magnetic field.

move. Interparticle interactions are included through a momentum damping term (discussed in section 1.4).

Consider a plane electromagnetic wave propagating along the z-axis at an angle θ to the magnetic field $\underline{B}$, which lies in the y-z plane (see figure 1.1). The interaction of the wave with the plasma occurs via the electric field of the wave $\underline{E}$, and the equation of motion of the electrons is

$$m_e \frac{d\underline{v}}{dt} = -e\underline{E} - e\underline{v} \times \underline{B} - \nu m_e \underline{v} \qquad (1.1)$$

where $\underline{v}$ is the electron velocity, and ν is the effective collision frequency for momentum transfer to the ions. Assuming that the plane wave has a phase factor $\exp(i\omega t)$, where ω is the wave frequency, then with the substitution $d/dt = i\omega$ and the definition of the current

density $\underline{J}$

$$\underline{J} = -en_e\underline{v} \tag{1.2}$$

where n_e is the electron density, the equation of motion, on expansion, gives an expression for Ohm's law with a reciprocal conductivity tensor $\underline{\underline{\sigma}}^{-1}$

$$\underline{E} = \underline{\underline{\sigma}}^{-1}.\underline{J} \tag{1.3}$$

where

$$\underline{\underline{\sigma}}^{-1} = \frac{m_e}{e^2 n_e} \begin{bmatrix} i\omega + \nu & \omega_{ce}\cos\theta & -\omega_{ce}\sin\theta \\ -\omega_{ce}\cos\theta & i\omega + \nu & 0 \\ \omega_{ce}\sin\theta & 0 & i\omega + \nu \end{bmatrix} \tag{1.4}$$

and where $\omega_{ce} = eB/m_e$ is the electron cyclotron frequency. The second stage in the theory is to derive Ohm's law with a conductivity tensor $\underline{\underline{\sigma}}$, namely

$$\underline{J} = \underline{\underline{\sigma}} \cdot \underline{E} \tag{1.5}$$

The dispersion relation for wave propagation then follows from the requirement that equations 1.3 and 1.5 are self-consistent.

The conductivity tensor is derived by considering Faraday's and Ampere's laws, with an explicit current density $\underline{J}$

$$\nabla \times \underline{E} = -\frac{\partial \underline{B}}{\partial t} \tag{1.6}$$

$$\nabla \times \underline{H} = \underline{J} + \frac{\partial \underline{D}}{\partial t} \tag{1.7}$$

A plane wave propagating along the z-axis with a phase factor given by

$$\exp(i\omega t - \hat{k}z) \tag{1.8}$$

where $\hat{k}$ is a complex phase coefficient defined as

$$\hat{k} = \alpha + i\frac{\omega}{c}\mu \tag{1.9}$$

where μ is the refractive index and α is the attenuation coefficient, must satisfy these equations. Substitution into equations 1.6 and 1.7, along with the constitutive relations

$$\underline{D} = \varepsilon_o \underline{E} \quad \text{and} \quad \underline{B} = \mu_o \underline{H} \tag{1.10}$$

where both the relative permittivity and permeability are unity, and eliminating the $\underline{H}$ components gives the conductivity tensor

$$\underline{\underline{\sigma}} = i\omega\varepsilon_o \begin{bmatrix} \hat{\mu}^2 - 1 & 0 & 0 \\ 0 & \hat{\mu}^2 - 1 & 0 \\ 0 & 0 & -1 \end{bmatrix} \tag{1.11}$$

where $\hat{\mu}$ is a complex refractive index defined as

$$\hat{\mu} = \mu - i\frac{c}{\omega}\alpha \tag{1.12}$$

For equations 1.3 and 1.5 to be self-consistent

$$(\underline{\underline{\sigma}}^{-1} \cdot \underline{\underline{\sigma}} - \underline{\underline{I}}) \cdot \underline{E} = 0 \tag{1.13}$$

where $\underline{\underline{I}}$ is the unit tensor. This equation represents a set of three simultaneous equations, and the determinant of the coefficients must be zero for a non-trivial solution to exist. Therefore

$$\begin{vmatrix} (i\omega+\nu)(\hat{\mu}^2-1)+\frac{i\omega_{pe}^2}{\omega} & \omega_{ce}(\hat{\mu}^2-1)\cos\theta & \omega_{ce}\sin\theta \\ -\omega_{ce}(\hat{\mu}^2-1)\cos\theta & (i\omega+\nu)(\hat{\mu}^2-1)+\frac{i\omega_{pe}^2}{\omega} & 0 \\ \omega_{ce}(\hat{\mu}^2-1)\sin\theta & 0 & -(i\omega+\nu)+\frac{i\omega_{pe}^2}{\omega} \end{vmatrix} = 0 \qquad (1.14)$$

where $\omega_{pe} = (e^2 n_e/\varepsilon_o m_e)^{\frac{1}{2}}$ is the plasma frequency. The complex refractive index then follows by solving this determinantal equation [28]

$$\hat{\mu}^2 = 1 - \frac{\omega_{pe}^2}{\omega^2}\left\{\left[1-\frac{i\nu}{\omega}-\frac{\omega_{ce}^2\sin^2\theta}{2\omega^2(1-\frac{\omega_{pe}^2}{\omega^2}-\frac{i\nu}{\omega})}\right] \pm \left[\frac{\omega_{ce}^4\sin^4\theta}{4\omega^4(1-\frac{\omega_{pe}^2}{\omega^2}-\frac{i\nu}{\omega})^2}+\frac{\omega_{ce}^2\cos^2\theta}{\omega^2}\right]^{\frac{1}{2}}\right\}^{-1} \qquad (1.15)$$

This is Appleton's equation. It gives the refractive indices and attenuation coefficients for waves whose state of polarisation is determined by the ratios of the electric field component coefficients given by equation 1.13.

Two parameters are employed to describe the polarisation: the wave polarisation coefficient $R_{\pm}$, and the longitudinal polarisation coefficient S. These are defined as

$$R_{\pm} = \frac{E_x}{E_y} \quad \text{and} \quad S = \frac{E_z}{E_x} \qquad (1.16)$$

From equation 1.13, in the absence of damping, $R_{\pm}$ is given by

$$R_{\pm} = \frac{i}{F}\left(1 \mp (1+F^2)^{\frac{1}{2}}\right) \qquad (1.17)$$

where F is defined by

$$F = \frac{2\omega}{\omega_{ce}} \left(1 - \frac{\omega_{pe}^2}{\omega^2}\right) \frac{\cos\theta}{\sin^2\theta} \qquad (1.18)$$

and where the subscript taken, + or -, is the same as the sign taken in Appleton's equation. In the high frequency limit

$$\omega >> \omega_{pe} \; ; \; \omega_{ce} \; ; \; \nu \qquad (1.19)$$

the longitudinal polarisation coefficient is very small, so that there is only a negligable longitudinal electric field component. There are therefore two waves for each direction with a polarisation described by $R_{\pm}$, and these are called characteristic waves. They are the normal modes of electromagnetic oscillation in the plasma, and have the very useful property that they propagate without changing their polarisation state. They are generally elliptically polarised, and are orthogonal, with their major axes at 90° to each other, and with the same ellipticity but opposite handedness (see figure 1.2). Any polarised wave can be resolved into two waves with orthogonal polarisation. The ellipticities of the characteristic waves, which are determined from $R_{\pm}$, are given by

$$\varepsilon_+ = \frac{1}{F}(1-(1+F^2)^{\frac{1}{2}}) \qquad (1.20)$$

$$\varepsilon_- = \frac{1}{F}((1+F^2)^{\frac{1}{2}}-1) \qquad (1.21)$$

A non-characteristic wave propagating at an oblique angle to the direction of the magnetic field will have its polarisation modified by the plasma. How this occurs can be analysed by resolving the wave into two orthogonally polarised characteristic waves. These are then allowed to propagate through the plasma, subject to different refractive indices and attenuation coefficients. Finally, the

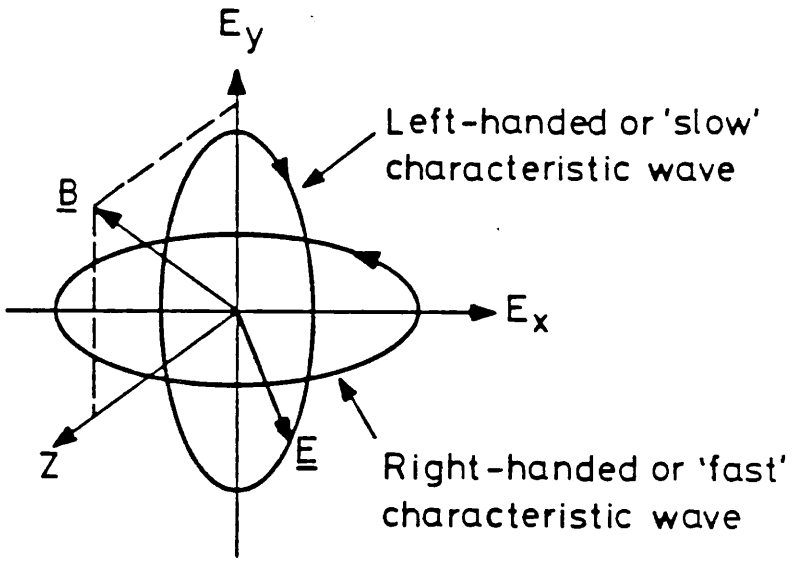

Figure 1.2

The general polarisation state of the characteristic waves.

polarisation state of the wave emerging from the plasma is obtained by a superposition of the characteristic waves, each with different phases and amplitudes. The polarisation change is usually a rotation of the major axis, and an increase in the polarisation ellipticity.

1.3 THE PRINCIPAL CHARACTERISTIC WAVES

There are two directions in the plasma which are of special interest. These are parallel and perpendicular to the magnetic field lines, and are called the principal directions. In this section, the refractive indices, attenuation coefficients, and state of polarisation of the characteristic waves for these directions are given. These waves are called the principal characteristic waves. It will be

assumed that the wave frequency satisfies the high frequency limit.

1.3.1 PROPAGATION PARALLEL TO THE MAGNETIC FIELD

For the case of wave propagation parallel to the magnetic field, $\theta = 0^\circ$, the wave polarisation coefficient has the following values

$$R_{\pm} = \mp i \qquad (1.22)$$

Assuming that the x components of the waves have unit amplitude and phase given by the real part of $\exp(i\omega t)$, the field components for the wave with $R_+ = -i$ are

$$E_x = \cos \omega t \text{ and } E_y = -\sin \omega t \qquad (1.23)$$

Superposition of these wave components gives a characteristic wave with circular polarisation. The direction in which the electric field describes the circle - the handedness - is clockwise for an observer looking towards the source of light. In plasma wave theory the wave is called left-handed, and is sometimes refered to as the 'slow' wave.

Similarly, the characteristic wave with $R_- = i$ has field components

$$E_x = \cos \omega t \text{ and } E_y = \sin \omega t \qquad (1.24)$$

Again the polarisation is circular, but the wave is now called the right-handed or 'fast' wave. The electric field vector describes the circle in an anti-clockwise manner, for an observer looking towards the light source.

These polarisations are shown in figure 1.3 and, included for comparison, is the direction of electron gyration. This corresponds to the direction of rotation of the right-handed wave. Unfortunately, the

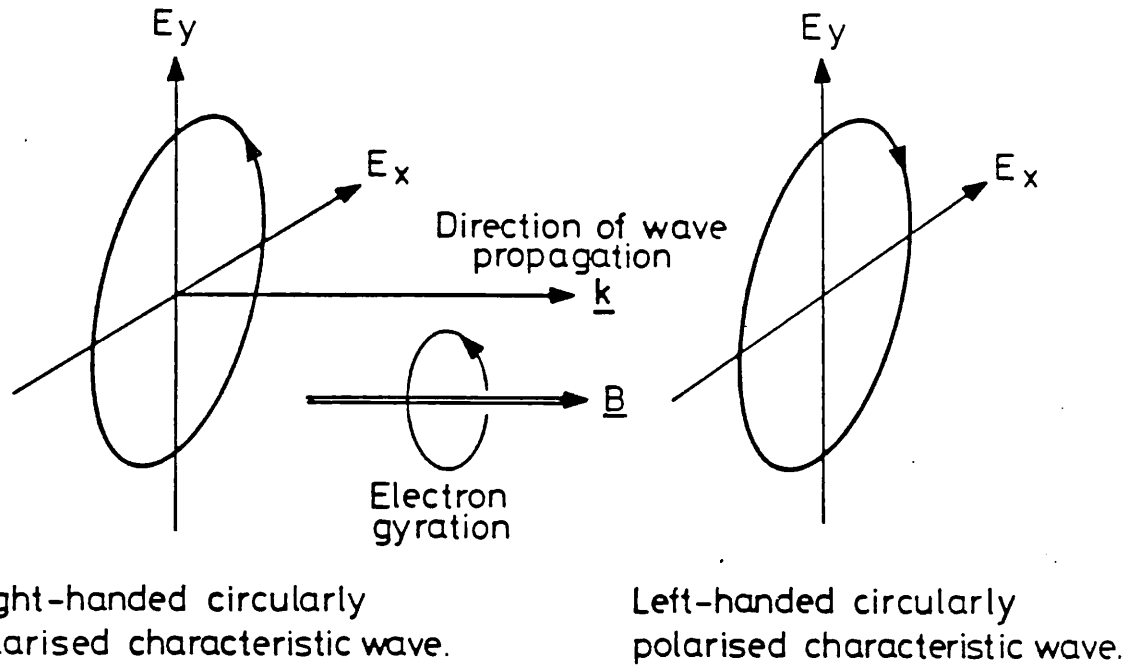

Figure 1.3

The circularly polarised principal characteristic waves.

labels used in plasma wave theory do not conform to the normal convention in optics, where the electric field vector rotates clockwise and anti-clockwise for right and left-handed polarisations respectively, for an observer looking towards the light source. This is because the label in plasma wave theory, describes how the wave compares with the direction of electron gyration. For the case of propagation anti-parallel to the magnetic field, $\theta = 180°$, the wave polarisation coefficient has the values

$$R_{\pm} = \pm i \qquad (1.25)$$

so that for the right-handed wave, the field components are as given by equations 1.23, which are those for a left-handed wave propagating parallel to the field. Thus, with respect to the magnetic field, the electric field vector of the right-handed wave will appear as shown in

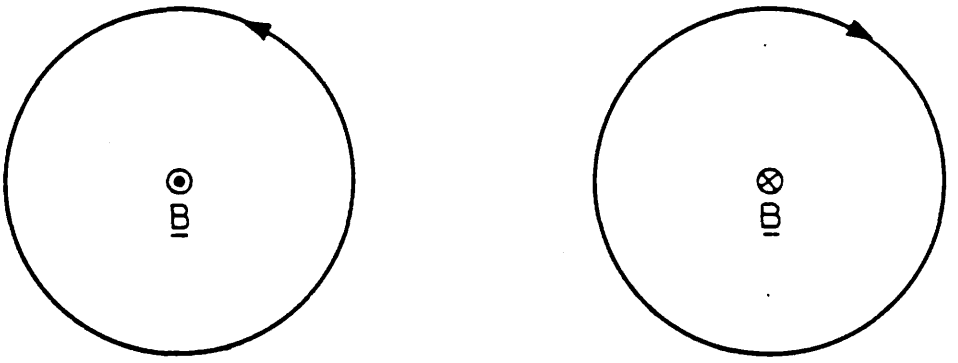

a) Parallel to the magnetic field.

b) Anti-parallel to the magnetic field, and normal optics convention.

Figure 1.4

The handedness of the right-handed circularly polarised principal characteristic wave with respect to the magnetic field.

figure 1.4. The conventional direction of rotation is also shown for comparison.

From Appleton's equation, the refractive indices and attenuation coefficients for these waves, in the high frequency limit, are [28]

Right-handed wave

$$\mu_R = \left(1 - \frac{\omega_{pe}^2}{\omega(\omega-\omega_{ce})} \right)^{\frac{1}{2}} \qquad (1.26)$$

$$\alpha_R = \frac{\omega_{pe}^2 \nu}{2c(\omega-\omega_{ce})^{3/2}\left(\omega-\omega_{ce}-\frac{\omega_{pe}^2}{\omega}\right)^{\frac{1}{2}}} \qquad (1.27)$$

Left-handed wave

$$\mu_L = \left(1 - \frac{\omega_{pe}^2}{\omega(\omega+\omega_{ce})} \right)^{\frac{1}{2}} \qquad (1.28)$$

$$\alpha_L = \frac{\omega_{pe}^2 \, \nu}{2c(\omega+\omega_{ce})^{3/2}\left(\omega+\omega_{ce} - \frac{\omega_{pe}^2}{\omega}\right)^{\frac{1}{2}}} \qquad (1.29)$$

The subscripts L and R refer to the left and right handed waves respectively.

1.3.2 PROPAGATION ORTHOGONAL TO THE MAGNETIC FIELD

The wave polarisation coefficient for wave propagation orthogonal to the magnetic field, $\theta = 90°$, has the values

$$R_+ = 0 \text{ and } R_- = \infty \qquad (1.30)$$

Taking these in turn, the $R_+ = 0$ result means that there is no wave component E_x. Thus the characteristic wave is linearly polarised with the electric field along the y-axis, and therefore parallel to the magnetic field. This wave is called the ordinary wave. For $R_- = \infty$, there is no E_y component, and the wave is linearly polarised along the x-axis, which in turn is perpendicular to the magnetic field. This characteristic wave is called the extraordinary wave. These characteristic waves are shown in figure 1.5.

From Appleton's equation, the refractive indices and attenuation coefficients for these waves, in the high frequency limit, are [28]

Ordinary wave

$$\mu_o = \left(1 - \frac{\omega_{pe}^2}{\omega^2} \right)^{\frac{1}{2}} \qquad (1.31)$$

$$\alpha_o = \frac{\omega_{pe}^2 \nu}{2c\omega(\omega^2-\omega_{pe}^2)^{\frac{1}{2}}} \qquad (1.32)$$

Extraordinary wave

$$\mu_{ex} = \left(1 - \frac{\omega_{pe}^2(\omega^2-\omega_{pe}^2)}{\omega^2(\omega^2-\omega_{pe}^2-\omega_{ce}^2)}\right)^{\frac{1}{2}} \qquad (1.33)$$

$$\alpha_{ex} = \frac{\omega_{pe}^2 \nu(\omega^2-2\omega_{pe}^2+\omega_{ce}^2)}{2c(\omega^2-2\omega_{pe}^2-\omega_{ce}^2)^{\frac{1}{2}}(\omega^2-\omega_{pe}^2-\omega_{ce}^2)^{3/2}} \qquad (1.34)$$

The subscripts '0' and 'ex' refer to the ordinary and extraordinary waves respectively.

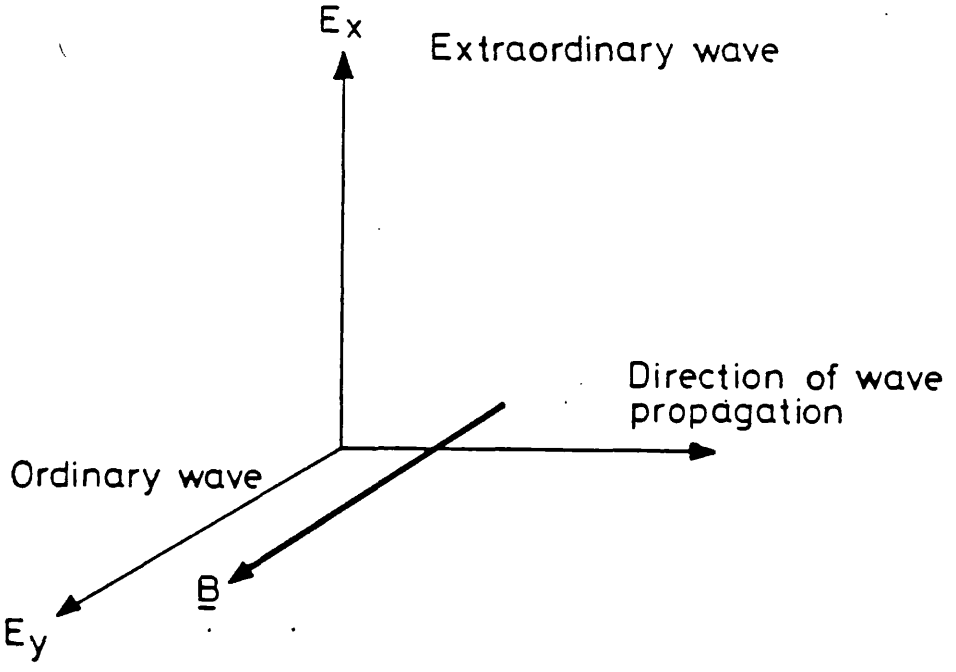

Figure 1.5

The linearly polarised ordinary and extraordinary principal characteristic waves.

1.4 THE EFFECTIVE COLLISION FREQUENCY

The attenuation of an electromagnetic wave in a plasma arises through momentum transfer from the electrons, oscillating in the electric field of the wave, to the background ions, via the Coulomb interaction. The attenuation coefficients given in the previous section are proportional to the effective collision frequency for momentum transfer, ν. This frequency is obtained by averaging the velocity dependent collision frequency over the velocity distribution of the electrons. For the case of a Maxwellian distribution, the result is [28]

$$\nu = \frac{4\sqrt{2\pi}}{3}\left(\frac{e^2}{4\pi\varepsilon_o}\right)^2 \frac{Z\, n_e\, \ell n\Lambda}{\sqrt{m_e}\,(k_B T_e)^{3/2}} \qquad (1.35)$$

In these equations, Z is the ionic charge, T_e is the electron temperature, and Λ is the Coulomb parameter, defined by Spitzer [29] as the ratio of the Debye length to the mean impact parameter for a 90° deflection of an electron by an ion, due to classical Rutherford scattering. This ratio is given by [29]

$$\Lambda_s = \frac{3(4\pi\varepsilon_o\, k_B\, T_e)}{2\sqrt{\pi}\, e^3 Z \sqrt{n_e}} \qquad (1.36)$$

However, this derivation considers the interaction of electrons with the plasma ions at the plasma frequency and not the wave frequency. It also ignores electron diffraction, which for temperatures $\gtrsim$ 80 eV becomes important. Taking these effects into account, the parameter Λ has the following limiting forms [28,30]

$$T_e \leq 77\ Z^2\ eV \qquad \ell n\Lambda = \ell n\{0.45 \left(\frac{\omega_{pe}}{\omega}\right) \Lambda_s\} \qquad (1.37)$$

$$T_e \geq 77\ Z^2\ eV \qquad \ell n\Lambda = \ell n\{2.24 \frac{k_B T_e}{\hbar\omega}\} \qquad (1.38)$$

1.5 THE APPROXIMATION OF GEOMETRICAL OPTICS

The theory of electromagnetic wave propagation discussed in sections 1.2 and 1.3, assumed an infinite homogeneous plasma. However, laboratory plasmas are inhomogeneous. Generally, the wave equation for studying wave propagation in such media is the inhomogeneous wave equation. But, since the wavelengths used in optical plasma diagnostics are typically very much less than the electron density scale length, then the plasma can be considered to exist as layers in which its optical properties are homogeneous. Thus, the homogeneous wave equation can be applied locally, and we need only consider the propagation of plane waves. More importantly, the solution to the homogeneous wave equation can be used to approximate propagation in an inhomogeneous plasma, because it will appear as a homogeneous medium with variable propagation coefficients. The solution has the following form

$$\underline{E}(z,t) = \underline{E}_o e^{-\int_L \alpha d\ell} . e^{i(\omega t - \frac{2\pi}{\lambda}\int_L \mu d\ell)} \qquad (1.39)$$

where λ is the wavelength of the wave, and where the attenuation and the optical path length are integrated over the wave trajectory, L.

The condition which must be fulfilled for this simplification to be

valid, is known as the approximation of geometrical optics, and is expressed by the inequality [31]

$$\mu \left| \frac{\partial \mu}{\partial z} \right|^{-1} >> \lambda \qquad (1.40)$$

This states that the refractive index scale length must be very much larger than the wavelength of the wave.

1.6 FARADAY ROTATION

In this section, the polarisation change experienced by an electromagnetic wave propagating through an inhomogeneous plasma, in a direction parallel to the magnetic field, will be discussed. It is assumed that the approximation of geometrical optics applies, so that the plasma appears homogeneous. It is also assumed that the wave frequency is sufficiently greater than the characteristic plasma frequencies for the results of section 1.3.1 to be valid. Initially, attenuation is neglected.

Consider a plane electromagnetic wave which is propagating through a magnetised plasma in a direction parallel to the magnetic field. This is a principal direction for which the characteristic waves have left and right hand circular polarisation. Since the initial polarisation is linear, then we can resolve the wave into characteristic waves of equal amplitude (see figure 1.6). If the initial polarisation is along the x-direction, then the x and y electric field components of the characteristic waves, from

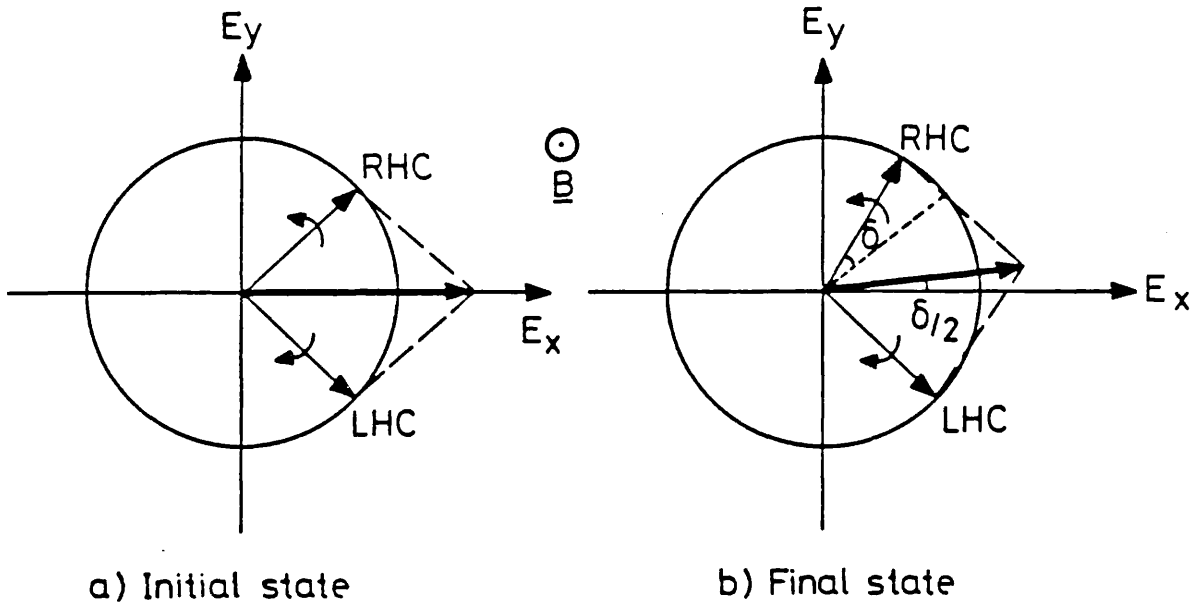

Figure 1.6

The change in the plane of polarisation from a) the initial state, to b) the final state, due to Faraday rotation.

equations 1.23 and 1.24, are given by

$$E_x^L = a_o \cos\omega t \ , \quad E_y^L = -a_o \sin\omega t$$

and $$E_x^R = a_o \cos\omega t \ , \quad E_y^R = a_o \sin\omega t \qquad (1.41)$$

where the superscripts L and R denote the left and right hand circular polarisation respectively, and a_o is the amplitude. These two characteristic waves initially have the same phase. After propagating through the plasma along an optical path L, the field components are given by

$$E_x^L = a_o \cos(\omega t - \phi^L) \ , \quad E_y^L = -a_o \sin(\omega t - \phi^L)$$

and $$E_x^R = a_o \cos(\omega t - \phi^R) \ , \quad E_y^R = a_o \sin(\omega t - \phi^R) \qquad (1.42)$$

with phases

$$\phi^L = \frac{2\pi}{\lambda} \int_L \mu_L \, d\ell \quad \text{and} \quad \phi^R = \frac{2\pi}{\lambda} \int_L \mu_R \, d\ell \qquad (1.43)$$

Superposing the waves, the resulting field components are

$$E_x = E_x^L + E_x^R = 2a_o \cos(\delta/2) \cos(\omega t - \bar{\phi})$$
$$E_y = E_y^L + E_y^R = 2a_o \sin(\delta/2) \cos(\omega t - \bar{\phi}) \qquad (1.44)$$

where δ is the phase difference $\phi^L - \phi^R$, and $\bar{\phi}$ is the mean phase of the characteristic waves $(\phi^L + \phi^R)/2$. The ratio of the electric field components is then given by

$$\frac{E_y}{E_x} = \tan \delta/2 \qquad (1.45)$$

From equations 1.26 and 1.28, it can be shown that μ_L is greater than μ_R. Therefore, the phase velocity of the right-handed characteristic wave is greater than that of the left-handed, and the phase difference δ is positive. Thus, since the ratio of the field components is independent of time, the polarisation is linear, and since the phase difference is positive, then the plane of polarisation is inclined at an angle $\delta/2$ from the x-axis, measured anti-clockwise. This rotation is called Faraday rotation, and is analogous to optical activity in crystalline media. Its magnitude, ψ, is given by

$$\psi = \frac{\pi}{\lambda} \int_L (\mu_L - \mu_R) d\ell \qquad (1.46)$$

The direction of rotation is in the same sense as the handedness of the faster characteristic wave, namely the right hand circularly polarised wave. From figure 1.3, this is in the same direction as electron gyration about the field lines.

The resultant wave electric field can now be written as

$$\underline{E}(t) = E_o\{\hat{\underline{i}}\cos\psi + \hat{\underline{j}}\sin\psi\}\cos(\omega t-\bar{\phi}) \qquad (1.47)$$

which is the equation of a plane wave with its plane of polarisation at an angle ψ from the x-axis, with a phase equal to the average phase of the characteristic waves. The amplitudes of the characteristic waves are therefore $E_o/2$.

Consider now the case where a plane wave propagates anti-parallel to the magnetic field. The phase velocity of the right-handed characteristic wave remains larger than that of the left-handed, but now, as shown in section 1.3.1, the equations for the field components of the characteristic waves are interchanged. After propagating along the path L, the resultant wave electric field vector is given by

$$\underline{E}(t) = E_o\{\hat{\underline{i}}\cos\psi - \hat{\underline{j}}\sin\psi\}\cos(\omega t-\bar{\phi}) \qquad (1.48)$$

which has the same phase and amplitude as before, but with the plane of polarisation below the x-axis at the angle ψ. Therefore, the Faraday rotation is clockwise. This is still in the same direction as the handedness of the right-handed wave and electron gyration. This result demonstrates that the process of Faraday rotation is non-reciprocal. If the wave were reflected back upon itself, the rotation would be additive. This is shown in figure 1.7.

The equation for Faraday rotation can be expanded by substituting equations 1.26 and 1.28 for the refractive indices, and on simplifying the square root terms, becomes

$$\psi = \frac{\pi}{\lambda}\int_L \frac{\omega_{pe}^2\,\omega_{ce}}{\omega^3}\,d\ell \qquad (1.49)$$

Substituting for the plasma frequency, the cyclotron frequency, and the

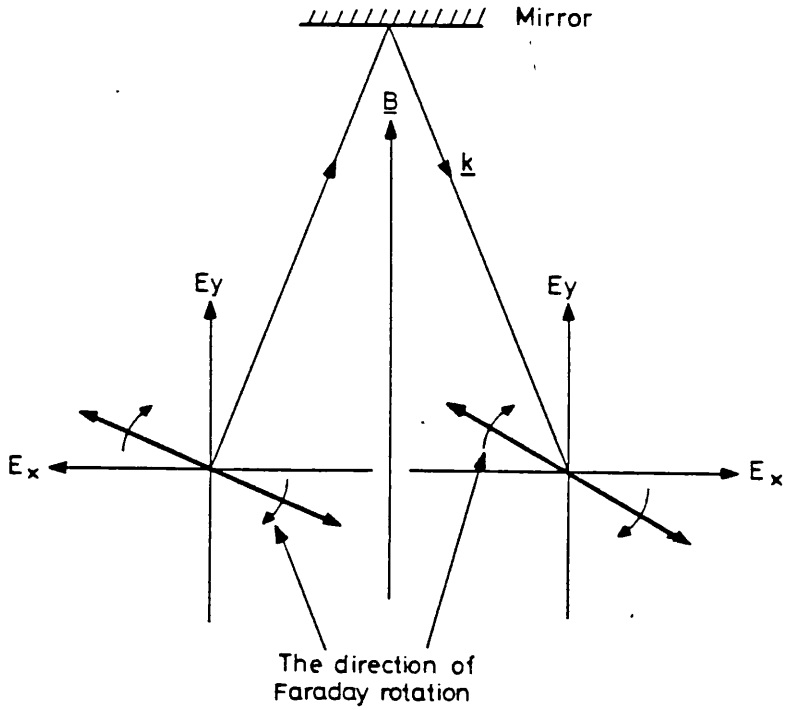

Figure 1.7

Faraday rotation is nonreciprocal

light wave frequency, gives

$$\psi = A\lambda^2 \cdot \int_L n_e B d\ell \qquad (1.50)$$

where $$A = \frac{e^3}{8\pi^2 \varepsilon_o m_e^2 c^3} = 2.63 \times 10^{-13} \text{ rad. Tesla}^{-1} \qquad (1.51)$$

From this equation, we see that Faraday rotation scales as the square of the wavelength, and is proportional to the line integral of the product of electron density and magnetic field.

1.6.1 THE CYLINDRICAL PLASMA MODEL

Consider the case of a plasma with cylindrical symmetry. If it carries an axial electrical current, the magnetic field lines also have cylindrical symmetry. If an axial magnetic field is superimposed, then the resultant field lines are helical. In these circumstances, a wave directed through the plasma will not in general travel along a principal direction. However, Faraday rotation will still occur, because there is a component of the field parallel to the wave path. The equation for Faraday rotation, neglecting the non-contributary orthogonal magnetic field component, can be written as

$$\psi = A\lambda^2 \int_L n_e \underline{B}.d\underline{\ell} \qquad (1.52)$$

If the wave is propagating in the r-θ plane (see figure 1.8), then for the geometry of this model, the equation for the Faraday rotation at an impact parameter h, is

$$\psi_\theta(h) = 2Ah\lambda^2 \int_h^a n_e(r) B_\theta(r) (r^2-h^2)^{-\frac{1}{2}} dr \qquad (1.53)$$

where B_θ is the azimuthal magnetic field, and a is the plasma radius. This assumes that the wave is not refracted by the plasma. If refraction is important, the line integral must be taken along the wave path.

This result, in addition to being applicable to linear laboratory plasmas, such as the Plasma Focus, is also applicable to toroidal plasmas. However, as will be shown, a measurement of this rotation will only yield the azimuthal magnetic field profile. In many cases the axial or toroidal magnetic field profile is unknown and requires

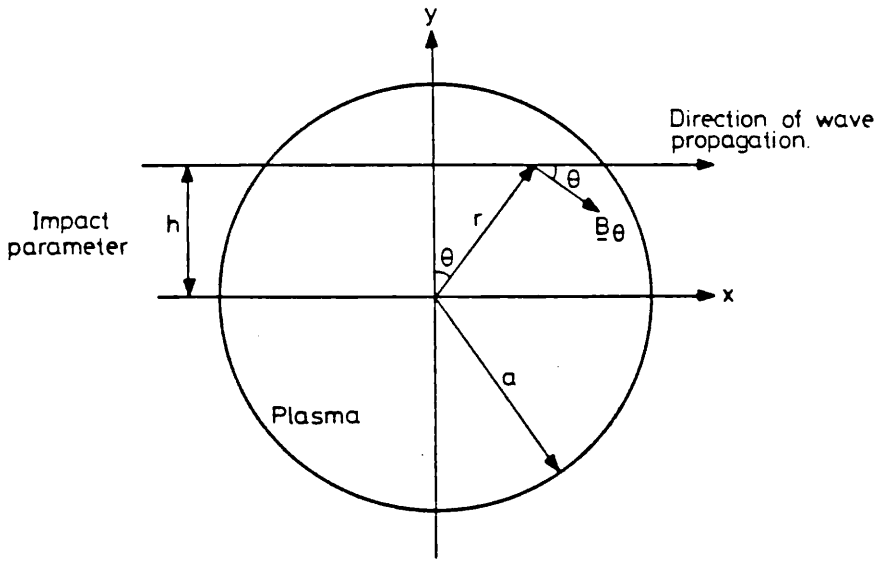

Figure 1.8

The cylindrical plasma model

measurement, as in the Reverse Field Pinch, or is sufficiently large, as in the Tokamak, that a possible misalignment of the probe beam, out of the r-θ plane, may induce an additional Faraday rotation leading to an erroneous measurement. In order to generalise the problem, so that both the measurement of an axial magnetic field by Faraday rotation and the possible effect of this field on the measurement of B_θ can be examined, consider the case where the beam is propagating through the plasma at an angle Ω from the r-θ plane (see figure 1.9). The corresponding parallel B_θ component, substituted into equation 1.52, gives the same result as equation 1.53 for the partial Faraday rotation angle ψ_θ [32]. This occurs because the increased optical path length through the plasma, exactly compensates for the diminished parallel azimuthal field component. Therefore, any experimental misalignment of the probe beam from the r-θ plane will not affect the value of ψ_θ.

The parallel axial magnetic field component gives rise to a partial

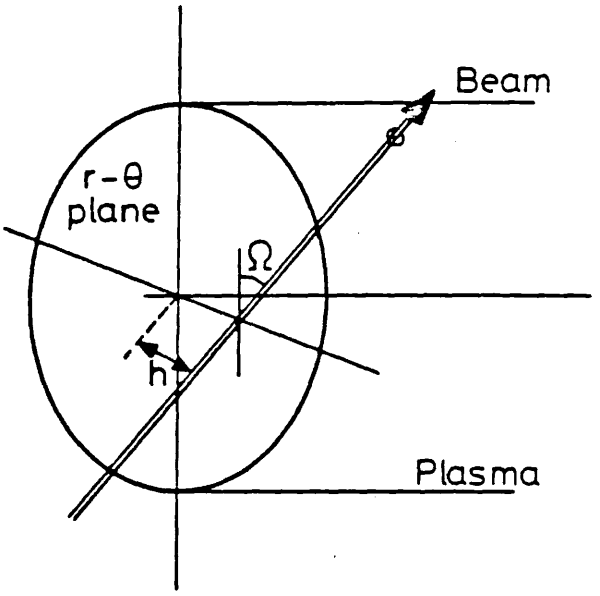

Figure 1.9

Probe beam propagation at an arbitrary angle to the r-θ plane.

Faraday rotation angle ψ_z [32], where

$$\psi_z(h) = 2A\lambda^2 \tan\Omega \int_h^a n_e(r) B_z(r) (r^2-h^2)^{-\frac{1}{2}} r dr \qquad (1.54)$$

and where B_z is the axial magnetic field. The total Faraday rotation angle experienced by the probe beam ψ_T is therefore $\psi_\theta + \psi_z$.

If the effect of the axial field is to be supressed in a measurement of ψ_θ, the angular misalignment of the probe beam from the r-θ plane, must be such that $\psi_z << \psi_\theta$.

The effect of the orthogonal field component has been neglected. In fact, it will change the polarisation state from linear to elliptical, and may also affect the degree of Faraday rotation. This property is called birefringence or the Cotton-Mouton effect, and is

discussed in section 1.7. However, as will be shown for the case where only the azimuthal field exists, if the initial plane of polarisation is such that the electric field of the wave is either parallel to, or orthogonal to, the axis of the plasma, then the effect will be small. This is because the wave will behave similarly to a characteristic wave for propagation perpendicular to the field. Faraday rotation will tend to make the wave less characteristic, but if the rotation is small, then the Cotton-Mouton effect will also be small.

1.6.2 THE ABEL INVERTED MAGNETIC FIELD PROFILES

Experimentally we are interested in the measurement of the magnetic field structure defined by the components $B_\theta(r)$ and $B_z(r)$. These can be extracted from two measurements of Faraday rotation, at many impact parameters, when $\Omega = 0$ and when $\Omega > 0$. Then, the partial Faraday rotation angles are

$$\psi_\theta(h) = \psi_T(h,\Omega=0)$$

and

$$\psi_z(h) = \psi_T(h,\Omega > 0) - \psi_T(h,\Omega = 0) \qquad (1.55)$$

The equations for these partial rotations, in cylindrical geometry, are a form of Abel's integral equation [33]

$$g(h) = 2\int_h^a rf(r)(r^2-h^2)^{-\frac{1}{2}}dr \qquad (1.56)$$

with solution

$$f(r) = -\frac{1}{\pi}\int_r^a \frac{dg}{dh}\,(h^2-r^2)^{-\frac{1}{2}}dh \qquad (1.57)$$

Assuming cylindrical geometry, from equation 1.53, we obtain the following equation for the azimuthal magnetic field

$$B_\theta(r) = \frac{-r}{\pi A\lambda^2 n_e(r)} \int_r^a \left\{ \frac{d}{dh}\left(\frac{\psi_\theta(h)}{h}\right)\right\} (h^2-r^2)^{-\frac{1}{2}}\, dh \qquad (1.58)$$

Similarly, from equation 1.54, the axial magnetic field is given by

$$B_z(r) = \frac{-1}{\pi A\lambda^2 \tan\Omega n_e(r)} \int_r^a \frac{d\psi_z(h)}{dh} (h^2-r^2)^{-\frac{1}{2}} dh \qquad (1.59)$$

These solutions depend on the derivatives $d/dh(\psi_\theta/h)$ and $d\psi_z/dh$. Therefore, experimental measurements of the Faraday rotation must be sufficiently precise for these to be accurately determined. The spatial electron density distribution must also be known before the magnetic field structure is calculated.

1.6.3 THE EFFECT OF DICHROISM ON FARADAY ROTATION

The effect of dichroism has not been considered. This is incorporated into the theory of Faraday rotation by including attenuation of the characteristic waves.

The amplitudes of the characteristic waves, as they propagate along the optical path L, are reduced to a_L and a_R for the left and right hand circular polarisations respectively, where

$$a_L = a_o e^{-\int_L \alpha_L d\ell} \quad \text{and} \quad a_R = a_o e^{-\int_L \alpha_R d\ell} \; . \qquad (1.60)$$

This attenuation occurs in addition to the phase change. The electric field components of the characteristic waves, are given by equations 1.42 with the amplitudes a_L and a_R. On superposing these components, and writing the amplitude of the left-handed wave as

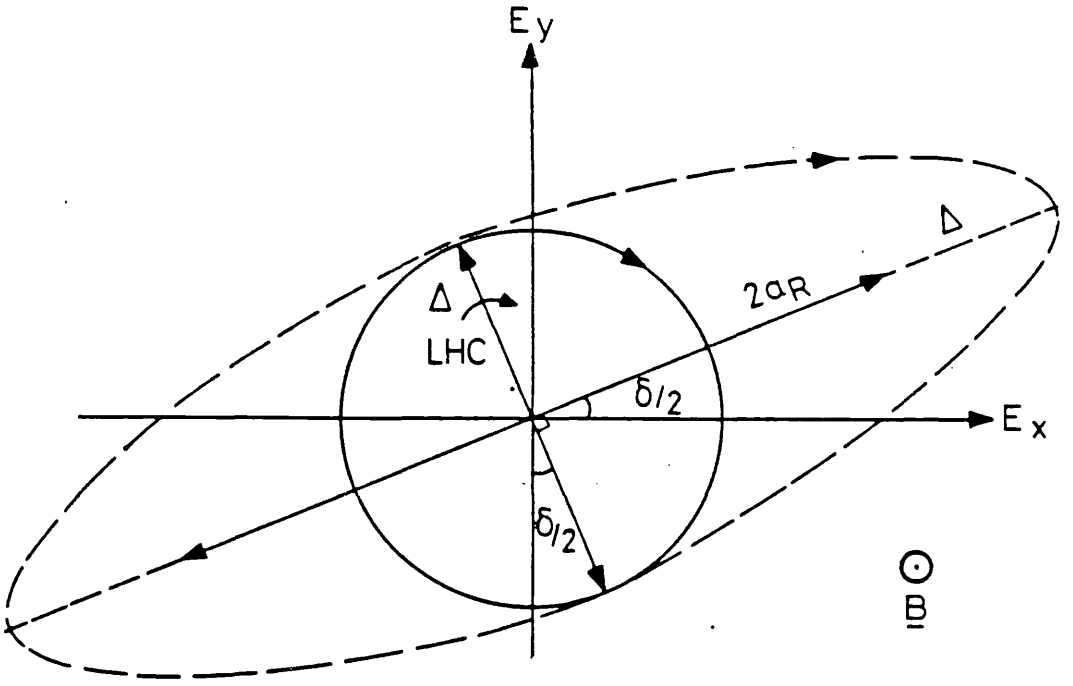

Figure 1.10

Ellipticity due to Dichroism.

$a_L = a_R + \Delta$, the resultant wave vectors become

$$E_x = 2a_R \cos(\frac{\delta}{2})\cos(\omega t - \bar{\phi}) + \Delta\cos(\omega t - \phi^L)$$

$$\text{and} \quad E_y = 2a_R \sin(\frac{\delta}{2})\cos(\omega t - \bar{\phi}) - \Delta\sin(\omega t - \phi^L) \qquad (1.61)$$

These equations give a resultant wave whose polarisation is equivalent to that produced by the superposition of a plane wave of amplitude $2a_R$, and phase $\bar{\phi}$, linearly polarised at an angle $\delta/2$ from the x-axis (the Faraday rotation angle), with a left-handed circularly polarised wave of amplitude Δ and phase ϕ^L (see figure 1.10). The resultant wave polarisation is elliptical, with the handedness of the least attenuated left-handed wave.

The ellipticity ε is obtained by considering the resultant wave amplitude when

$$(\omega t - \bar{\phi}) = \begin{cases} 0 \\ \pi/2 \end{cases} \tag{1.62}$$

and is given by

$$\varepsilon = \frac{\Delta}{a_R + a_L} \tag{1.63}$$

The azimuthal angle of the ellipse's major axis is the Faraday rotation angle.

The ellipticity, when small, can be expressed as

$$\varepsilon \cong \frac{1}{2}(1 - \frac{a_R}{a_L}) \tag{1.64}$$

and from equations 1.60, with the exponential expansion $\exp(x) \simeq 1+x$, is simplified to

$$\varepsilon \cong \frac{1}{2} \int_L (\alpha_R - \alpha_L) d\ell \tag{1.65}$$

From equations 1.27 and 1.29 for the attenuation coefficients, this equation becomes

$$\varepsilon \cong \frac{\pi}{2\lambda} \int_L \frac{\omega_{pe}^4 \, \omega_{ce} \, \nu}{\omega^6} \, d\ell \tag{1.66}$$

Substituting for the frequencies ω_{pe}, ω_{ce}, ω, and ν, we obtain

$$\varepsilon \cong C\lambda^5 \int_L n_e^3 B T_e^{-3/2} \, \ell n \Lambda \, d\ell \tag{1.67}$$

where

$$C = \frac{\sqrt{2\pi}\, e^9}{1536\pi^7 \varepsilon_o^4 c^6 m_e^{7/2} k_B^{3/2}} = 2.28 \times 10^{-43} m^3 K^{3/2} \text{Tesla}^{-1} \tag{1.68}$$

Therefore, the ellipticity due to dichroism scales as the fifth power of the wavelength, and is dependent on a line integral involving the magnetic field, the electron temperature to the minus three-halves power, and the cube of the electron density.

Thus, the general result is that a plane wave emerges from a

magnetised plasma with elliptical polarisation, after propagating parallel to the magnetic field. The major axis of the ellipse is rotated by Faraday rotation from the initial plane of polarisation, and the left-handed ellipticity arises from the preferential attenuation of the right-handed characteristic wave.

1.7 BIREFRINGENCE

The theory of birefringence in an inhomogeneous magnetised plasma, is similar to the theory of Faraday rotation. Birefringence, also called the Cotton-Mouton effect [27], arises from the anisotropy created by the magnetic field, and affects waves propagating in a direction perpendicular to the magnetic field. In the following theoretical review, the following assumptions are made: The inhomogeneous plasma is considered homogeneous, with the approximation of geometrical optics applicable. Also, the wave frequency is very much greater than the characteristic plasma frequencies. Initially, the effect of dichroism will be neglected.

Consider a plane electromagnetic wave propagating through a plasma in a direction perpendicular to the magnetic field. This is a principal direction for which the characteristic waves are linearly polarised, with the wave electric field either parallel to, or orthogonal to, the magnetic field. If the initial plane of polarisation is at an angle, θ, to the magnetic field direction (see figure 1.11), then the wave can be resolved into the electric field components corresponding to the ordinary and extraordinary principal

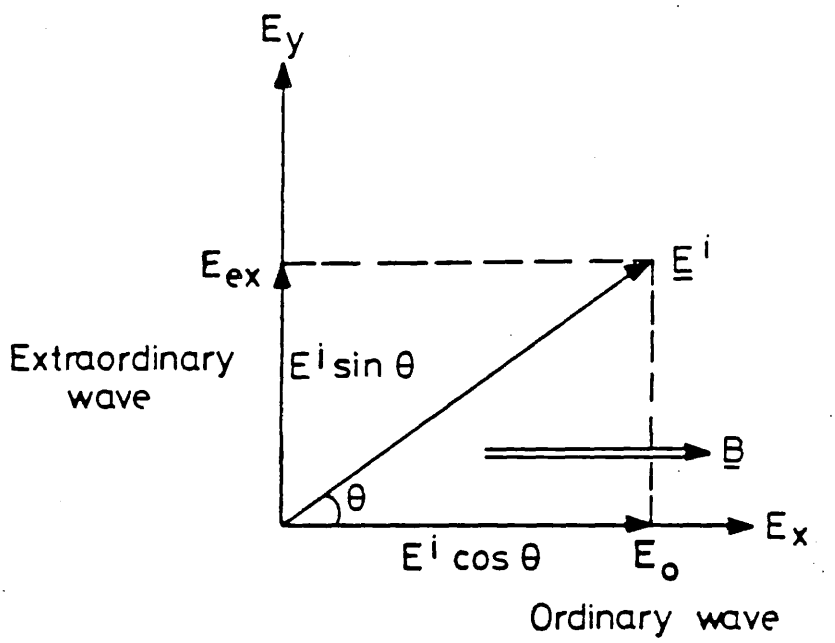

Figure 1.11

The ordinary and extraordinary characteristic wave components for wave propagation in a perpendicular direction to the magnetic field.

characteristic waves

$$E_o = E_x = a_x \cos \omega t \quad \text{and} \quad E_{ex} = E_y = a_y \cos \omega t \tag{1.69}$$

with amplitudes

$$a_x = E' \cos \theta \quad \text{and} \quad a_y = E' \sin \theta \tag{1.70}$$

where E' is the initial electric field amplitude. These initially have the same phase. After propagating through the plasma, along a path L, the characteristic waves have different phases due to their unequal phase velocities. The electric field components are then

$$E_o = a_x \cos(\omega t - \phi_o) \text{ and } E_{ex} = a_y \cos(\omega t - \phi_{ex}) \tag{1.71}$$

with phases

$$\phi_o = \frac{2\pi}{\lambda} \int_L \mu_o d\ell \quad \text{and} \quad \phi_{ex} = \frac{2\pi}{\lambda} \int_L \mu_{ex} d\ell \tag{1.72}$$

The equation for the resultant electric field is then obtained [34] by eliminating ωt from these equations, and the result is

$$\left(\frac{E_o}{a_x}\right)^2 + \left(\frac{E_{ex}}{a_y}\right)^2 - \frac{2E_o E_{ex}\cos\delta}{a_x a_y} = \sin^2\delta \qquad (1.73)$$

where $\delta=\phi_o-\phi_{ex}$ is the phase difference. This is the equation for an ellipse, which has the following properties: The azimuthal angle, ψ, of the major axis, measured anti-clockwise from the x-axis, is given by

$$\tan 2\psi = \tan 2\theta \cos \delta \qquad (1.74)$$

and the ellipticity, ε, by

$$\varepsilon = \tan \chi \qquad (1.75)$$

where $\chi\left(-\frac{\pi}{4} \leq \chi \leq \frac{\pi}{4}\right)$ is an angle defined by

$$\sin 2\chi = \sin 2\theta \sin \delta \qquad (1.76)$$

From equation 1.74, if the phase difference is small, such that $\cos\delta \cong 1$, the major axis of the ellipse will be parallel to the initial plane of polarisation. If it is not small, then only by having the initial plane of polarisation at the angle 0 or 90 degrees to the magnetic field will this be true. For a small phase difference which satisfies $\sin\delta \cong \tan\delta$, from equations 1.75 and 1.76, the ellipticity is approximately given by

$$\varepsilon \cong \frac{1}{2}\delta \sin 2\theta \qquad (1.77)$$

and has a maximum value when θ = 45 degrees. If θ = 0 or 90 degrees, the ellipticity is zero. Thus, birefringence will not be observed if the initial plane wave is also a characteristic wave.

The handedness of the polarisation ellipticity depends on the sign of $\tan\chi$, which in turn depends on the sign of $\sin\delta$. If δ is positive, then the polarisation is right-handed for an observer looking towards the source of light. If δ is negative, then the polarisation is left-handed. These labels correspond to the usual convention in optics, as discussed in section 1.3.1. In our case δ is positive, and so the polarisation is right-handed.

The phase difference, δ, can be expressed in terms of the plasma parameters by substituting the refractive indices for the ordinary and extraordinary waves, equations 1.31 and 1.32, giving

$$\delta = \frac{\pi}{\lambda} \int_L \frac{\omega_{pe}^2 \, \omega_{ce}^2}{\omega^4} \, d\ell \qquad (1.78)$$

Substituting for the plasma frequency, the cyclotron frequency, and the wave frequency, gives

$$\delta = D\lambda^3 \int_L n_e B^2 \, d\ell \qquad (1.79)$$

where

$$D = \frac{e^4}{16\pi^3 \varepsilon_o \, m_e^3 \, c^4} = 2.46 \times 10^{-11} \; m^{-1} T^{-2} \qquad (1.80)$$

Ellipticity due to birefringence therefore depends upon the cube of the wavelength, and the line integral of the product of electron density and the square of the magnetic field.

1.7.1 THE CYLINDRICAL PLASMA MODEL

In this section, the polarisation ellipticity arising from birefringence, for the case of an initially plane polarised wave propagating through a cylindrically symmetrical plasma, will be considered. For simplicity, the following assumptions apply. The wave propagates unrefracted only in the r-θ plane. The initial plane of

polarisation is at an angle σ from the plasma axis. The magnetic field is azimuthal.

The appropriate field factor for describing birefringence with this plasma geometry, is the square of the perpendicular field component. Substituting this factor, together with the expression for the optical path increment, into equation 1.79, gives the phase difference experienced by the wave at an impact parameter h

$$\delta(h) = 2D\lambda^3 \int_h^a n_e(r) B_\theta^2(r) (r^2-h^2)^{\frac{1}{2}} \frac{dr}{r} \qquad (1.81)$$

From equation 1.77, the ellipticity, assuming δ is small, is given by

$$\varepsilon(h) = \tfrac{1}{2}\delta(h) \sin 2\sigma \qquad (1.82)$$

Faraday rotation due to the parallel field component occurs simultaneously with the Cotton-Mouton effect. Since this will alter the azimuthal angle of the state of polarisation, then equation 1.82 is only approximate. A better approximation is obtained by adding the Faraday rotation angle to the initial azimuthal angle, i.e. equation 1.82 becomes

$$\varepsilon(h) \cong \tfrac{1}{2}\delta(h) \sin 2(\sigma+\psi(h)) \qquad (1.83)$$

From this equation, we see that in order to minimise the ellipticity - a requirement of accurate Faraday rotation measurements - the initial plane of polarisation must be chosen such that, with Faraday rotation, the wave appears most like either the ordinary or the extraordinary principal characteristic wave. Another factor which aids the minimisation of the ellipticity, is by a suitable choice of wavelength. Since the ellipticity scales as the wavelength cubed, while Faraday rotation scales only as the square, then by shortening the wavelength,

the ellipticity will decrease more rapidly than Faraday rotation. An optimum point will eventually be reached where the measurement becomes feasible.

The generalised problem of arbitrary wave propagation across a cylindrical plasma carrying both azimuthal and axial magnetic fields is not simply treated using the explicit methods so far adopted in this chapter. The coupling between Faraday rotation and birefringence cannot easily be included. This topic is covered in section 1.8.

1.7.2 THE EFFECT OF DICHROISM ON BIREFRINGENCE

The effect of characteristic wave attenuation on birefringence, can be shown by substituting the amplitudes of the field components given by equations 1.71, with the attenuated amplitudes. Thus, these equations become

$$E_o = a_x \, e^{-\int_L \alpha_o d\ell} \cos(\omega t - \phi_o)$$
$$E_{ex} = a_y \, e^{-\int_L \alpha_{ex} d\ell} \cos(\omega t - \phi_{ex}) \qquad (1.84)$$

and the problem is now equivalent to that when the initial plane of polarisation subtends an angle τ from the magnetic field, where τ is given by

$$\tan \tau = \tan \theta \, e^{-\int_L (\alpha_{ex} - \alpha_o) d\ell} \qquad (1.85)$$

rather than the true angle θ. The orientation of the polarisation ellipse, ψ, is then given by

$$\tan 2\psi = \tan 2\tau \cos \delta \qquad (1.86)$$

and the ellipticity from

$$\sin 2\chi = \sin 2\tau \sin \delta \qquad (1.87)$$

Therefore, the effect of dichroism is to alter both the angular position of the polarisation ellipse and its ellipticity. From equations 1.32 and 1.34, it can be shown that α_{ex} is greater than α_o. Therefore, τ is smaller than θ, and the ellipse lies closer to the x-axis with decreased ellipticity.

1.7.3 BIREFRINGENCE DUE TO DENSITY INHOMOGENEITY

If the approximation of geometrical optics is not satisfied, then effects can occur which lead to polarisation changes similar to birefringence [35]. This can be seen by considering the inhomogeneous wave equation for an unmagnetised, and therefore isotropic, plasma

$$\nabla^2 \underline{E} + \frac{1}{\varepsilon} \nabla(\underline{E}.\nabla\varepsilon) + \varepsilon k^2 \underline{E} = 0 \qquad (1.88)$$

where ε is the permittivity given by

$$\varepsilon = 1 - \frac{\omega_{pe}^2}{\omega^2} = \mu_o^2 \qquad (1.89)$$

If the plasma is cylindrically symmetric, so that the permittivity has a radial dependence only, then the scalar product $\underline{E}.\nabla\varepsilon = 0$ for waves polarised with their electric field parallel to the z-axis. It is non-zero for waves polarised orthogonally to the axis, and is given by

$$\frac{1}{\varepsilon}\nabla(\underline{E}.\nabla\varepsilon) \cong -\frac{\underline{E}}{L_n^2} \qquad (1.90)$$

where L_n is the electron density scale length. This leads to a phase retardation per unit length, δ', between these polarised waves of

$$\delta' \cong \frac{\lambda}{4\pi\mu_o L_n^2} \qquad (1.91)$$

which can become large if $(\lambda/L_n) >> 1$ i.e. if the approximation of

geometrical optics is not satisfied, or if $\mu_o \to 0$ which can occur if the wave frequency approaches the plasma frequency.

In conclusion, an inhomogeneous plasma will appear homogeneous to a wave if the condition of geometrical optics is satisfied, and will not be birefringent if the wave frequency is very much greater than the plasma frequency. Otherwise, birefringence can be minimised by choosing an initial plane of polarisation either parallel or perpendicular to the axis of symmetry.

1.8 A GENERAL THEORY OF FARADAY ROTATION AND BIREFRINGENCE

The theories derived for Faraday rotation and birefringence, neglected the coupling between these effects when a wave is not propagating along a principle direction, as in the cylindrical plasma model. Heald [36] examined this coupling for the particular case of wave propagation in a homogeneous plasma with a helical magnetic field. However, de Marco and Segre [37] were the first to consider the general problem of wave propagation in an inhomogeneous plasma with a spatially varying magnetic field. This work was further developed by Craig [38], and by Segre [39]. It is this latter work which is described below. The approximation of geometrical optics is assumed, as is the high frequency limit. Dichroism is neglected.

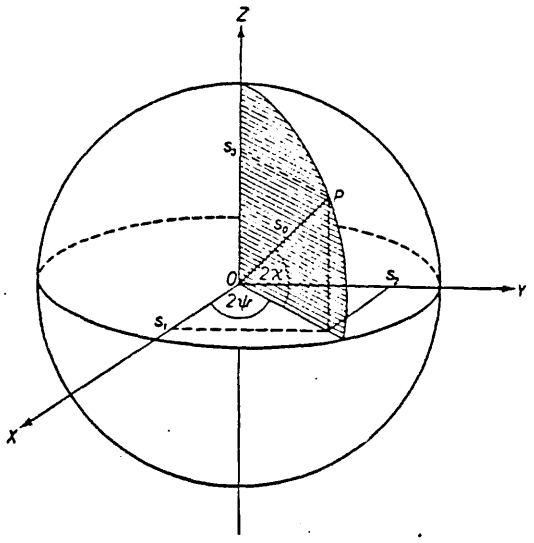

Figure 1.12

The Poincaré sphere.

The two angles ψ and χ define the state of elliptical polarisation (cf section 1.7). From these two angles, every state of polarisation can be uniquely specified.

On the surface of a sphere of unit radius, called the Poincaré sphere [34,40,41], each state of polarisation is represented by a point S, whose latitude and longitude are 2χ and 2ψ respectively, as shown in figure 1.12. The cartesian coordinates of the point S are called the Stokes parameters, and define the polarisation vector $\underline{S}$ [34]

$$\underline{S} = \begin{bmatrix} \cos 2\chi \cos 2\psi \\ \cos 2\chi \sin 2\psi \\ \sin 2\chi \end{bmatrix} \qquad (1.92)$$

Any polarised wave can be resolved into two orthogonally polarised waves, and two states of polarisation (χ_1, ψ_1), (χ_2, ψ_2) are orthogonal

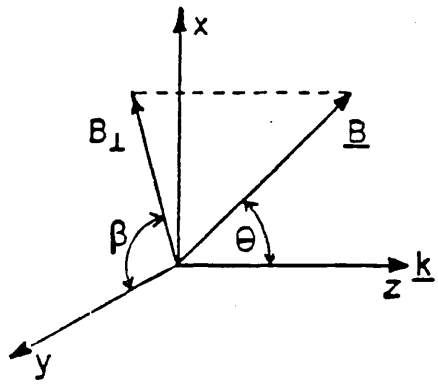

Figure 1.13

Coordinate system for wave propagation in an arbitrary direction to the magnetic field.

if

$$\psi_2 = \psi_1 + \frac{\pi}{2} \text{ and } \chi_2 = -\chi_1 \qquad (1.93)$$

These are represented on the surface of the Poincaré sphere by two diametrically opposite points.

The change in the polarisation state of a plane wave propagating in the Z direction, at an angle θ to the magnetic field, through a thin slab of plasma, as shown in figure 1.13, can be represented on the Poincaré sphere by a rotation of the point S, representing the wave's initial polarisation state, about an axis which joins the diametrically opposite points representing the orthogonally polarised characteristic waves. The angle of rotation is the phase difference arising after propagating through the slab, and the direction of rotation clockwise for an observer looking towards the origin of the vector representing the fastest characteristic wave [40,41]. The change in the

polarisation state is then described by the differential equation [37,39]

$$\frac{d\underline{S}}{dz} = \underline{\Omega} \times \underline{S} \qquad (1.94)$$

where

$$\underline{\Omega} = \frac{\omega}{c}(\mu_S - \mu_F)\underline{S}_F \qquad (1.95)$$

is the vector which describes the rotation of the Poincare' sphere, and has the direction of the vector which describes the fast characteristic wave. The subscripts S and F refer to the slow and fast characteristic waves respectively.

The polarisation vector of the fast characteristic wave, $\underline{S}_F$, is obtained from the wave polarisation coefficient R_- (see section 1.2), and from the orientation of the magnetic field. For the coordinate system employed (see figure 1.13), the azimuthal angle of the fast characteristic wave ψ_F is given by

$$\psi_F = -\beta \qquad (1.96)$$

where β is the angle between the y-axis and the perpendicular component of the magnetic field. The ellipticity is given by equation 1.21, and therefore

$$\tan \chi_F = \frac{1}{F}\left((1+F^2)^{\frac{1}{2}}-1\right) \qquad (1.97)$$

where F is defined by equation 1.18. The polarisation vector follows [39]

$$\underline{S}_F = \begin{Bmatrix} \cos 2\beta\ (1+F^2)^{-\frac{1}{2}} \\ -\sin 2\beta\ (1+F^2)^{-\frac{1}{2}} \\ F(1+F^2)^{-\frac{1}{2}} \end{Bmatrix} \qquad (1.98)$$

The difference of the refractive indices $\mu_S - \mu_F$ is obtained from Appleton's equation (equation 1.15), and in the high frequency limit, is given in terms of the magnetic field cartesian components by

$$\mu_S - \mu_F = \frac{\mu_S^2 - \mu_F^2}{\mu_S + \mu_F} = \frac{\omega_{pe}^2}{\omega^4}\left(\frac{e}{m_e}\right)^2 \left\{ \frac{B_x^2 + B_y^2}{1 - \frac{\omega_{pe}^2}{\omega^2}} \right\} \frac{(1+F^2)^{\frac{1}{2}}}{(\mu_S + \mu_F)T} \qquad (1.99)$$

where the dimensionless parameter T is defined as

$$T = 1 - \left(\frac{e}{\omega m_e}\right)^2 \left\{ \frac{B_x^2 + B_y^2}{1 - \frac{\omega_{pe}^2}{\omega^2}} + B_z^2 \right\} \qquad (1.100)$$

For the generalised magnetic field geometry, with respect to the wave's direction of propagation as depicted in figure 1.13, substituting the relavant sines and cosines of the angles θ and β, in terms of the x,y, and z magnetic field components, gives the vector $\underline{\Omega}$ describing the rotation of the Poincare' sphere

$$\underline{\Omega} = \frac{\omega_{pe}^2}{(\mu_S + \mu_F)c\omega^3 T} \begin{bmatrix} \left(\frac{e}{m_e}\right)^2 \left[\frac{B_y^2 - B_x^2}{1 - \omega_{pe}^2/\omega^2}\right] \\ -\left(\frac{e}{m_e}\right)^2 \left[\frac{2B_x B_y}{1 - \omega_{pe}^2/\omega^2}\right] \\ 2\omega\left(\frac{e}{m_e}\right) B_z \end{bmatrix} \qquad (1.101)$$

The evolution of the Stokes vector $\underline{S}$ along the optical path of the wave, may be determined by solving the three coupled first-order differential equations (equation 1.94)

$$\begin{aligned} \frac{dS_x}{dz} &= S_z\Omega_y - \Omega_z S_y \\ \frac{dS_y}{dz} &= S_x\Omega_z - \Omega_x S_z \\ \frac{dS_z}{dz} &= S_y\Omega_x - \Omega_y S_x \end{aligned} \qquad (1.102)$$

These would normally be solved numerically, starting from the initial polarisation state (χ_o, ψ_o) and the initial position Z_o. The path of integration is that of the wave through the plasma. Since

$S_x^2 + S_y^2 + S_z^2 = 1$, it is possible to reduce the number of coupled equations to two, but in order to check the accuracy of the numerical solution, all three must be retained. The azimuthal angle and ellipticity of the wave emerging from the plasma, are obtained from the final polarisation vector component values, and are given by

$$\psi = \frac{1}{2} \tan^{-1}\left(\frac{S_y}{S_x}\right) \tag{1.103}$$

and

$$\varepsilon = \frac{S_z}{1 + (1-S_z^2)^{\frac{1}{2}}} \tag{1.104}$$

This theoretical treatment can be applied to any magnetic field geometry when the cartesian components of the magnetic field along the optical path of the wave can be specified. For the particular case when the wave propagates parallel to the magnetic field, i.e. $\theta = 0^\circ$, the wave should experience Faraday rotation without change in polarisation ellipticity. With the magnetic field components B_x and B_y set to zero, the dimensionless parameter T is given by

$$T = 1 - \frac{\omega_{ce}^2}{\omega^2} \tag{1.105}$$

In the high frequency limit $\omega_{ce} << \omega$; and therefore $T \cong 1$. Also the sum of the refractive indices $\mu_S + \mu_F \cong 2$. Thus, the rotation vector $\underline{\Omega}$ is given by

$$\underline{\Omega} = \left(0,\ 0,\ \frac{\omega_{pe}^2\ \omega_{ce}}{c\omega^2}\right) \tag{1.106}$$

and the evolution of the Stokes vector by

$$\frac{d\underline{S}}{dz} = (-\Omega_z S_y,\ \Omega_z S_x,\ 0) \tag{1.107}$$

Since $dS_z/dz = 0$, then $\sin 2\chi$ or the ellipticity of the wave remains constant, as expected. Therefore, holding χ constant, and differentiating S_x explicitly with respect to Z, we obtain

$$\frac{dS_x}{dz} = -2S_y \frac{d\psi}{dz} = -\Omega_z S_y \qquad (1.108)$$

The evolution of the azimuthal angle, i.e. Faraday rotation, along the optical path is then given by

$$\frac{d\psi}{dz} = \frac{1}{2} \frac{\omega_{pe}^2 \omega_{ce}}{c\omega^2} \qquad (1.109)$$

which on integration, gives a result identical to equation 1.49 for pure Faraday rotation.

1.9 REFRACTION

In the theory described in the previous sections, it was assumed that refraction of the wave propagating across the plasma was negligible. However, if this is not so, the line integrals must be taken over the actual ray trajectory. In this section, the theory of refraction is reviewed.

A ray incident on a cylindrically symmetrical plasma in the r-θ plane, follows a path which satisfies Bouguer's formula [34]

$$\mu(r)\, r \sin\phi = \text{constant} \qquad (1.110)$$

where ϕ is the angle between the tangent at a point on the ray path and the radius vector to the point. If h is the ray's impact parameter (see figure 1.14), then at the plasma radius a, the refractive index is unity, and $\phi=\pi-\sin^{-1}\frac{h}{a}$. Therefore the constant in Bouguer's formula is just the impact parameter h.

If (r,θ) are the polar coordinates of a plane curve, then the angle

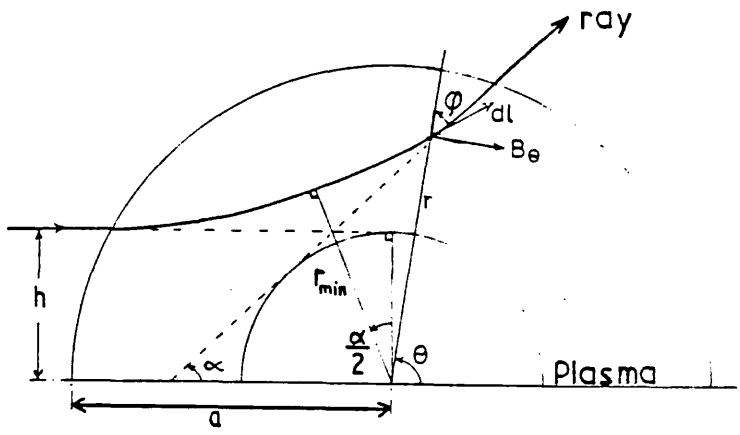

Figure 1.14

Refraction of a ray by a cylindrical plasma.

θ is given by

$$\sin \phi = r\left(r^2 + \left[\frac{dr}{d\theta}\right]^2\right)^{-\frac{1}{2}} \qquad (1.111)$$

Substitution into equation 1.110, squaring and rearranging, gives the ray path derivative [34]

$$\frac{d\theta}{dr} = \pm \frac{h}{r}\left(\mu^2 r^2 - h^2\right)^{-\frac{1}{2}} \qquad (1.112)$$

This simple result can also be derived from Snell's law as by Wort [42], and from Fermat's principle using the calculus of variations as by Schreiber et al [43].

From this result, the derivative $dr/d\theta$ is zero when $h = \mu(r)r$. This occurs when the ray has approached the axis to a minimum distance r_{min} given by

$$r_{min} = \frac{h}{\mu(r_{min})} \tag{1.113}$$

At this point, $\phi = \frac{\pi}{2}$ and $\theta = \frac{1}{2}(\pi+\alpha)$, where α is the refraction or deflection angle. On exit from the plasma, both θ and ϕ have minimum values θ_m and ϕ_m respectively, related by

$$\theta_m = \alpha + \phi_m \tag{1.114}$$

Therefore, integrating equation 1.112 between the radial limits r_{min} and a, then gives

$$\int_{\frac{1}{2}(\pi+\alpha)}^{\alpha+\phi_m} d\theta = -h \int_{r_{min}}^{a} \frac{1}{r} (\mu^2 r^2 - h^2)^{-\frac{1}{2}} dr \tag{1.115}$$

From Bouguer's formula, $\phi_m = \sin^{-1} \frac{h}{a}$, and so the refraction angle is given by

$$\alpha = 2\cos^{-1}(\frac{h}{a}) - 2h\int_{r_{min}}^{a} \frac{1}{r} (\mu^2 r^2 - h^2)^{-\frac{1}{2}} dr \tag{1.116}$$

If this is not negligible, then the incremental change in path length along the ray trajectory is given by

$$d\ell = \mu r (\mu^2 r^2 - h^2)^{-\frac{1}{2}} dr \tag{1.117}$$

These results can be extended to the case of a ray incident on a cylindrically symmetrical plasma, at an angle Ω from the r-θ plane and with an impact parameter h (see figure 1.15). Bouguer's formula then becomes [44]

$$\mu(r) r \sin\phi \cos\omega = h \cos\Omega$$

with $$\mu(r) \sin\omega = \sin\Omega \tag{1.118}$$

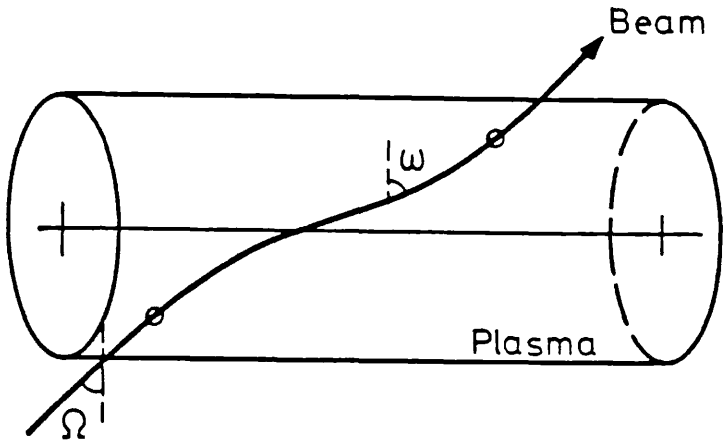

Figure 1.15

Refraction of a ray propagating at an arbitrary angle to the r-θ plane.

The angle Ω is as before, and the angle ω is that angle between the tangent to the ray at a point and the r-θ plane at the point. The second of these equations implies that the ray will emerge from the plasma in a plane inclined at the incidence angle Ω from the r-θ plane.

The ray path derivatives can be derived from Snell's law as by Heald [44]. However, an extension to the work of Schreiber et al [43], by the inclusion of a third dimension, is less cumbersome algebraically and gives identical results. The mathematical details of this extension are given in Appendix A. The ray path derivatives derived therein are

$$\frac{dz}{dr} = \pm\, r\sin\Omega(\mu^2 r^2 - r^2\sin^2\Omega - h^2\cos^2\Omega)^{-\frac{1}{2}}$$

$$\frac{d\theta}{dr} = \pm\, (\frac{h}{r})\cos\Omega(\mu^2 r^2 - r^2\sin^2\Omega - h^2\cos^2\Omega)^{-\frac{1}{2}} \qquad (1.119)$$

The minimum radius r_{min} is given by

$$r_{min} = h \cos\Omega \quad (\mu^2(r_{min})-\sin^2\Omega)^{-\frac{1}{2}} \tag{1.120}$$

and following a similar argument to that above, the refraction angle is given by

$$\alpha = 2\cos^{-1}(\frac{h}{a}) - 2h\cos\Omega\int_{r_{min}}^{a}\frac{1}{r}(\mu^2r^2-r^2\sin^2\Omega-h^2\cos^2\Omega)^{-\frac{1}{2}}dr \tag{1.121}$$

In addition to a θ deflection, the ray will suffer an axial displacement ΔZ. If the ray enters the plasma at an axial position $Z = 0$, it will emerge at the position Z_1 given by

$$Z_1 = 2\sin\Omega\int_{r_{min}}^{a} r(\mu^2r^2-r^2\sin^2\Omega-h^2\cos^2\Omega)^{-\frac{1}{2}}dr \tag{1.122}$$

In the absence of plasma, the ray would have arrived at the position Z_o given by

$$Z_o = 2\tan\Omega(a^2-h^2)^{\frac{1}{2}} \tag{1.123}$$

Therefore, the axial displacement is simply given by the difference

$$\Delta Z = Z_1 - Z_o \tag{1.124}$$

The incremental change in path length is given by

$$d\ell = \mu r(\mu^2r^2-r^2\sin^2\Omega-h^2\cos^2\Omega)^{-\frac{1}{2}}dl \tag{1.125}$$

1.10 APPLICATION OF THE THEORY

In this section, the theories of Faraday rotation, dichroism, birefringence, and refraction, are applied to the particular case of a cylindrically symmetrical plasma, in which the electron density varies linearly with radius, and in which the axial current density is constant. In addition, the effect of a constant axial magnetic field will be examined. The aim is to derive simple analytic expressions useful to the experimentalist.

The linear electron density profile may be represented by

$$n_e(r) = n_{eo}(1 - \frac{r}{a}) \tag{1.126}$$

where n_{eo} is the axial electron density, and a is the plasma radius. The azimuthal magnetic field also varies linearly with radius, as a result of the constant axial current density, and is expressed by

$$B_\theta(r) = \frac{\mu_o I_p}{2\pi a^2} r \tag{1.127}$$

where I_p is the plasma current.

1.10.1 FARADAY ROTATION

The Faraday rotation experienced by a probe beam propagating in the r-θ plane of the plasma is given by equation 1.53. Substituting for the electron density and azimuthal magnetic field profiles, on integration, we obtain

$$\psi_\theta(h) = \frac{A\mu_o n_{eo} I_p \lambda^2 h}{2\pi a^2} \left\{ (a^2-h^2)^{\frac{1}{2}} - \frac{h^2}{a} \ln\left[\frac{a+(a^2-h^2)^{\frac{1}{2}}}{h} \right] \right\} \quad (1.128)$$

The maximum value, $\psi_{m\theta}$, occurs when h = 0.45a, and is given by

$$\psi_{m\theta} = 1.42 \times 10^{-20} n_{eo} I_p \lambda^2 \quad (1.129)$$

This is a useful result. It gives a good estimate of the Faraday rotation that may be expected from a plasma having approximately linear density and magnetic field profiles.

Consider, for example, the Faraday rotation of a ruby laser probe beam by a Plasma Focus. At the wavelength of this laser, 694.3 nm, the approximation of geometrical optics and the high frequency limit are both satisfied. Assuming an axial electron density of 4.0×10^{25} m^{-3}, and a plasma current of 340 kA (the measured values at peak compression of the pinch), the maximum Faraday rotation angle, assuming linear profiles, would be 93 mrad or 5.3 degrees. The maximum rotation observed in the Plasma Focus experiment, apart from that when axial filamentation occured, was approximately 0.5°, which is smaller than expected by a factor 10. This discrepency arises because the magnetic field of the Plasma Focus, at this time, is located at the plasma edge due to the skin effect, and does not vary linearly as assumed by equation 1.129. When the experiment was originally conceived, the plasma current was thought to be nearer 500 kA, which gave a very

optimistic estimate of the Faraday rotation angle.

If the plasma has an axial magnetic field, then the partial Faraday rotation angle experienced by a probe beam at an angle Ω from the r-θ plane, due to the parallel component of axial field, is given by equation 1.54. On substituting for the electron density, and integrating, we obtain

$$\psi_z(h) = A\lambda^2 B_z n_{eo} \tan \Omega \left\{ (a^2-h^2)^{\frac{1}{2}} - \frac{h^2}{a} \ell n \left[\frac{a+(a^2-h^2)^{\frac{1}{2}}}{h} \right] \right\} \qquad (1.130)$$

which has a maximum value when h = 0. This is dependent upon the plasma radius, unlike ψ_θ.

A useful result is obtained by comparing the partial rotation angles ψ_z and ψ_θ, as the ratio ψ_z / ψ_θ. Then,

$$\frac{\psi_z}{\psi_\theta} = \tan \Omega \left(\frac{a}{h} \right) \left(\frac{B_z}{B_{\theta a}} \right) \qquad (1.131)$$

where $B_{\theta a}$ is the value of the azimuthal magnetic field at the plasma radius. This equation quantifies the effect of probe beam misalignment from the r-θ plane, in the presence of an axial magnetic field. A maximum tolerable misalignment angle, Ω_m, can be determined given a maximum tolerable partial rotation ψ_{zm}. Setting ψ_{zm} as 10% of ψ_θ, so that $\psi_z / \psi_\theta = 0.1$, the maximum misalignment angle becomes

$$\Omega_m = \tan^{-1} \left\{ 0.1 \left(\frac{h}{a} \right) \left(\frac{B_{\theta a}}{B_z} \right) \right\} \qquad (1.132)$$

For example, if the field ratio $B_{\theta a}/B_z = 1$, then at an impact parameter of h = 0.45a, which gives maximum ψ_θ, the maximum misalignment angle is 2.6°. In Tokamak plasmas, the field ratio is nearer 0.25, and so the problem is more accute as the tolerable

misalignment angle becomes 0.64°. This may be a serious problem in these devices.

In the Plasma Focus, a self generated axial magnetic field may exist [45], with approximately the magnitude of the azimuthal magnetic field. Assuming this is correct, then the first result above applies to the Plasma Focus.

1.10.2 DICHROISM

Given an azimuthal magnetic field only, and a constant electron temperature profile, a probe beam propagating in the r-θ plane will experience ellipticity due to dichroism given by

$$\varepsilon(h) = \frac{C\mu_o I_p n_{eo}^3 \ell n\Lambda \lambda^5 h}{\pi a^2 T_{eo}^{3/2}} \left\{ (a^2-h^2)^{\frac{1}{2}} \left[\frac{1}{4} + \frac{13h^2}{8a^2}\right] - \frac{3h^2}{2a} \ell n \left[\frac{a+(a^2-h^2)^{\frac{1}{2}}}{h}\right]\right\} \tag{1.133}$$

where T_{eo} is the electron temperature. This expression is obtained from equation 1.67, after substitution for the appropriate plasma profiles, by integrating with the assumption that $\ln\Lambda$ is constant. The ellipticity has a maximum value when h = 0.9a, i.e. at the plasma edge. Of interest is the ellipticity at impact parameter h = 0.45a, which is

$$\varepsilon(0.45a) = 3.3\times10^{-51} \lambda^5 n_{eo}^3 I_p T_{eo}^{-3/2} \ell n\Lambda \tag{1.134}$$

Taking again the Plasma Focus as an example, a plane polarised ruby laser probe beam will emerge with an ellipticity of 4×10^{-9}, assuming an electron temperature of 800 eV at peak compression. This value of ellipticity is very small, which is typical of the ellipticity obtained with most laboratory plasmas at wavelengths suitable for Faraday

rotation experiments. The estimate calculated on the assumption of a constant temperature is an underestimate, as near to the plasma edge where the major contribution exists, the electron temperature is least and the plasma more collisional.

The theory so far developed has assumed classical collisionality. In plasmas where anomalous collisionality occurs, the ellipticity will be larger than that calculated by a factor given by the enhancement of the actual collision frequency over the classical frequency. In the Plasma Focus, the rapid magnetic field diffusion observed after peak compression of the pinch, has been interpreted as being due to an anomalous resistivity approximately 6000 times the classical value. Therefore, the ellipticity of the probe beam must be larger than that calculated by this factor, and so, $\varepsilon = 2.4 \times 10^{-5}$. However, this is not large enough to have affected the measurement of Faraday rotation.

1.10.3 BIREFRINGENCE

In the absence of an axial magnetic field, the phase difference between the ordinary and extraordinary characteristic waves of a plane polarised probe beam in the r-θ plane, on integration of equation 1.81 with the assumed linear plasma profiles, is given by

$$\delta = \delta_m (a^2 - \frac{5}{2}h^2)(a^2-h^2)^{\frac{1}{2}} \qquad (1.135)$$

where

$$\delta_m = \frac{D\mu_o^2 I_p^2 n_{eo} \lambda^3}{24\pi^2 a^4} \qquad (1.136)$$

is the maximum value, and occurs when h = 0. At an impact parameter h = 0.45a, the phase difference is

$$\delta(0.45a) = 1.03 \times 10^{-25} \frac{\lambda^3 n_{eo} I_p^2}{a} \qquad (1.137)$$

At peak compression of the Plasma Focus, the plasma radius is 2.35 mm. For the ruby laser probe beam, the phase difference between the characteristic waves is 6.8×10^{-5}. The maximum ellipticity due to birefringence is $\delta/2$, i.e. 3.4×10^{-5}, and occurs when the initial plane of polarisation is approximately 45° to the r-θ plane. This value of ellipticity is larger than that due to dichroism, and would not have affected the measurement of Faraday rotation. In the experiment, the initial plane of polarisation was approximately 10° from the r-θ plane, giving an ellipticity of 1.2×10^{-5}.

Consider the effect of a constant axial magnetic field. Assuming $B_z >> B_\theta$, then for propagation in the r-θ plane, the phase difference between the characteristic waves is

$$\delta(h) = D\lambda^3 n_{eo} B_z^2 \left\{ (a^2-h^2)^{\frac{1}{2}} - \frac{h^2}{a} \ln\left[\frac{a+(a^2-h^2)^{\frac{1}{2}}}{h} \right] \right\} \qquad (1.138)$$

which has a maximum value when h = 0. Therefore, the maximum value of polarisation ellipticity is

$$\varepsilon = \frac{1}{2} D\lambda^3 n_{eo} B_z^2 a \qquad (1.139)$$

This result is useful when plasmas such as the Tokamak are considered for Faraday rotation experiments.

1.10.4 REFRACTION

The problem of refraction is not easily solved analytically. One approach is to solve the refraction equations numerically assuming appropriate electron density profiles. The dependence on wavelength and electron density can then be analysed. Only the deflection angle α, for refraction in the r-θ plane, will be considered.

From equation 1.116, substituting the dimensionless parameters H = h/a and R = r/a, we obtain

$$\alpha(H) = 2\cos^{-1} H - 2H\int_{R_m}^{1} (\mu^2 R^2 - H)^{-\frac{1}{2}} \frac{dR}{R} \qquad (1.140)$$

where μ is the refractive index, and R_m is the normalised minimum radius. From this expression, we see that the deflection angle is independent of the plasma radius. Writing the electron density as $n_e(r) = n_{eo} f(R)$, where f(R) is a function describing the profile, the refractive index, assumed to be that of the ordinary characteristic wave and given by equation 1.31, is

$$\mu(R) = \left(1 - \frac{n_{eo}}{n_c} f(R)\right)^{\frac{1}{2}} \qquad (1.141)$$

where n_c is the critical electron density, defined by

$$n_c = \frac{4\pi^2 c^2 \varepsilon_o m_e \lambda^2}{e^2} \qquad (1.142)$$

Therefore, apart from the functional form of the electron density profile, the deflection angle is dependent only on the ratio n_{eo}/n_c.

Assuming a linear electron density profile, numerical solution of equation 1.140 shows that the maximum deflection occurs at an impact parameter $h \cong 0.5a$. The magnitude of the maximum deflection, α_m, varies approximately linearly with the ratio n_{eo}/n_c, and is given by

$$\alpha_m \cong 0.7\ (n_{eo}/n_c) \text{ radians}, \qquad (1.143)$$

valid in the ratio range $0.001 \leqslant n_{eo}/n_c \leqslant 0.1$. Since the critical electron density scales as $1/\lambda^2$, the maximum deflection is proportional to the wavelength squared. It is also proportional to the axial electron density.

If a parabolic density profile is assumed, expressed by $n_e(R) = n_{eo}(1 - R^2)$, numerical solution of equation 1.140, gives the

result that the maximum deflection occurs at an impact parameter $h \cong 0.65a$. The magnitude of the maximum deflection also varies linearly with the ratio n_{eo}/n_c, and is given by

$$\alpha_m \cong (n_{eo}/n_c) \text{ radians} \qquad (1.144)$$

valid within the range quoted above.

Consider, for example, the refraction experienced by a ruby laser beam probing the Plasma Focus. For the ruby laser wavelength, the critical electron density is 2.3×10^{27} m^{-3}. Therefore, assuming an axial electron density of 4.0×10^{25} m^{-3}, the ratio $n_{eo}/n_c = 0.0174$. From equations 1.143 and 1.144, the maximum beam deflection is 12.2 mrad (0.7 degrees) and 17.4 mrad (1.0 degree) for linear and parabolic density profiles respectively. The maximum refraction angle that can be expected from the Plasma Focus, at peak compression of the pinch, is therefore 17.4 mrad. This result is in good agreement with the values measured by Morgan [46].

CHAPTER 2 DESCRIPTION OF THE PLASMA FOCUS AND DIAGNOSTICS

In this chapter, a description of the Plasma Focus device and its associated diagnostics, electrical and optical, Faraday rotation excepted, are given. The timing control system used to synchronise the Plasma Focus with the ruby laser diagnostics, is also discussed.

2.1 DESCRIPTION OF THE PLASMA FOCUS

The Culham Plasma Focus device [15], its operation, and its electrical and neutron diagnostics, are described in this section. Theoretical descriptions of the physics of the Plasma Focus, have been given by Mather [14], and by Morgan [46], and are not discussed here.

2.1.1 MECHANICAL CONSTRUCTION

The mechanical layout of the Plasma Focus electrodes, vacuum vessel, and electrical connections, are shown schematically in figure 2.1. The centre electrode (1) - the anode - was a solid copper cylinder of diameter 50 mm, with a heavy metal section (95% W + 5% Cu) of length 30 mm, at the lower end. This reduced electrode erosion due to electron bombardment. A small hole at the centre of the capped end was necessary for reproducible operation. The centre electrode was connected to the brass high-voltage plate (2).

The copper outer cylindrical electrode (3) was of internal diameter 92 mm, and length 230 mm. It was perforated by 228 regularly arranged

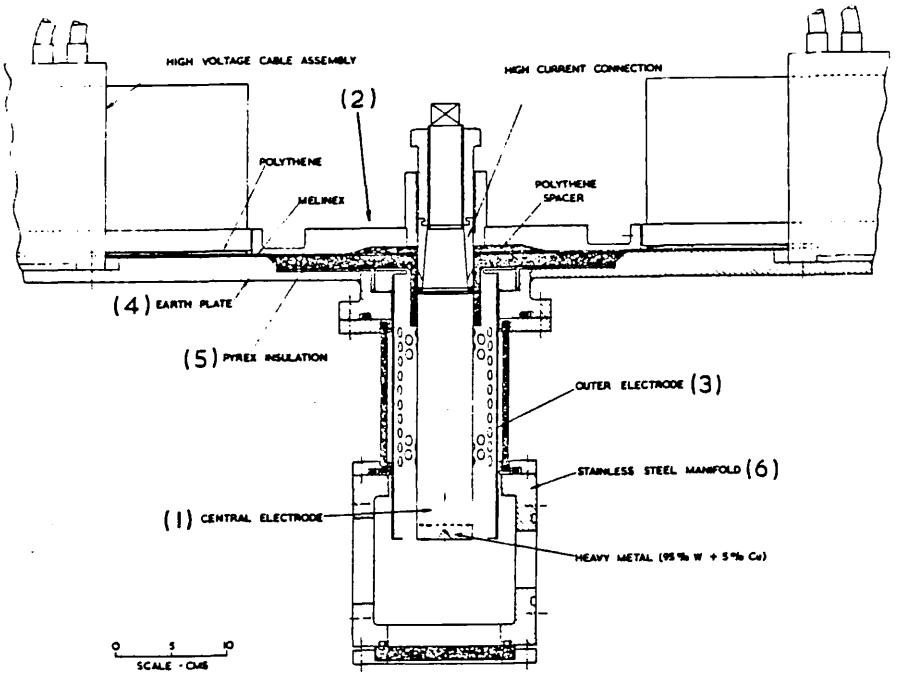

Figure 2.1

Mechanical construction of the Plasma Focus.

9.5 mm diameter circular holes, which improved machine performance [47]. The electrode was connected to the brass earth plate (4). The high voltage plate was insulated from the earth plate by interleaved polythene and melinex sheets.

A 'top-hat' pyrex insulator (5) separated the two electrodes. The tubular sleeve of this insulator had an outer diameter of 63.5 mm, and extended 46 mm into the gun.

The two electrodes projected into an octagonal stainless steel vacuum chamber (6), with five 50 mm diameter and three 75 mm diameter diagnostic ports, arranged one per side. Below the gun was a 100 mm diameter port. Attached to this was a 600 mm long pyrex tube, used to

trap eroded material and dissipate the kinetic energy of the plasma.

2.1.2 THE CAPACITOR BANK AND SUPPLY LINES

Electrical energy was stored in a 40 kV (maximum), 93.85 micro-Farad capacitor bank. Typically, this bank was charged to a voltage of 24.1 kV, where the stored energy was 27.25 kJ. The 32 capacitors, each of capacity ≅ 3 micro-Farads, were charged by a high voltage d.c. power supply consisting of a step-up transformer and half-wave rectifier, in conjunction with a voltage doubling circuit. A maximum current of 200 mA at 50 kV could be delivered to the capacitor bank by this supply.

The capacitor bank was modular in design. Each of the four modules was divided into two separate circuits, individually switched by a 3-electrode swinging-cascade spark-gap. These switches connected the capacitors to the high voltage and earth plates of the Plasma Focus via 216 parallel coaxial cables. This number of parallel cables, in addition to the 8 parallel spark-gap switches, resulted in a low source inductance of 33.7 nH, and a source resistance of 2.25 milli-Ohms.

The spark-gaps were triggered by a 35 kV Blumlein cable, itself switched by a master spark-gap. This master spark-gap was triggered by a 15 kV thyratron voltage pulse. Typically, 25 ± 5 ns elapsed between application of the trigger pulse and current conduction. The eight spark-gaps were well synchronised in comparison to the 2.8 micro-seconds quarter period of the discharge.

2.1.3 THE VACUUM AND GAS FILLING SYSTEM

A 150 mm diameter oil diffusion pump, backed by a single stage rotary oil pump of capacity 450 litres per minute at 100 torr pressure, evacuated both the vacuum chamber and electrode gun assembly. To reduce oil vapour pressure in the vacuum chamber, a refrigerated baffle was used in the throat of the diffusion pump. Adjacent to this baffle was a remotely controlled isolation valve. Typically a base pressure of 5×10^{-5} torr was achieved.

Pressures were measured using three guages. For the pressure range 100 to 10 torr, a Pirani guage was used. Pressures below 1 milli-torr were measured with an ionisation guage. Accurate pressure filling of the system with deuterium was achieved with a mercury manometer. The deuterium gas filling was introduced by a hot-wire leak valve, remotely operated from the control panel.

2.1.4 OPERATION OF THE PLASMA FOCUS DEVICE

The operation of the Plasma Focus was as follows:

a) The chamber was evacuated to a base pressure of $\sim 5 \times 10^{-5}$ torr.

b) The diffusion pump isolation valve was closed.

c) The chamber and gun were filled with deuterium to the operating pressure of 1.8 torr.

d) The Blumlein trigger cable was charged to 35 kV.

e) The capacitor bank was charged to the operating voltage of 24.1 kV.

f) The discharge was initiated.

Typically 10 to 20 discharges were fired on a single gas filling before the procedure was repeated.

When the machine had been pumped down from atmospheric pressure, approximately 50 shots were fired to condition the electrodes. This aided reproducibility.

Optimum energy transfer to the plasma was achieved when the operating voltage and filling pressure were chosen so that peak compression of the pinch occured at the time of the discharge circuit current maximum. At this time, all the energy is stored inductively (the capacitor bank voltage is approximately zero), and the plasma can extract energy from a maximised magnetic field. The operating conditions used in this experiment (24.1 kV, 1.8 torr D_2) were chosen for optimum energy transfer.

2.1.5 BASIC DIAGNOSTICS

There were three basic diagnostics used on the Plasma Focus. These monitored the supply current, the gun voltage, and the total neutron yield of the plasma.

Rogowskii Coil

The discharge current from the capacitor bank was measured using a Rogowskii coil looped around the gun between the high voltage and earth plates, enclosing the current flow. The voltage proportional to dI/dt induced in this coil, was sampled using a potential divider, and integrated using a passive RC integrating circuit with a 80 micro-seconds time constant. The output voltage of the integrating circuit was proportional to the discharge current. Calibration was

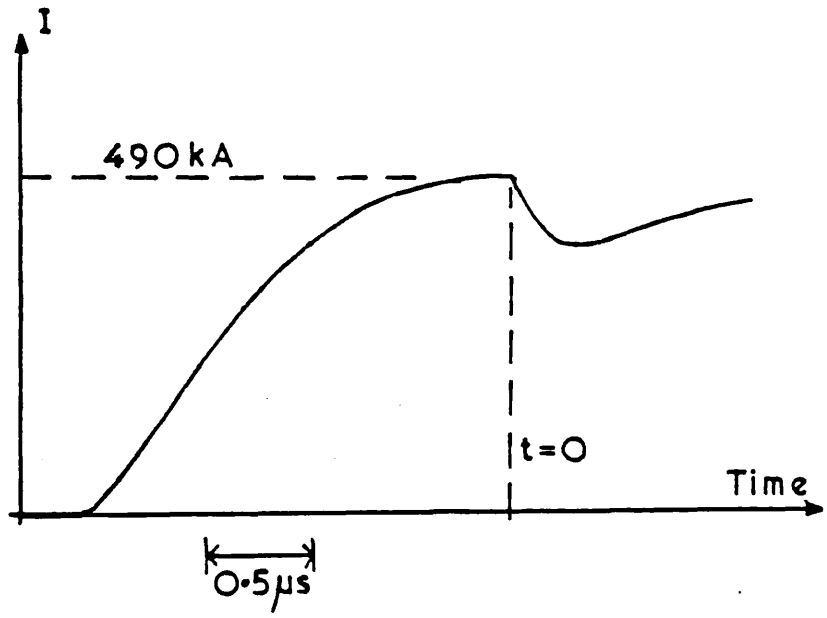

Figure 2.2

Plasma Focus current waveform.

achieved by observing the 'ringing' of the circuit current when the high voltage and earth plates were short circuited.

A current waveform observed during a discharge is shown in figure 2.2. Peak current is approximately 490kA. The dip in the waveform is characteristic of the Plasma Focus. It begins at peak compression of the pinch, and is due to the rapid inductive changes that occur at this time.

The Rogowskii coil voltage was extremely useful as a timing marker. At the time of peak compression, the coil voltage rapidly increased to a maximum, then oscillated before decaying. This rapid first voltage rise, shown in figure 2.3, is called the 'dI/dt singularity', and coincided exactly with the time when peak compression of the pinch occured adjacent ($Z < 10$ mm) to the centre electrode, as observed by

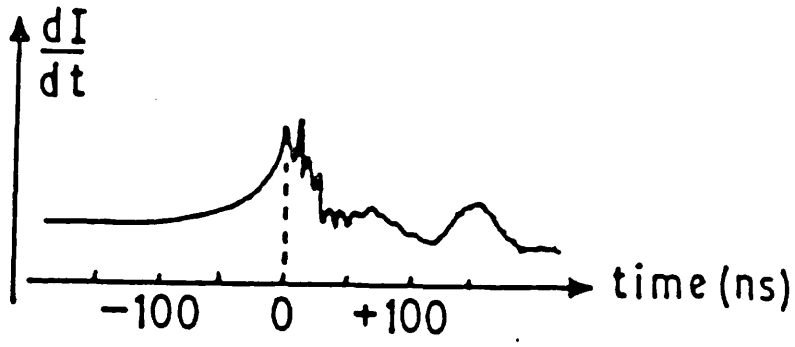

Figure 2.3

The Plasma Focus dI/dt waveform.

holographic interferometry. By comparing the time of the dI/dt singularity with the time when the Faraday rotation probe beam was incident on the plasma, accurate chronology was obtained. The time of the dI/dt singularity was set at t = 0.

Gun Voltage

A high-impedence voltage divider monitored the voltage between the high voltage and earth plates. The small voltage sampled, was proportional to the voltage between the two electrodes at the 'top-hat' insulator. The inductance of the two electrodes (approximately 28 nH maximum), was sufficiently large to prevent direct observation of the voltage across the plasma. At peak compression of the pinch, the insulator voltage was several times the initial capacitor bank voltage, due to the very rapid change in inductance at this time. This high voltage caused current leakage across the insulator, amounting to

150 kA at peak compression (the Rogowskii coil measurement was 490 kA, and the plasma current, subsequently measured by Faraday rotation, was 340 kA).

Total Neutron Monitor

The total neutron yield for each discharge was monitored using a silver activation technique. A Geiger-Muller tube with a thin silver window, was mounted within a block of polythene. This block moderated the 2.45 Mev neutrons produced by D-D reactions in the plasma. These thermalised neutrons activated the silver, whose subsequent beta-decay (half-life 2.4 minutes) was detected by the Geiger-Muller tube. An amplifier-scaler (Nuclear Enterprises Scaler-Timer ST6) counted the number of pulses produced by the detector during the 100 second time interval immediately following each discharge. The total count obtained was proportional to the total neutron production of the plasma discharge.

This monitor was used uncalibrated, but provided an indicator of the quality of the focus discharge, so that data recorded on a shot to shot basis could be compared. A good discharge yielded approximately 10^9 neutrons [46], and a poor discharge $\lesssim 10^6$. In a poor discharge, the plasma column was not focussed onto the machine axis, the current waveforms did not exhibit the characteristic dip, the dI/dt singularity was absent, and no appreciable voltage appeared at the gun insulator.

2.2 LASER DIAGNOSTICS

The co-operative laser scattering [48,49], holographic interferometry, and Faraday rotation diagnostics used on the Plasma Focus, all made use of a ruby laser oscillator. This oscillator, together with the co-operative scattering system and the holographic interferometry, are described in this section. In addition, the clipping system used to produce a 1.5 ns FWHM ruby laser pulse for holographic interferometry, is described.

2.2.1 THE RUBY LASER OSCILLATOR

The Korad K1 694.3 nm ruby laser oscillator, consisted of a 10 mm diameter, 100 mm long ruby rod, pumped by a helical flash tube, between a 100% reflecting dielectric mirror and a 26% reflecting sapphire output mirror forming the laser cavity. Between the 100% mirror and the ruby rod was a multi-stack polariser and a Pockel cell. The C-axis of the ruby crystal was orientated to give maximum gain to horizontally polarised light. However, the polariser had a minimum transmittance with this polarisation. Therefore, while the Pockel cell was unstressed, lasing could not occur. Q-switching of the cavity was accomplished when the Pockel cell was stressed by a 40 kV voltage pulse from a thyratron switched Blumlein cable. This voltage corresponded to the Pockel cell's half-wave voltage, i.e. that voltage which rotates the plane of polarisation by 90 degrees. To achieve maximum power from the oscillator, Q-switching was timed to occur at maximum population inversion, approximately 1 ms after initiation of the flash-tube discharge. Thermal stabilisation of the ruby rod and cavity mirrors, was accomplished by circulating deionised cooling water maintained at a temperature of $15 \pm 1^{\circ}C$.

The output energy was 0.5 J, measured using a TRG Control Data Corp. 107 Thermopile. The pulse shape, approximately Gaussian, was monitored with an ITL S-20 vacuum photodiode (risetime 0.2 ns). The pulse width was normally 20 ns FWHM for both the co-operative scattering and the holographic interferometry (unclipped pulse). The pulse was lengthened for the Faraday rotation measurements to approximately 30 ns FWHM, by de-tuning the laser cavity.

2.2.2 CO-OPERATIVE LASER SCATTERING

Co-operative laser scattering from a 300 MW, 20 ns FWHM, ruby laser pulse (oscillator pulse amplified to 6 J), was observed simultaneously for three differential scattering vectors. Three sets of collection optics viewed approximately identical scattering volumes, 10 mm below the centre electrode. Two scattering angles of 10 and 45 degrees, having differential scattering vectors perpendicular to the Z-axis of the Plasma Focus (the direction in which current driven effects are not observed), were used to study thermal levels of scattered light. This gives information on electron and ion temperatures. A second 10 degree scattering direction, was in the plane defined by the incident laser beam and the Z-axis, resulting in a differential scattering vector parallel to the Z-axis. The scattered light observed in this direction contained information on current driven instabilities.

Spectral analysis was performed by a triple slit (one per scattering direction) Monospec 1000 monochromator, coupled to a gated Princeton Applied Research Corp. optical multichannel analyser. The wavelength resolution was 0.018 nm per channel. Details of this diagnostic, together with results, are given by Kirk [49].

2.2.3 HOLOGRAPHIC INTERFEROMETRY

Holographic interferometry of the Plasma Focus, was used to observe the temporal evolution of the electron density radial profile during the time period around peak compression of the pinch. This information was required so that magnetic field data could be extracted from Faraday rotation measurements. In addition, it gave useful information on the plasma's behaviour. The imaged holographic technique used, is a standard diagnostic for this type of plasma. Reviews of the method, together with theory, are given by Jahoda and Siemon [50], Faw and Dullforce [51], and Collier, Burckhardt, and Lin [52]. A short ruby laser pulse (1.5 ns FWHM), was required to prevent smearing, due to plasma motion, of the phase shift to be measured. Both the optical layout used to provide a short laser pulse, and the holographic optical arrangement, are described in the following sections.

2.2.3.1 RUBY LASER CLIPPING SYSTEM

The optical layout used to produce a 1.5 ns ruby laser pulse is shown in figure 2.4. One important requirement of the holographic method used is good spatial coherence of the laser beam. In order to obtain this, the oscillator Q-switched pulse was expanded by a x2 telescope, and passed through an OB10 blue glass stop of diameter 8 mm, so that only the central 4 mm portion of the oscillator's output was used. Following this stop, the beam was passed through a $\lambda/2$ plate, which rotated the plane of polarisation from the horizontal to the vertical. The beam then passed through an unstressed Pockel cell (Electro Optics Developments Ltd. PC125, with a rise time of 0.3 ns) and was reflected in the horizontal plane from a 'crossed' Glan-Thomson polarising prism. The beam was then incident on a nitrogen pressurised

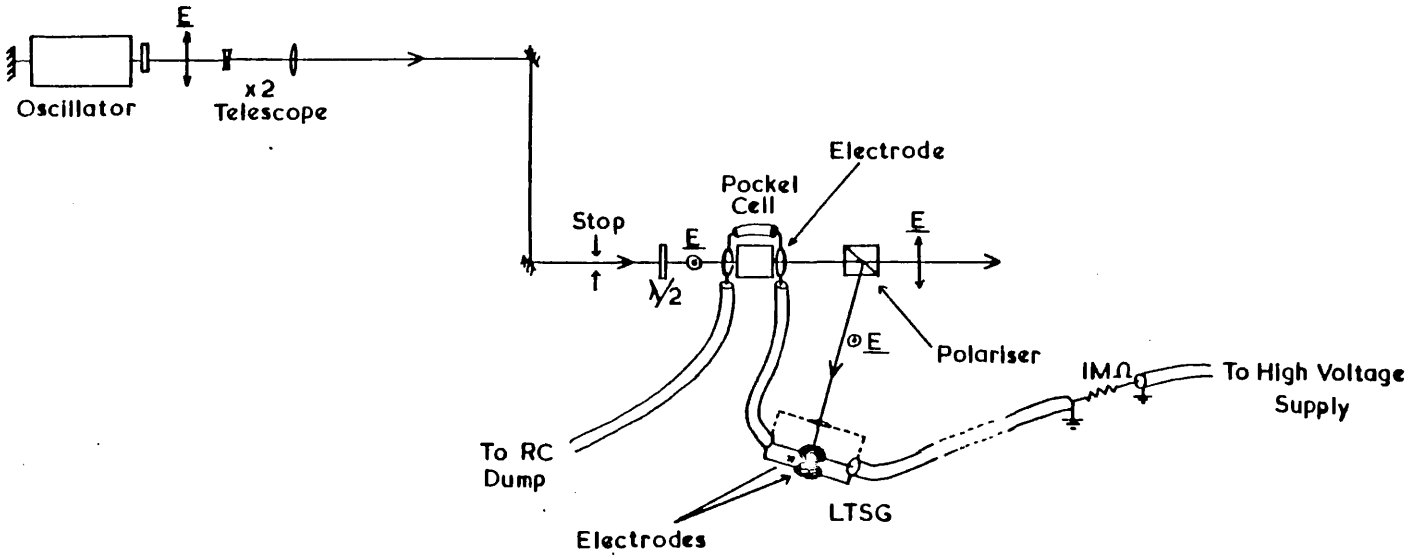

Figure 2.4

The optical layout of the ruby laser 1.5 ns clipping system.

laser triggered spark gap (LTSG). The LTSG consisted of a hollow annular anode, containing a positive lens which focussed the laser onto the adjacent cathode. The anode-cathode spacing was 300 microns. The Pockel cell had two 50 Ohm high voltage BNC sockets for each electrode, with impedence matching between them.

The electrical circuit, also shown in figure 2.4, consisted of a Brandenburg high voltage power supply which charged a coaxial cable linking LTSG and Pockel cell, via a 1 Meg-Ohm charging resistor. The braiding of the cable was held at earth potential, and the central conductor at a negative voltage suitable for half-wave switching of the Pockel cell. The cathode of the LTSG and both Pockel cell electrodes were at this voltage. At the end of the cable, an RC dump was used to prevent voltage pulse reflections. The length of cable between LTSG and power supply was tens of meters long, ensuring that no reflected pulses would switch the Pockel cell during the laser pulse. A short length of coaxial cable ($\sim$100 mm) connected both Pockel cell electrodes.

The circuit works as follows: When the LTSG is broken down by the leading edge of the laser pulse, a voltage pulse propagates into the transmission line. When it arrives at the first Pockel cell electrode, a potential difference across the crystal arises, and the Pockel cell becomes stressed (the other electrode remains at the original potential). The voltage pulse continues to propagate, and after a delay time determined by the length of the joining coaxial cable, arrives at the second electrode. The potential difference falls, and the Pockel cell returns to its former unstressed state. The voltage pulse continues to propagate along the line until it is dumped.

When the Pockel cell was stressed, the polarisation of the laser was rotated into the horizontal plane. Light was therefore transmitted by the polarising prism. Only a short laser pulse was transmitted. The duration of the pulse, was determined by the rise time of the voltage step, the rise time of the Pockel cell, and the length of transmission line joining both electrodes. The minimum pulse duration obtained with this arrangement was approximately 1.5 ns FWHM. Both the LTSG voltage and pressure were trimmed for optimum clipping, approximately 5 kV and 60 psi respectively. Maximum energy throughput was achieved by clipping at the peak of the oscillator output pulse. This was accomplished by a suitable choice of cable length between LTSG and Pockel cell, and by varying the illumination of the LTSG. Typically, the pulse energy was 20 mJ.

2.2.3.2 HOLOGRAPHIC INTERFEROMETRY OPTICAL LAYOUT

The optical layout of the holographic interferometry is shown in figure 2.5. The 1.5 ns clipped ruby laser pulse was divided by a 50% reflecting dielectric beam-splitter into a scene beam and a reference beam. Each of these is described in turn.

Scene Beam

The scene beam was reflected by three steering mirrors M1, M2, and M3. A x10 expansion Galilean telescope followed. The scene beam then passed into the vacuum chamber, interacted with the plasma, and emerged through another vacuum window to be imaged by the lens L1, of focal length +650 mm and diameter 75 mm, onto the holographic plate. The overall beam expansion was 22, and the magnification of the plasma image was 2.2.

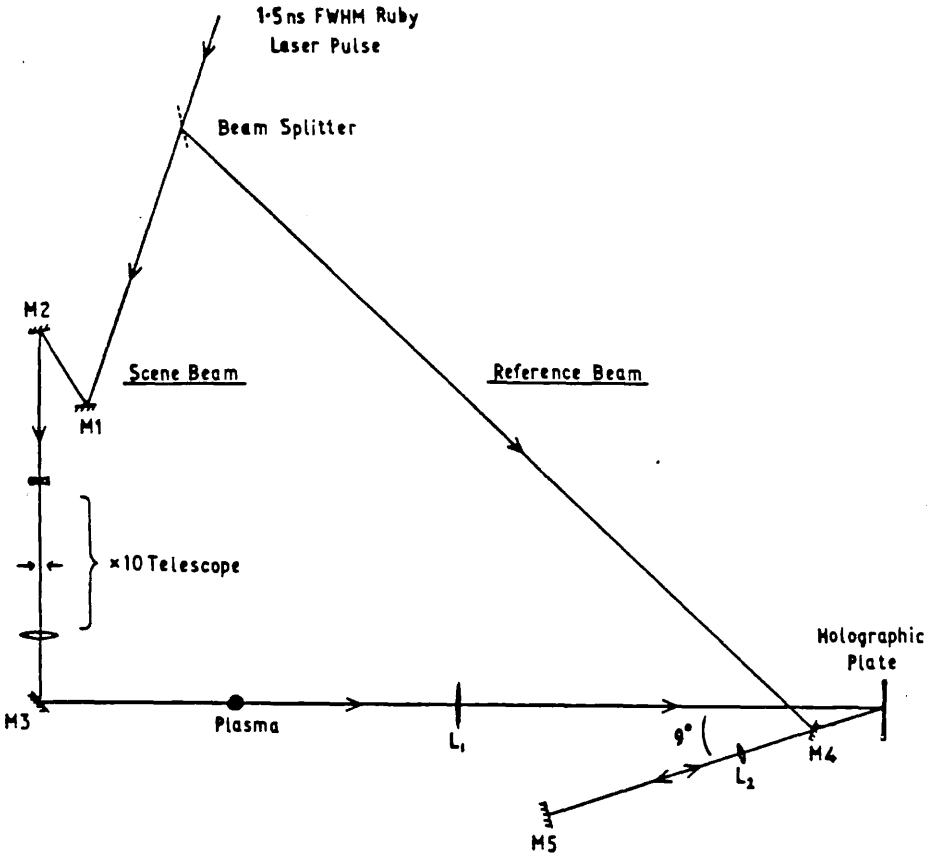

Figure 2.5

Holographic interferometry optical layout.

Reference Beam

The reference beam was reflected by a 100% dielectric mirror M4 placed adjacent to and below the holographic plate. The beam was expanded by a +10 mm focal length lens (L2), and reflected from a 100% reflecting dielectric mirror M5. At the holographic plate, the beam expansion was 22. This matched the expansion of the scene beam.

Discussion

An imaged holographic technique was used in this experiment. This had the advantage over normal diffuse methods in that noise due to speckle pattern was reduced [50]. A double exposure of the hologram was made without plasma after mirror M5 had been tilted slightly to vertically displace the reference beam. This had a twofold purpose. Firsly, by making a reference exposure in the absence of plasma, the phase shift of the scene beam with plasma is revealed by the Moire' pattern of fringes. Secondly, by tilting the mirror, horizontal reference fringes are introduced, making the phase shift readily measureable. The reduction in speckle pattern had the additional advantage of increasing the Moire' fringe resolution [50].

The holographic plates used were Agfa-Gevaert 10E75, with a resolution of 2800 lines per mm. The exposure required for an optical density of unity was approximately 5×10^{-2} Jm^{-2}. The holographic plates were protected from plasma and background light by an interference filter, whose transmission was centred at 694.3 nm. The plates were developed with Neofin-Blue, a surface developer. The amplitude holograms obtained after the development process, were converted to phase holograms with ferricyanide bleach. This had the advantage of giving bright reconstructed holograms with sharp fringes. Processing techniques and bleach recipes are reviewed by Faw and Dullforce [51].

The imaged holographic technique used was sensitive to poor spatial coherence of the laser, which produced fringe splitting in the interference patterns and decreased fringe contrast. Sufficiently good spatial coherence was obtained by working with only a small area of the available beam, and correctly overlapping both scene and reference beams at the holographic plate. In this way, interfering rays

originate from the same part of the laser beam and therefore have identical coherence properties. Temporal coherence was also important. The laser linewidth, $\cong 0.01$ nm, corresponded to a coherence length of $\lesssim 10$ mm. Therefore, the scene and reference beams optical path lengths had to be identical to within this coherence length. This was accomplished by adjusting the positions of steering mirrors M1 and M2.

2.3 THE PLASMA FOCUS-DIAGNOSTIC RELATIVE TIMING CONTROL SYSTEM

The Plasma Focus-diagnostic relative timing was controlled by a system which worked as follows: The ruby laser flash tube was triggered manually using a Culham trigger unit 8287. After a delay of approximately 1 ms (by a Culham delay unit 8288), the Plasma Focus master spark gap was triggered. Once the plasma discharge was near to the open end of the electrodes, approximately 2 micro-seconds after the trigger pulse, light from the plasma sheath, monitored by a narrow collimator through one of the holes in the outer electrode, was transmitted by fibre optic to an optical trigger (Culham type 8283). This produced a trigger pulse for a delay unit (Space Technology Laboratories Inc. nanosecond delay pulse generator), which Q-switched the oscillator. This latter delay unit (STL) provided the fine adjustment required for the relative timing between the Plasma Focus and the laser. The STL also provided an oscilloscope trigger pulse, which could be further delayed with fixed cable delays.

CHAPTER 3 DESCRIPTION OF THE POLARIMETER

3.1 INTRODUCTION

In this chapter, a full theoretical and experimental description is given of the differential half-shade polarimeter designed, developed, and successfully used in the measurement of Faraday rotation of an optical probe beam in a Plasma Focus discharge.

A plane polarised Q-switched ruby laser (cf section 2.2.1), of pulse duration $\cong$ 30 ns FWHM and energy 0.5 J, was used as the probe beam. It was judged to be the most appropriate laser source for the folowing reasons: At the laser's wavelength, 694.3 nm, the expected Faraday rotation angle of $\lesssim$ 5 degrees, was considered sufficiently large for accurate measurements. Also, both refraction of $\lesssim$ 1 degree and polarisation ellipticity due to dichroism and birefringence of $\sim 2\times10^{-5}$, were not too large (maximum limits were 2 degrees and 10^{-2} for refraction and ellipticity respectively). The ruby laser, having an output power of $\sim$15 MW, was also sufficiently powerful to be detected after transmission by an analyser near to the crossed position.

The polarimeter was designed to view a single plasma chord, of diameter 250 microns, at any chosen position 5 mm below the Plasma Focus centre electrode, within a 20 mm wide ruby laser probe beam. The diameter of this chord was chosen to correspond to approximately one tenth of the minimum observed plasma radius (2.35 mm). Faraday

rotation of the probe beam along this chord, was observed throughout the ruby laser pulse with a detection system having a temporal resolution of 2.5 ns. The polarimeter was designed to operate at any chosen half-shade angle. The optimum half-shade angle for the Plasma Focus measurement, when probe beam refraction and polarisation ellipticity are considered, was approximately 2 degrees, the angle used, and gave a noise limited angular rotation resolution of approximately 0.02 degrees.

The detailed temporal evolution of the Faraday rotation angle observed along the single chord, at a fixed chord impact parameter, was built-up over several plasma shots. The spatial variation was obtained by repeating the measurement over several impact parameters. This measurement procedure was aided by two factors: Firstly, the ruby laser pulse detected from the viewing chord, was observed to be approximately twice as long as the Q-switched pulse, measured using the whole beam. This effectively doubled the amount of data taken per plasma shot. Secondly, the polarimeter was designed so that the impact parameter could be changed between shots without disturbing the optical alignment.

The polarimetry was based on the differential half-shade method [25]. This relies on dividing the probe beam from the plasma into two equally intense beams. These beams are analysed by separate polarisers, each set at a small angle from the crossed position. This small angle is called the half-shade angle. The orientations of the analysers are chosen so that when Faraday rotation occurs, the intensity transmitted by one analyser increases while that by the other decreases. The Faraday rotation angle is obtained by detecting the light transmitted by the analysers using square law detectors, and

determining from the observed signals, the ratio of signal difference to signal sum. Comparison of this ratio value with a calibration curve, prepared by simulating Faraday rotation, gives the Faraday rotation angle. The advantage of this method is that by taking the above ratio, the result is independent of the laser light intensity. This was useful, as the laser's output fluctuated by as much as 50% in amplitude during a shot.

The probe beam was divided using a multilayer dielectric beam-splitter. However, as a result of the differences in the amplitude reflection coefficients for light having s and p polarisations, i.e. light polarised perpendicular and parallel to the reflection plane respectively, the polarisation of the reflected light varied little with Faraday rotation, reducing the polarimeter's sensitivity. This problem was solved by firstly reflecting the light from a similar beam-splitter. The pair of beam-splitters were arranged so that they were orthogonal (see figure 3.1). The first beam-splitter (BS1), was positioned so that the horizontal initial plane of polarisation was approximately parallel to the p-plane. This initial plane of polarisation was chosen to minimise the effects of plasma birefringence. In this orientation, the light reflected from BS1 has a polarisation change greater than that due to Faraday rotation. In other words, it magnifies Faraday rotation. By having BS1's reflection properties identical to those of the second beam-splitter (BS2), the initial magnification exactly balances out the demagnification that occurs on reflection from BS2. As a by product of this compensation scheme, which was achieved by reflecting only 20% of the probe beam from BS1, the polarisation change of the light transmitted by BS2 was twice the change due to Faraday rotation. This gave rise to a polarimeter having a non-symmetrical response curve, and a higher

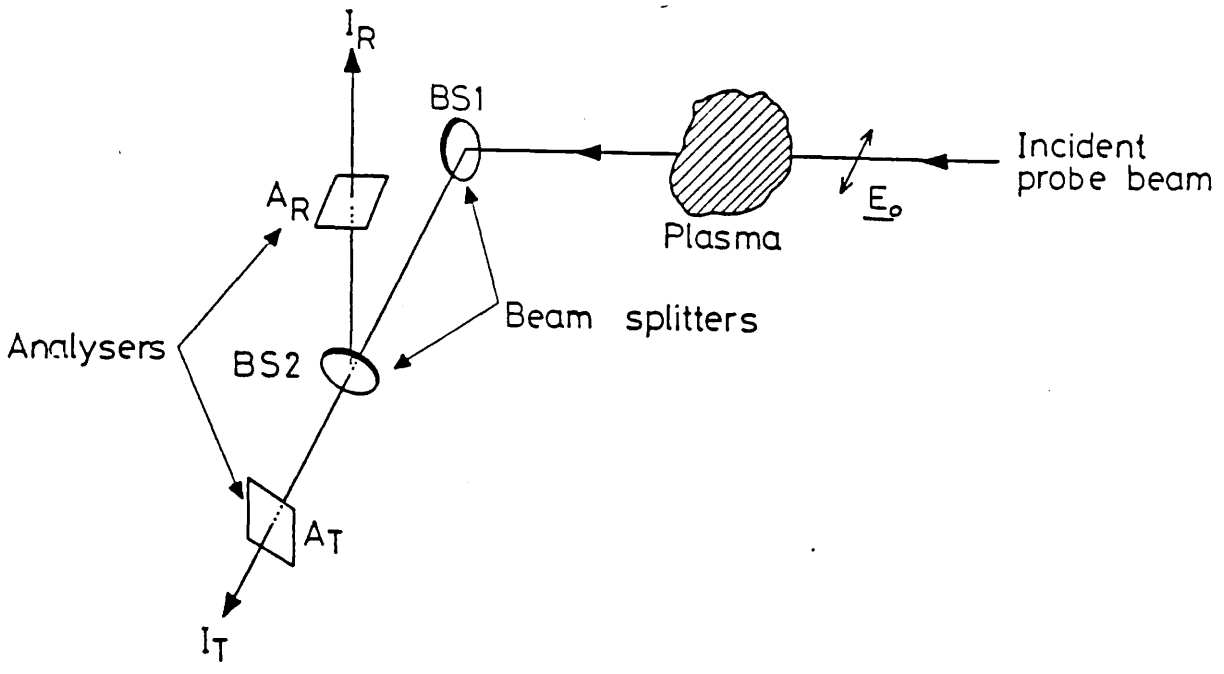

Figure 3.1

Basic optical arrangement of the polarimeter.

sensitivity at a given half-shade angle than a standard half-shade device (a standard half-shade polarimeter is one in which the probe beam is divided equally in a manner which does not affect the magnitude of the polarisation change, e.g. a polarimeter based on a Wollaston prism). The gain in sensitivity was achieved at the cost of decreasing the polarimeter's dynamic range, and increasing its sensitivity to polarisation ellipticity.

Only one detector was used to observe the light transmitted by the two analysers. This was accomplished by transmitting the light to the detector along two high transmission fibre-optic links having unequal lengths. The difference in their length, was chosen so that the two detector signals observed were well separated in time. This scheme was useful for three reasons: Firstly, the problem of balancing the two detectors common in differential measurements did not exist. Secondly,

the detector was positioned in the screened room, and therefore protected from electrical interference associated with the Plasma Focus device. Thirdly, the two signals were displayed together on the single trace of a fast storage oscilloscope, avoiding the jitter normal between the two traces of dual beam oscilloscopes.

Imaging optics were used in the polarimeter to correct for refraction of the probe beam. This ensured that the plasma chord viewed remained fixed during the shot. However, refraction resulted in the angle of incidence at BS1 changing, and therefore the values of the s and p reflection coefficients. This affected the polarisation magnification factor, and therefore the plane of polarisation of the light reflected.

Refraction did not affect the angle of incidence on BS2. However, because the probe beam was imaged to a fixed point, while the point of reflection from BS2 varied with refraction angle, the orientation of the reflection plane, and correspondingly the p-plane, was modified.

The change in polarisation angle that occured at BS2 on reflection and transmission, depended on the angular shift of the reflection plane. Since the reflection plane was rotated, while the analysers were fixed, the half-shade angles, defined in relation to the reflection plane of BS2, were also altered. As a result, an increased polarisation change occuring at BS2 due to refraction was analysed by an analyser with a larger half-shade angle, thereby reducing the overall effect.

Experimentally, the effects of refraction could be studied by calibrating the polarimeter at several impact parameters. This was

because plasma chords viewed at different impact parameters were equivalent to a single plasma chord viewed at a fixed impact parameter, but with a variety of equivalent refraction angles. The theoretical analysis given in section 3.4, shows that the polarimeter has a unique operating point where the effects of probe beam refraction are minimal. This has been confirmed experimentally. The location of this operating point in the parameter space of the polarimeter's response curve, depends upon several factors: The initial plane of polarisation with respect to the p-plane of BS1, the reflection properties of both beam-splitters, the change in the reflection coefficients of BS1 with incidence angle, the relative misalignment between the two beam-splitters s and p planes, the imaging optics, and finally, the ratio of fibre-optic transmittances. Finding the position of the operating point experimentally is done in a trial and error manner. The Faraday rotation measurements from the Plasma Focus, were taken with the polarimeter operating from this optimum operating point. Essentially, the optimum operating point arises because all the effects of refraction cancel out, i.e. the change in BS1's polarisation magnification factor cancels out the effect of the change in the reflection plane at BS2.

Probe beam polarisation ellipticity decreases the sensitivity of the polarimeter to Faraday rotation, and complicates the problem of the polarimeter's behaviour to refraction. It also determines the optimum sensitivity or half-shade angle of the polarimeter. This topic is examined, along with similar effects produced by the rejection ratios of the analysers, in section 3.6.

3.2 DETAILS OF THE EXPERIMENT

The optical arrangement, selection of optical components, and alignment of the polarimeter, are discussed below.

3.2.1 DESCRIPTION OF THE EXPERIMENTAL ARRANGEMENT

In this section, the experimental optical arrangement is described. The details of the optical layout are shown in figure 3.2, and a colour illustration is shown in figure 3.3. All of the optical elements were anti-reflection coated, and all the lenses were manufactured from low stress Schott BK7 glass. Each optical component is described in sequence.

Polarising Prism: In order to define the ruby laser probe beam's plane of polarisation, together with the removal of any elliptical polarisation component, the light was passed through a high quality Glan-Thomson polarising prism. The 10 mm square aperture prism, with rejection ratio $\sim 10^{-6}$, was fixed within a 360 degree rotation mount, which had a Vernier scale resolution of 5 minutes of arc.

The setting of the polarising prism determined the initial plane of polarisation of the ruby probe beam. This plane was therefore the reference plane from which subsequent rotations were measured. Once the polarimeter was aligned and the analysers set, this prism was manually rotated, simulating Faraday rotation, and the polarimeter calibrated. The prism had therefore to be rigidly mounted, to ensure that the only rotation imposed was that intended, and was not due to any pivotal movement of the prism within its support. The error in

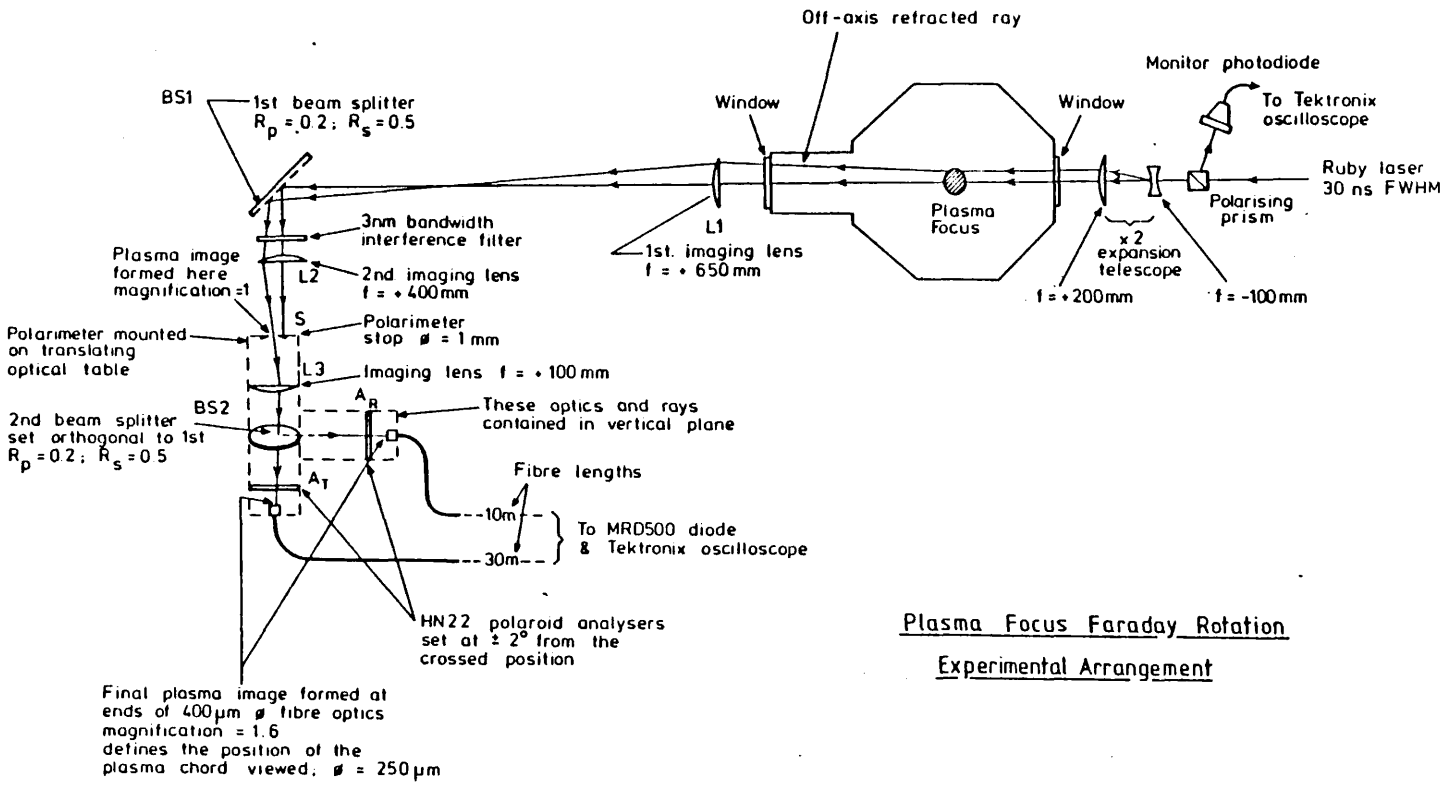

Figure 3.2

Optical layout of the experimental apparatus.

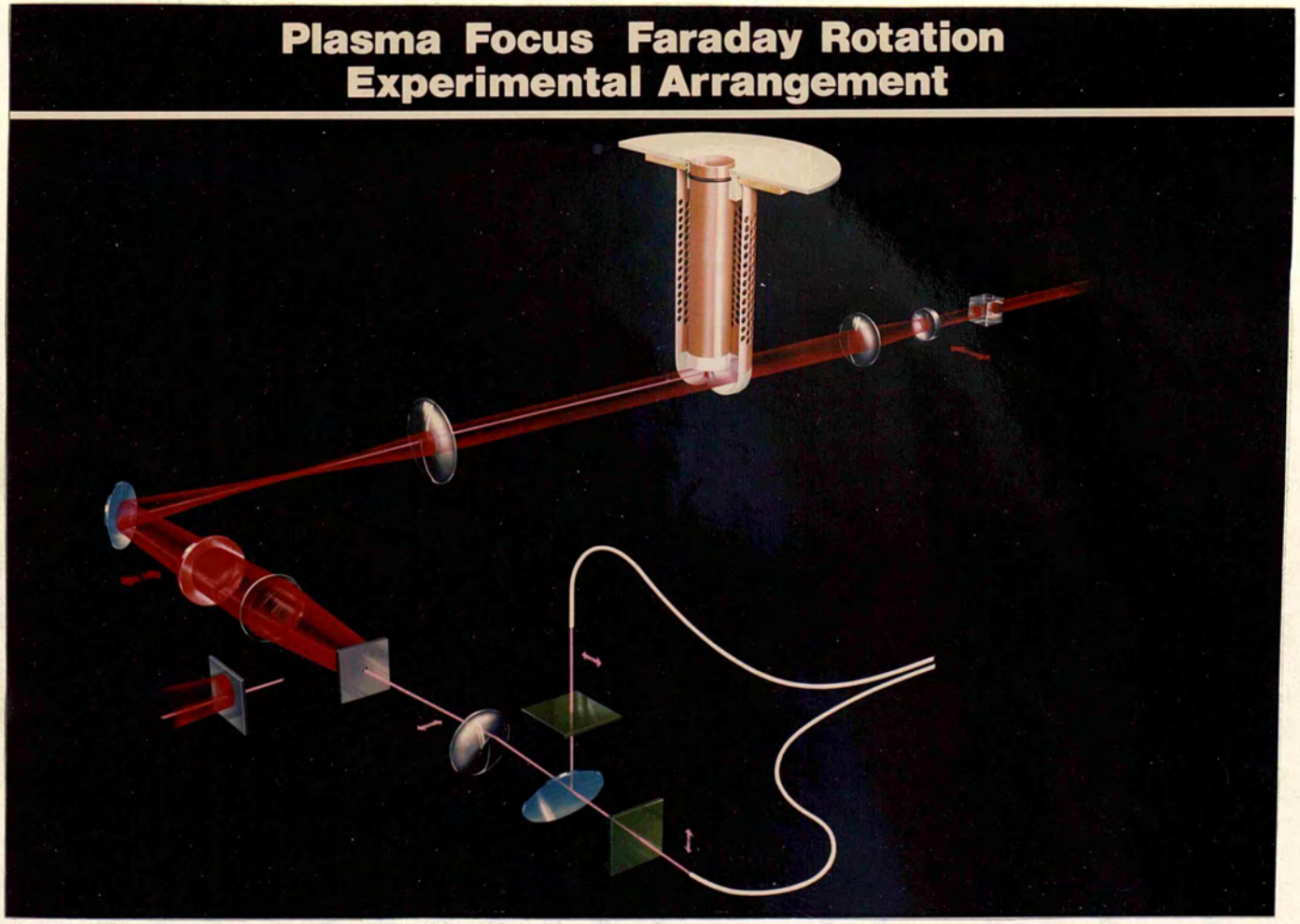

Figure 3.3

An illustration of the experimental arrangement.

setting the plane of polarisation was approximately the vernier scale resolution of the rotation mount.

Light rejected by the prism was detected by an ITL vacuum photodiode (0.2 ns risetime) and the signal displayed on a 7844 dual-beam Tektronix oscilloscope. This served as a timing reference for comparison with the simultaneously displayed Rogowskii coil dI/dt waveform, enabling the synchronisation of both plasma and probe beam.

The Expansion Telescope: In order to cover a 20 mm wide region of interest within the plasma focus, the ruby laser probe beam, of diameter 10 mm, was expanded by a Galilean telescope.

The Plasma And Vacuum Chamber: After expansion by the telescope, the probe beam passed through a 10 mm thick, 75 mm diameter, plate glass window into the plasma focus vacuum chamber. With the ruby laser pulse synchronised to the plasma, both Faraday rotation and refraction of the probe beam occurred. The beam then passed out of the machine through a 10 mm thick, 130 mm diameter, plate glass window at the end of the pumping port T-piece. In comparison with the other optical elements within the system, these windows were of poor quality. They had transmittances of 78% at 694.3 nm, and caused polarisation ellipticity of approximately 5×10^{-3} due to stress-birefringence. Better windows were not used, as after a few discharges a thin film of tungsten, sputtered from the centre electrode, was deposited on the vacuum surfaces. Consequently, the windows had to be replaced periodically.

The First Imaging Lens (L1): In order to prevent wandering of the probe beam and loss of information, the refracted light was collected

by a lens - the first imaging lens - which, together with two other lenses, L2 and L3, formed an image of the central plane of the plasma. It was within this image that local Faraday rotation measurements were made.

The first imaging lens was plano-convex, with a focal length of +650 mm, and diameter 70 mm. Its position was approximately 1 metre from the plasma, and collected light refracted through angles up to 35 mrad. The magnification provided by this lens was 2.2.

The First Beam-splitter (BS1): The first stage in the polarisation analysis was to reflect the light collected by the first imaging lens with a multilayer dielectric beam-splitter. The beam-splitter used had intensity reflectivities $R_s = 0.50$ and $R_p = 0.205$ at the laser wavelength for the 45 degree angle of incidence. The substrate was silica glass, of thickness 3 mm, and diameter 50 mm. It was mounted in a gimbal with micrometer adjustment.

Interference Filter: Background light emitted by the plasma was removed by a multi-layer dielectric interference filter, having a 3 nm bandwidth centered at the ruby wavelength. Peak transmission was 60%.

Second Imaging Lens (L2): A second imaging lens was used in conjunction with the first to form a real image of the plasma at the polarimeter stop S. The diameter was 50 mm, and its focal length +400 mm, giving an overall magnification at the stop of 1.03.

Polarimeter Stop (S): To minimise the amount of light within the polarimeter, an iris diaphram stop closed to a diameter of 1 mm was used. Onto this stop, an image of the plasma plane was formed, which

prevented vignetting of the probe beam, and simplified the alignment procedure (see section 3.2.3). It was within the area of the plasma image seen through this aperture that the Faraday rotation measurement was made. This stop was the first optical element on the translating optical table.

Third Imaging Lens (L3): A +100 mm focal length plano-convex lens was used to image the stop, containing the plasma plane image, onto the ends of two fibre-optics via the second beam-splitter and analysers. Its diameter was 40 mm, and was mounted on the polarimeter translating table. The magnification of the stop at the image plane was 1.6, and the overall magnification of the plasma plane at the fibre-optics was 1.65.

The Second Beam-splitter (BS2): This beam-splitter was manufactured from an identical substrate to the first. Its reflectivities at 694.3 nm, for the 45 degree angle of incidence, were R_s = 0.55 and R_p = 0.23. It was mounted similarly to the first, and was attached to a rigid column on the translating optical table. All the optics relating to the reflected beam were mounted on this column.

The Analysers (A_T and A_R): These were Polaroid type HN22 sheet analyser, having a transmittance of 59% at 694.3 nm for the preferred polarisation [40], and a transmittance of 3×10^{-6} when crossed. They were of diameter 40 mm, and were attached to rotatable circular mounts, engraved in one degree increments. They were both set at approximately 2 degrees from the crossed position, i.e. the half-shade angle was 2 degrees.

The Fibre-Optics: These relayed the light transmitted by the analysers to the screened room for detection, minimising noise pick-up by the detector from the Plasma Focus discharge. The type used was Quartz et Silice QSE 400-C quartz fibre, of diameter 400 microns, attenuation of 40 dB per kilometre, and lengths 10 m and 30 m. The difference in attenuation was therefore 0.8dB (17%). Two different lengths were employed so that the analysed signals were time delayed with respect to each other, simplifying detection. Since the final image of the probe beam in the plasma plane was formed at the ends of these fibres, then by back-projection, the diameter of the fibres determined the diameter of the plasma chord viewed. This was 250 microns. Both fibres were aligned to view the same plasma chord.

The Translating Optical Table: All the optics behind the polarimeter stop were mounted on a translating optical table. By moving this table, any plasma chord across a diameter, at a constant axial position 5 mm below the centre electrode of the Plasma Focus, could be viewed. The positioning error was approximately 100 microns.

Detection and Measurement of Faraday Rotation: The light carried by the fibre-optics was detected by a single photo-detector (Motorola MRD500), which ensured equal detector detectivities for both analysed beams and so removed the usual problem encountered with differential measurements of balancing one detector with another. This was accomplished by having different fibre lengths, and these were 10 m and 30 m for the fibres carrying the reflected and transmitted light respectively. The difference in length, 20 m, was chosen such that the optical delay time, approximately 110 ns, was greater than the duration of the ruby laser pulse. The detector output therefore consisted of two signal waveforms representing the two polarisation analysed laser

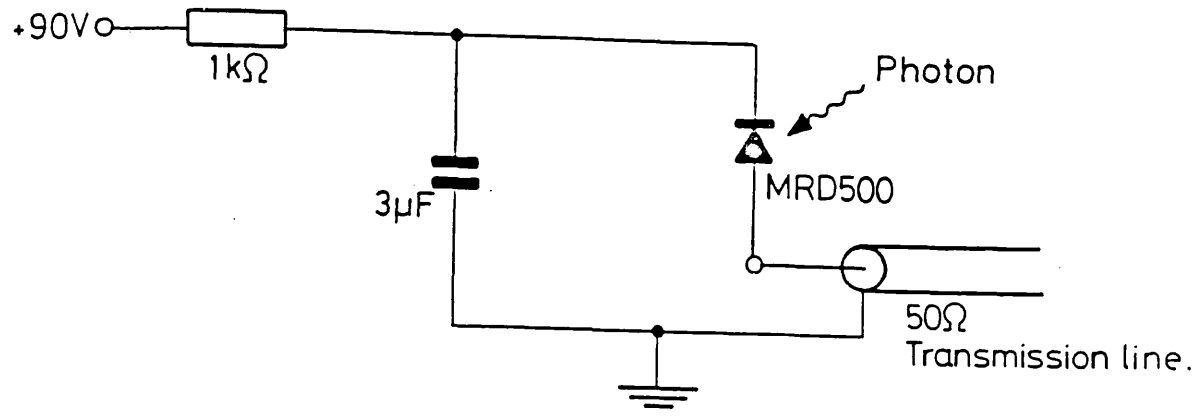

Figure 3.4

The detector circuit.

intensity waveforms.

The detector circuit is shown schematically in figure 3.4. The diode was reversed biased to 90 volts, and was in parallel with a 3 micro-Farad capacitor to avoid current limitation of the diode rise time of 1 ns (50 Ohm load) during the detection period. The diode had a positive spherical lens at the entrance aperture, which increased the intensity of light falling on the detector surface from the adjacent fibre-optic ends. In the mode of operation used, the detector was equivalent to a current source, with the current proportional to light intensity. The load was the 50 Ohm impedance of the oscilloscope amplifier, and so the signal displayed was proportional to light intensity. A 400 MHz 7834 Tektronix storage oscilloscope, with a 500 MHz 7A19 plug-in amplifier, was used to display the laser waveforms.

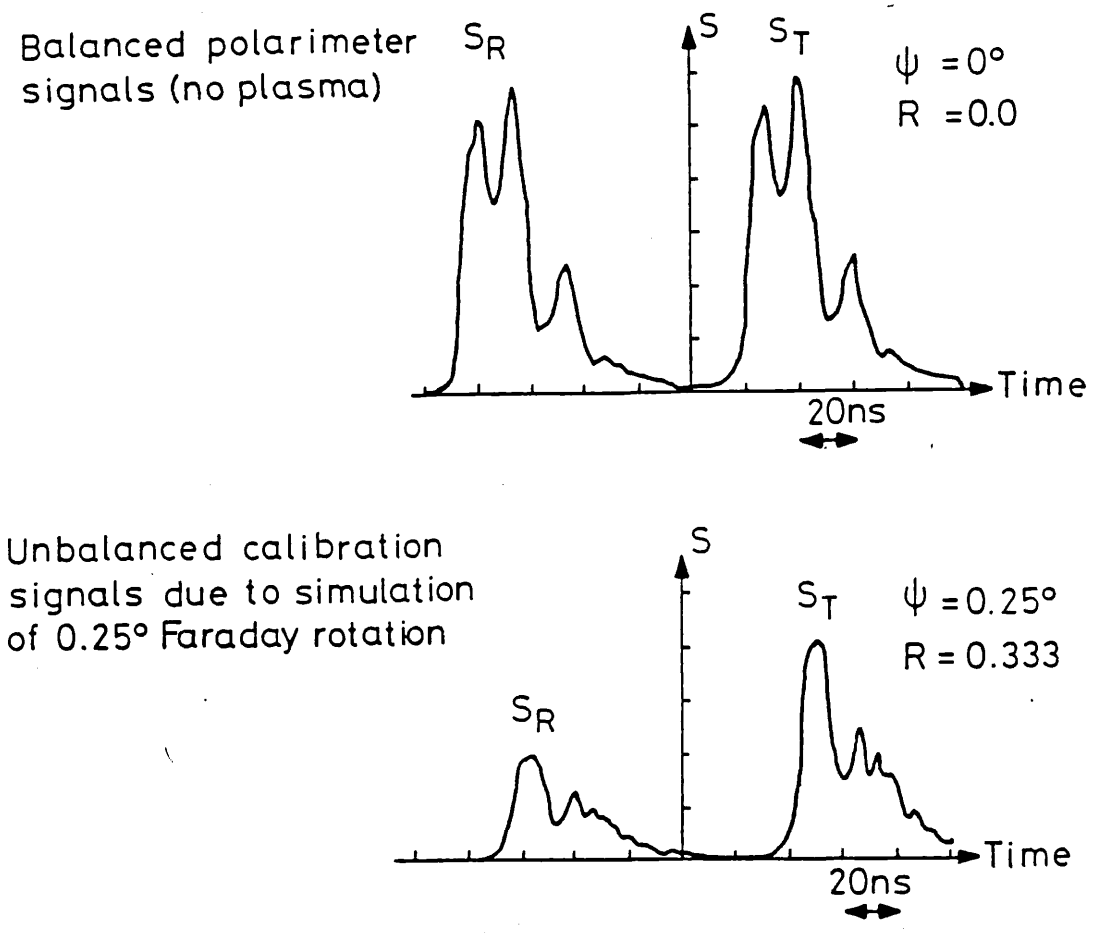

Figure 3.5

Detector output signal with and without simulated Faraday rotation.

The detection scheme adopted, namely to display both analysed laser waveforms on an oscilloscope screen, is probably the simplest possible. The Faraday rotation angle is determined by measuring the ratio of signal difference to signal sum at corresponding positions within Polaroid oscillographs of the displayed waveforms, and comparing with calibration data. Figure 3.5 shows the detector output in the absence of plasma when the signals are balanced, and when Faraday rotation of 0.25 degrees is simulated. These demonstrate the relative time delay between the signals due to the difference in fibre-optic length, the

change in the signal amplitude with rotation angle (one increases while the other decreases), and, apart from amplitude, the similarity between the waveforms. This latter feature would not exist if the rotation angle were not constant during the laser pulse, as during a focus discharge, or if the two fibre-optics were not viewing the same area of the laser beam, i.e. the same plasma chord.

3.2.2 THE CHOICE OF OPTICS

All of the optical components used in the experimental arrangement, had to have a low level of stress birefringence, sufficient to produce a polarisation ellipticity of less than 10^{-2}. They were chosen by examining each component between crossed polarisers. Stress-birefringence revealed itself as a variation in the intensity transmitted across the component, resulting in a mottled or patterned appearence, easily seen against the uniform dark background of the area adjacent to the component.

Care had to be taken in mounting the optical components, as this could cause stressing. This was avoided by clamping lightly, and checking each component in its optical mount between crossed polarisers.

Dust can also be a problem, as its presence on optical surfaces causes local depolarisation of the probe beam. Each optical element was kept dust free by frequent application of an air jet.

3.2.3 ALIGNMENT

There were several unusual alignment problems with this experimental arrangement. These were with regard to the positioning of the beam-splitters, the polarising prism, and the analysers. These are described below, as are the procedures followed for the relative alignment of the fibre-optics, and the imaging of the plasma plane.

The alignment started with the experimental arrangement devoid of all lenses, the analysers, and the interference filter. Both vacuum windows were present on the machine, and the polarimeter stop was fully open. The optic axis through the machine, which intersected the z-axis of the plasma at the point of interest, 5 mm $\pm$ 250 microns below the centre electrode, was defined by a He-Ne laser from the ruby laser bench.

The first beam-splitter was positioned such that the He-Ne laser was reflected from its central portion, with an angle of incidence $\sim$45 degrees, through BS2 to the fibre-optic, in the horizontal plane. The position of this fibre-optic defined the p-plane of BS1, and also the optic axis in this part of the arrangement. Once BS1 and the fibre-optic were set, all other optical elements were aligned relative to them.

The polarising prism was set so that the initial plane of polarisation of the probe beam was approximately co-planar with the p-plane of BS1. It will be shown later that this is not necessarily the best orientation.

The p-plane of BS2 was that plane containing both fibre-optics and

the point of reflection from BS2. This plane was set approximately co-planar with the s-plane of BS1. As this was the vertical plane, then the fibre-optic above BS2 was positioned vertically above both the reflection point and the other fibre-optic. This ensured that the angle of incidence was $\sim$ 45 degrees.

Both fibre-optics were to view the same plasma chord, and be imaged in the plane of the polarimeter stop. The alignment method used, was to illuminate the ends of the fibre-optics, with a He-Ne laser, at the detector end within the screened room, so that they became sources within the polarimeter itself. The +100 mm lens, L3, was then positioned to give an image of the fibre, seen through BS2, in the stop plane, without deviation of the optic axis. The image plane was checked by observing the lack of parallax between image and stop. The image of the fibre, seen reflected from BS2, was also formed in the stop plane, and was obtained by adjusting the vertical height of the fibre. Again the parallax method was used to check the location of the image plane. The images of the two fibres were then overlapped, by closely observing their images in the stop plane, and by adjusting BS2.

The first imaging lens was positioned to image the emitting filament of a small light bulb in the plasma plane, onto the film plane of the holographic interferometer camera (cf section 2.2.3), without deviation of the optic axis. The second imaging lens was then positioned to image the bulb in the polarimeter stop plane, again without optic axis deviation. It was then fine adjusted to image the illuminated fibre-optics in the plasma plane, confirmed by the lack of parallax between the image and the aperture of an auxilliary stop placed on the centre electrode. The magnification of the first and second lens combination was determined by translating the optical

table, and observing the fibre-optics' image within the aperture of the auxilliary stop. The measured translation distance required for the image to move across a complete diameter gave the magnification.

The analysers were set for a half-shade angle ε_H = 2 degrees by the following method. The analyser in the transmittance arm of the polarimeter, A_T, was set by crossing it with the He-Ne alignment laser when the polarising prism was rotated by $\varepsilon_H/2$ = 1 degree, where the factor 2 is the polarisation magnification factor produced by the beam-splitters. The analyser in the reflection arm of the polarimeter, A_R, was set by crossing it with the He-Ne when the prism had been rotated by ε_H in the opposite direction from the initial starting point. The prism was then reset to its initial orientation.

The expansion telescope was then aligned, the polarimeter stop closed down to a diameter of 1 mm, and the interference filter positioned with the reflected He-Ne light co-incident with the optic axis.

The final adjustment took place within the screened room. With the polarising prism set for the chosen initial plane of polarisation, the two fibre-optic ends were adjusted relative to the photodiode, until the amplitudes of the observed ruby laser waveforms were identical.

3.3 THEORY OF THE POLARIMETER

In this section, a full theoretical analysis is given of the polarimetry. The expression relating the response of the polarimeter, i.e. the ratio of signal difference to signal sum, to the Faraday rotation angle, is derived. This derivation includes the effects of refraction, impact parameter, the relative misalignment between the beam-splitters, polarisation ellipticity, analyser rejection ratio, imaging optics, the reflection and transmission properties of dielectric beam-splitters, and fibre-optic transmittances.

The state of polarisation of the probe beam from the plasma, is defined by two orthogonal electric field vectors, $\underline{E}$ and $\underline{\Delta}$, which have the magnitudes of the major and minor wave components of the polarisation ellipse respectively. These components differ in phase by 90 degrees. The ellipticity is defined as $\varepsilon = \Delta/E$.

The initial plane of polarisation is defined with respect to the p-plane of BS1, and is given by the angle ψ_o measured anti-clockwise from the p-plane (see figure 3.6). The Faraday rotation angle ψ, is defined with respect to, and measured anti-clockwise from, the initial plane of polarisation. Therefore, the major wave vector $\underline{E}$ subtends an angle $\psi + \psi_o$ from the p-plane of BS1. Similarly, because they are orthogonal, the minor wave vector $\underline{\Delta}$ subtends an angle $\psi + \psi_o$ from the s-plane of BS1, measured anti-clockwise.

The polarimeter's polarisation properties are analysed by considering the polarisation and amplitude changes experienced by both major and minor waves vectors explicitly at each optical component.

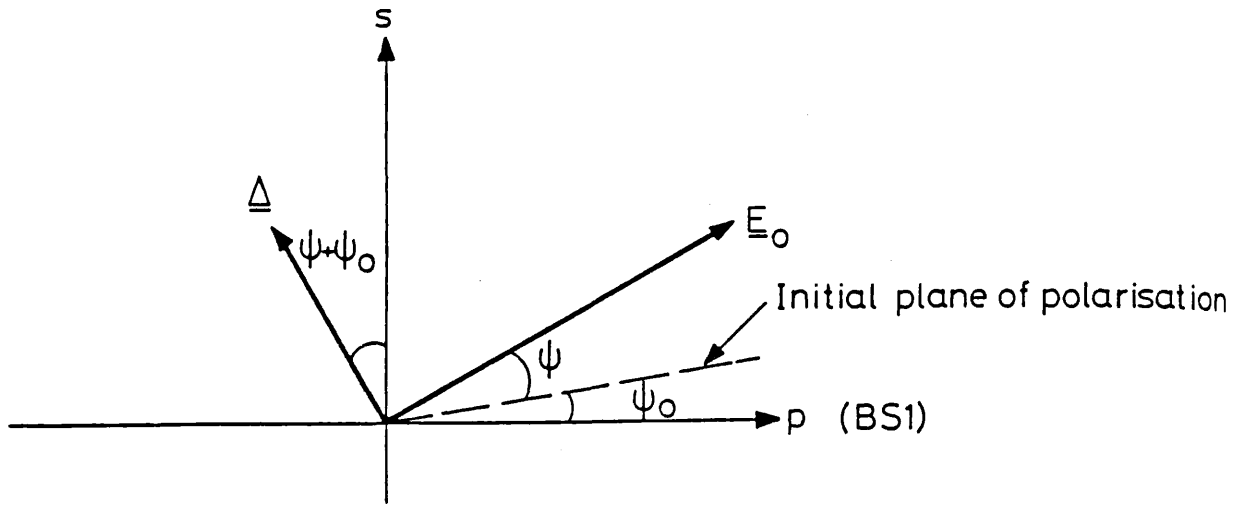

Figure 3.6

The s and p plane coordinate frame of BS1 for defining the initial and Faraday rotated major and minor wave vectors.

Assuming that the ellipticity of the probe beam arises from stress-induced birefringence in the Plasma Focus vacuum windows only, then both waves can be treated separately, as they differ in phase by 90 degrees and can only interfere if birefringence is present. Transmission losses common to both waves are not included as they do not affect the polarimeter's properties.

3.3.1 REFLECTION FROM THE FIRST BEAM-SPLITTER

Consider the reflection of the probe beam from BS1. If the amplitude reflection coefficients for the p and s components are r_{p1} and r_{s1} respectively, then, as shown in figure 3.7, the amplitudes of the reflected components are, for the major wave

$$E_p = r_{p1} E_o \cos(\psi+\psi_o) \quad \text{and} \quad E_s = r_{s1} E_o \sin(\psi+\psi_o) \tag{3.1}$$

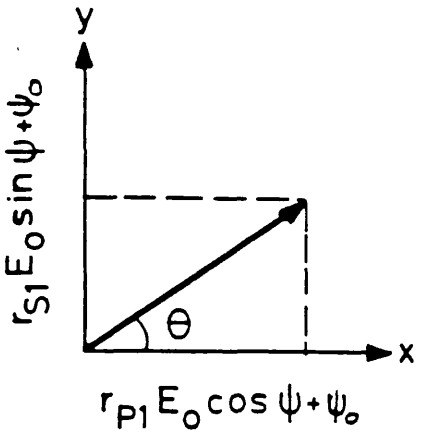

a) Polarisation state of beam incident upon BS2 after reflection from BS1

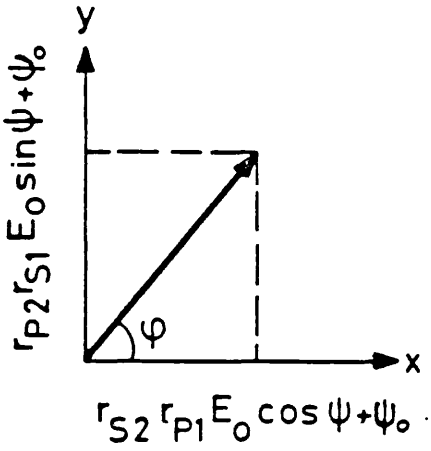

b) Polarisation state of beam reflected from BS2

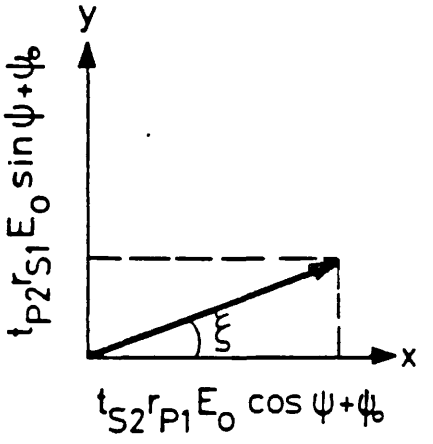

c) Polarisation state of beam transmitted by BS2

Figure 3.7

The orientation of the major wave vector a) after reflection from BS1, b) reflected from BS2, and c) transmitted by BS2.

where E_p and E_s are the p and s polarised components respectively, and are

$$E_p^{\varepsilon} = -r_{p1}\,\varepsilon E_o \sin(\psi+\psi_o) \quad \text{and} \quad E_s^{\varepsilon} = r_{s1}\,\varepsilon E_o \cos(\psi+\psi_o) \qquad (3.2)$$

for the minor wave, where the superscript ε refers to the minor wave.

The resultant major and minor waves are at angles θ from the p-plane of BS1 and θ^{ε} from the s-plane respectively, given by

$$\tan\theta = \alpha_1 \tan(\psi+\psi_o) \qquad (3.3)$$

and

$$\tan\theta^{\varepsilon} = \frac{1}{\alpha_1} \tan(\psi+\psi_o) \qquad (3.4)$$

where $\alpha_1 = r_{s1}/r_{p1}$ defines the polarisation magnification provided by BS1. For the reflection properties of BS1, $\alpha_1 = -1.56$, resulting in θ lying further away from the p-plane, and θ^{ε} nearer to the s-plane. Therefore, the major and minor wave components are no longer orthogonal.

Change In The Angle Of Incidence

Refraction and impact parameter both affect the angle of incidence τ on BS1, and so allowance must be made for the variation in the value of α_1. If $\delta\tau$ is the change in the angle of incidence, then α_1 is given by $\alpha_1^{0}+(\partial\alpha_1/\partial\tau)\delta\tau$, where α_1^{0} is the value applying to rays travelling parallel to the optic axis.

A probe beam passing through a cylindrical plasma in a direction perpendicular to the axis of symmetry, is refracted in a plane parallel to the beam and normal to the axis. This plane is approximately the p-plane of BS1, and so only the effect of a changing angle of incidence

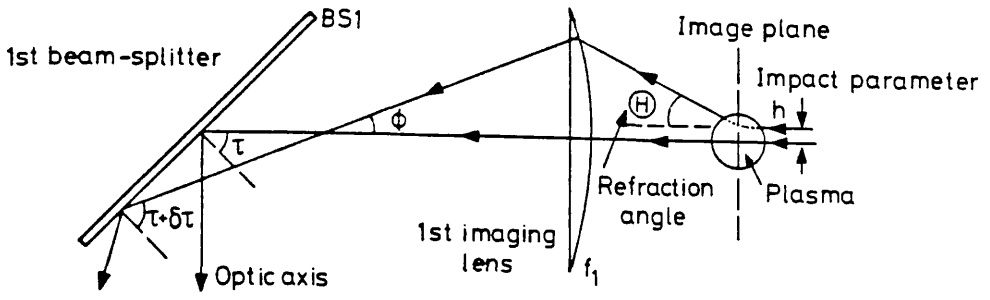

Figure 3.8

Change in the angle of incidence on BS1 with plasma refraction and impact parameter.

for rays in this plane need be considered.

Consider a ray at an impact parameter h, refracted by the plasma through an angle Θ, in the horizontal plane. After passing through the first imaging lens, the ray will intersect the optic axis at an angle Φ (see figure 3.8), given by

$$\tan \Phi = \frac{1}{m_1} \tan \Theta + \frac{h}{f_1} \qquad (3.5)$$

where m_1 is the magnification of this lens, and f_1 its focal length. This angle is also the change in the incidence angle on BS1, i.e. $\delta\tau = \Phi$. Therefore, for a minimal change in the angle of incidence, both the magnification and focal length of the lens must be large.

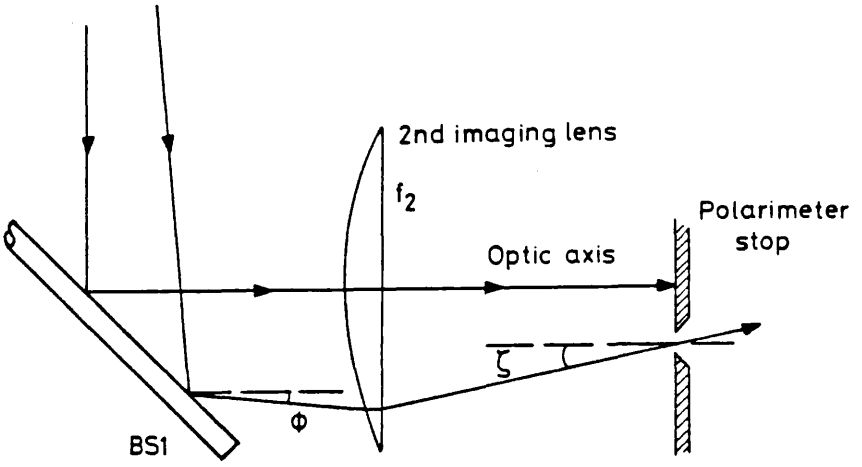

Figure 3.9

Ray trajectory through the polarimeter stop.

3.3.2 REFLECTION FROM THE SECOND BEAM-SPLITTER

The refracted ray of figure 3.8, is reflected from BS1 at an angle Φ from the optic axis, and after the second imaging lens, of focal length f_2 and absolute magnification m_2, passes through the polarimeter stop at an angle ζ from the axis (see figure 3.9). This angle is given by

$$\tan \zeta = \frac{m_1 h}{f_2} - \frac{1}{m_2} \tan \Phi \qquad (3.6)$$

After passing through the final imaging lens, of focal length f_3 and magnification m_3, the ray subtends an angle γ from the axis (see figure 3.10), which is given by

$$\tan \gamma = \frac{1}{m_3} \tan \zeta \qquad (3.7)$$

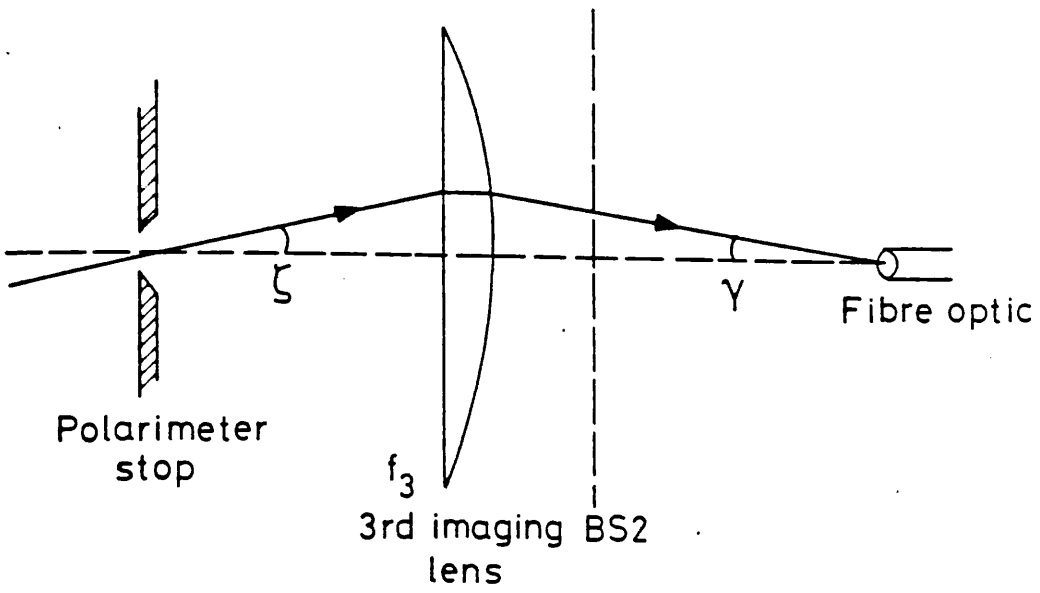

Figure 3.10

Angle of incidence on BS2 and fibre optics.

The magnitude of this angle has important consequences on the polarimeter's behaviour.

How this angle affects the angle of incidence on BS2 can be seen from figure 3.11. If the incident ray is in the direction of the unit vector $\hat{\underline{u}}$, given by

$$\hat{\underline{u}} = \hat{\underline{i}}(-\sin\gamma) + \hat{\underline{j}}(-\cos\gamma) + \hat{\underline{k}}(0) \qquad (3.8)$$

and the reflected ray is in the direction of the unit vector $\hat{\underline{v}}$, given by

$$\hat{\underline{v}} = \hat{\underline{i}}(-\sin\gamma) + \hat{\underline{j}}(0) + \hat{\underline{k}}(\cos\gamma) \qquad (3.9)$$

where $\hat{\underline{i}}$, $\hat{\underline{j}}$, and $\hat{\underline{k}}$, are unit vectors along the x, y, and z, axes of the Cartesian co-ordinate frame shown, then the angle between the incident and reflected rays, σ, being twice the angle of incidence, is given by

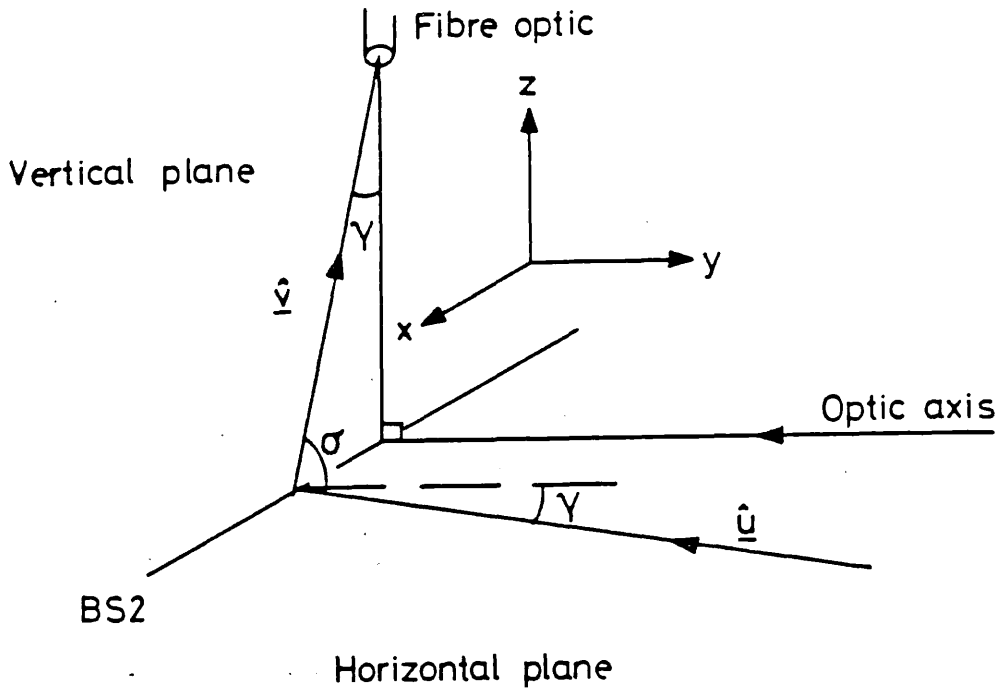

Figure 3.11

The angle of incidence and reflection plane of BS2.

$$\cos\sigma = \hat{u}.\hat{v} = \sin^2\gamma \qquad (3.10)$$

From the derivative

$$\frac{d\sigma}{d\gamma} = 2\frac{d\tau}{d\gamma} \cong 2\gamma << 1 \qquad (3.11)$$

we see that τ, the angle of incidence, is insensitive to γ. Therefore, the reflection and transmission properties of BS2 will not be affected by refraction or changing impact parameter.

However, angular changes at BS2 alters the orientation of the s and p planes. This is demonstrated in figure 3.12, where the new planes are denoted s' and p' respectively. A ray imaged onto the fibre-optic and incident on BS2 at an angle γ from a parallel to the optic axis, is reflected in a plane - the p-plane - which is inclined at the angle γ from both the vertical and the horizontal. This is equivalent to an

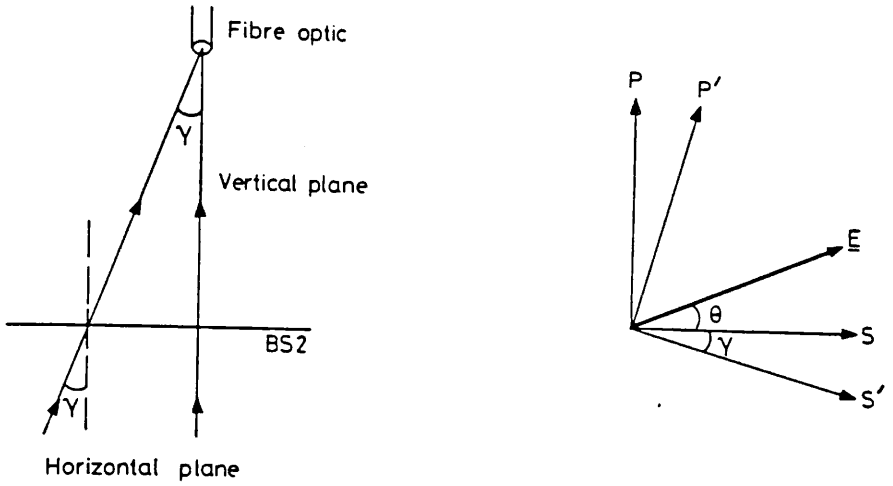

Figure 3.12

a) The change in incidence angle at the fibre optics, defined by the angle γ, causes b) a change in the reflection plane of BS2 from p to p'

angular rotation of the incident plane of polarisation by an amount γ. In addition, if η is the misalignment angle between the p-plane of BS1 and the s-plane of BS2 for rays travelling along the optic axis, i.e. $\gamma = 0$ (see figure 3.13), then on reflection from BS2, the electric field components of the major and minor wave vectors, in the s'-p' co-ordinate frame of BS2, are given by (cf figure 3.7)

Major

$$E_s = r_{s2}E_o\{r_{p1}\cos(\psi+\psi_o)\cos(\gamma+\eta) - r_{s1}\sin(\psi+\psi_o)\sin(\gamma+\eta)\} \qquad (3.12)$$

$$E_p = r_{p2}E_o\{r_{p1}\cos(\psi+\psi_o)\sin(\gamma+\eta) + r_{s1}\sin(\psi+\psi_o)\cos(\gamma+\eta)\}$$

Minor

$$E_s^{\varepsilon} = -\varepsilon r_{s2}E_o\{r_{p1}\sin(\psi+\psi_o)\cos(\gamma+\eta) + r_{s1}\cos(\psi+\psi_\rho)\sin(\gamma+\eta)\} \qquad (3.13)$$

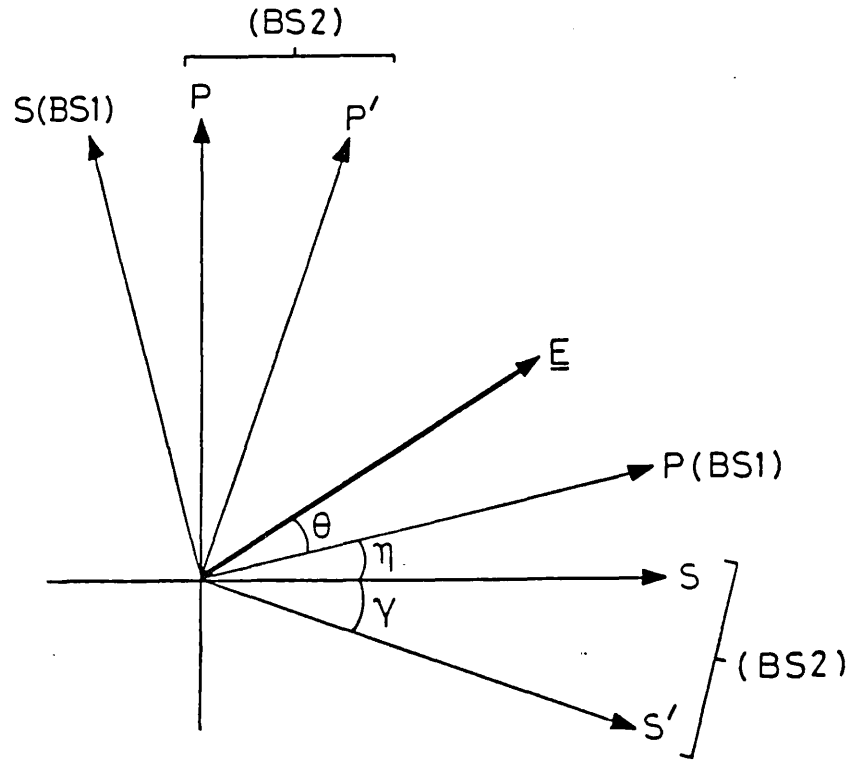

Figure 3.13

The beam-splitter misalignment angle η is defined with respect to the p-plane of BS1 and the s-plane of BS2 when $\gamma = 0$.

$$E_p^{\varepsilon} = -\varepsilon r_{p2} E_o \{-r_{p1}\sin(\psi+\psi_o)\sin(\gamma+\eta) + r_{s1}\cos(\psi+\psi_o)\cos(\gamma+\eta)\} \quad (3.13)$$

where r_{s2} and r_{p2} are the s and p amplitude reflection coefficients of BS2 respectively.

Similar expressions for the components transmitted by BS2 are obtained by replacing r_{s2} and r_{p2} with t_{s2} and t_{p2} respectively, which are the corresponding amplitude transmittances.

3.3.3 POLARISATION ANALYSIS AND DETECTION

The Reflected Beam

The resultant reflected major wave is polarised at an angle ϕ from the s′-plane of BS2, measured anti-clockwise, and is given by

$$\tan\phi = \alpha_2 \left\{ \frac{\tan(\gamma+\eta) + \alpha_1 \tan(\psi+\psi_o)}{1 - \alpha_1 \tan(\gamma+\eta)\tan(\psi+\psi_o)} \right\} \qquad (3.14)$$

Similarly, the orientation angle of the resultant reflected minor wave vector, ϕ^{ε}, measured anti-clockwise from the p'-plane of BS2, is given by

$$\tan\phi^{\varepsilon} = \frac{1}{\alpha_2} \left\{ \frac{\tan(\gamma+\eta) + \frac{1}{\alpha_1}\tan(\psi+\psi_o)}{1 - \frac{1}{\alpha_1}\tan(\gamma+\eta)\tan(\psi+\psi_o)} \right\} \qquad (3.15)$$

where $\alpha_2 = r_{p2}/r_{s2}$ is the polarisation magnification factor for light reflected from BS2 alone.

The intensities I_R and I_R^{ε}, for the major and minor waves respectively, are given by

$$I_R = \left[\frac{E_s}{\cos\phi} \right]^2$$

and

$$I_R^{\varepsilon} = \left[\frac{E_p^{\varepsilon}}{\cos\phi^{\varepsilon}} \right]^2 \qquad (3.16)$$

The transmission axis of the analyser A_R is fixed with respect to the s-p geometry of BS2 when the ray travels along the optic axis. If ε_R is the angle between the crossed axis of the analyser and the s-plane of BS2 when $\gamma = 0$, then for a ray with $\gamma \neq 0$, i.e. an off-axis ray, the orientation of the crossed axis becomes $\varepsilon_R+\gamma$ (see figure 3.14), which is equivalent to a rotation of the analyser. Therefore, the intensity transmittances T_R and T_R^{ε}, for the major and minor waves respectively, are

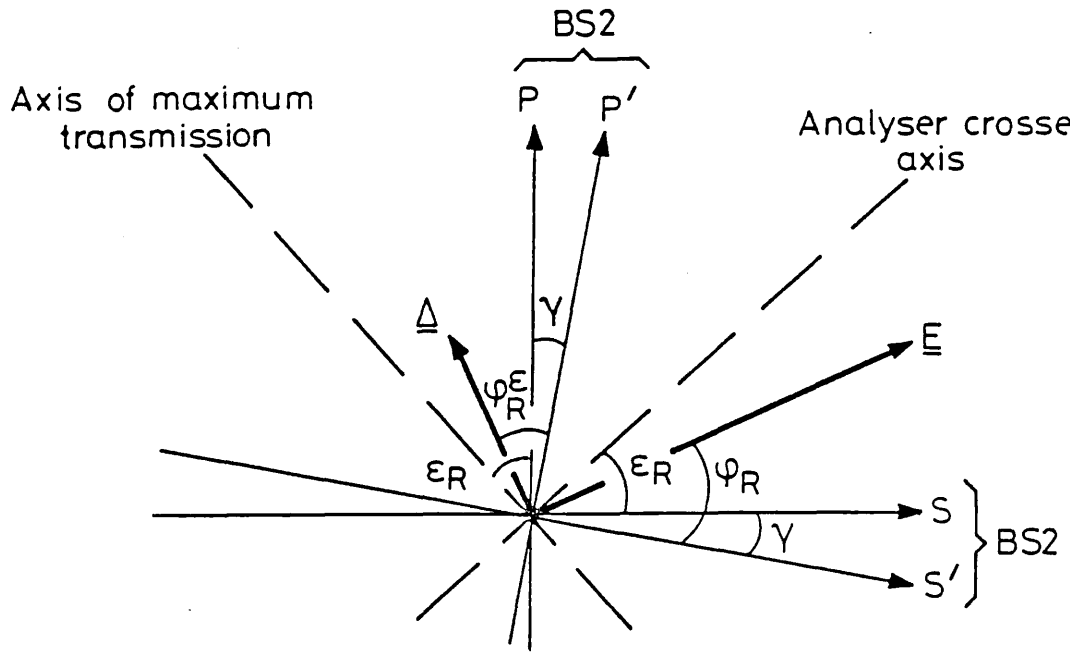

Figure 3.14

The orientation of the analyser crossed axis is defined with respect to the s and p planes of BS2 when $\gamma = 0$.

$$T_R = T_A \sin^2(\varepsilon_R+\gamma-\phi) + R_A \cos^2(\varepsilon_R+\gamma-\phi) \qquad (3.17)$$

and

$$T_R^\varepsilon = T_A \cos^2(\varepsilon_R+\gamma-\phi^\varepsilon)$$

where T_A is the analyser transmittance for the preferred plane of polarisation, and R_A is the transmittance when crossed. The intensity transmitted to the fibre-optic, I_{RF}, is therefore

$$I_{RF} = T_R I_R + T_R^\varepsilon I_R^\varepsilon \qquad (3.18)$$

The Transmitted Wave

The resultant major wave vector of the beam transmitted by BS2, is polarised at an angle ξ from the s′-plane of BS2, measured anti-clockwise, and is given by

$$\tan \xi = \frac{\beta_2}{\alpha_2} \tan \phi \qquad (3.19)$$

Similarly, the resultant minor wave vector of the beam transmitted by BS2 is polarised at an angle ξ^{ε} from the p'-plane of BS2, measured anti-clockwise, and is given by

$$\tan \xi^{\varepsilon} = \frac{\alpha_2}{\beta_2} \tan \phi^{\varepsilon} \qquad (3.20)$$

where $\beta_2 = t_{p2}/t_{s2}$ is the polarisation magnification factor, and t_{p2} and t_{s2} are the amplitude transmittance coefficients.

The intensities I_T and I_T^{ε}, for the major and minor waves respectively, are given by

$$I_T = \left(\frac{E_s}{\cos\xi}\right)^2 \qquad I_T^{\varepsilon} = \left(\frac{E_p^{\varepsilon}}{\cos\xi^{\varepsilon}}\right)^2 \qquad (3.21)$$

If ε_T is the angle between the analyser A_T's crossed axis and the s-plane of BS2 when $\gamma = 0$, then, similarly to the case of the reflected beam, the analyser intensity transmittances T_T and T_T^{ε}, for the major and minor waves respectively, are

$$T_T = T_A \sin^2(\epsilon_T+\gamma-\xi) + R_A \cos^2(\epsilon_T+\gamma-\xi)$$
$$T_T^{\varepsilon} = T_A \cos^2(\varepsilon_T+\gamma-\xi^{\varepsilon}) \qquad (3.22)$$

and therefore, the total intensity transmitted to the fibre, I_{TF}, is

$$I_{TF} = T_T I_T + T_T^{\varepsilon} I_T^{\varepsilon} \qquad (3.23)$$

Detection

The probe beam intensities transmitted by the analysers, are relayed by the fibre-optics to the single detector. The resulting signals, S_T and S_R for the transmitted and reflected beams respectively, are

$$S_T = \eta_D t_{FT} I_{TF} \qquad (3.24)$$

$$S_R = \eta_D t_{FR} I_{RF}$$

where η_D is the detector detectivity, and t_{FT} and t_{FR} are the transmittances of the fibre-optics relaying the light comprising the beams transmitted and reflected from BS2 respectively.

3.3.4 THE POLARIMETER RESPONSE CURVE

The parameter which defines the response of the polarimeter is the ratio of the signal difference to signal sum, R, given by

$$R = \frac{S_T - S_R}{S_T + S_R} = \frac{t_{FT} I_{TF} - t_{FR} I_{RF}}{t_{FT} I_{TF} + t_{FR} I_{RF}} \qquad (3.25)$$

This can be re-expressed in terms of the analyser transmittances as

$$R = \frac{(AT_T - T_R) + B(T_T^{\varepsilon} - CT_R^{\varepsilon})}{(AT_T + T_R) + B(T_T^{\varepsilon} + CT_R^{\varepsilon})} \qquad (3.26)$$

where the dimensionless parameters A, B, and C, are given by

$$A = \left[\frac{t_{FT}}{t_{FR}}\right]\left[\frac{T_{s2}}{R_{s2}}\right]\left[\frac{\cos\phi}{\cos\xi}\right]^2$$

$$B = \varepsilon^2 \left[\frac{t_{FT}}{t_{FR}}\right]\left[\frac{T_{p2}}{R_{s2}}\right]\left[\frac{\cos\phi}{\cos\xi^{\varepsilon}}\right]^2 \left\{\frac{\alpha_1 - \tan(\psi+\psi_o)\tan(\gamma+\eta)}{1 - \alpha_1 \tan(\psi+\psi_o)\tan(\gamma+\eta)}\right\}^2$$

$$C = \left(\frac{t_{FT}}{t_{FR}}\right)^{-1}\left(\frac{R_{p2}}{T_{p2}}\right)\left(\frac{\cos\xi^{\varepsilon}}{\cos\phi^{\varepsilon}}\right)^{2} \qquad (3.27)$$

3.4 THE PREDICTED BEHAVIOUR OF THE POLARIMETER TO REFRACTION

Once the experimental arrangement has been set-up, aligned, and an experimental plasma run initiated, two variables exist which can change the value of R measured during a plasma shot. These are the Faraday rotation angle and the refraction angle. Ellipticity due to plasma birefringence is negligible. In addition, changing the impact parameter between shots modifies the polarimeter response curve. Parameters such as the analyser settings, the misalignment angle between the beam-splitters, and the inclination angle of the initial plane of polarisation with respect to the p-plane of BS1, are constants whose values affect the behaviour of the polarimeter to these two variables, and affect the manner in which this behaviour is modified with impact parameter. The influence of some of these parameters on the theoretical behaviour of the polarimeter to refraction is examined below. The half-shade angles ε_R and ε_T are 2 degrees.

The behaviour of the polarimeter at a given impact parameter to plasma refraction, can be simulated by changing the impact parameter, as they are indistinguishable in their effect on the angles Φ and γ. Comparison of the response curves at different impact parameters therefore reveals the effect of refraction at one impact parameter. Of

course, it would be simpler to assume a refraction angle, and then calculate what effect it would have on the polarimeter response. However, this would be difficult to verify experimentally. It is easier to compare the polarimeter response at different impact parameters, as this is directly observable, and so simulate the effect of plasma refraction.

The change in the probe beam angle of incidence on BS1, produced by refraction of Θ at an impact parameter h, is equivalent to a change in the impact parameter of Δh with zero refraction. From equation 3.5, with f_1 = +650 mm and m_1 = 2.2, a change in the impact parameter of 5 mm, simulates refraction of 0.97 degrees. This is approximately the maximum refraction angle that can be expected, at the ruby laser wavelength, from the Plasma Focus (cf section 1.10). The resulting value of γ, from equations 3.5, 3.6, and 3.7 with h = 0, is 0.36 degrees.

Table 3.1 gives a list of constant parameters, together with their values, which describe the behaviour of the polarimeter. The parameters ψ_o, η, t_{FT}, and t_{FR}, are variables. The analyser crossed positions, ε_T and ε_R, are also constants, whose values depend upon the parameters α_1, α_2, β_2, ψ_o, and η. This is because they are set by crossing them with the He-Ne alignment laser (see section 3.2.3), at zero impact parameter and therefore zero γ, when the polarising prism is orientated to give a change in the plane of polarisation at the analysers of $\pm$ 2 degrees. For the analyser A_R, the prism is rotated such that $\psi=\varepsilon_H/\alpha_1\alpha_2$ = 2 degrees, when ε_H is the required half-shade angle. Crossing occurs when $\varepsilon_R=\phi$ with $\psi+\psi_o=\psi_o$ + 2 degrees. The value of ε_R then follows. Similarly, the analyser A_T is set when the prism is rotated to give $\psi=\varepsilon_H/\alpha_1\beta_2$ = - 1 degrees, so that crossing

TABLE 3.1 VALUES OF THE OPTICAL PARAMETERS

PARAMETER	VALUE
α_o^1	-1.58114
$\partial\alpha_1/\partial\tau\|_{\tau=45°}$	-0.0359 per degree
α_2	-0.64667
β_2	1.30809
(T_{s_2}/R_{s_2})	0.81818
T_A	0.59
R_A	3.0×10^{-6}

occurs when $\varepsilon_T=\xi$ with $\psi_o+\psi = \psi_o-$ 1 degrees. The value of ε_T then follows.

3.4.1 THE OPTIMUM OPERATING POINT

The essential details of the polarimeter's behaviour is obtained by considering the case when both the polarisation ellipticity and the rejection ratio of the analysers are zero. Taking the simplest possible case, i.e. $\psi_o = \eta = 0$, and $(t_{FT}/t_{FR}) = (T_{s2}/R_{s2})^{-1} = 1.22$, it can be shown that the range of possible values of R is from +1 to -1, when $\phi = \varepsilon_R + \gamma$ and $\xi = \varepsilon_T + \gamma$ respectively. These are just the positions where the analysers are crossed. The position where R = 0 is called the operating point, as this is the position on the response curve from which Faraday rotation measurements are made. For this case, the polarimeter's non-symmetrical response curves for three

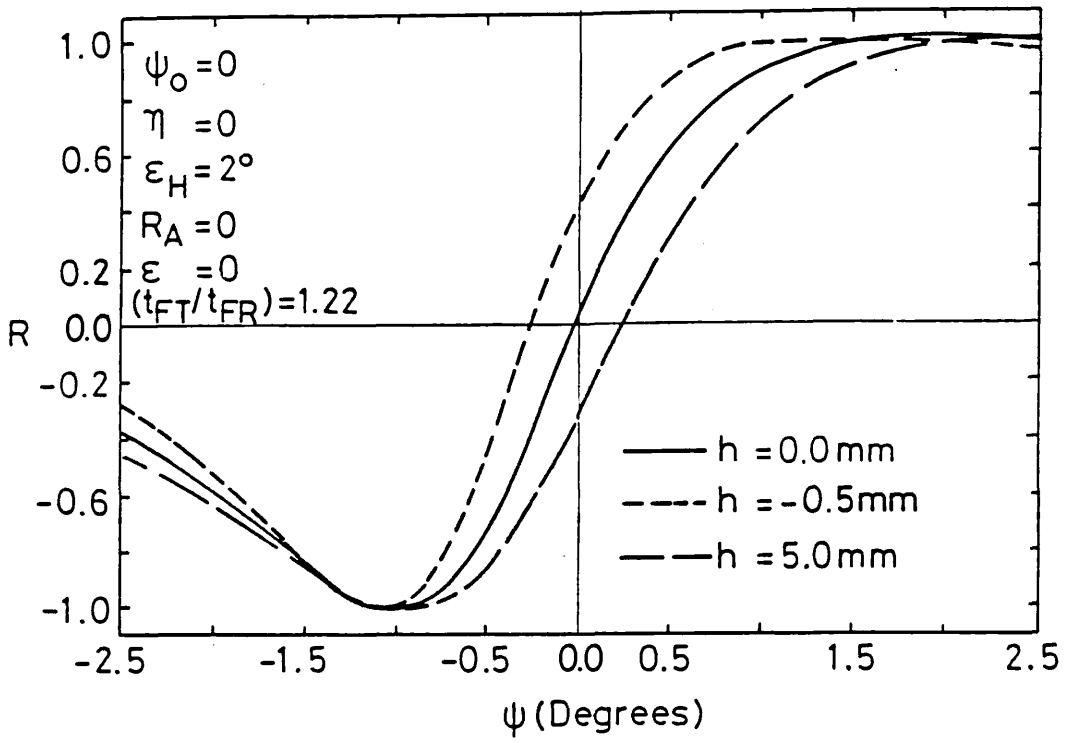

Figure 3.15

The predicted polarimeter response curve for an initial plane of polarisation ψ_o = 0 degrees.

impact parameters 0, ± 5 mm, are shown in figure 3.15. The two outer curves are equivalent to the response curves for a probe beam with impact parameter h = 0 mm, but with refraction of ± 0.97 degrees. Two features are particularly important. The first of these is the separation of the curves at the operating point. If Faraday rotation were absent during a plasma shot, a considerable change in the measured value of R could arise due to refraction alone, which would be subsequently wrongly interpreted as being due to Faraday rotation. At the impact parameter h = 0 mm, with a refraction angle of ≅ 1 degrees, a change in R ≅ 0.3 will occur. This is large in comparison to the measurement noise error $\delta R \cong \pm 0.025$ (discussed in section 3.5.3). Therefore, for this case, the polarimeter would be totally unsuitable for Faraday rotation measurements. The second important feature, is the difference in the gradients of the curves. This is discussed below.

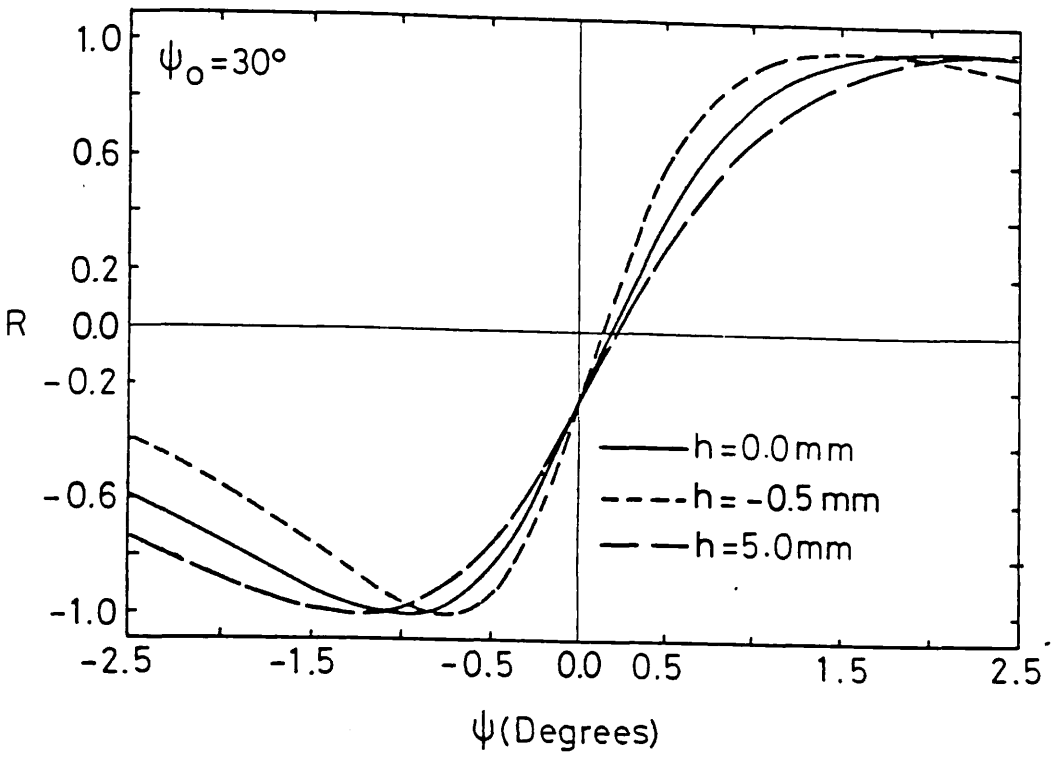

Figure 3.16

The predicted polarimeter response curve for an initial plane of polarisation ψ_o= 30 degrees.

Exploring ψ_o parameter space, a position is found where the behaviour of the polarimeter becomes suitable. For the parameters and impact parameters used above, the polarimeter's response curves for an initial plane of polarisation ψ_o = 30 degrees, are shown in figure 3.16. All three curves intersect at approximately the same point, eliminating the error due to curve separation. If this intersection point occured at the point R = 0, this would be the optimum operating point for the polarimeter, where the effect of refraction is smallest. A change in the measured value of R due to refraction will still occur however. This arises through the difference in the gradients of the curves at the operating point. Faraday rotation must be present for the effect to take place. Its magnitude $\delta R_{\textcircled{H}}$ is given by

$$\delta R_{\textcircled{H}} \cong \left\{ \frac{d}{d\,\textcircled{H}} \left(\frac{dR}{d\psi} \Big|_{R=0} \right) \right\} \psi\,\textcircled{H} \qquad (3.28)$$

where $dR/d\,\psi|_{R=0}$ is the gradient of the response curve at the operating point, and defines the sensitivity of the polarimeter. For convenience, $\delta R_{\textcircled{H}}$ is best compared with the change in R due to Faraday rotation alone, δR_{ψ}, given by

$$\delta R_{\psi} = \left(\frac{dR}{d\psi} \Big|_{R=0} \right) \psi \qquad (3.29)$$

For the parameters used, these gradients are

$$\frac{d}{\partial\,\textcircled{H}} \left(\frac{dR}{d\psi} \Big|_{R=0} \right) \cong 0.34\ \textcircled{H} \text{ and } \frac{dR}{d\psi} \Big|_{R=0} \cong 1.38 \qquad (3.30)$$

Therefore the ratio $\delta R_{\textcircled{H}}/\delta R_{\psi} \cong 0.24$ and so an error of 24% will result if refraction of 1 degree occurs. Typically, the refraction from the Plasma Focus is 0.5 degrees. Therefore, the typical error will be 12%, assuming that the polarimeter is operated from the optimum operating point.

The fibre-optic transmittance ratio (t_{FT}/t_{FR}), affects the location of the intersection and operating points, although not as strongly as ψ_o. Changing the value of this ratio alters the position of the intersection point with respect to the R-axis, leaving the ψ-axis position relatively unaltered. Consequently, the position of the intersection point can be manipulated until the optimum operating point is achieved.

The misalignment angle η similarly affects the location of the intersection point with respect to the R and ψ axes. However, the effect is weak and requires large angles, $\sim \pm 30$ degrees, to make a small change.

Experimentally, the optimum operating point can be found by adjusting the angle ψ_o and the ratio (t_{FT}/t_{FR}). This can be done without affecting the optical alignment. The transmittance ratio can be considered to be the coupling efficiency between the fibres and the detector, and is easily variable in practice. The angle ψ_o is also easily variable with the polarising prism. The misalignment angle is not variable as it is fixed by the alignment procedure.

The intersection region occurs because the effects of refraction cancel each other out. The parameter which is responsible for cancelling the effects at the second beam-splitter, is the gradient of the first beam-splitter's polarisation magnification factor with angle of incidence, $\partial\alpha_1/\partial\tau$. Although this term is small, its contribution becomes significant when the angle ψ_o is large.

The positions where the response curves turn over at the extremes of their range, i.e. at $R = \pm 1$, are different on either side of the operating point (cf figures 3.15 and 3.16). For a Faraday rotation angle of 2 degrees, the zero impact parameter curve of figure 3.16 has a value R = +1, while for an angle of -1 degrees, the value is -1. This non-symmetry arises because the net effect of the beam-splitter combination amplifies the change in polarisation of the beam transmitted by BS2 by a factor $|\alpha_1\beta_2| \cong 2$, while it is essentially unaltered for the beam reflected from BS2. The response curve reaches the value R = -1 when ψ = -1 degrees, because the analyser is in the crossed position.

3.4.2 THE EFFECT OF ANALYSER REJECTION RATIO

The effect of the analyser rejection ratio, R_A, depends very much on its magnitude, and on the half-shade angle of the polarimeter. It can be neglected however if the inequality

$$R_A << \frac{1}{2} T_A \tan^2 \varepsilon_H \qquad (3.31)$$

is satisfied. Otherwise, the effect will reduce the range of the ratio R, and also the sensitivity to Faraday rotation. It would also complicate the behaviour of the polarimeter with refraction, spreading out the intersection region and confusing the position of the optimum operating point. The effect must be kept minimal, and limits the half-shade angle that can be used by the polarimeter. The optimum half-shade angle, when limited by analyser rejection ratio, is discussed in section 3.6.1.

3.4.3 THE EFFECT OF POLARISATION ELLIPTICITY

As for the analyser rejection ratio, the effect of polarisation ellipticity, if significant, will reduce the range of the ratio R, and also the polarimeter's sensitivity to Faraday rotation. Again it will confuse the position of the optimum operating point. From equations 3.16 and 3.21, the intensity ratios (I_R^{ε}/I_R) and (I_T^{ε}/I_T) are approximately $\varepsilon^2\alpha_1^2\alpha_2^2 \cong \varepsilon^2$ and $\varepsilon^2\alpha_1^2\beta_2^2 \cong 4\varepsilon^2$ respectively. Therefore, the intensity of the minor wave component at the analyser A_T is approximately four times that at the analyser A_R, and so, unlike the case for the analyser rejection ratio, the effect will be greatly enhanced in the neigbourhood of the point R = -1. The effect of polarisation ellipticity sets a lower limit to the half-shade angle of the polarimeter. The optimum sensitivity, with ellipticity a limit, is

discussed in section 3.6.2.

3.5 EXPERIMENTAL OBSERVATIONS

In this section, experimental observations of the polarimeter's behaviour are described.

3.5.1 MAGNIFICATION OF THE POLARISATION CHANGE

The relationship between the angles ϕ and ξ with Faraday rotation, was directly observed when the analysers were crossed with the He-Ne alignment laser during the procedure followed to set the half-shade angle. From equations 3.14 and 3.19, with $\psi_o = 0$, $\eta = 0$, and $\gamma = 0$, these relationships are approximately

$$\phi \cong \psi \quad \text{and} \quad \xi \cong -2\psi \tag{3.32}$$

Plots of ϕ and ξ, or equivalently the analyser settings at which crossing occurs, against ψ, should therefore be linear with gradients 1 and 2 respectively. In figure 3.17, the experimentally observed relationship is shown. As predicted, the points measured are a good fit to linear curves with these gradients.

3.5.2 OBSERVATION OF THE OPTIMUM OPERATING POINT

The first step in the experimental procedure followed to measure Faraday rotation, is to calibrate the polarimeter. This is done by rotating the polarising prism, which simulates Faraday rotation, and observing the polarimeter's response curve $R(\psi)$. However, this

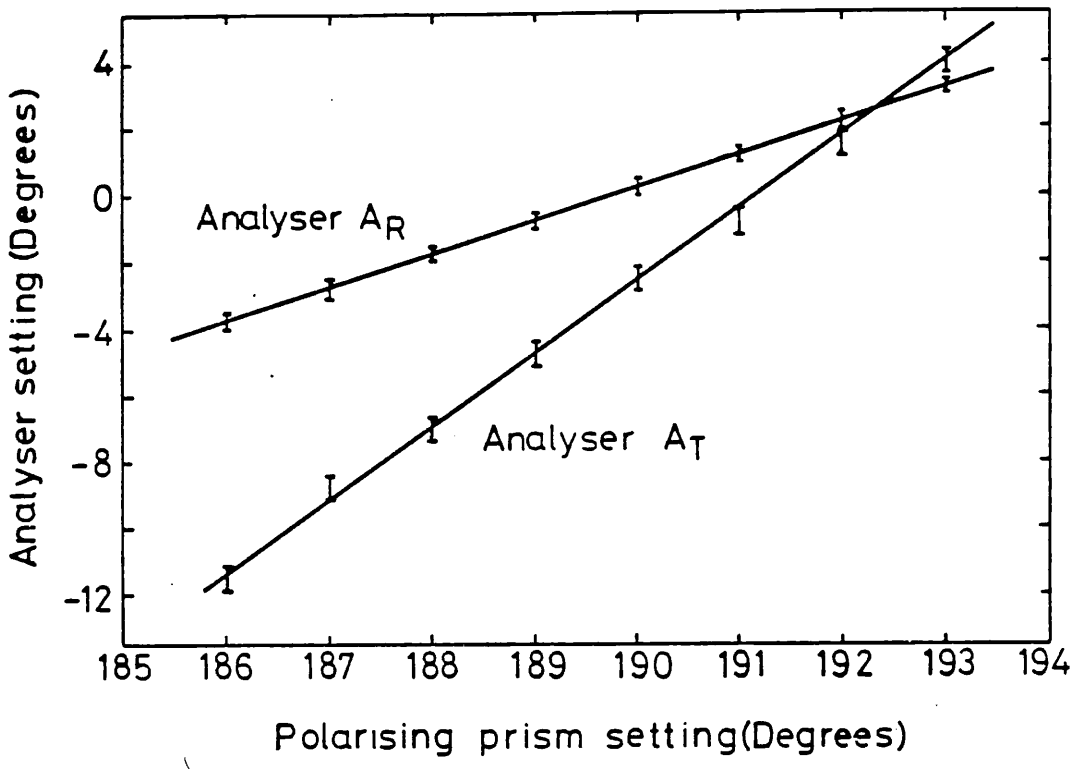

Figure 3.17

Experimental observations of the polarisation magnification produced by the beam-splitters.

procedure is complicated as the calibration must occur at the optimum operating point of the polarimeter (see section 3.4.1). The problem is locating this point.

It was shown in section 3.4.1, that the initial plane of polarisation strongly affects the location of the optimum point. The strategy adopted to locate the optimum point, was therefore to chose an initial ψ_o angle, roughly corresponding to the p-plane of BS1, set the half-shade angle, and then plot three calibration curves at impact parameters 0, $\pm$ 5 mm. From the positions of the curves with respect to each other, assuming the optimum point is not found, the direction in which ψ_o must be changed can be determined. This procedure is then repeated until the point is found. The final calibration occurs after both ψ_o and the fibre transmittances t_{FT} and t_{FR} have been adjusted so that the optimum operating point is reached, i.e. when the

intersection point lies close to or at the line R = 0.

Figure 3.18 shows a set of three calibration curves observed experimentally for an initial plane of polarisation defined by the polarising prism setting of 187.5 degrees. The half-shade angle was 1.5 degrees. Clearly, the intersection point had not been found. The positioning of these curves indicated that the angle ψ_o was too small. Figure 3.19 shows the set of calibration curves observed when the polarising prism setting was 191 degrees, giving a larger angle ψ_o. For this case, the optimum point had been found. Both these sets of experimental curves are very similar to the sets of theoretically predicted curves shown in figures 3.15 and 3.16.

Figure 3.20 shows the actual set of calibration curves used in the Plasma Focus experiment. The half-shade angle was 2 degrees. Some departure from that predicted is shown by the curve for the impact parameter +5 mm. This was because the observed probe beam had passed through different parts of the machine vacuum windows, and consequently, the polarisation ellipticity was different. From this graph, the value of R at the -1 turning point, for zero impact parameter, is approximately -0.93. It will be shown in section 3.6.2, that this is due to a polarisation ellipticity of 4.5×10^{-3}. As the response curves peak at a value of +1, then the effect of the analyser rejection ratio is unobserved.

The sensitivity of the polarimeter $dR/d\psi|_{R=0} \cong 1.2$ per degree, and the change in the sensitivity due to refraction approximately 0.28 per degree squared. Therefore, the ratio of the change in R due to refraction to that due to Faraday rotation, from equations 3.28

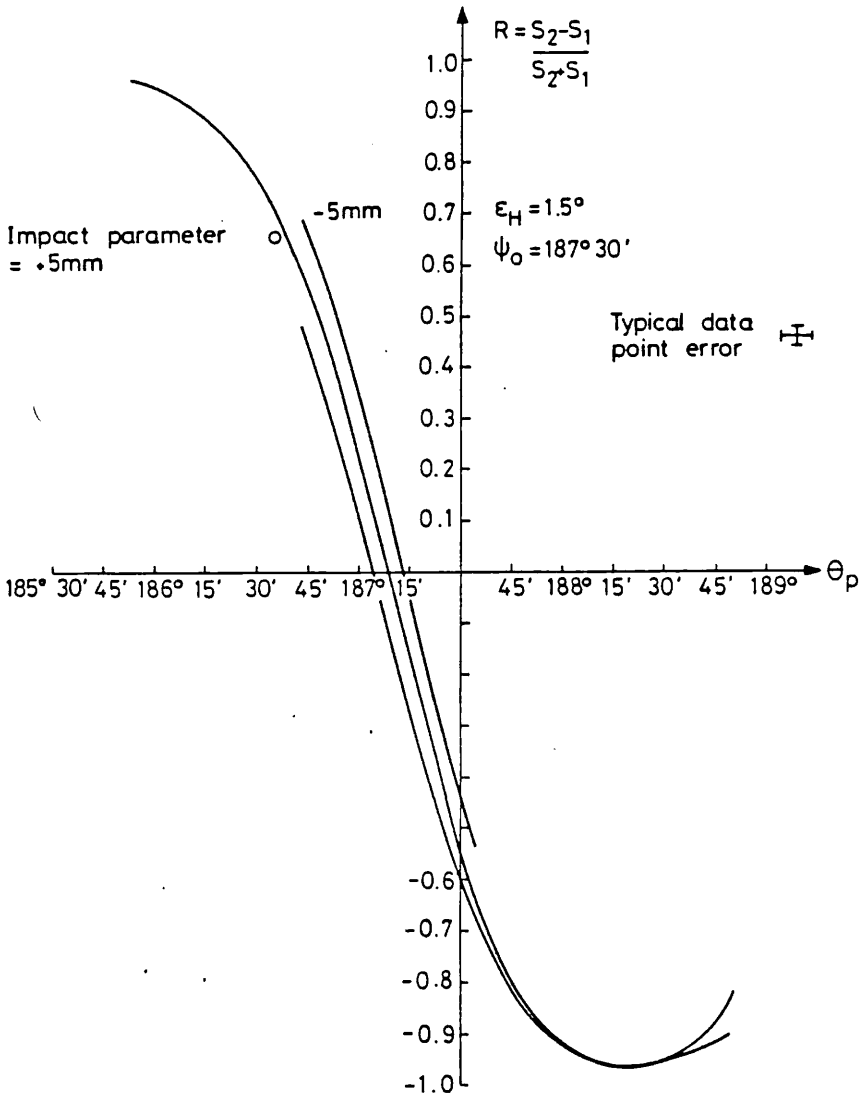

Figure 3.18

The experimentally observed polarimeter response curve away from the optimum operating point.

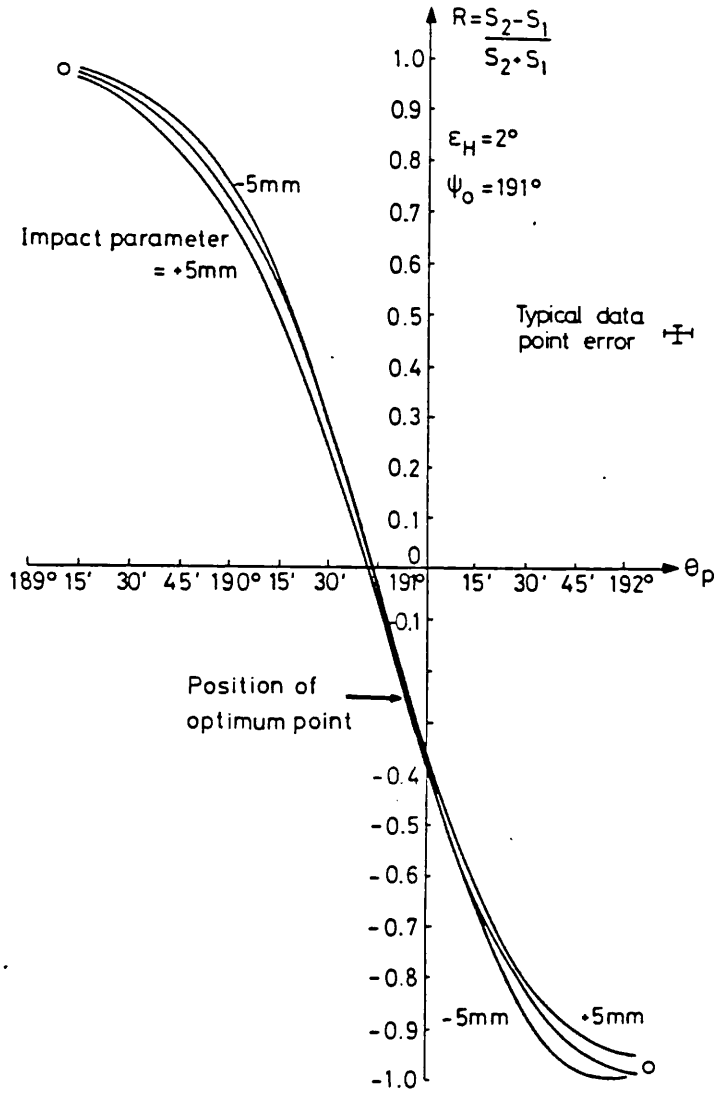

Figure 3.19

The experimentally observed polarimeter response curve near to the optimum operating point.

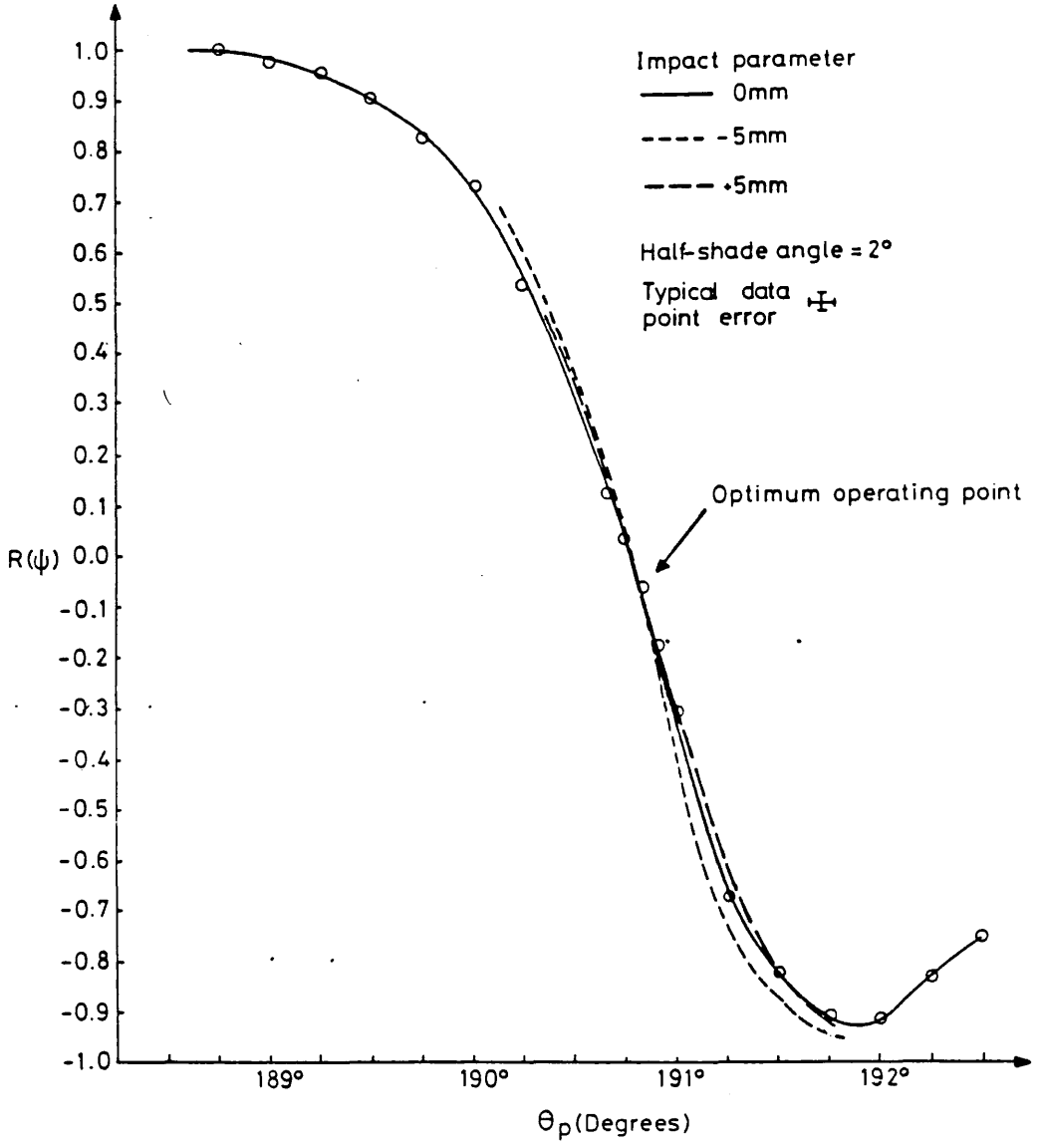

Figure 3.20

The calibration curve of the polarimeter used in the Faraday rotation experiment.

and 3.29, is given by

$$\delta R_{\oplus} / \delta R_{\psi} \cong 0.2 \oplus \tag{3.33}$$

and so an error of 20% will result if refraction of 1 degree occurs. Typically, the error will be 10%.

3.5.3 THE MINIMUM OBSERVABLE FARADAY ROTATION ANGLE

The minimum observable Faraday rotation angle, ψ_{min}, is defined as that angle which produces a change in the polarimeter's response which is indistinguishable in its magnitude to that due to noise. If the level of noise is δR_N, then the minimum observable rotation is

$$\psi_{min} = \left(\frac{dR}{d\psi} \Big|_{R=0} \right)^{-1} \delta R_N \tag{3.34}$$

Therefore, ψ_{min} is defined as that angle which gives a signal to noise ratio of unity.

Noise can originate from several sources within the experimental set-up. The first is due to plasma light emission which may have a random polarised component. However, no plasma light was observed due to the effective screening of the interference filter. The second is due to detector noise. As the detector was housed within the screened room, then it was protected from electrical interference. Both shot noise and diode recombination noise were not observed. Another source was due to amplifier and oscilloscope noise. Again this was not observed. The final noise source was observable however. This was due to the slight difference in the regions of the ruby laser observed by the two fibre-optics. The small difference in the two viewing chord positions, resulted in the laser intensities carried by the fibres having slightly different time histories. This effect was greatly

exagerated by the differencing technique. Another contribution to this noise, may have arisen from the difference in the convolution of laser intensity pattern at the entrance apertures of the fibres with the surface admittances.

Experimentally, noise was observed by measuring the ratio R at many corresponding points within the laser waveforms observed for calibration shots. For these, ψ is fixed and so R is constant. Noise is then observed by statistically averaging over many shots and many measurements, and determining the standard deviation. For the experiment, the standard deviation was 0.025 and had no significant correlation with either signal level or value of R. Therefore, the noise observed was constant. Taking the noise $\delta R_N = 0.025$, the corresponding minimum observable Faraday rotation angle was 0.02 degrees or 0.35mrad.

3.6 THE OPTIMUM SENSITIVITY OF THE POLARIMETER

The polarimeter's sensitivity essentially depends upon the half-shade angle used. However, the dynamic range is proportional to half-shade angle, and so large sensitivity can only be achieved at the cost of small dynamic range. In addition, small half-shade angle results in small analyser transmission, setting a minimum illumination power requirement, or a minimum feasible half-shade angle with the source used. In the following sections, new criteria for determining the optimum sensitivity of the polarimeter when limited by analyser

rejection ratio and polarisation ellipticity, are presented. It is assumed that dynamic range and source illumination are both sufficient.

3.6.1 LIMITATION BY ANALYSER REJECTION RATIO

Consider the polarimeter's response curve for the simple case when $\psi_o = \eta = \gamma = 0°$ and $t_{FT}/t_{FR} = 1.22$. The polarisation ellipticity is assumed zero, and the analysers rejection ratio R_A is assumed finite and equal for both. The values of the optical parameters are as given in table 3.1. The half-shade angle will be considered variable.

The sensitivity $(dR/d\psi)_{R=0}$, from equations 3.26 and 3.27, is expressed explicitly by

$$\left.\frac{dR}{d\psi}\right|_{R=0} = \frac{\alpha_1(\beta_2-\alpha_1)(R_A-T_A)\sin 2\varepsilon_H}{2(T_A\sin^2\varepsilon_H + R_A\cos^2\varepsilon_H)} \qquad (3.35)$$

where the half-shade angle ε_H is assumed equal for both analysers. This is plotted in figure 3.21 against half-shade angle for various analyser rejection ratios. The effect of R_A clearly limits the maximum posssible sensitivity. The half-shade angle giving rise to the maximum sensitivity, ε_{min}, from equation 3.35, is given by

$$\varepsilon_{min} = \sqrt{\frac{R_A}{3T_A}} \qquad (3.36)$$

which is similar to that derived by Jarboe [53]. This angle is plotted in figure 3.22 against the ratio R_A/T_A. For the HN22 analysers, maximum sensitivity would be achieved with a half-shade angle of 0.15 degrees. However, at this setting the dynamic range, $\sim 1.5\,\varepsilon_H = 0.225$ degrees, would be very small. If a larger dynamic range was needed, then obviously the minimum half-shade angle would be

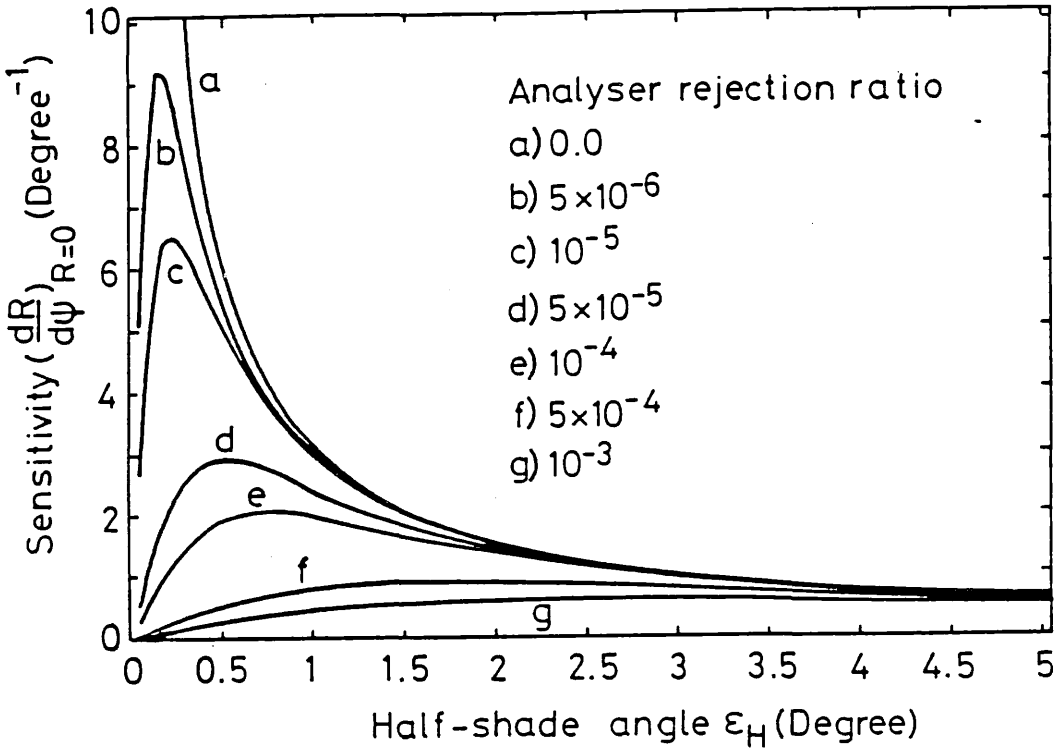

Figure 3.21

Polarimeter sensitivity plotted against half-shade angle for various values of analyser rejection ratio.

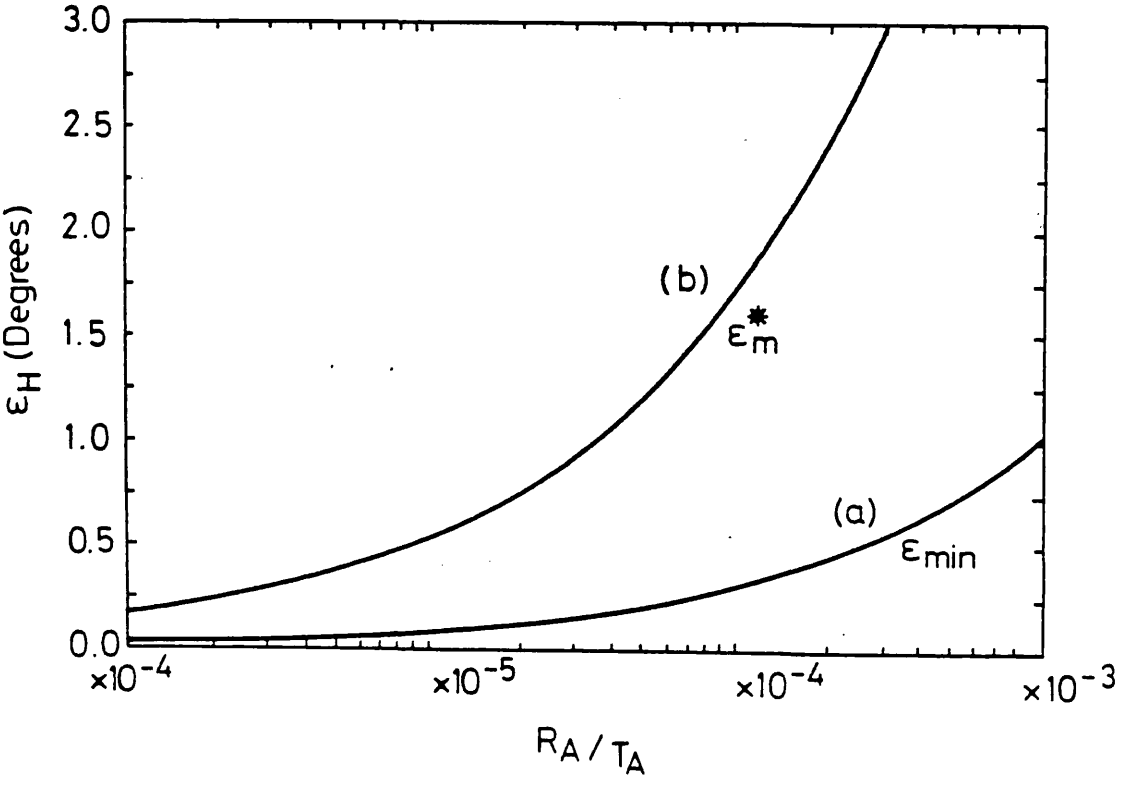

Figure 3.22

The optimum polarimeter half-shade angle determined a) by maximum sensitivity, and b) by minimising refraction effects.

chosen accordingly.

This minimum half-shade angle was determined without considering the effect of refraction. A better choice, if dynamic range is not a limitation, is found by considering the value of the ratio R when $\psi=\varepsilon_H/\alpha_1\beta_2$; i.e. when the analyser A_T is crossed with the probe beam. This point is chosen because it is a good indicator of polarimeter performance, and is more sensitive than at the corresponding point when the analyser A_R is crossed. This is because the magnification factor $\alpha_1\beta_2$ effectively reduces the half-shade angle at this point. From equations 3.26 and 3.27, the value of the ratio at this point, R_{-1}, is given by

$$R_{-1} = -\left(1 + \frac{64R_A}{\varepsilon_H^2 T_A(1-\frac{\alpha_2}{\beta_2})^2}\right)^{-1} \qquad (3.37)$$

This is plotted in figure 3.23 against the ratio R_A/T_A for various half-shade angles. For the half-shade angle given by equation 3.36, the value of R_{-1} is constant, having the approximate value -0.3. This value is too low. The best polarimeter performance is obtained when R_{-1} is in the range -0.9 to -1.0, when the effect of the analyser rejection ratio is small, and does not alter significantly the location of the optimum operating point. Using this as the new criterion to ensure that the polarimeter is optimised for both sensitivity and minimal refraction effects, the optimum polarimeter half-shade angle ε_m^*, is given by

$$\varepsilon_m^* = \left(\frac{20\ R_A}{T_A(1-\alpha_2/\beta_2)}\right)^{\frac{1}{2}} \qquad (3.38)$$

This is also plotted in figure 3.22. It is approximately six times larger than the angle given by equation 3.36. For the 2 degrees half-shade angle used in the experiment, the effect of the HN22

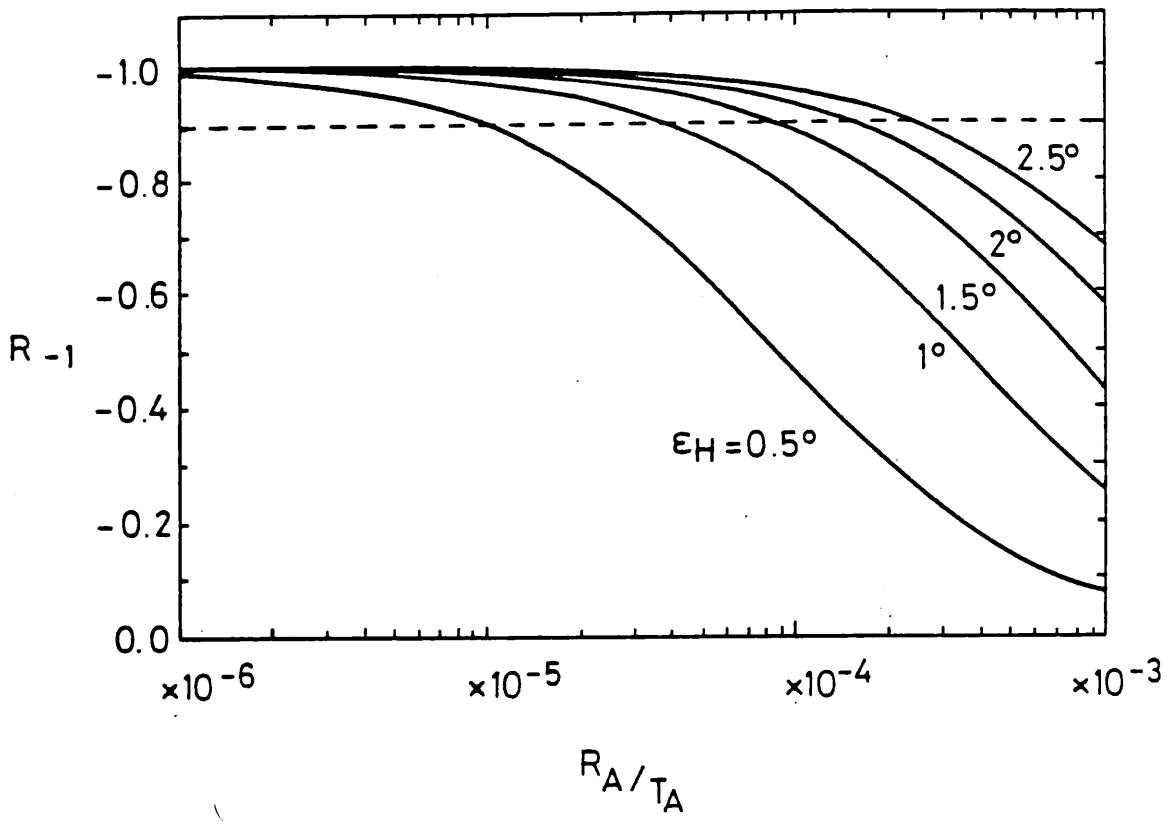

Figure 3.23

Ratio value R_{-1} against analyser rejection ratio for various half-shade angles.

analyser rejection ratio should be negligible as $R_{-1} = -0.99$. Even if the actual rejection ratio were worse by one order of magnitude, then R_{-1} would still be greater than -0.9, and the position of the optimum operating point would be unaffected.

3.6.2 LIMITATION BY POLARISATION ELLIPTICITY

The criterion used in the previous section to determine the optimum half-shade angle when limited by analyser rejection ratio applies equally well to the problem of determining the optimum half-shade angle when limited by polarisation ellipticity. This is because the effects of both on the behaviour of the polarimeter are similar. Assuming again the case used previously, but now with the analyser rejection ratio assumed zero, and the ellipticity finite, the value of the polarimeter's response curve at the R_{-1} turning point, from

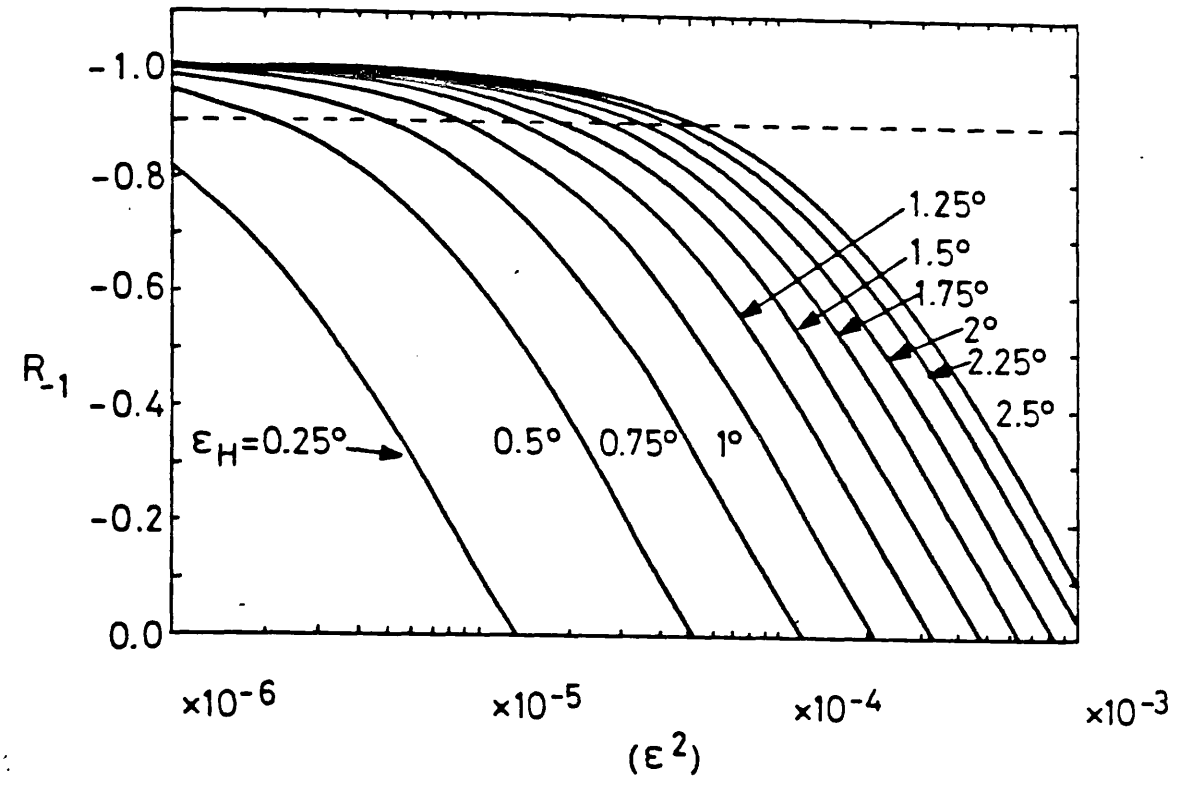

Figure 3.24

Ratio value R_{-1} against polarisation ellipticity squared for various half-shade angles.

equations 3.26 and 3.27, is given by

$$R_{-1} = \frac{4(\beta_2^2-\alpha_2^2)\ \alpha_1^2\varepsilon^2 - \varepsilon_H^2(1-\alpha_2/\beta_2)^2}{4(\beta_2^2-\alpha_2^2)\ \alpha_1^2\varepsilon^2 + \varepsilon_H^2(1-\alpha_2/\beta_2)^2} \qquad (3.39)$$

This is plotted in figure 3.24 against ellipticity squared for various half-shade angles. Best overall polarimeter performance is again obtained with a half-shade angle which gives $R_{-1} \geq -0.9$. This optimised half-shade angle ε_m^*, is given by

$$\varepsilon_m^* = \left(\frac{4\ \alpha_1^2\varepsilon^2\ (19\beta_2^2-\alpha_2^2)}{(1-\alpha_2/\beta_2)^2} \right)^{\frac{1}{2}} \qquad (3.40)$$

and is plotted in figure 3.25.

For the polarimeter to have an optimum half-shade angle of 2 degrees, the polarisation ellipticity would have to be 6×10^{-3}. From the experimentally observed calibration curves shown in

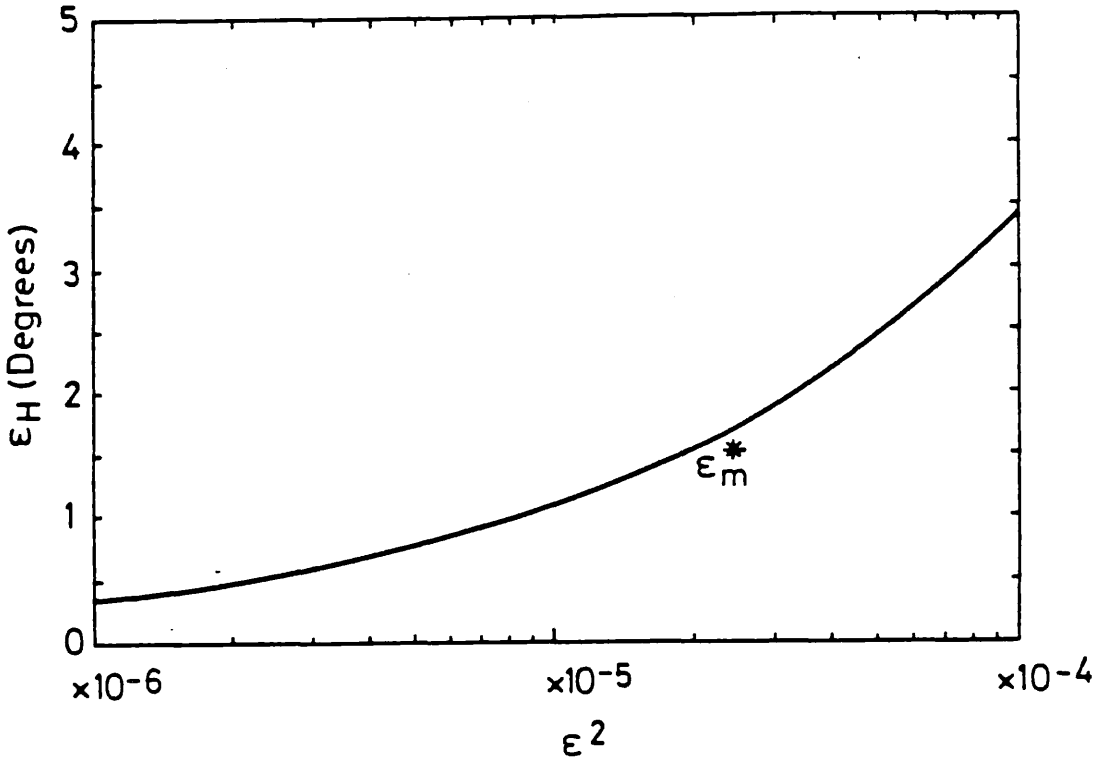

Figure 3.25

The optimum half-shade angle determined

by minimising refraction effects.

figure 3.20, the R_{-1} turning point has the range of values -0.95 to -0.90. From figure 3.24, this corresponds to a polarisation ellipticity of between 4.5×10^{-3} and 6.0×10^{-3}. Therefore, the polarimeter was used with optimum sensitivity at the half-shade angle used in the Plasma Focus Faraday rotation experiment. The source of this ellipticity was identified as being due to stress birefringence within the machine's vacuum windows.

From section 1.10, the ellipticity produced by dichroism and birefringence, even assuming anomalous collisionality, was in the range 10^{-4} to 10^{-5}. This is significantly lower than the ellipticity due to stress birefringence. Therefore, neither dichroism or birefringence affects the measurement of Faraday rotation.

CHAPTER 4 RESULTS, ANALYSIS OF RESULTS, AND INTERPRETATION

The results of holographic interferometry and Faraday rotation measurements of the Plasma Focus are presented. From these measurements, the azimuthal magnetic field structure of the pinch is determined. Descriptions of the data analysis, the errors, and the interpretation of the results, are given.

The measurements were taken with identical initial conditions, which were 24.1 kV capacitor bank voltage, and 1.8 torr filling pressure of deuterium gas.

4.1 RESULTS

Typical results of holographic interferometry and Faraday rotation polarimetry, are given in this section.

4.1.1 HOLOGRAPHIC INTERFEROMETRY

A sequence of ruby laser 1.5 ns double exposure holographic interferograms of the Plasma Focus were obtained in the time interval ranging from $t = -100$ ns to $t = +50$ ns with the experimental arrangement described in section 2.2.3.

The sequence of three reconstructed holograms shown in figure 4.1, show the evolution of the Plasma Focus during the collapse phase. Each was taken during a separate discharge. At time $t = -30$ ns, the

radially pinching current sheath is clearly visible against the background reference fringes. Also visible is the position where the current sheath folds over to become the return sheath. This position is marked with an arrow. The axial length of the plasma column, and radius at a Z-axis position 5 mm below the centre electrode, are 19 mm and 9 mm respectively. Instabilities of small amplitude are visible. At time t = -10 ns, the plasma column is more developed with a smaller radius of 3.6 mm and an axial length of 21 mm. The compact fringe structure at the plasma edge is similar to that shown for the earlier time, and indicates small edge density scale lengths. Instabilities with larger amplitude are observed. However, the plasma appears symmetric. At time t = 0 ns, peak compression of the plasma column occurs over an axial length of $\sim$ 10 mm from the the centre electrode. Axial electron densities of 4×10^{25} m^{-3} are achieved in a plasma column of radius 2.35 mm. The axial length of the plasma is 21.5 mm. The fringe shift distribution across the plasma image indicates a relatively uniform density gradient. Instabilities become more severe at this time, although the symmetry has not been destroyed. This latter hologram depicts the end of the collapse phase and the beginning of the dense pinch phase.

The three reconstructed holograms of figure 4.2, show the plasma at various times during the dense pinch phase. At time t = +5 ns, the plasma appears similar to that at peak compression (cf. figure 4.1). Instabilities have not yet destroyed the pinch. At time t = +20 ns, the plasma has clearly expanded in the area adjacent to the centre electrode. This expansion appears formless. It is also apparent that the plasma column has divided into two separate dense regions. This occurs as the result of a large amplitude m = 0 or sausage instability. Finally, at time t = +35 ns, the plasma in the neighbourhood of the

centre electrode is undetectable. From the sensitivity of the interferometer, an upper limit to the electron density of 3×10^{22} m^{-3} for this region is estimated. The remaining dense plasma column downstream is strongly perturbed by large amplitude $m = 0$ instabilities. This frame depicts the last stages of the dense pinch phase, with peak compression occuring in the region where the return current sheath is formed.

4.1.2 FARADAY ROTATION

Oscillographs of the polarimeter detector output were taken for a time range between -100 and +100 ns from peak compression of the plasma. The Z-axis position of the plasma plane observed was 5 mm below the centre electrode. Over 500 shots were recorded for a variety of impact parameters varying between $\pm$ 10 mm. In this section, typical Polaroid oscillographs are shown and discussed.

In figure 4.3, oscillographs of the detector output at impact parameters -3 and +4 mm are shown. Both were recorded at similar times during separate discharges. Most of the structure seen in the waveforms is due to the laser's output. Faraday rotation manifests itself by both changing the relative amplitudes at corresponding signal positions and, because it is time dependent, by modifying the waveform shapes differently. For the oscillograph taken at impact parameter -3 mm, the large increase in amplitude seen at the beginning of the second waveform, relative to the first, is due to Faraday rotation of approximately 0.3 degrees. After this time, the two waveforms become very similar indicating much less Faraday rotation. This time history of the Faraday rotation arises as follows: When the current sheath moves through the polarimeter's field of view, Faraday rotation is

observed. Once the plasma sheath's radius is less than the impact parameter, the probe beam passes through vacuum and the Faraday rotation is zero. Therefore, it is simply the plasma sheath moving across the viewing chord that is observed. The handedness of the rotation observed agrees with that predicted on the basis of the known magnetic field direction. The oscillographs taken for impact parameter +4 mm shows the same behaviour, although the direction of Faraday rotation is reversed. This reversal occurs because the polarimeter's field of view is on the opposite side of the magnetic axis.

Within the shot to shot variations observed in the experiment, no difference between the data taken on opposite sides of the magnetic axis was seen. Therefore, from the data, the plasma appears cylindrically symmetric.

During some plasma shots, very large departures - spikes - in the waveforms were observed. Figure 4.4 shows two typical shots. These spikes, one a rapid increase in amplitude, the other a similarly rapid decrease, occur at corresponding points within the two waveforms and are due to large Faraday rotation angles (approximately 1 degree which is twice the maximum normally observed). The two results shown were for impact parameters +1.5 mm and 0 mm. The observation of spikes at zero impact parameter indicates that there are large magnetic field strengths in the neighbourhood of the axis, and that the magnetic axis of the plasma may not necessarily correspond to the geometrical axis of the device. The spikes observed at impact parameter +1.5 mm are for a Faraday rotation with an opposite handedness to that at 0 mm, indicating that the magnetic axis lies between these points.

Figure 4.1

Typical interferograms during the collapse phase,

and at peak compression of the plasma.

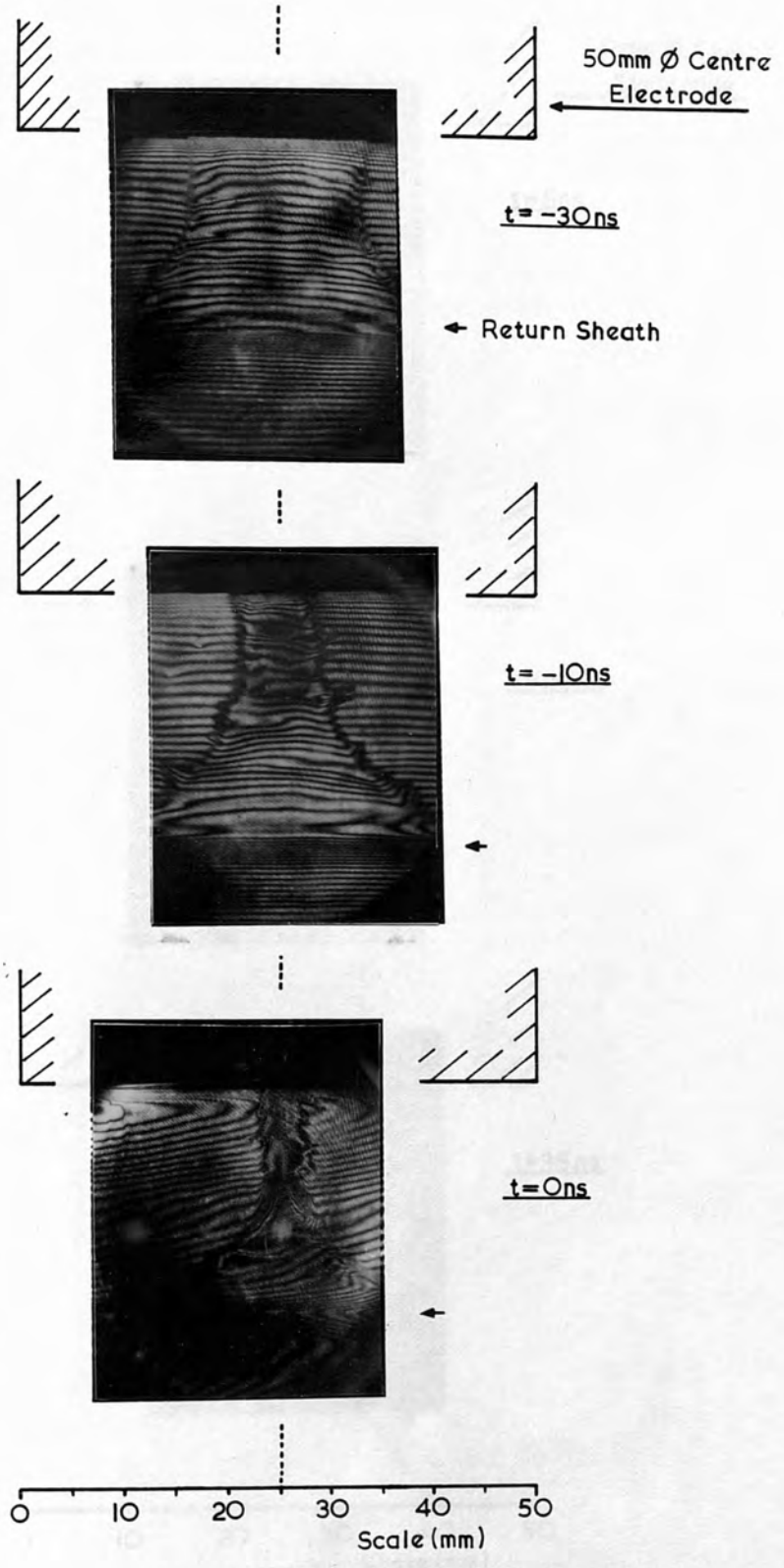

Figure 4.2

Typical interferograms during the dense pinch phase.

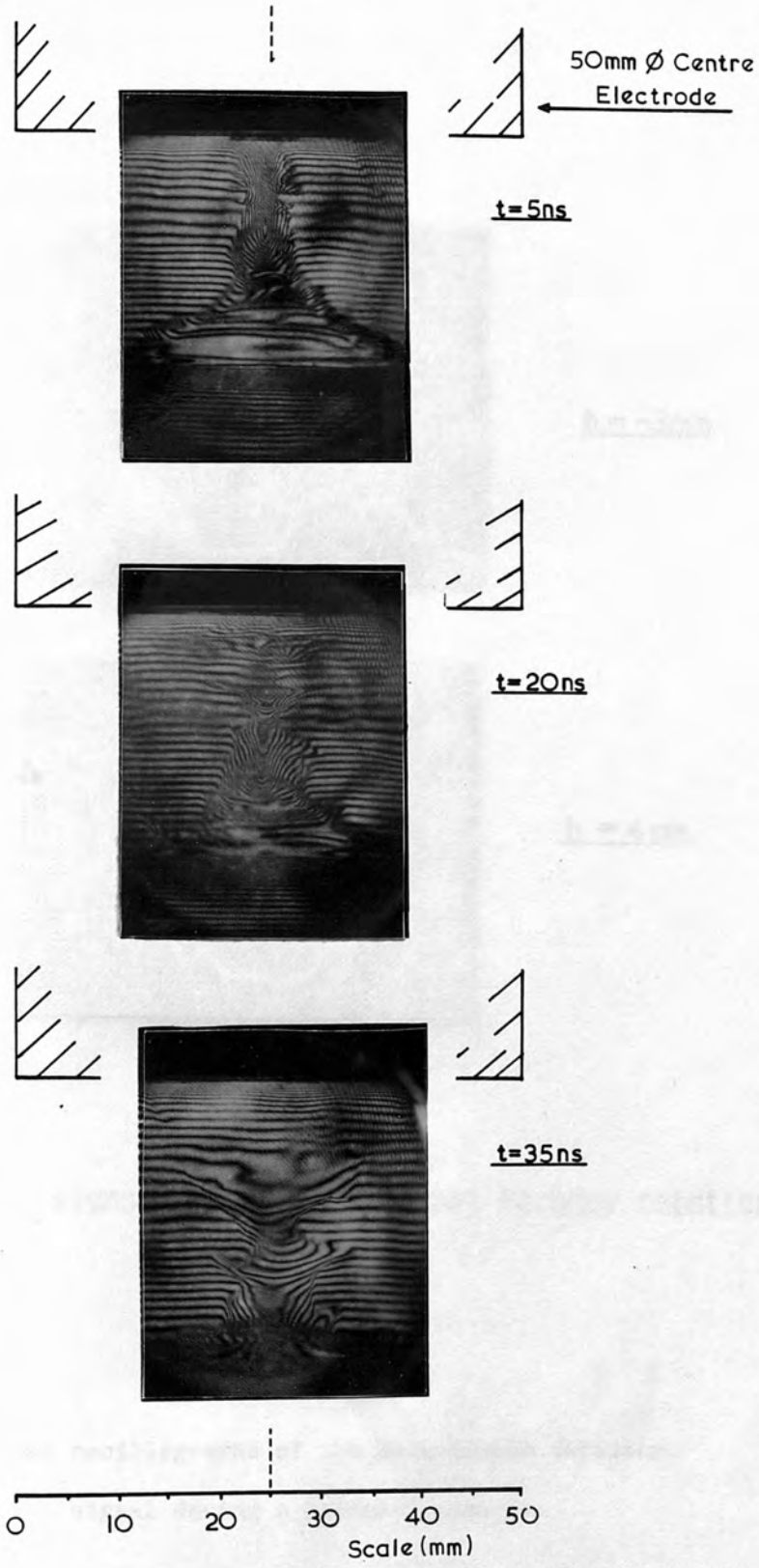

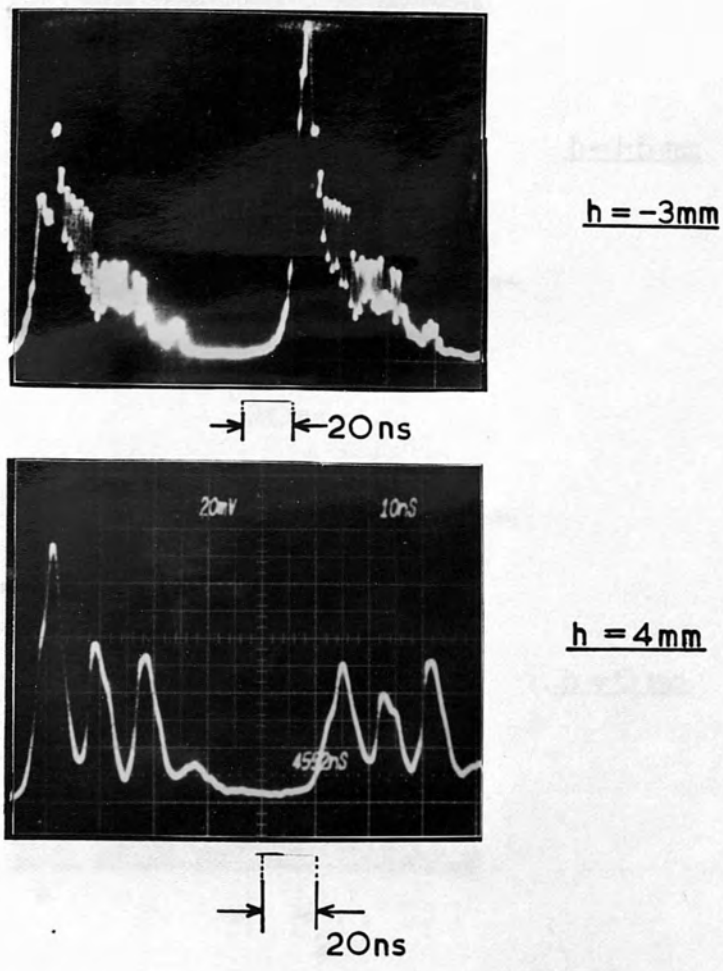

Polarimeter signals displaying normal Faraday rotation

Figure 4.3

Typical oscillographs of the polarimeter detector signal during a plasma discharge.

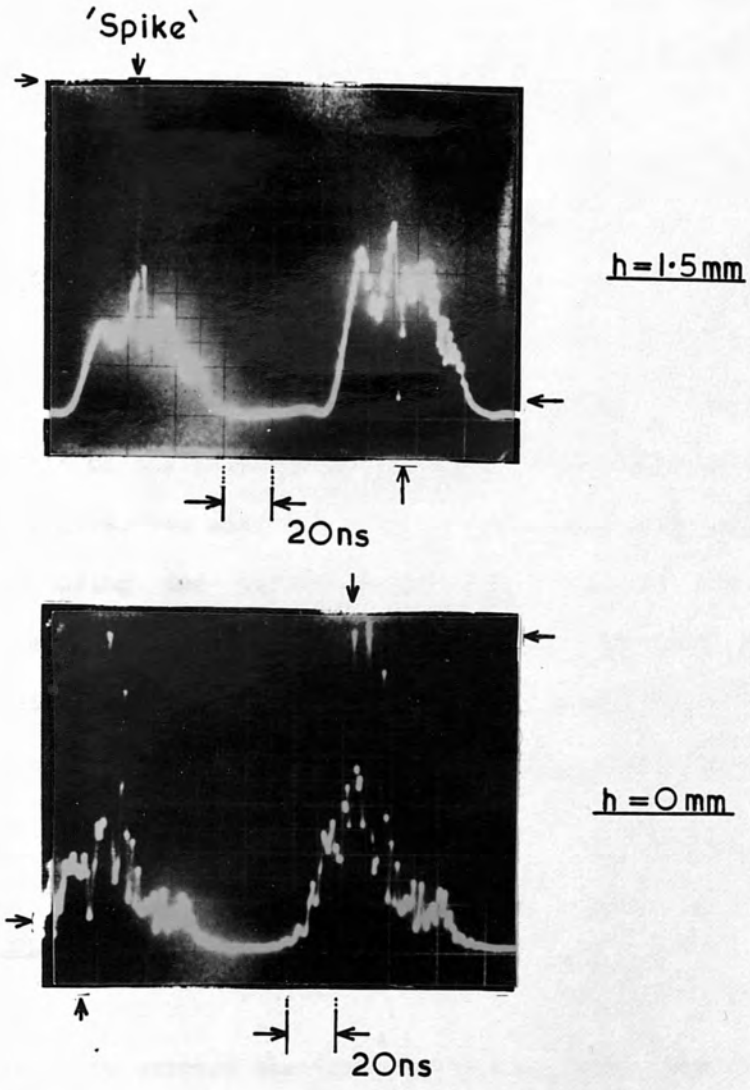

Polarimeter signals displaying Faraday rotation spikes due to axial current filaments

Figure 4.4

Oscillographs of the polarimeter detector signal exhibiting Faraday rotation due to short lived axial current filaments.

The duration of these spikes is approximately 2.5 ns, which corresponds to the 400 MHz bandwidth of the recording system. The magnitude of the observed rotations, 0.95 degrees, does not depend on impact parameter out to a value of 1.5 mm. These two results indicate that the measurements may be bandwidth limited.

4.2 ANALYSIS OF HOLOGRAPHIC INTERFEROGRAMS

Analysis of the interferometric fringe shift data contained in the holograms, gives the electron density radial distributions at a variety of times during the evolution of the discharge. In addition, the temporal evolution of both the plasma radius and the return sheath axial position can be determined. The procedures followed in the analysis of the holograms are described below. The accuracy of the unfolding is also discussed.

4.2.1 HOLOGRAM RECONSTRUCTION

In order to extract the interferometric data, the holograms had firstly to be reconstructed. White light reconstruction was accomplished using the optical arrangement of Jahoda and Siemon [50], shown schematically in figure 4.5. Light from a lamp P was collected by a condenser lens C, behind which was placed the hologram, H, to be reconstructed. With the lamp and lens positioned such that the light cone converged through the hologram to a focal point, F, two similarly converging first order diffracted light cones were produced on either side. A photographed image of the hologram taken in the light of one of these first order diffracted light cones, produced the reconstructed

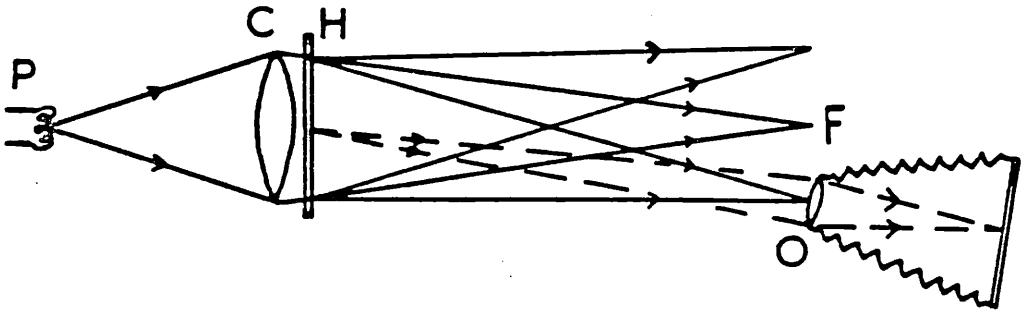

Figure 4.5

Hologram reconstruction

interferograms as shown in figures 4.1 and 4.2. This was most easily done by positioning the camera's objective lens, O, at the focus of one of the diffracted light cones. The images were recorded on Polaroid type 55 positive/negative film.

The type 55 negatives were examined by projecting from a 4x5 inch enlarger onto a large screen, giving an overall real space magnification of the interferograms of approximately 12. The observed spatial positions of the interferometric fringes, at their points of intersection with a line drawn between two corresponding vacuum fringes on either side of the plasma image, at the Z-axis position of interest, gave the radial distribution of the fringe shifts. The actual fringe shift was given by the number of fringes crossing the line between the plasma radius and the point, plus the fringe itself. On the axis, an additional fractional fringe shift was estimated using linear

interpolation.

4.2.2 ABEL INVERSION

The Plasma Focus is, to a good approximation, azimuthally symmetric. Therefore, a cylindrical model can be used to analyse the data. The fringe shift, F, caused by light propagating through the plasma at an impact parameter h, in the r-θ plane, is given by [54]

$$F(h) = \frac{1}{\lambda n_c} \int_h^a n_e(r) r (r^2-h^2)^{-\frac{1}{2}} dr \qquad (4.1)$$

where λ is the probe beam wavelength, and n_c is the critical electron density for that wavelength. For the 694.3 nm wavelength of the ruby laser used, $n_c = 2.3 \times 10^{27}\ m^{-3}$. Equation 4.1 is a form of Abel's integral equation, with the solution for the electron density profile given by

$$n_e(r) = \frac{-2\lambda n_c}{\pi} \int_r^a \left\{ \frac{dF(h)}{dh} \right\} (h^2-r^2)^{-\frac{1}{2}} dh \qquad (4.2)$$

This integral depends upon the gradient of the fringe shift profile with impact parameter. Therefore, for accurate density unfolding, the fringe shift profile must be precisely known. This also implies that good profile fitting to the raw data is necessary. The observed fringe shift profiles did not in general correspond to known analytic solutions. Therefore, the Abel inversion integral was determined numerically. This was most conveniently done using the method of Bockasten [55], which assumes cylindrical symmetry.

The raw data consisted of the positions of the integer fringe shifts, the fractional axial fringe shift value, and the plasma radius. Through this data, a continuous curve was fitted numerically using

library Fortran subroutines on a Prime 500 computer. This curve consisted of a set of N-1 cubic splines, where N is the number of data points, each defined only within the interval between the N-1 pairs of adjacent points. Typically, 10 - 15 data points were used. From this curve, a sequence of fringe shift values F_k, were calculated for equidistant impact parameter values, $h_k = ka/n$ $(k = 0,1,2,\ldots,n-1)$, where a is the plasma radius, and n is an integer. From these F_k values, n values of the electron density, $n_e(r_j)$, at the radial positions $r_j = ja/n$ $(j = 0,1,2,\ldots,n-1)$, were calculated using the Abel inversion equation [55]

$$n_e(r_j) = \frac{2\lambda n_c}{a} \sum_k \alpha_{jk} F_k \qquad (4.3)$$

where the coefficients α_{jk} are tabulated by Bockasten for cases when the integer n = 10, 20, or 40. The latter set of coefficients is given only for $j \geq 30$, and enables a more detailed study of the edge of the distribution. For the analysis of the interferometric data reported in this thesis, the value of n used was 20. This provided sufficient accuracy over the whole distribution.

Three typical fringe shift profiles for times t = -25, 0, and +10 ns are shown in figure 4.6. The fringe shift profile at time t = -25 ns, is similar to that taken from the reconstructed hologram shown in figure 4.1 at time t = -20 ns. The fringe shift increases rapidly at the plasma edge, reaches a maximum value, and then decreases slightly towards the axis. This profile is characteristic of a hollow electron density distribution, peaked near to the plasma-vacuum boundary. The fringe shift profile at time t = 0 ns, is strongly peaked on axis, with approximately 14 fringe shifts observed. At time t = +10 ns, the profile remains peaked on axis, and has a similar gradient to that at time t = 0 ns. Only the boundary region shows any

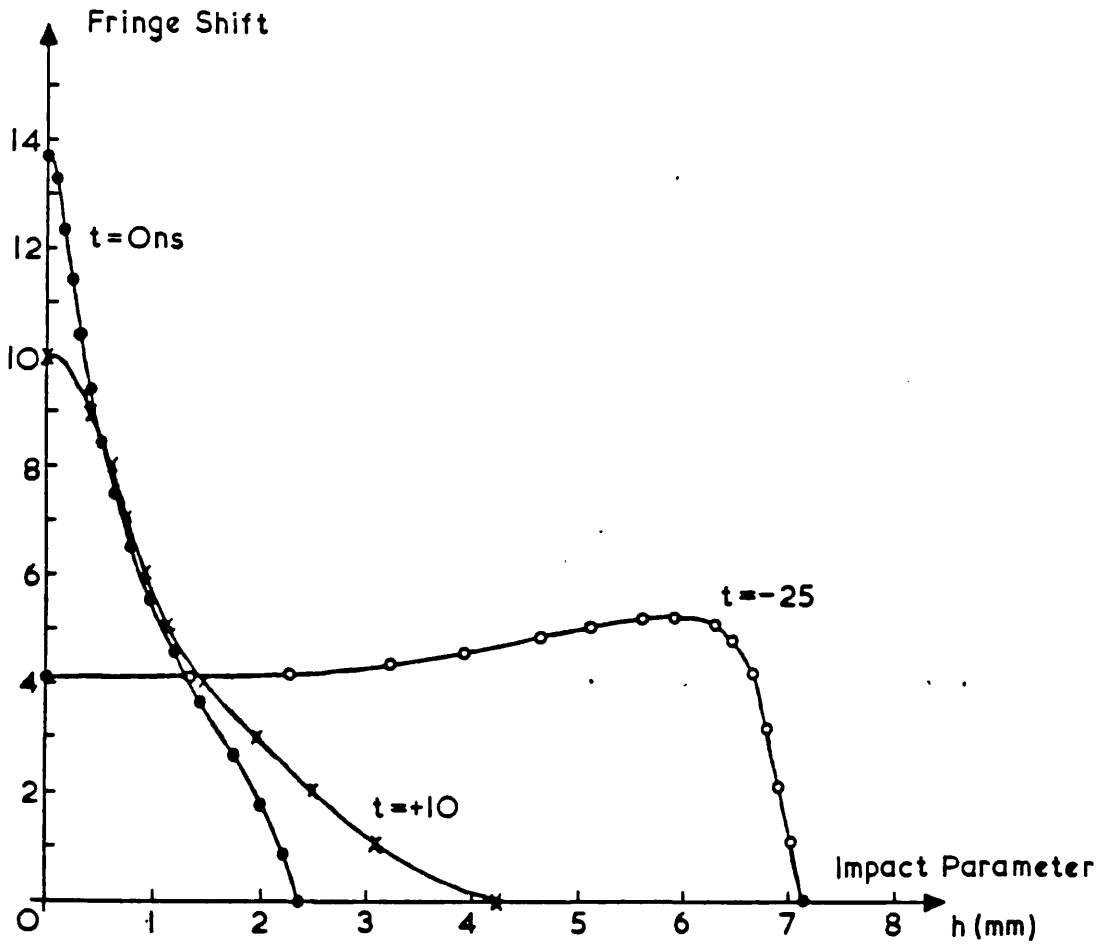

Figure 4.6

Typical fringe shift profile.

significant modification. This is due to the relaxation of the density distribution after peak compression.

4.2.3 ABEL INVERTED ELECTRON DENSITY PROFILES

A sequence of Abel inverted electron density distributions during the collapse phase, from times t = -44 ns to t = -7.5 ns, are shown in figure 4.7. The axial positions of these profiles lie in the range 5 - 10 mm below the centre electrode. At the earliest time, t = -44 ns, the pinching sheath is well defined, with a peak electron density 1.2×10^{24} m^{-3}. The axial density is 8.0×10^{22} m^{-3}, which is 60% of the density for completely ionised deuterium gas at the 1.8 torr filling pressure used. Although not shown, approximately 6 ns later the axial density has increased to 1.3×10^{23} m^{-3}, which corresponds to the filling density. The peak density at this time is 1.4×10^{24} m^{-3}. As time progresses, both the peak sheath density and axial density continue to rise. The radial distribution of the electron density reaches an almost constant value of 4.0×10^{24} m^{-3}, approximately 10 ns before peak compression. This represents an increase in axial density by a factor of 50 from the earlier time of t = -44 ns, and an increase in peak density by a factor of 3.3. Following this time to peak compression, the distribution maximises on axis and grows rapidly, as demonstrated by the plot at time t = -7.5 ns.

Figure 4.8 shows a sequence of Abel inverted electron density distributions during the dense pinch phase, from peak compression until a time t = +20 ns. Again the axial positions of these profiles lie in the range 5 - 10 mm. At peak compression, the plasma radius is 2.35 mm, and the axial electron density 4.2×10^{25} m^{-3}. This density is approximately 500 times larger than the axial density at t = -44 ns,

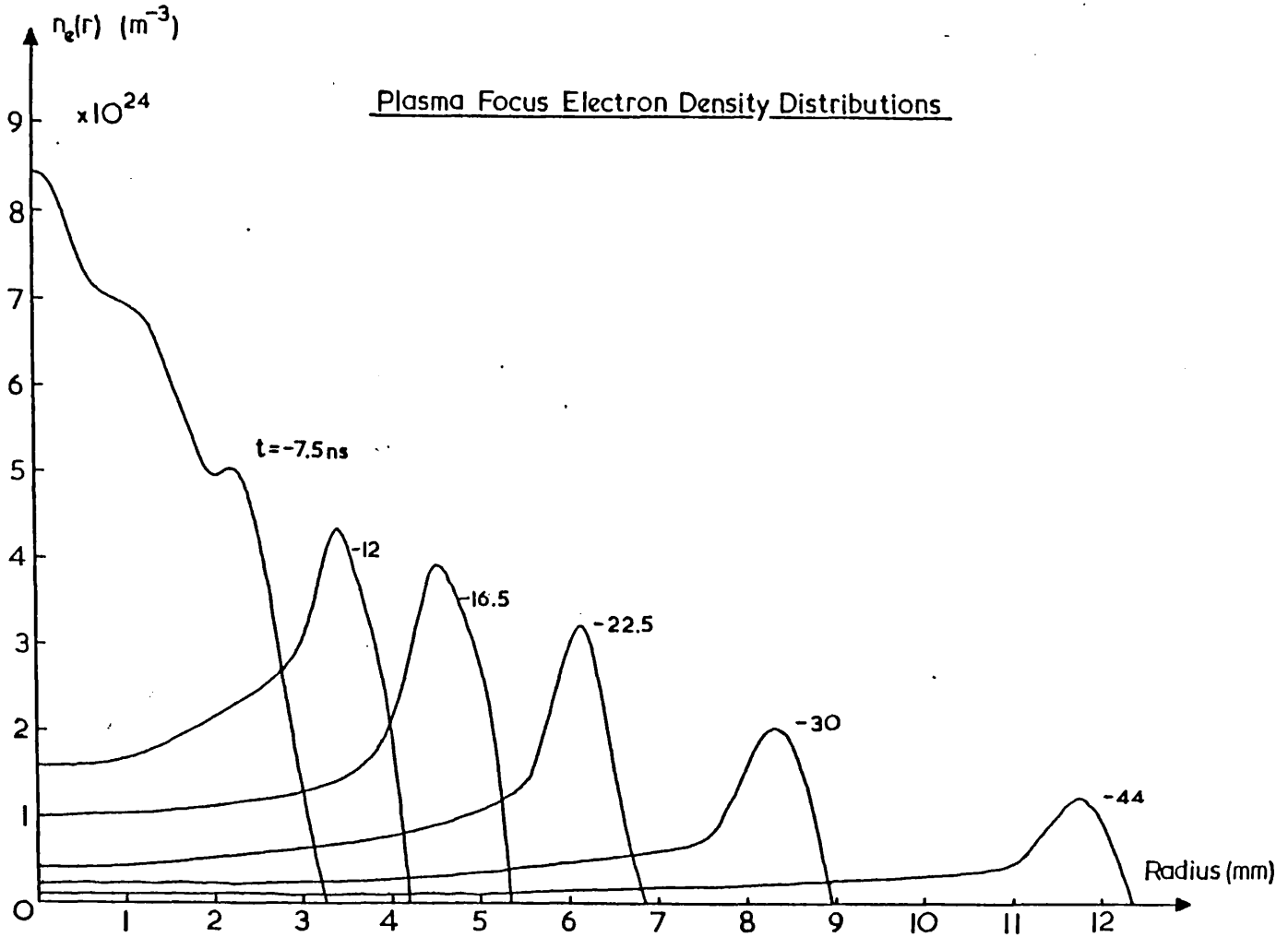

Figure 4.7

Abel inverted electron density distributions

during the collapse phase.

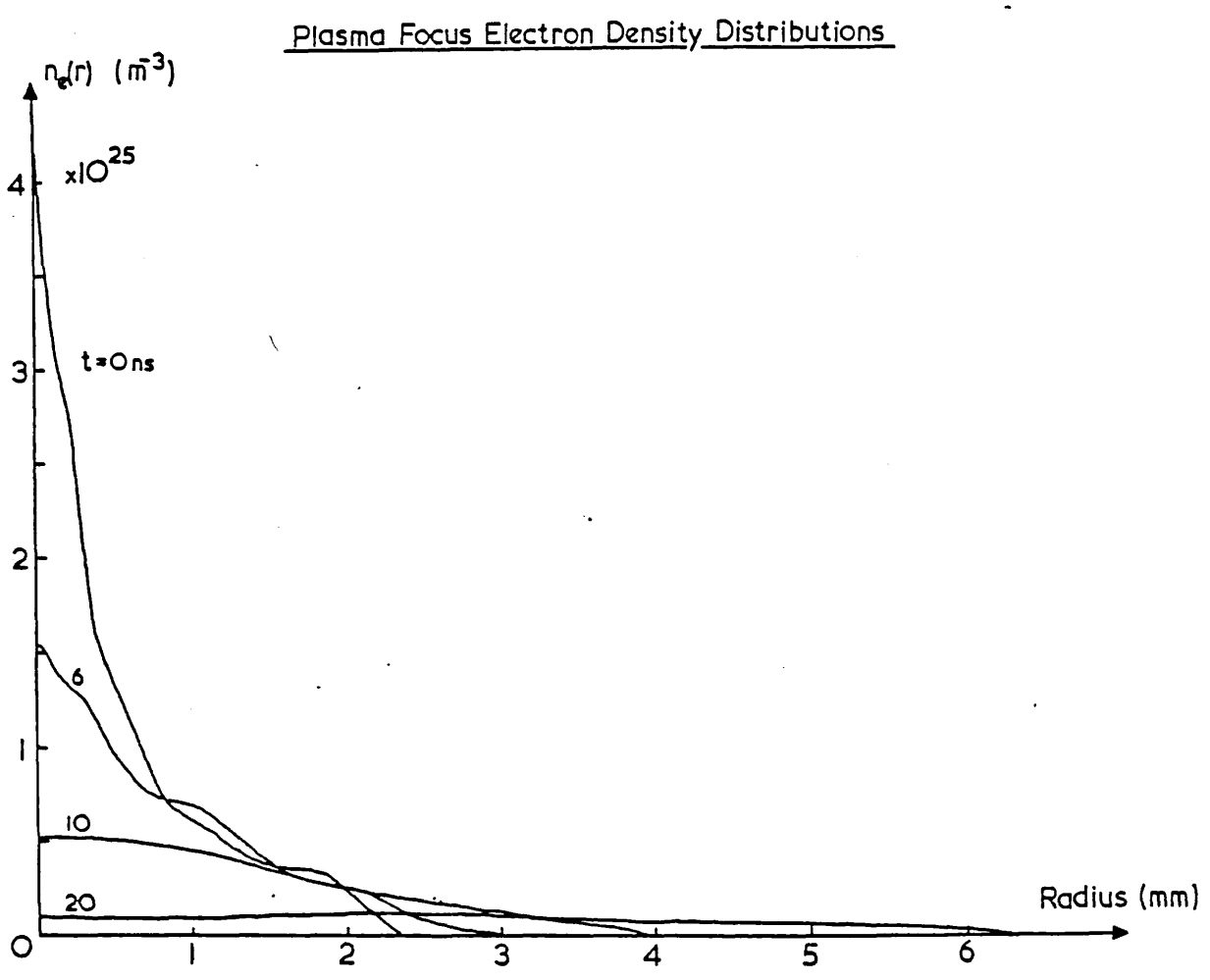

Figure 4.8

Abel inverted electron density distributions

during the dense pinch phase.

and 300 times the filling density. At the time t = +6 ns, the axial electron density has dropped by a factor 2.7 to 1.56×10^{25} m^{-3}. At the time t = +10 ns, the axial density is 5.2×10^{24} m^{-3}, which is a decrease by a factor 8.4 from peak compression. During the last 10 ns time period of the collapse phase, the density increases by a similar factor. Thus, within a 10 ns window on either side of peak compression, the electron density profiles are similar. At a time t = +20 ns, the axial electron density has decreased to 10^{24} m^{-3}, and the profile clearly shows the relaxation of the density distribution.

These results are in good agreement with an earlier investigation of the Plasma Focus by Morgan [46], who used Mach-Zehnder interferometry. In Morgan's investigation, the device was operated with different initial conditions to the present work. These conditions were: 30 kV capacitor bank energy, and 2.5 torr filling pressure of deuterium with 4% Argon.

During the time period covered by figures 4.7 and 4.8, the plasma column was perturbed by Raleigh-Taylor instabilities. As a direct result, it was not possible to obtain from every analysed hologram the electron density profiles at a Z-axis position 5 mm below the centre electrode, which was the position where the Faraday rotation measurements were made. Therefore, in order to cover the time interval of interest, several profiles from adjacent axial locations were utilised. Fortunately, it was found that the profiles did not have a significant axial dependence when $Z \leq 10$ mm. Thus, the electron density profiles reported in this thesis, and used in the analysis of Faraday rotation, are composed of plots from a variety of axial positions, with $Z \leq 10$ mm.

Figure 4.9 shows an isometric plot of the temporal behaviour of the electron density distribution, between the times t = -44 ns and +20 ns. This was constructed using the experimental data shown in figures 4.7 and 4.8. Linear interpolation was used to generate data at times other than those for which profiles were known.

4.2.4 THE PLASMA RADIUS AND SHEATH VELOCITY

In addition to electron density information, the holographic interferograms give details of the temporal evolution of the plasma radius at various axial positions. Figure 4.10 shows the observed time dependence of the plasma radius at an axial position Z = 5 mm. It is seen that the radius decreases linearly with a velocity of 2.35×10^5 ms^{-1}, until a time approximately 15 ns before peak compression, after which, the velocity drops to zero at peak compression. The plasma then expands, and the rate of expansion is similar to the rate of contraction before peak compression.

The minimum plasma radius was 2.35 mm, and this occured at the time when the dI/dt singularity was observed on the Rogowskii coil waveform. This is peak compression of the pinch, and it is with reference to the dI/dt singularity that all timings are made.

The curve fitting the data points of figure 4.10 is hyperbolic, having the form

$$a(t) = a_1\left(1 - \frac{1}{a_2^2}(t-t_o)^2\right)^{\frac{1}{2}} + a_3 \qquad (4.4)$$

where the constants a_1, a_2, a_3, and t_o, are defined as follows: The sum $a_1 + a_3$, is the minimum plasma radius and occurs at a time t_o. The ratio a_1/a_2, is the gradient of the hyperbola's asymptote and is also

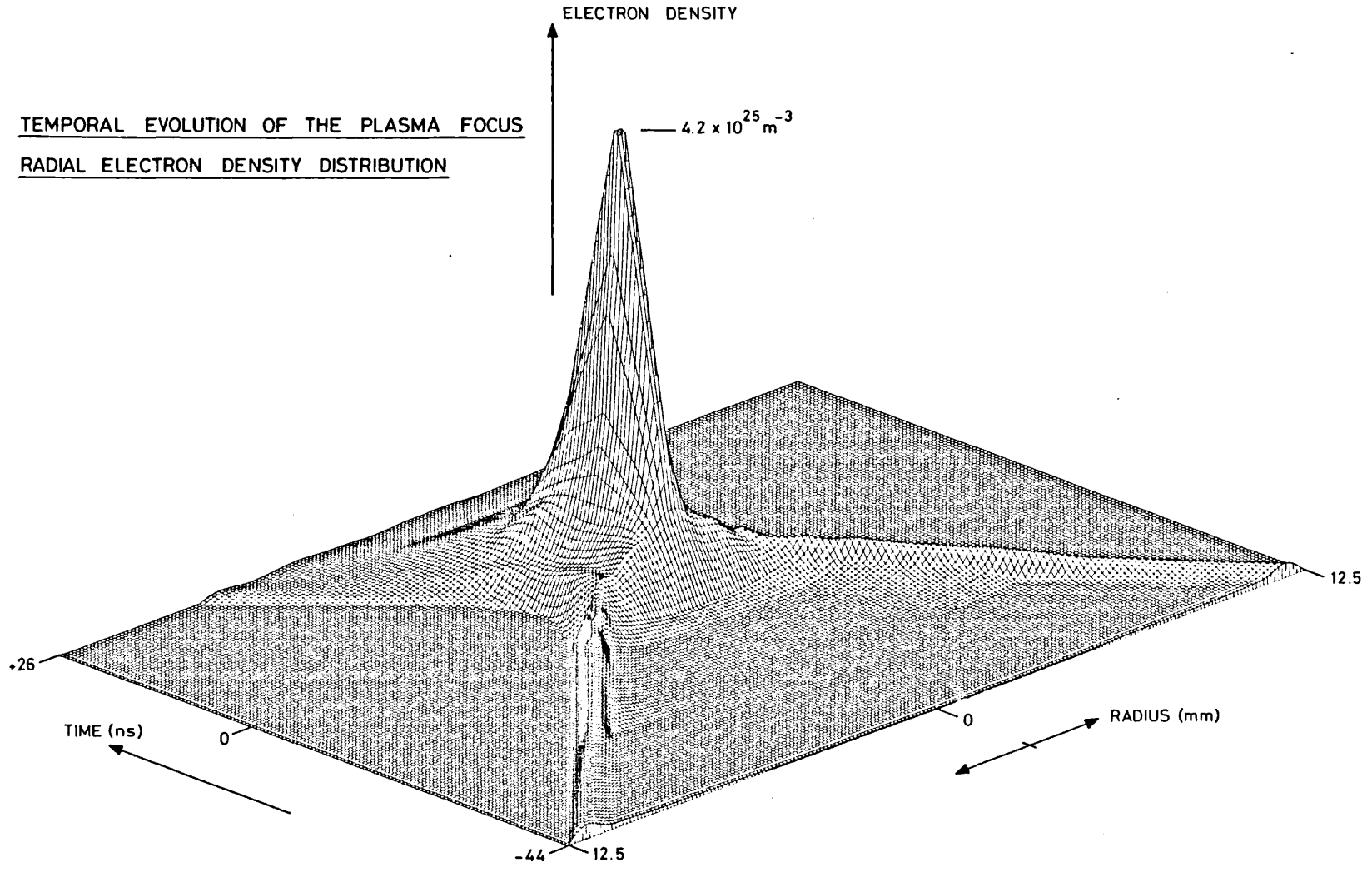

Figure 4.9 Temporal behaviour of the electron density distribution as observed by holographic interferometry.

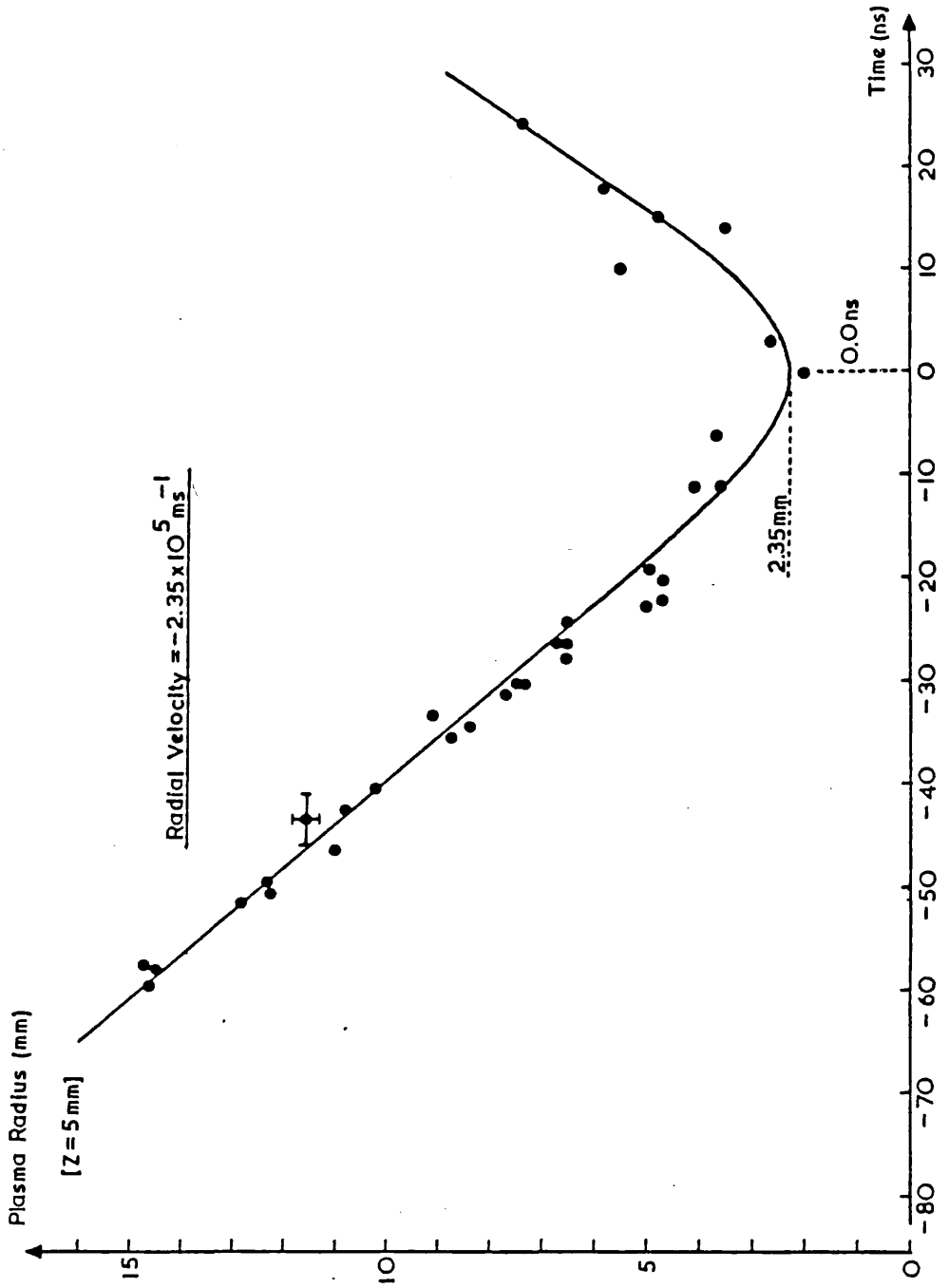

Figure 4.10

Time evolution of the plasma radius at Z = 5 mm.

the velocity of the plasma-vacuum boundary. Finally, the constant a_3 is the value of the radius at the intersection point between the asymptote and the line $t = t_o$. The gradient of the asymptote was found by least-squares fitting the data, with a $\geq$ 6 mm, to a linear curve. The parameter a_3 can be considered to be half the sheath thickness, because, when the sheath converges on axis and is reflected, during the reflection period it overlaps itself. From the data collected for the three axial positions Z = 5, 7.5, and 10 mm, the sheath thickness is approximately 1.4 mm. This value agrees well with the width of the shock as determined from the electron density profiles shown in figure 4.7, and is approximately twice the magnetic field penetration depth as observed by Faraday rotation and discussed later.

For axial positions > 10 mm, the hyperbolic fit to the data is poorer after peak compression than before. This is because at these locations, the plasma column is less reproducible, due to the effects of plasma instability.

The three curves shown in figure 4.11, summarise the results observed for the axial and temporal behaviour of the plasma radius. The axial dependence of asymptotic radial velocity shown, indicates that the sheath is slowest adjacent to the centre electrode, and is fastest when Z $\geq$ 10 mm. Between the axial points 5 and 10 mm, the velocity increases from $2.35 \times 10^5 ms^{-1}$ to $2.65 \times 10^5 ms^{-1}$. For Z $\geq$ 10 mm, the velocity is approximately constant at $2.7 \times 10^5 ms^{-1}$. This behaviour of the radial velocity with axial position is different to that observed by Morgan [46], who observed a decrease in velocity with axial position. The axial dependence of minimum plasma radius, shows that the greatest compression occurs at the axial position Z = 7.5 mm. At the neighbouring points Z = 5 and 10 mm, the values of minimum radius

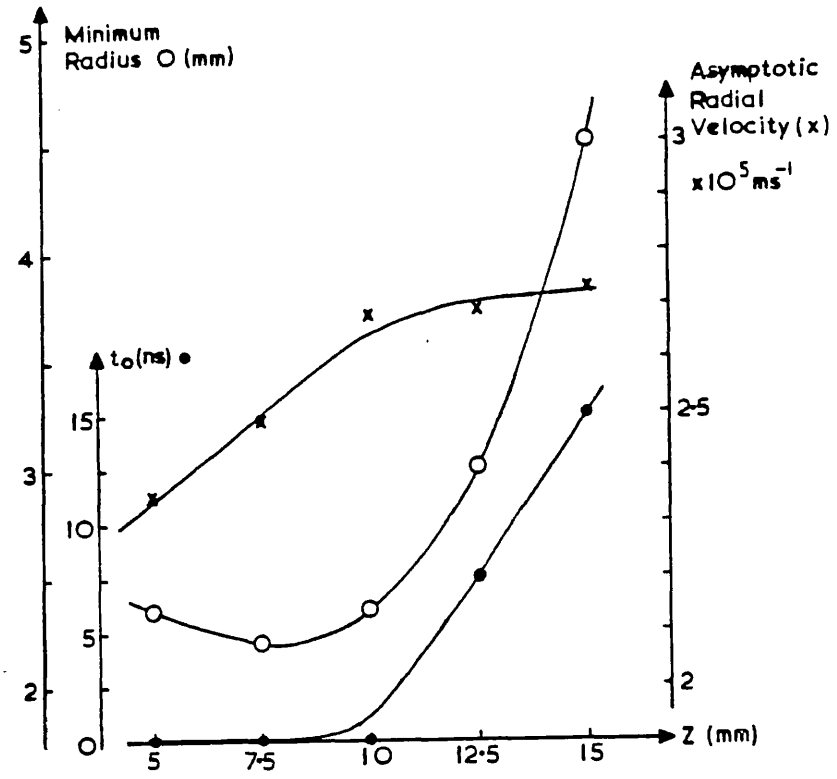

Figure 4.11

The axial behaviour of the plasma boundary radial asymptotic velocity, the mimimum plasma radius, and the timing of peak compression with respect to the dI/dt singularity.

are marginally larger. For $Z \geq 10$ mm, there is a rapid increase in the minimum plasma radius. Therefore, plasma compression decreases with axial position. This is possibly due to axial flow of plasma from positions closer to the centre electrode. The axial behaviour of the time when maximum plasma compression occurs, t_o, is also shown. At axial locations $Z \leq 8$ mm, peak compression occurs at time $t = 0$, i.e. the time of the dI/dt singularity. At axial locations > 8 mm, peak compression occurs after the dI/dt singularity, reaching +15 ns at $Z = 15$ mm. At $Z = 10$ mm, peak compression occurs at approximately +1 ns, which, together with the minimum plasma radius behaviour, validates the assumption that for $5 \leq Z \leq 10$ mm the plasma's electron density distributions are similar. Only the asymptotic velocity shows any significant difference. However, only the density profiles between times -10 and +10 ns are required for unfolding the magnetic field results from the Faraday rotation measurements, when the velocities are

far from their asymptotic values.

4.2.5 PLASMA AXIAL LENGTH

Figure 4.12, shows the observed axial length of the plasma column against time. The data points were measured from the centre electrode shadow to the maximum axial position where the interferometric fringe shift pattern first appeared distorted. This distortion was due to the plasma return sheath. This particular feature of the reconstructed holograms is shown by arrows in figure 4.1. The observed initial axial velocity of the return sheath was 1.57×10^5 ms^{-1}. This was constant until approximately t = -25 ns, afterwhich it decreased over a 30 to 40 ns period. At times > +10 ns, the velocity remained constant at $\sim 7.5 \times 10^4$ ms^{-1}. Therefore, over the period around peak compression, the axial velocity dropped by approximately a factor 2.

A simple snow-plough model of the plasma return sheath can be used to explain why the velocity decreases. Assuming a perfect snow-plough, the rate of change of momentum per unit volume of the plasma sheath must balance the magnetic force per unit volume driving it. Therefore [56]

$$\frac{1}{2\mu_o} B_\theta^2 = \rho v_z^2 \qquad (4.5)$$

where ρ is the mass density of the filling gas, B_θ is the azimuthal magnetic field, and v_z is the axial sheath velocity. From this model, the sheath velocity is proportional to the magnetic field strength, or equivalently, the plasma current. Therefore, the observed reduction in the sheath velocity by a factor 2 would indicate that the plasma current has also decreased by a similar amount. It will be shown later that the plasma current at peak compression, measured using Faraday

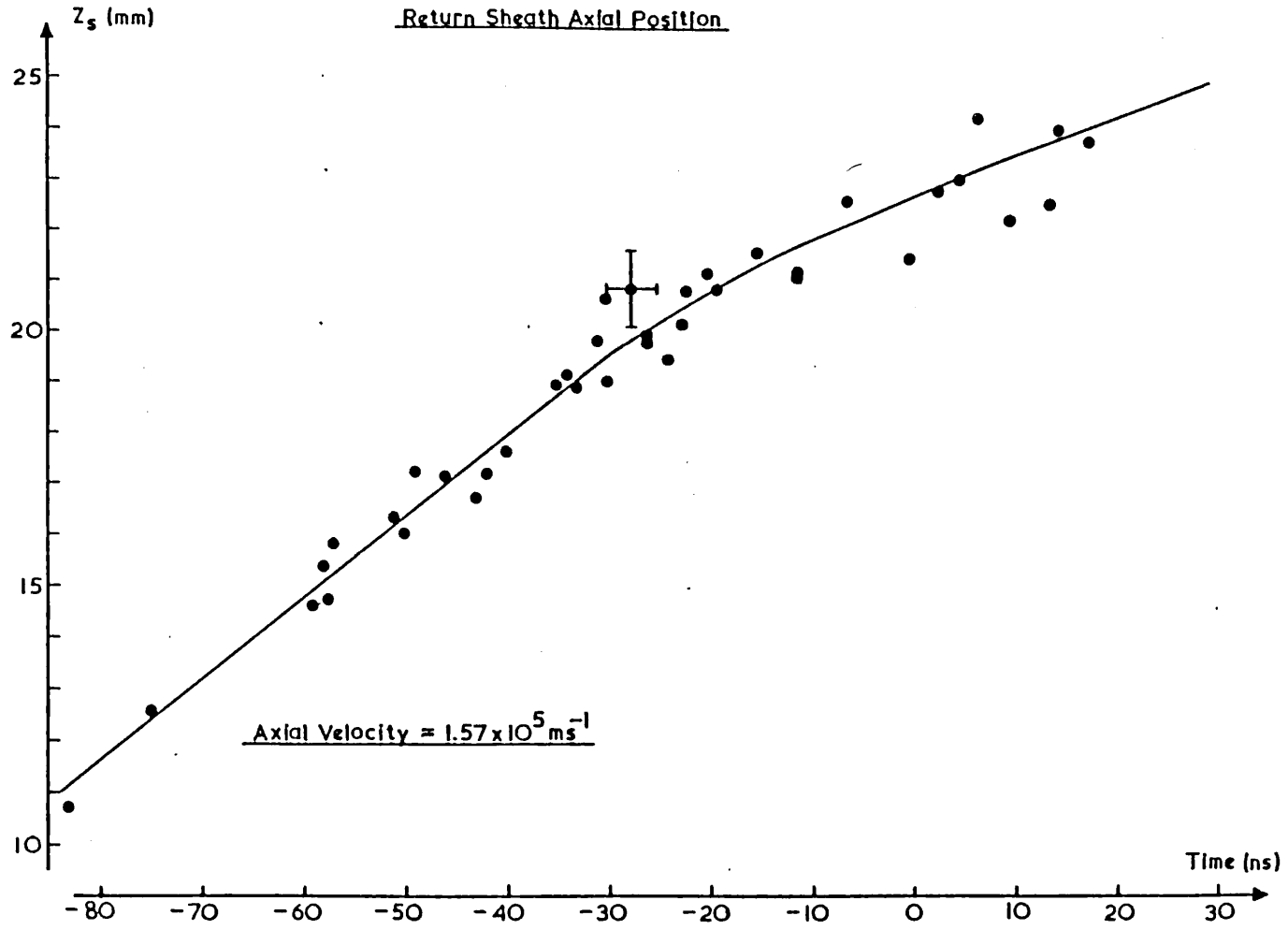

Figure 4.12

Temporal evolution of the plasma column axial length.

rotation, is 340 kA. This is approximately 70% of the current from the capacitor banks. At this time, the high voltages generated by the rapid changes in plasma inductance, cause current leakage across the insulator between the electrodes, as observed by Gourlan et al [57]. This leakage is significant only in the time period around peak compression. Thus, the reduction in sheath velocity is due to this current leakage.

This result supports the conclusion that insulator leakage is the cause of the low plasma current measured by Faraday rotation, rather than another mechanism in which the current is conducted in a low density plasma outside the pinch column, as considered by Bernard et al [21,22,58] to explain magnetic probe measurements. This latter mechanism is not supported by the velocity observations as the diffuse plasma must carry most of the 150 kA current not within the dense plasma column, which would result in only a small change in magnetic field strength at the return sheath position, and therefore, a small change in the axial sheath velocity, contrary to that observed.

4.2.6 ACCURACY OF THE ANALYSIS

The distributions of electron density and the data demonstrating the temporal evolution of the plasma radius and length, were subject to a variety of errors. These errors fall into the following classes:

a) Inaccuracies in the measurement of fringe shifts and lengths from the reconstructed holograms.

b) Imperfect hologram reconstruction.

c) Errors due to poor laser spatial coherence.

d) Errors arising from the unaccounted additional phase shift due

to the return current sheath.

e) Errors due to incomplete compensation for the effects of scene beam refraction.

f) The systematic Abel inversion error.

These are now considered in sequence:

a) The fringe shift positions could be determined within the reconstructed hologram images to an accuracy of $\sim$1 mm. Therefore, with a real space magnification of 12, the error in this measurement was 0.1 mm. With the background fringe spacing employed, approximately 1 - 1.5 per mm, the equivalent fringe shift error, δF, was 0.1.

Only holograms in which the fringe structure could clearly be seen were used in the analysis. This ensured that the error in counting the fringes was zero.

The error in determining the plasma radius was typically 0.25 mm. This is equivalent to a 10% relative error in a single measurement of the plasma radius at peak compression. It is less at all other times. This error arises because at the plasma-vacuum boundary the deviation of the interferometric fringes from the vacuum reference fringes is gradual, with the result that it is difficult to pin-point exactly where the deviation begins.

The error in determining the plasma length was 0.75 mm. This is larger than the uncertainty in the plasma radius, but represents a smaller relative error ($\sim$4% as typically Z $\sim$ 20 mm).

b) Care was taken during the reconstruction of the holograms to

correctly image the interferogram onto the Polaroid film. The film and hologram planes were parallel within 5 degrees, and the magnification about unity, so that length contraction was less than 1%. This error is sufficiently small to be neglected.

c) Imperfect laser spatial coherence - ruby lasers generally have poor spatial coherence - manifests itself as a variation in the pattern of reference fringes across the interferogram. Ideally, the reference fringes should all be parallel. A typical hologram was tested by comparing the reference fringes at several points with parallel linear lines drawn through the reference fringes. It was observed that the fringes varied on average by approxmately 0.1 mm, which was equivalent to a fringe shift error of 0.1.

Holograms taken when the laser's spatial coherence was poor were easily identified because some reference fringes were split into pairs. Holograms exhibiting these split fringes were analysed for plasma radius and length only.

d) The phase shift distribution recorded for a plasma discharge, represents the optical path length experienced by the scene beam due to the central plasma column and the outer return sheath through which it passes twice. As the field of view was $\sim$ 40 mm, with the plasma radius much less in general, while the diameter of the return sheath was 90 mm, any phase shift due to the return sheath would have been approximately constant over the range of impact parameters, and would be experienced equally by both that portion of the scene beam which passed through the central plasma column and that portion which generated the reference fringes. The effect of the return current sheath would therefore be undetected, and so the errors are therefore

negligible.

e) The scene beam was in general refracted by the plasma due to radial electron density gradients. Although imaging optics were employed to correct for refraction, this method of correction is not perfect. The error in the phase shift, due to the actual optical path through the plasma rather than the apparent, is estimated by Morgan [46] as

$$\delta F = \frac{a^3 \lambda^3}{6} \left(\frac{e^2}{8\pi^2 \varepsilon_o c^2 m_e} \frac{\partial n_e}{\partial r} \right)^2 \qquad (4.6)$$

For the electron density profile observed at peak compression, the axial density is 4.2×10^{25} m^{-3}, and the plasma radius 2.35 mm. Therefore, $dn_e/dr \cong 1.79 \times 10^{28}$ m^{-2}, and the resulting fringe shift error is 0.05.

f) The accuracy of the Abel inversion was assesed by using analytic expressions for the fringe shift profile which had known analytic solutions to Abel's integral equation. By direct comparison of the numerically evaluated solution with the known solution, the accuracy was determined. This method also tested the accuracy of the cubic spline curve fitting to the data points. Gorenflo [59], in addition to giving several numerical Abel inversion methods, lists several useful analytic solutions. For the Bockasten [55] method, the overall error was generally $\sim$ 1% on and near to the axis, increasing to $\sim$ 5% at the plasma edge.

The total error in the fringe shift is obtained by compounding all the separate errors, and is 0.15. This is similar to the fringe shift error of Morgan [46].

4.2.7 ACCURACY OF THE ELECTRON DENSITY ABEL INVERSION

The error in the Abel inverted electron density, δn_e, at the radial point r_j, from equation 4.3, is given by

$$\delta n_e(r_j) = \left\{ \left[\frac{\partial n_e}{\partial a} \delta a \right]^2 + \sum_k \left[\frac{\partial n_e}{\partial F_k} \delta F_k \right]^2 \right\}^{\frac{1}{2}} \qquad (4.7)$$

where δa is the error in the plasma radius, and δF_k is the error in the fringe shift at impact parameter h_k. From this equation, the relative error at the radial point r_j is

$$\left. \frac{\delta n_e}{n_e} \right]_{r_j} = \left\{ \left[\frac{\delta a}{a} \right]^2 + \frac{\sum_k (\alpha_{jk} \delta F_k)^2}{(\sum_k \alpha_{jk} F_k)^2} \right\}^{\frac{1}{2}} \qquad (4.8)$$

Thus, the minimum relative error is given by the relative error in the plasma radius. Since the fringe shift error is constant over impact parameter, then

$$\left. \frac{\delta n_e}{n_e} \right]_{r_j} = \left\{ \left[\frac{\delta a}{a} \right]^2 + \frac{4\lambda^2 n_c^2 \delta F^2}{a^2 n_e^2(r_j)} \sum_k \alpha_{jk}^2 \right\}^{\frac{1}{2}} \qquad (4.9)$$

The relative error in the electron density is therefore given by combining the plasma radius relative error with a relative error due to the fringe shift uncertainty. This latter error depends upon the sum $\sum_k \alpha_{jk}^2$, which varies from 370 to 2 for the cases when j = 0 to 19 respectively. Therefore, with $\delta F = 0.15$, the axial electron density relative error is

$$\left. \frac{\delta n_e}{n_e} \right]_{r=0} = \left\{ \left[\frac{\delta a}{a} \right]^2 + 8.56 \times 10^{43} (a n_e(r=0))^{-2} \right\}^{\frac{1}{2}} \qquad (4.10)$$

and the relative error at the plasma edge, where r = 19a/20, is

$$\left. \frac{\delta n_e}{n_e} \right]_{j=19} = \left\{ \left[\frac{\delta a}{a} \right]^2 + 4.6 \times 10^{41} (a n_e(r_{19}))^{-2} \right\}^{\frac{1}{2}} \qquad (4.11)$$

For the electron density distribution observed at peak compression, these relative errors are 14% on axis and 35% at the plasma edge. The error at the plasma edge is therefore considerably higher than on axis.

The relative error in the centre of the distribution, given when $j = 10$ and $\sum_k \alpha_{jk}^2 = 9.4$, is

$$\left.\frac{\delta n_e}{n_e}\right]_{j=10} = \left\{\left[\frac{\delta a}{a}\right]^2 + 2.2\times10^{42}(an_e(r_{10}))^{-2}\right\}^{\frac{1}{2}} \qquad (4.12)$$

For the profile at peak compression, the relative error is 13%.

The radial distribution of the measurement error generally follows the above pattern, with a 10 - 15% central relative error, increasing rapidly at the plasma edge to 30 - 40%. The error distribution will of course depend upon the actual density profile.

4.2.8 INITIAL INTERPRETATION

Line Density: Additional information about the plasma is obtained by calculating the electron line density N_e. This quantity is the total number of electrons contained within a unit length of plasma, and is given by

$$N_e = 2\pi \int_o^a n_e(r) r dr \qquad (4.13)$$

This was evaluated from the Abel inverted electron density profiles by fitting the 20 data points unfolded with a curve composed of cubic splines, and integrating numerically using Simpson's rule to an error $\sim 1\%$.

The accuracy of the line density calculation can be estimated by considering the integral to be approximated by the sum

$$N_e \cong 2\pi\Delta r \sum_{j=0}^{n} n_e(r_j) r_j \qquad (4.14)$$

where $\Delta r = a/n$. The relative error is then given by

$$\frac{\delta N_e}{N_e} = \left\{ \left[\frac{\delta a}{a}\right]^2 + \frac{\sum_j (r_j \delta n_e(r_j))^2}{(\sum_j r_j n_e(r_j))^2} \right\}^{\frac{1}{2}} \qquad (4.15)$$

With a 5% relative error in the plasma radius, the total relative error is typically 15 - 20%.

Figure 4.13 shows the time history of the calculated electron line density. During the time interval -50 ns to -20 ns, N_e increases slowly from 1.6×10^{20} m^{-1} to 1.88×10^{20} m^{-1}. This increase, approximately 15%, occurs during the period when the pinching sheath is snow-ploughing incompletely ionised gas. At the latter time, the line density becomes approximately constant, which is due to an equilibrium between particle gain by the snow-ploughing of the sheath and particle loss by axial flow caused by the oblique nature of the sheath front. This axial flow masks any additional gain of electrons from impurity ions evolving to higher ionisation states.

In the time interval t = -20 ns to peak compression, the line density drops by a factor 2.35 to 8.0×10^{19} m^{-1}. During the dense pinch phase, t = 0 to +30 ns, the line density increases very slightly, and may be considered to be constant. This behaviour is interpreted as follows: After t = -20 ns, the average density begins to increase rapidly, and the velocity of the plasma-vacuum boundary decreases. This slowing down of the plasma boundary reflects the increasing internal kinetic pressure of the plasma. As the pinch is two dimensional with the plasma radius increasing with axial position, the plasma pressure downstream, i.e. greater axial position, will be less

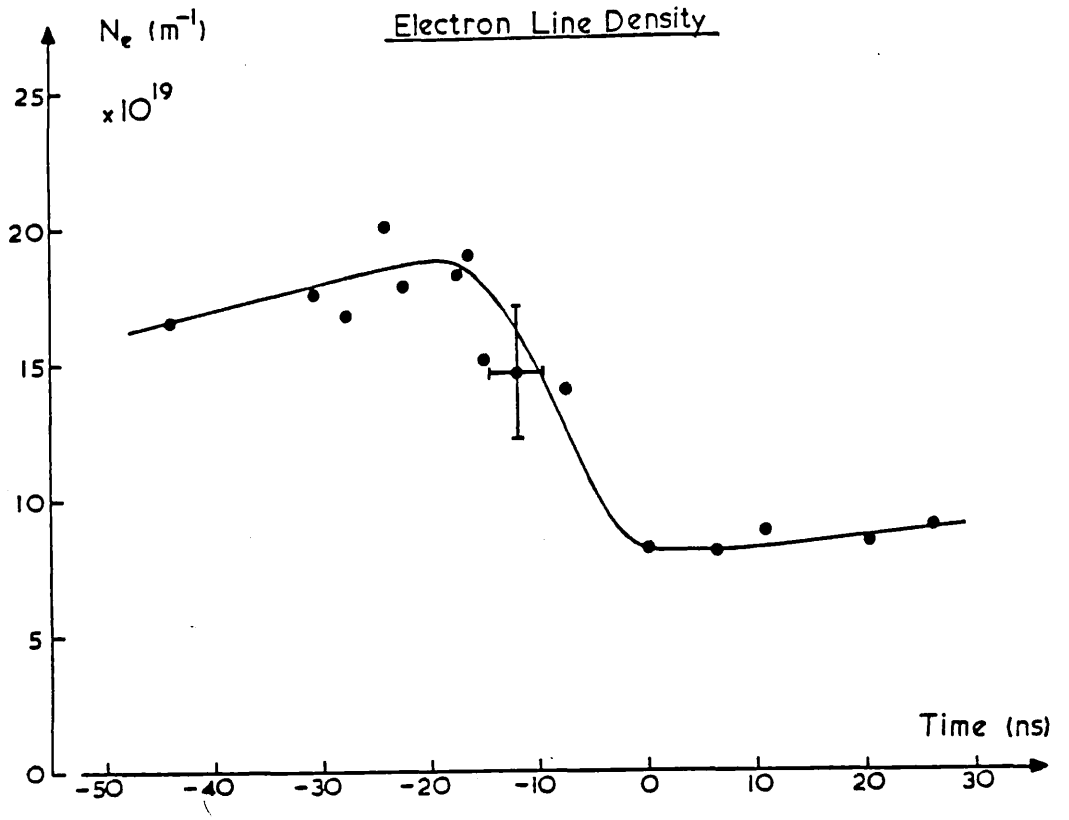

Figure 4.13

Temporal evolution of the electron line density.

and so axial plasma diffusion will occur, leading to a decrease in the line density. Axial flow upstream towards the centre electrode could occur if the plasma in the neighbourhood of the electrode was colder. However, as particles would be trapped there, then the pressure would quickly rise due to a local increase in line density and so evolve to an equilibrium pressure with the plasma downstream. Therefore, axial flow upstream would quickly stop, leaving only downstream axial flow.

The decrease in line density stops at peak compression because at this time maximum internal pressure is achieved. After peak compression, the line density remains constant as there is always a region downstream where peak compression is occuring, effectively blocking any further axial flow. As the volume of high density plasma, at low Z, is greater during the dense pinch phase than at its onset, then any particles gained by axial flow from downstream will be

dispersed and relatively unobserved. This may explain the slight increase observed in N_e during the dense pinch phase.

The electron line densities evaluated by Morgan [46] are larger than those determined in the present study by a factor 2. In addition, while the observed time histories of N_e are similar during the collapse phase, both showing the decrease at peak compression, Morgan observes a recovery in line density during the dense pinch phase to approximately its peak value during the collapse phase, which is contrary to that now observed.

Average Electron Density: The average electron density, $\bar{n}_e$, is obtained by dividing the electron line density by the cross-sectional area of the plasma, i.e. $\bar{n}_e = N_e/\pi a^2$. Figure 4.14 shows the time variation in the observed average electron density. Initially it increases relatively slowly, rises rapidly between the times t = -15 ns to -10 ns, and then grows to a peak value of 4.7×10^{24} m^{-3} at time t = 0 ns. During the dense pinch phase, the observed fall in the electron density is to a good approximation an exponential decay, with an e-folding time of 11.8 ns. A similar e-folding time can be determined from the data of Morgan [46].

Focusing Efficiency: When the sheath spills out of the two electrodes at the start of the collapse phase, and radially implodes to the axis, all the atoms contained within a cylinder of unit length and radius equal to the radius of the inner electrode (25 mm), would be fully ionised and compressed on axis if the focusing efficiency were 100%. The electron line density would then be given by $N_e = \pi r^2 n_f$, where n_f is the filling density of deuterium atoms. For a filling pressure of 1.8 torr of diatomic deuterium, $n_f = 1.27 \times 10^{23}$ m^{-3}, and

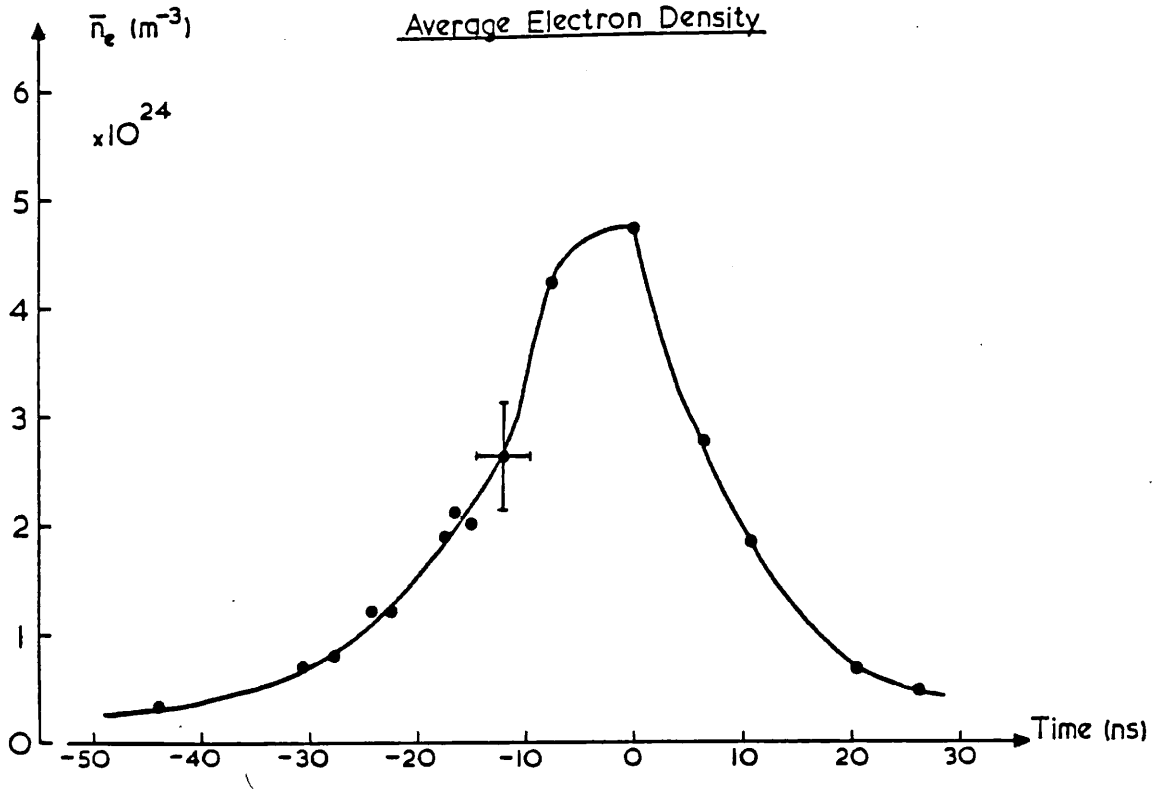

Figure 4.14

Temporal evolution of the average electron density.

therefore the maximum possible line density is 2.49×10^{20} m^{-1}. At peak compression of the pinch, $N_e = 8 \times 10^{19}$ m^{-1} and so the focussing efficiency is 32%, with the remaining 68% lost by axial flow. This is considerably higher than the 5% efficiency found by Morgan [46] for the Plasma Focus working at a higher bank voltage (30 kV) and with a 2.5 torr filling pressure of deuterium seeded with Argon.

The total number of electrons contained by the plasma column, of length $\sim$ 23 mm, is approximately 1.84×10^{18} at peak compression. The total number of electrons released by ionising all the deuterium gas swept-up by the Plasma Focus from the start of the discharge to peak compression, is approximately 1.3×10^{20}. Therefore, the overall compression efficiency of the Plasma Focus is 1.4%.

Axial Flow Loss Rate: The rate of axial particle loss during the collapse phase can be determined only within the time period t = -20 ns to 0 ns. At earlier times, the filling gas is incompletely ionised, and possibly any axial flow is hidden by an electron source provided by increasing impurity ionisation. Prior to peak compression, a considerable drop in line density, equal to 8.0×10^{19} m^{-1}, is observed. The actual loss may be greater, as the possible electron source from impurity ions is unknown. Therefore, the minimum particle loss rate over this period is 5.4×10^{27} $m^{-1} s^{-1}$.

Ionisation Energy Expenditure: The dissociation energy of diatomic deuterium to monatomic deuterium is $\cong$ 1 eV. Combining this with the 13.6 eV ionisation energy per atom, the energy expended on ionising each deuterium molecule is 28.2 eV. The total volume swept-up by the plasma from the beginning of the discharge to peak compression is approximately 1.05×10^{-3} m^{-3}, and therefore, with an initial gas filling pressure of 1.8 torr, equivalent to a D_2 density of 6.35×10^{22} m^{-3}, the ionisation energy used is $\cong$ 300 J. As the initial energy stored capacitively was 27.25 kJ, then the net expenditure of energy for ionisation alone is 1.1%.

4.3 ANALYSIS OF FARADAY ROTATION RESULTS

Analysis of the Polaroid oscillographs showing the polarimeter detector output, gave the Faraday rotation raw data. From this data, in combination with the electron density profiles, the azimuthal magnetic field distribution was evaluated. The various steps in the analysis and the results obtained are described below.

4.3.1 OSCILLOGRAPH ANALYSIS

The first step was to analyse the oscillographs. This was done by tracing one waveform, and superposing the other to ensure accurate time correlation. The corresponding signal heights were then measured at several time points within the combined waveforms. The ratio of the signal difference to signal sum, R, was then calculated for these points. This analysis was carried out on all the oscillographs, giving the temporal evolution of the ratio value at the impact parameters used in the experiment.

4.3.2 THE FARADAY ROTATION DATA

The Faraday rotation data were determined from the ratio measurements by comparing with calibration curves. Allowance was made for the finite value of the ratio value in the absence of plasma. Figure 4.15 shows the observed temporal evolution of the Faraday rotation angle during the collapse phase, at the impact parameter 3 mm. The data points shown are those of several sets of points, each from different plasma discharges. Through the collection of points a best fit curve is drawn, with its shape determined by that normally observed for a single plasma shot. The large scatter is due to shot to shot variations.

The azimuthal magnetic field profile is obtained by Abel inverting the spatial distribution of the Faraday rotation data at a given time. Since the data was collected at discrete impact parameter settings, which gave the temporal behaviour and not the spatial, the next step in the analysis was to construct a three dimensional representation of the data. This was done by drawing the contours of constant Faraday

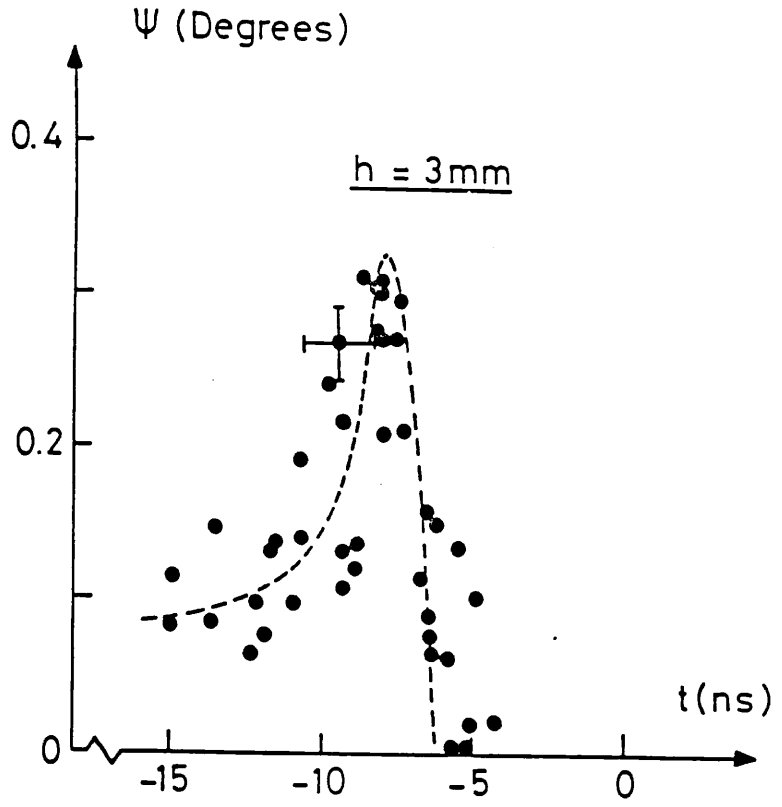

Figure 4.15

The observed Faraday rotation angle plotted against time for impact parameter h = 3 mm.

rotation angle in time and space. This procedure ensured that the data were self-consistent, smoothing the effect of the large shot to shot variations observed. It also made it possible to read the data spatially rather than temporally. Data from both sides of the magnetic axis were used. The contour map constructed from the observed data is shown in figure 4.16. The data collected were sufficient for an accurate analysis during the time period -10 to +10 ns.

This contour map shows that the maximum observed Faraday rotation angle, approximately 0.5 degrees, occurs close to the plasma-vacuum boundary, and is smaller by a factor ≅ 10 from that predicted in section 1.10. This reduction arises because, as will be shown, the magnetic field is located in the plasma skin, where the electron density is least. After peak compression, the contours redistribute, with the position of maximum rotation radially contracting. This will

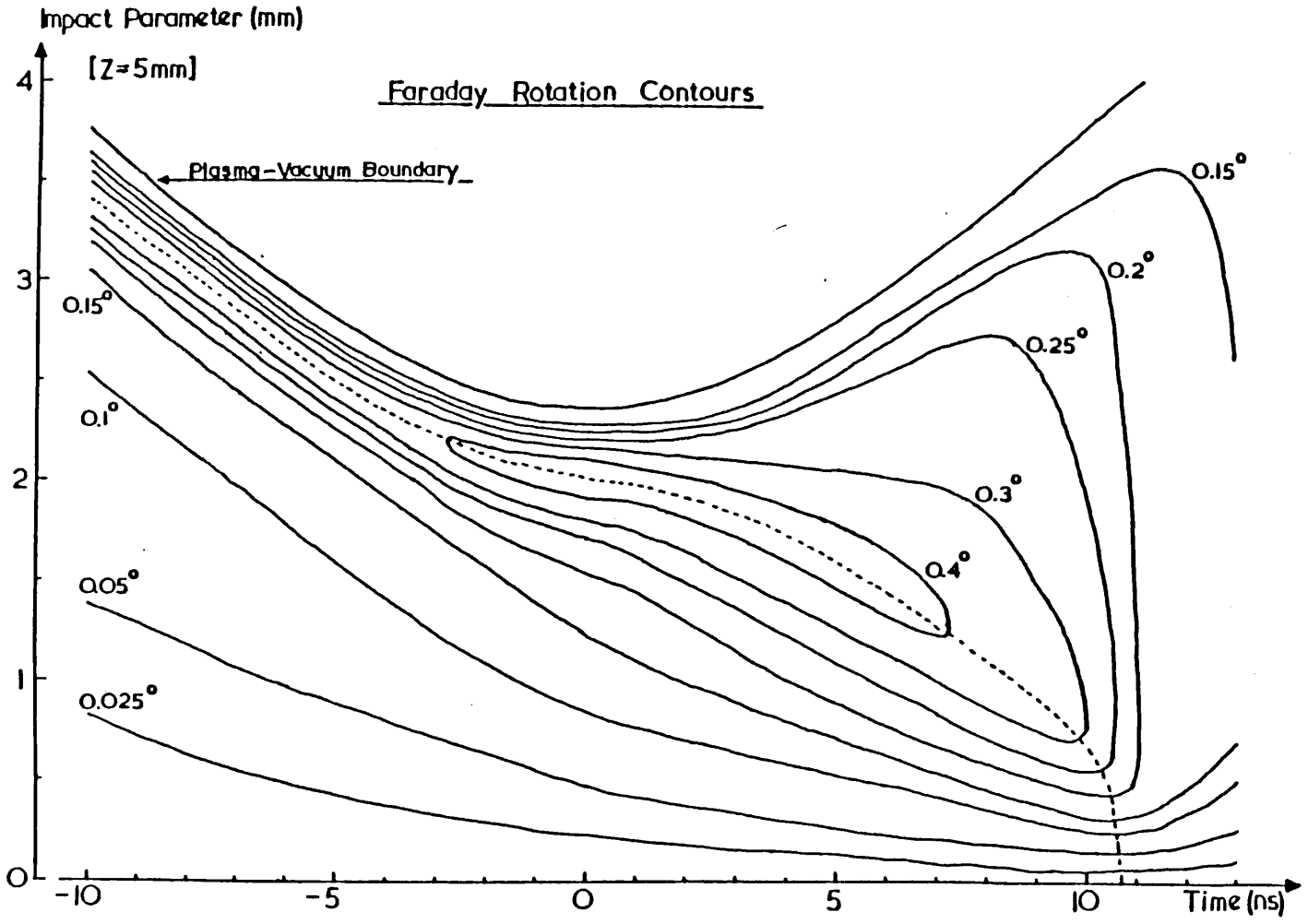

Figure 4.16

Faraday rotation contour map.

be shown to be due to rapid magnetic field diffusion into the plasma column. The magnitude of the rotation does not change during this period, as might have been expected considering the larger electron density. This is because most of the electrical current remains attached to the plasma skin, resulting in low internal magnetic field strengths. After time t = +10 ns, the contours rapidly shift outwards. This is because the electron density distribution decays (the e-folding time of the average density during this period is 11.4 ns).

4.3.3 ABEL INVERSION

As with the interferometric data, the plasma was assumed cylindrically symmetric. Therefore, the results of section 1.6.2, for the Abel inversion of Faraday rotation data, were then applied to give the magnetic field structure. Bockasten's inversion method [55] was again used, with n = 20. This number of points gave suitable accuracy over the distribution. From equation 1.58, the magnetic field profiles were computed using the expression

$$B_\theta(r_j) = \frac{r_j}{aA\lambda^2 n_e(r_j)} \sum_k \alpha_{jk}\left[\frac{\psi_k}{h_k}\right] \qquad (4.16)$$

where r_j and h_k are as defined in section 4.2.2, the α_{jk} are the Bockasten coefficients, and ψ_k is the Faraday rotation angle at the impact parameter h_k.

The data to be Abel inverted consisted of the spatial positions of the Faraday rotation contours, read from the contour map of figure 4.16, together with the magnitude of the rotation. Cubic splines were fitted to the data to give a smooth continuous curve. The technique used was identical to that used in the interferometric fringe shift profile fitting, discussed in section 4.2.2. From this curve, 20

data points were determined and used in the Abel inversion routine. Figure 4.17 shows three Faraday rotation spatial profiles, for times -5, 0, and +5 ns. The errors shown in these profiles are the uncertainties in the positions of the contours, and the points shown are those used to generate a smooth profile.

4.3.4 ABEL INVERTED MAGNETIC FIELD PROFILES

Figure 4.18 gives a sequence of magnetic field profiles during the collapse phase, from times t = -10 ns to peak compression, as determined by Abel inversion of the Faraday rotation data. The electron density profiles used were obtained from those observed interferometrically. The observed field profiles were found to exist only in the skin region of the plasma, where the magnetic field strength increases from a value of $\sim$ 20 Tesla at time t = -10 ns, to $\sim$ 40 Tesla at peak compression. The average value of magnetic field penetration depth is 0.56 mm, which is approximately half the sheath thickness as determined from the studies of plasma radius at early times during the collapse phase. This depth also approximately corresponds to the distance between maximum electron density in the sheath and the vacuum boundary. The magnetic field strength in the neighbourhood of the axis is zero.

This penetration depth is very much less than the value of 7 mm computed by Potter [60] with a two dimensional numerical fluid model. It is also smaller than the 1.5 mm skin-depth estimated from non Abel inverted Faraday rotation measurements on a Plasma Focus by Fillipov et al [18].

Figure 4.19 shows the magnetic field profiles during the dense

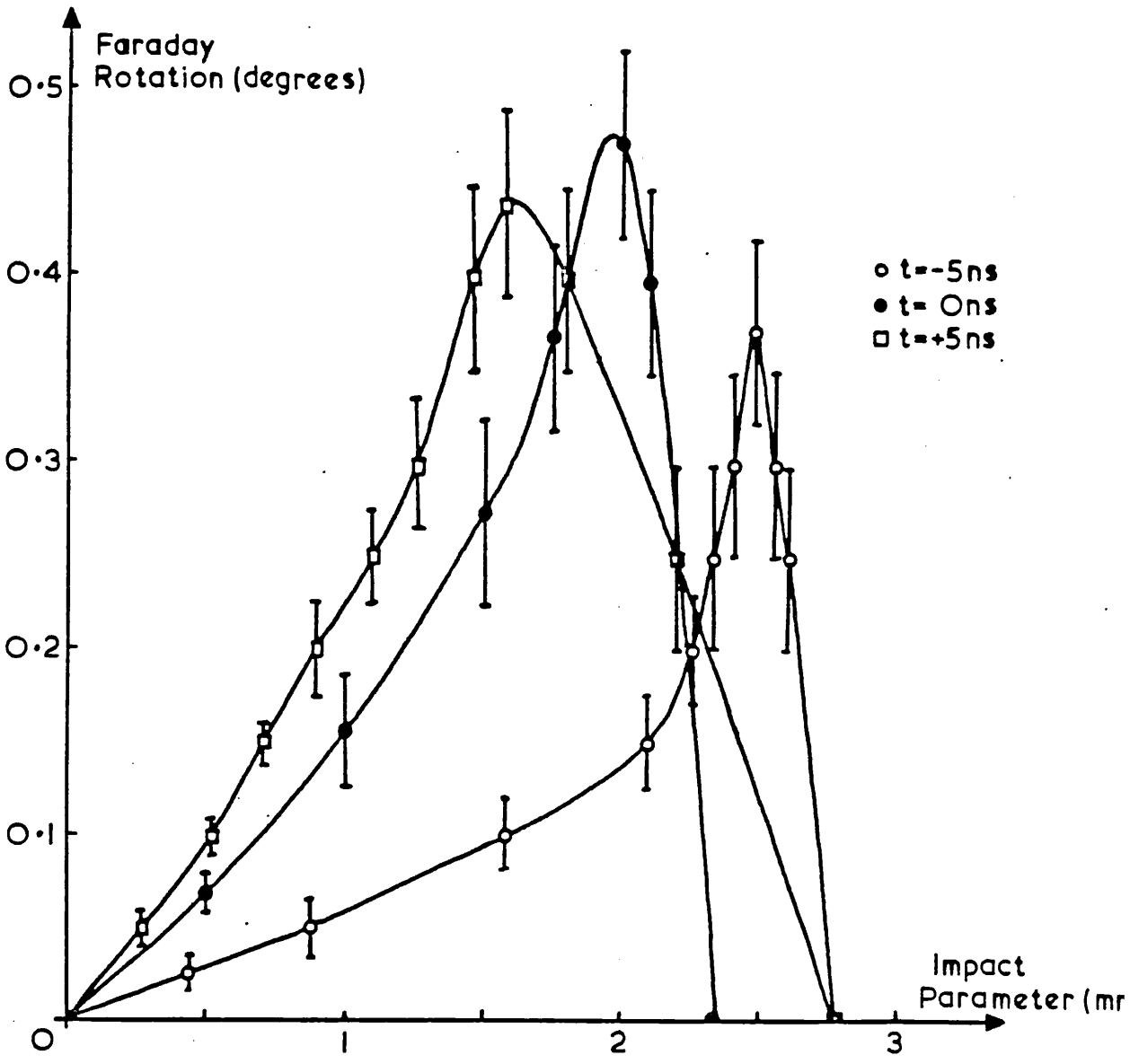

Figure 4.17

Faraday rotation spatial profiles.

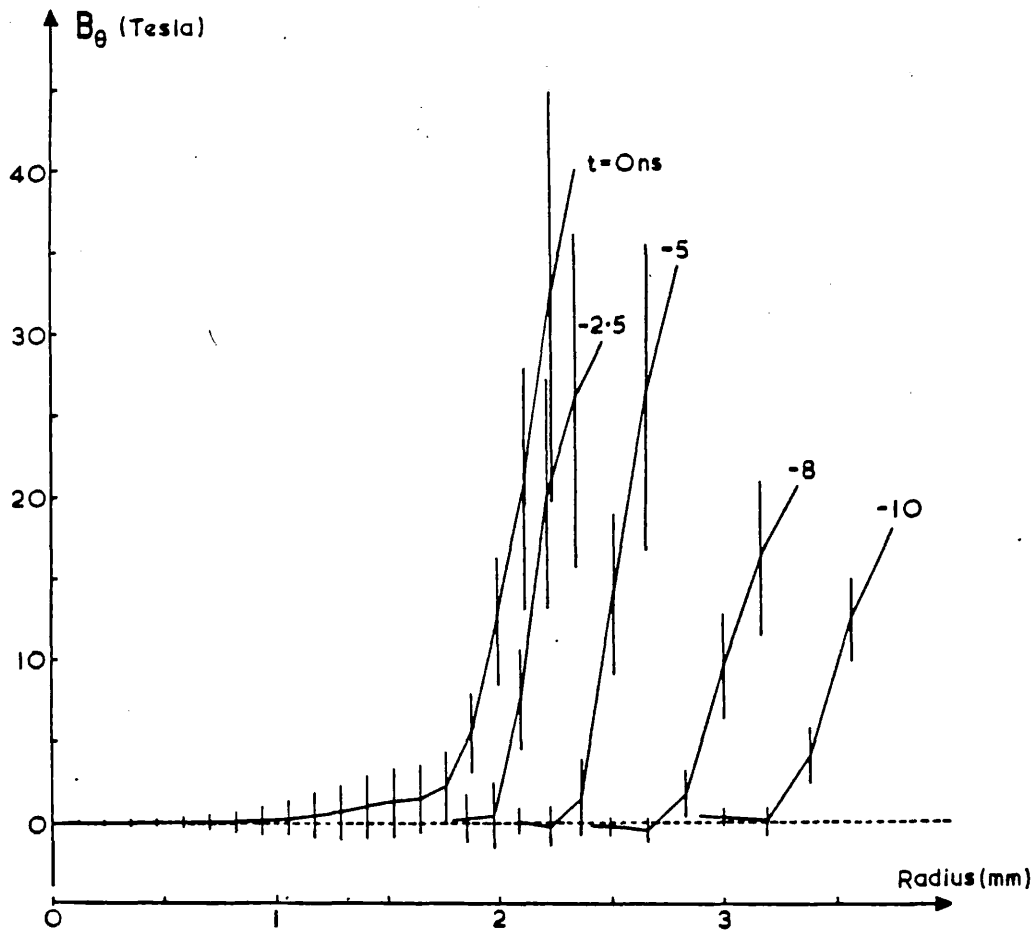

Figure 4.18

Abel inverted magnetic field profiles

during the collapse phase.

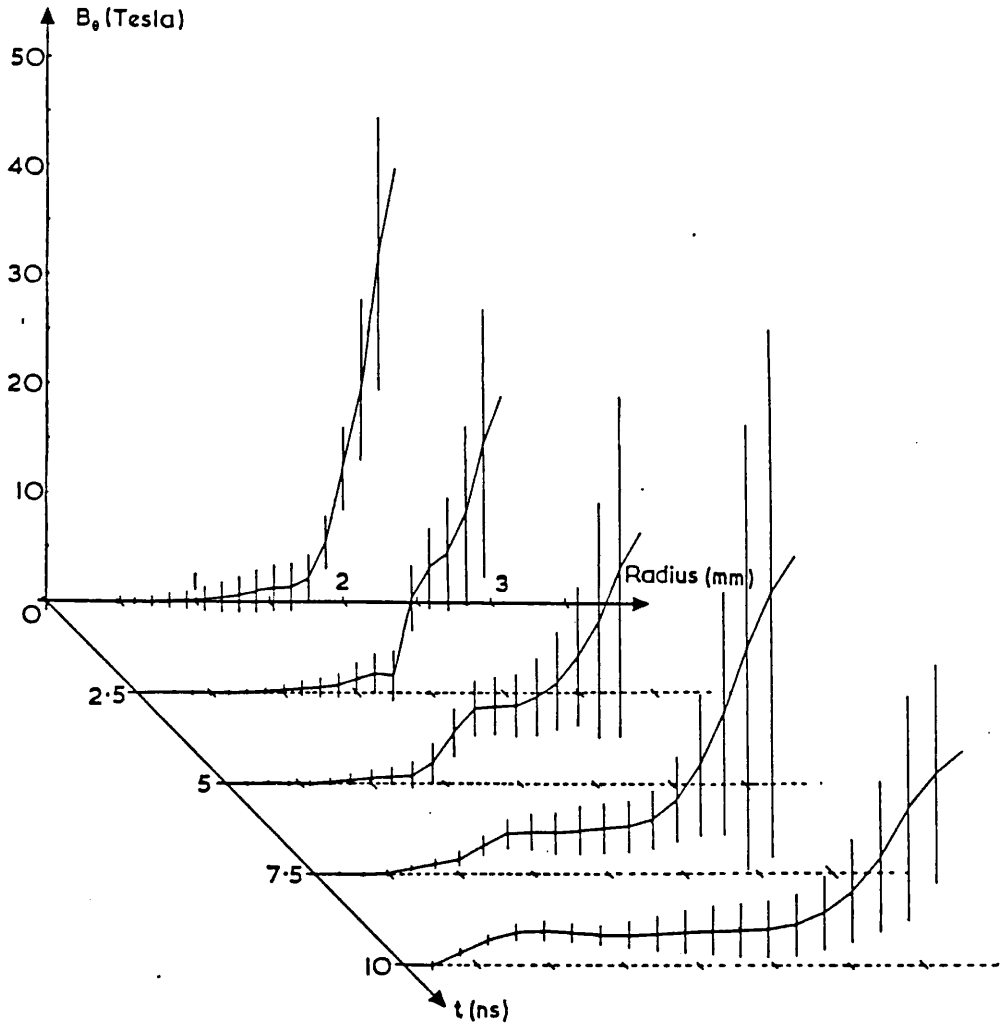

Figure 4.19

Abel inverted magnetic field profiles

during the dense pinch phase.

pinch phase obtained by Abel inversion. Initially the field is confined to the skin region, but after approximately 2.5 ns radial diffusion towards the axis occurs. By the time t = +10 ns, the field has diffused almost to the axis. During this period, the low internal magnetic field strength of the radially contracting region, decreases from approximately 15 Tesla to 3 Tesla.

The magnitudes of the magnetic field strengths measured, are marginally lower than those measured by Peacock et al [20]. The discrepancy between the two sets of measurements, made on the same device, may be a result of the different initial conditions. In Peacock's study, the plasma current was larger by 10%, and the minimum plasma radius smaller.

The magnetic field observations during the collapse phase are contrary to the magnetic probe measurements of Bernard et al [21,22,58]. The conclusions of Bernard's work was that only a small fraction of the plasma current, approximately 15%, is carried by the dense plasma sheath, with most of the current confined to a low density highly turbulent region following behind and outside the sheath. In the present work, it will be shown that 70% of the capacitor bank current is carried by the dense plasma sheath, with the remaining current lost to insulator current leakage. Bernard's observations may be a result of the perturbing diagnostic technique that was used.

During the dense pinch phase, Bernard et al [21,22,58] concluded that the dI/dt singularity was due to enhanced resistance, which led to a diminution of the plasma current. This resistance regime subsequently gave way to a regime in which the current was transported by intense beams of ions and electrons. In the present study, the

rapid magnetic field diffusion observed during the dense pinch phase, is interpreted as being due to anomalous resistivity. The Faraday rotation 'spikes' observed are also interpreted as being due to current filamentation on axis. These two results are in close agreement with Bernard's conclusions.

4.3.5 PLASMA CURRENT

The Abel inversion method used, evaluated the magnetic field strength out to a radial position 19a/20 only. Therefore, the magnetic field strength at the plasma radius was unknown. However, by determining the axial current density at this end point, and then assuming a linear radial dependence out to the plasma radius where the current density is zero, integration gives an approximate value of the current flowing within this outermost region. By adding this fractional current to the current flowing within the remaining plasma, as determined from the field strength at the outermost point, the total plasma current and therefore the magnetic field strength at the plasma radius is determined. For the field profiles shown in figures 4.18 and 4.19, the average value of the plasma current calculated is 340 kA, with a standard deviation of 70 kA, i.e. 20%. This is approximately 70% of the 490 kA current from the capacitor banks observed at this time with the Rogowskii coil.

The current of 150 kA not accounted for, is probably lost by current leakage across the insulator which is known to occur with Plasma Focus devices [57]. The leakage can become large when large voltages are induced across the insulator due to rapid changes in the plasma's inductance. Inductive voltages peak at the time of peak compression, and so maximum insulator leakage occurs at this time. It

is estimated from the results of a numerical model of the Plasma Focus electrical circuit, discussed in section 4.4.11, that the insulator resistance at this time is approximately 0.25 Ohms.

Figure 4.20 shows the magnetic field contours in time and space for a 340 kA plasma. This contour map was constructed from the magnetic field results by normalising the data to that of a 340 kA plasma. The straight parallel contours are those of the vacuum field.

4.3.6 AXIAL CURRENT FILAMENTS

Analysis of those oscillographs showing the Faraday rotation spikes (see figure 4.4) revealed that none represented Faraday rotation angles greater than 0.95 degrees. This was regardless of impact parameter. The 2.5 ns duration of the spikes was equivalent to the bandwidth of the measurement, suggesting that the measurements were bandwidth limited, and that therefore the duration of the spikes was probably less and the actual rotation probably larger. The spikes were observed at times between t = +10 and +15 ns. From the known plasma radius at these times, the possible Faraday rotation profiles were plotted. These are shown in figure 4.21. Only two data points were used, with the curves drawn through the spatial error bar of the axial point.

Abel inversion of these possible profiles gives the magnetic field distributions shown in figure 4.22. These distributions are highly peaked near the axis. It will be shown later that the current density profiles are also highly peaked on axis. Therefore one interpretation is that the spikes arise due to current filamentation on the axis. The magnetic field strengths of 44 and 57 Tesla for the times t = +10 and +15 ns respectively, are due to currents of 42 and 72 kA respectively.

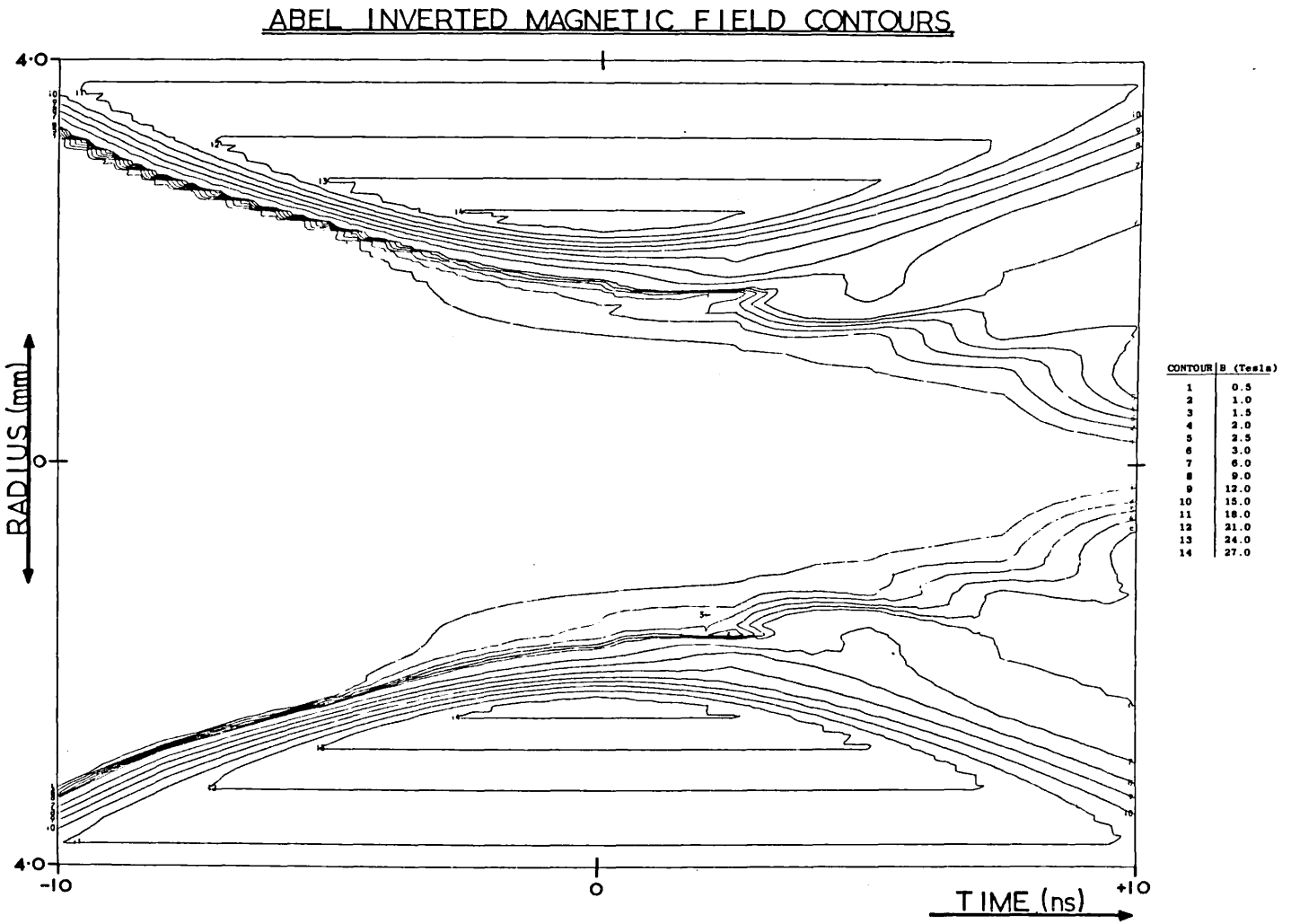

Figure 4.20

Magnetic field contours of a 340 kA plasma.

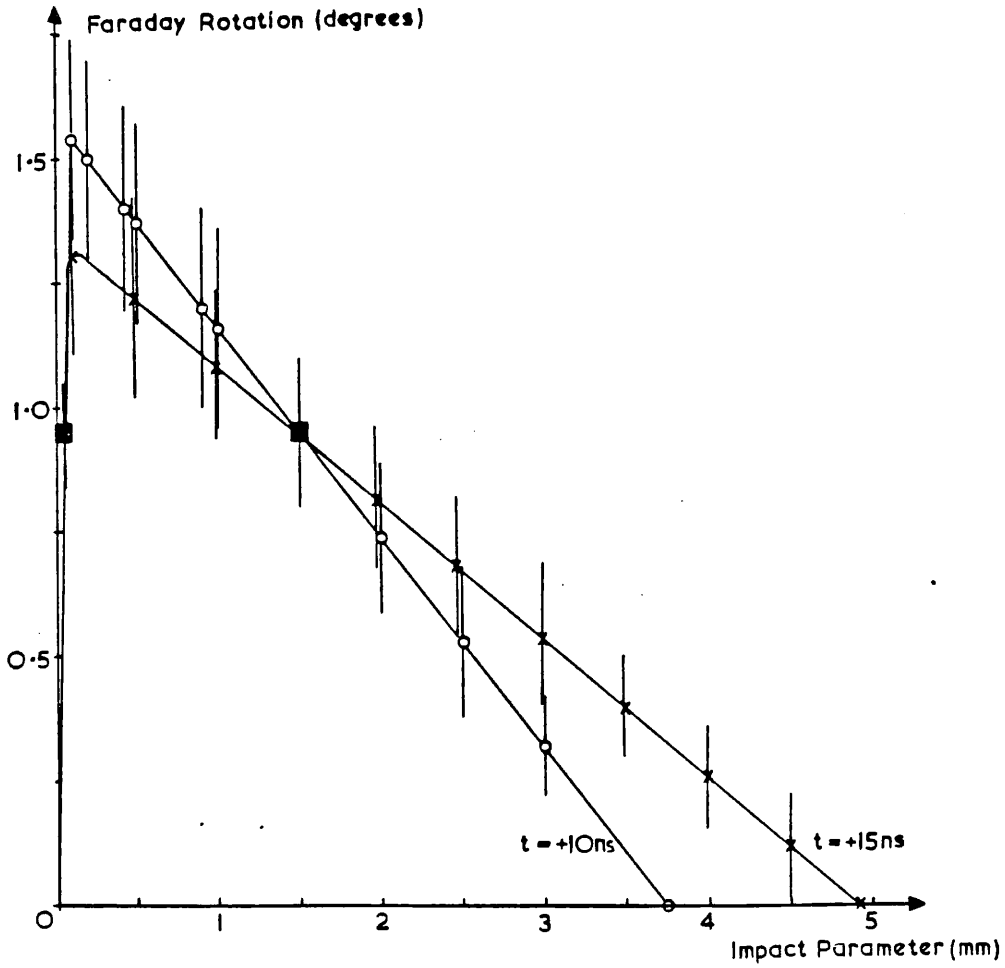

Figure 4.21

Faraday rotation spatial profiles of plasma with axial current filaments.

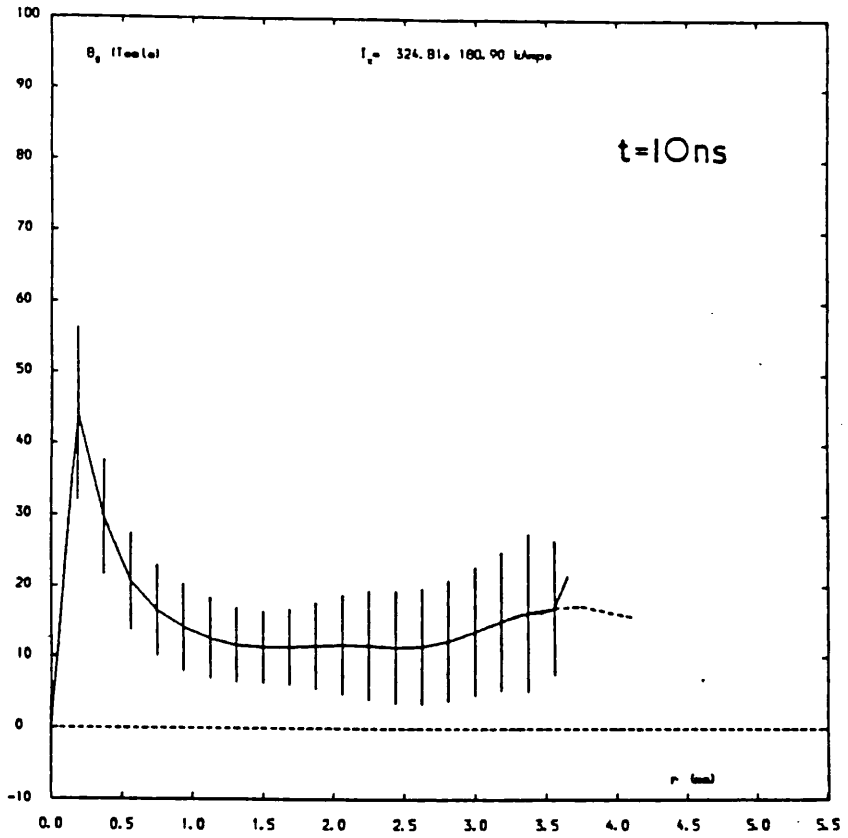

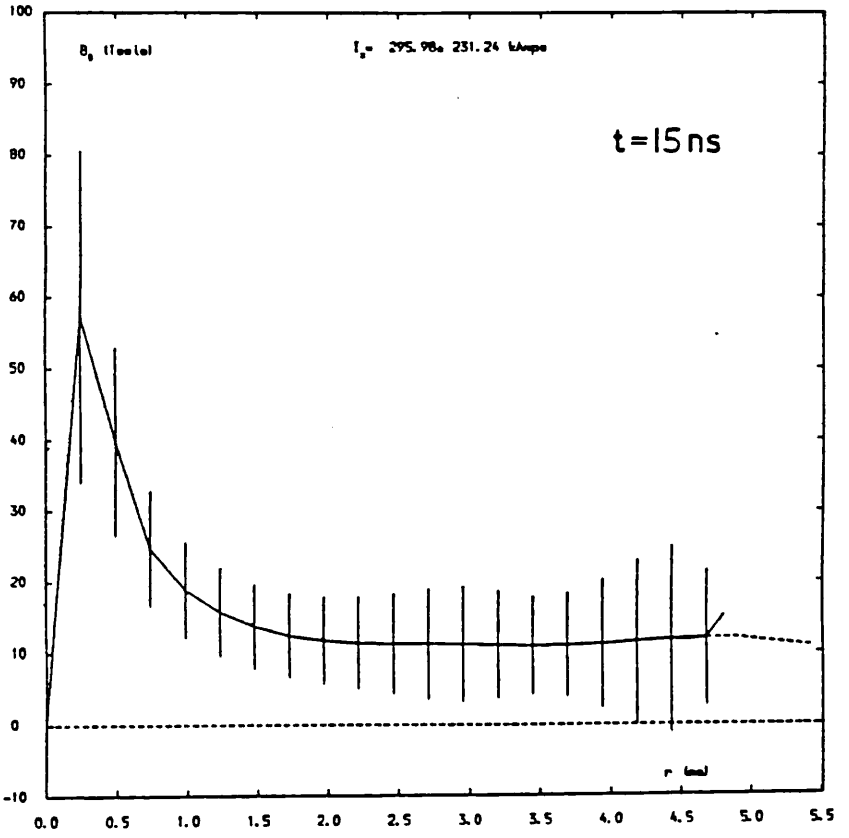

Figure 4.22

Abel inverted magnetic field profiles

of plasma with axial current filaments.

These currents are approximately 12 - 21% of the plasma current. The radius of the filament is in the range 190 to 250 microns.

This result is comparable to the observations of Neff et al [61], where subnanosecond electron beams, of energy > 0.5 MeV, were monitored using a Cerenkov detector external to the plasma. The time duration of the electron beam was less than 0.4 ns. Their estimated beam current was 40 kA, which is similar in magnitude to the current carried by the filament in the present study.

Observations by Kirk [49], using co-operative laser scattering (described in section 2.2.2), during the time period when Faraday rotation 'spikes' were observed (the measurements were not made simultaneously) demonstrated that scattering with a differential scattering vector parallel to the current was highly enhanced (up to a factor 30) over thermal levels of scattering. These observations have led to the conclusion that the ratio of electron drift velocity to thermal velocity must, at least, be of the order of unity, indicating that the current is carried by particle beams. From the calculated value of filament current density, the drift parameter is determined to be of the order of 5%. This discrepancy in the drift parameter, arises because the value of the filament radius is over-estimated, which is a result of the bandwidth limitation and the finite dimensions of both the plasma chord viewed and the Abel inversion space mesh. The over-estimation of the filament radius results in a value of current density which is too small, and correspondingly a drift velocity which is too small. This interpretation of the Faraday rotation 'spikes' data, leads to the conclusion that very much larger magnetic field strengths than measured exist in the neighbourhood of the axis. This topic is again examined in sections 4.4.5 and 4.4.6.

4.3.7 ACCURACY OF THE FARADAY ROTATION DATA

The Faraday rotation data were subject to a variety of errors from both the experimental technique and the data analysis. The accuracy of the magnetic field profiles has been determined by examining the effect of the error in the Faraday rotation data and the error in the electron density profile on the Abel inversion. Firstly however, the error in the Faraday rotation data must be assesed. The errors are classified as follows:

a) Errors in the measurement of the ratio of signal difference to signal sum from Polaroid oscillographs.
b) Errors due to noise on the detector output.
c) Inaccuracy due to the effects of probe beam refraction.
d) The additional Faraday rotation due to the double traversal of the return current sheath.
e) Errors in the calibration.
f) Errors due to detection system bandwidth limitation.
g) Imperfect construction of the rotation contour map.

These are now examined in turn:

a) For a given oscillograph, the error in the measurement of the signal difference to signal sum ratio, depends upon several factors: The oscillograph waveform trace width; the uncertainty in the zero datum position; the quality of the camera imaging; and the values of the signals themselves. Typically, the error in the ratio value resulting from these factors is 0.025.

b) The amplitude of noise on the detector output (possible sources

are discussed in section 3.5.3), was studied in the following manner. As the value of the ratio R was constant for any given calibration shot, regardless of signal amplitude, analysis of these calibration shots gave the noise error or standard deviation in the value of R. Allowing for the measurement error itself, the relative error in a measurement of the signal amplitude due to noise was 1.6%.

c) The effect of refraction on the ratio measurement was discussed in section 3.4. Based on the observed behaviour of the calibration curves with impact parameter, the error resulting from refraction is given by $\delta R = g R \Theta$, where Θ is the refraction angle, and g is a constant defined by

$$g = \left\{ \frac{d}{d\Theta}\left(\frac{dR}{d\psi}\right)\right\}\left(\frac{dR}{d\psi}\right)^{-1} \qquad (4.17)$$

The gradient $dR/d\psi$ is the slope of the calibration curve at the operating point. From the calibration curves, $g \cong 0.23$ per degree.

The maximum refraction expected, and observed by Morgan [46] using Schlieren techniques, was $\cong$ 17 mrad at peak compression. Taking half this value as being typical, the error due to refraction is 10%. This error will only exceed the measurement error when the Faraday rotation angle is greater than 0.22 degrees.

d) The Faraday rotation experienced by the probe beam on its double pass through the return sheath was negligible for the following reasons: Along the optical path of the beam through the sheath, the angle subtended by the magnetic field was approximately constant at 10 degrees. Therefore, from equation 1.50, it is reasonable to expect that the Faraday rotation angle is given by

$$\psi = 2A\lambda^2 B_{||} \bar{n}_e L \qquad (4.18)$$

where L is the thickness of the return sheath, and $\bar{n}_e$ is the average electron density. If the rotation is to be negligible, ≤ 0.01 degrees, then this can only be achieved with an electron density $\leq 10^{24}$ m^{-3}, as $B_{||} \cong 0.136$ Tesla, and $L \cong 5$ mm. The actual density can be estimated as follows. If the line densities of the inner plasma column and the return sheath were similar, then the ratio of the average densities will be given by $\bar{n}_{e1}/\bar{n}_{e2} \cong r_1^2/2Lr_1$, where r_1 and r_2 are the radii of the inner plasma column and the return current sheath respectively. With $r_1 \cong 2.5$ mm, and $r_2 \cong 50$ mm, the ratio is approximately 0.01. Thus, the density of the return sheath will be approximately two orders of magnitude less than that in the pinch. However, for the rotation due to the return sheath to be observed, the densities must be similar.

e) The calibration curves used to convert the data from ratio values to Faraday rotation angles, were composed of some 19 points, each the statistical average of several ratio measurements. The distribution of these points was over the full range $\pm$ 1, and was concentrated around the operating point. Taking into account the number of points, their distribution, and the accuracy by which the polarising prism could be set ($\sim$0.04 degrees), the relative error in the curve gradient at the operating point was 4%.

The error in the conversion from the ratio value to the Faraday rotation angle is given by

$$\delta\psi = \left\{ G^2 (\delta R^2 + \delta R_o^{\,2}) + \psi^2 \left[\frac{\delta G}{G} \right]^2 \right\}^{\frac{1}{2}} \qquad (4.19)$$

where $\delta\psi$ is the error in the Faraday rotation angle, R_o is the value of

the ratio in the absence of plasma, δR_o is the error in R_o, δR is the error in the ratio measurement R, G is the gradient $d\psi/dR$ of the calibration curve at the operating point, and δG is the error in the gradient G. With the values, G = 0.8, $\delta G/G = 0.04$, $\delta R_o = 0.001$, and $\delta R = 0.025$, the Faraday rotation error is

$$\delta\psi = \{(0.35 \text{ mrad})^2 + (0.04\ \psi)^2\}^{\frac{1}{2}} \qquad (4.20)$$

Therefore, the uncertainty in the Faraday rotation angle is 0.35 mrad compounded with a 4% relative error due to the uncertainty in the calibration curve gradient. Typically, $\psi \cong 0.25$ degrees and therefore a 4% relative error is 0.17 mrad. Thus, the main contribution to the uncertainty arises from the measurement of the signal ratio, and not from the calibration.

f) There was no evidence in the data, other than those of the Faraday rotation 'spikes', to suggest that there was an uncertainty due to the 400 MHz bandwidth of the detection system. Measurements made with half this bandwidth did show evidence of this limitation, as the magnitude of the Faraday rotation was attenuated by a factor up to 2. In order to examine this topic, consider the plasma movement that occurs in a 2.5 ns time interval. From the contour map of figure 4.16, the greatest movement occurs in the time period from t = -10 ns to -7.5 ns, and results in a decrease in the plasma radius of approximately 0.5 mm. This is twice the diameter of the plasma chord viewed by the polarimeter. During the same period, the Faraday rotation angle at an impact parameter of 3 mm rises to a maximum. The gradient of angle with impact parameter at this point is approximately 0.4 degrees per mm. Therefore, a plasma movement of 0.5 mm is equivalent to a change in the Faraday rotation angle of 0.2 degrees. This is large in comparison to the 0.3 degrees maximum rotation

observed. Thus, it may be that the data for this period is affected by the finite bandwidth.

For times $\geq$ -5 ns, the plasma movement and rates of change in Faraday rotation angle are smaller than during the earliest period. Therefore, any effect will be smaller. However, during the period t = +5 ns to +10 ns, there is a considerable restructuring of the Faraday rotation contours. It may be that during this period, smoothing of the data detailing this restructuring occurs, due to the bandwidth limitation.

From the Abel inverted magnetic field profiles during the collapse phase, shown in figure 4.18, no significant change in profile, other than that due to the reciprocal radius change in the vacuum field magnitude, is observed. The field penetration depth, and the value of plasma current within the estimated errors, both remain constant. From these observations, no evidence for bandwidth limitation is seen. In conclusion, the bandwidth of the detection system used in this experiment was sufficient, but probably only marginally. For future studies, the bandwidth should be increased to a minimum of 1 GHz. No error due to this effect will be considered in this error analysis. It is assumed that the 0.05 degree shot to shot variation error, discussed below, is sufficient to include any effect.

There is evidence that the data for the Faraday rotation 'spikes' were affected by bandwidth limitation. As it is difficult to estimate the actual error due to this effect, it is assumed that the error is four times the normal shot to shot variation, i.e. $\delta\psi = \pm 0.2$ degrees.

g) The final error arises from the construction of the contour map.

The shot to shot variation in the observed Faraday rotation angle due to plasma irreproducibility was approximately $\pm$ 0.05 degrees before peak compression, and $\pm$ 0.1 degrees after. This latter variation was greater the larger the impact parameter, due to uneven expansion of the plasma column caused by instabilities. However, by using the average of the data points, the error was reduced to approximately 0.05 degrees. This is larger than the inaccuracy of the technique, and so there would be no gain in improving the sensitivity of the experimental method.

The overall error in the measurement of the Faraday rotation angle is therefore that of the shot to shot variation, which is 0.05 degrees.

Precautions were observed during the experiment to ensure that the uncertainties were kept minimal. The first was to take calibration data throughout the experimental run. The second to take many reference shots in the absence of plasma giving the value of R_o'. And finally, to check the value of the ratio R at the -1 turning point. This latter precaution was taken as thermally induced stress-birefringence in the vacuum windows can arise during the experimental run, and may have been initially present in replacement windows. The first two precautions enable any variation in the behaviour of the polarimeter to be followed.

4.3.8 ACCURACY OF THE ABEL INVERSION

The error in the Faraday rotation measurement, $\delta\psi$, combined with the error in the electron density data, δn_e, results in a magnetic field error, δB_θ, given by

$$\delta B_\theta = \left\{ \left[\frac{\partial B_\theta}{\partial a} \delta a \right]^2 + \left[\frac{\partial B_\theta}{\partial n_e} \delta n_e \right]^2 + \left[\frac{\partial B_\theta}{\partial \psi} \delta \psi \right]^2 \right\}^{\frac{1}{2}} \qquad (4.21)$$

where a is the plasma radius, and δa is the error in a. From equation 4.16, the relative error is

$$\left. \frac{\delta B_\theta}{B_\theta} \right]_{r_j} = \left\{ \left[\frac{\delta a}{a} \right]^2 + \left[\frac{\delta n_e}{n_e} \right]^2 + \frac{\sum_k \left[\alpha_{jk} \frac{\delta \psi_k}{h_k} \right]^2}{\left\{ \frac{a}{r_j} A\lambda^2 n_e(r_j) B_\theta(r_j) \right\}^2} \right\}^{\frac{1}{2}} \qquad (4.22)$$

Thus, the relative error in the magnetic field is given by the combined relative errors of the electron density and plasma radius with a relative error due to the Faraday rotation measurement uncertainty.

For simplicity, consider the field error at the edge of the distribution due to the uncertainty in the Faraday rotation angle only. This error, which is greater than the error at any point inside the plasma, is obtained when k = 19, and has a magnitude given by

$$\delta B_\theta(r_{19}) = \frac{1.4\ \delta \psi}{A\lambda^2\ a\ n_e(r_{19})} \qquad (4.23)$$

From the previous section, the error in the Faraday rotation angle is 0.05 degrees. Therefore, from this equation, at time t = -5 ns, δB_θ = 4.7 Tesla. This gives a relative error due to the rotation measurement uncertainty alone of 18%. At peak compression, δB_θ = 5.3 Tesla, which gives a relative error of 16%. At time t = +5 ns, the edge error δB_θ = 11 Tesla, which corresponds to a relative error of 55%. This large relative error arises because at this time the edge electron density is lower than during the previous times. These error are typical of the edge errors due to the rotation measurement error alone.

The magnetic field error at points within the distribution, again

due to the measurement uncertainty alone, can also be determined from equation 4.22 and expressed in a form similar to equation 4.23. This involves calculating the sum $\sum_k (\alpha_{jk}\ \delta\psi_k/h_k)^2$. However, this can only be done if either the rotation error is constant over impact parameter, or if the error has a known dependence with impact parameter. Generally, neither of these is satisfied. In the error analysis presented here, it is assumed that the error decreases to zero at the axis, with the full error applied to the plasma edge distribution only. This may be seen from the error bars in the plots of Faraday rotation angle against impact parameter shown in figure 4.17. Thus, only at the edge can the error be simply expressed. At points within the distribution, the important parameter which determines the error is the value of electron density. High densities result in low errors.

The total magnetic field error is given by combining the Faraday rotation measurement error with the error due to electron density and plasma radius. Therefore, at the plasma edge, where the rotation error of typically 18% is a maximum, and where the electron density error of typically 35% is also a maximum, the total magnetic field error of typically 40% is a maximum. Within the distribution itself, the relative error in the electron density is approximately constant at 10%, and the magnitude of the magnetic field is small, approximately 1 Tesla. When the relative error given by equation 4.22 is computed, the result is of order unity. However, the magnitude of the field error, $\delta B_\theta \sim 1$ Tesla, is approximately a factor 5 less than the edge error due to the rotation measurement error alone. This improvement in accuracy is a result of the large electron densities found inside the plasma. In the neighbourhood of the magnetic axis, the magnetic field strength is approximately zero. In this region, the estimated error is 0.5 Tesla. The distribution of errors across the profile, will of

course depend on the actual distribution.

The Abel inverted magnetic field profiles shown in figures 4.18 and 4.19, are given complete with the estimated errors. From these plots, the large edge errors are clearly seen. The small uncertainties in the neighbourhood of the axis are also seen.

As discussed in section 4.2.6, the error introduced by the Abel inversion method was approximately 1% on and near to the axis, and approximately 5% at the plasma edge. These values of error are insignificant in comparison with the sources of error already described.

The method used to analyse the Faraday rotation data assumed that the plasma was cylindrically symmetric. There was no evidence from either holographic interferometry or from the Faraday rotation data to suggest that this assumption was incorrect.

4.4 INTERPRETATION OF RESULTS

In this section, the results obtained from the Faraday rotation measurements and holographic interferometry are interpreted in terms of other plasma parameters in an attempt to understand the physical processes occuring in the Plasma Focus.

4.4.1 TEMPERATURE CALCULATIONS

Four different temperature estimates are made during the collapse and dense pinch phases of the Plasma Focus. The first two are based on the assumption of pressure balance, the third on a magnetic piston model, and the fourth on the free expansion of the plasma. These are discussed in turn. For the first three temperature calculations, the magnetic field profiles for the times t = -5, 0, and +7.5 ns, were normalised to give an edge magnetic field strength consistent with a 340 kA plasma. This was done to ensure that the external magnetic pressure terms employed were comparable.

Pressure Balance

During the early stages of the collapse phase, the observed sheath velocity remained constant. This implies that there was an equilibrium between the forces acting upon the sheath. Neglecting the comparitively small snow-plough pressure term (ρV_r^2) at this time, the equilibrium of the forces is expressed by the pressure balance equation [62]

$$2n_e(r)k_B\bar{T}(r) + \frac{1}{2\mu_o} B_\theta^2(r) = \frac{1}{2\mu_o} B_{\theta a}^2 \qquad (4.24)$$

where $\bar{T}$ is the average particle temperature, i.e. $\bar{T} = (T_e + T_i)/2$, B_θ is the internal azimuthal magnetic field strength, and $B_{\theta a}$ is the magnetic field strength at the plasma-vacuum boundary. From the magnetic field profiles obtained, and the electron density data, the average temperature can be estimated using this expression.

During the time period t = -10 to 0 ns, the average temperature profiles are as shown by the solid curves of figure 4.23 a). These profiles indicate that the hottest region is the current sheath, where the temperature rises from approximately 150 eV to 500 eV between the

times t = -10 ns and peak compression. During the same period, the axial temperature falls from 85 eV to 25 eV. These low axial temperatures are probably the result of applying too simple a plasma model. Hollow temperature profiles were predicted by the numerical fluid model of Potter [60]. In this model, peak temperatures of $T_e \cong T_i$ = 1.5 keV were calculated.

Within the time period t = 0 to +10 ns, the average temperature profiles calculated on the assumption of pressure balance are as shown in figure 4.23 b). During this period, the edge temperature increases from 500 eV at peak compression to 680 eV at the time t = +7.5 ns. It then decreases to 460 eV 2.5 ns later. Again the axial temperatures of approximately 25 eV are low.

The second average temperature estimate is obtained from the well known Bennett equation describing the pressure balance between a simple linear pinch and its self-magnetic field [62]

$$\mu_o I_p^2 = 16 \pi N_e k_B \overline{T} \qquad (4.25)$$

where N_e is the electron line density. From the electron line densities calculated in section 4.2.8 and the measured plasma current of 340 kA, the Bennett temperature at the time t = -10 ns is 125 eV. This temperature increases to a value of 228 eV at peak compression due to the fall in line density. It then remains constant during the dense pinch phase.

From the co-operative scattering measurements of Kirk [16,49], the average ion temperatures across the plasma column are similar to the edge temperatures calculated using pressure balance. Although the scattering measurements were made at an axial position 10 mm below the

centre electrode, and there may be an axial dependence of temperature as computed by Potter [60], it is reasonable to assume a peak average temperature of 500 eV. This is contrary to the Bennett temperature of 228 eV. Therefore, the plasma is not in pressure equilibrium, and the plasma beta, or ratio of kinetic to magnetic pressure, is approximately 2. Thus, the plasma is confined inertially, and not through the action of the magnetic field.

Sheath Momentum

It was observed that the sheath velocity decreased during the final stages of the collapse phase. This implies that equilibrium between the forces did not exist, contrary to the assumption of pressure balance. The internal kinetic pressure of the plasma therefore exceeds the magnetic pressure, as concluded above. An estimate of the excess internal pressure can be made by determining the rate of change of the sheath's momentum. Assuming that the mass of the sheath is the mass of that region occupied by the magnetic field, the rate of change of momentum is

$$\frac{d}{dt}(mv) = 2\pi\ddot{r}m_i \int_{a-\delta}^{a} n_e(r)rdr \qquad (4.26)$$

where δ is the field penetration depth, and $\ddot{r}$ is the sheath deceleration. From the observed hyperbolic relationship between plasma radius and time, the deceleration can be calculated, and has a maximum value of 4.4×10^{13} ms^{-2} at peak compression of the pinch. This value of deceleration is similar to that observed by Morgan [46]. The penetration depths and calculated sheath masses during the collapse phase are approximately constant, having the values 0.56 mm and 5.1×10^{-8} Kgm^{-1} respectively.

The excess kinetic pressure, Δp, is given by

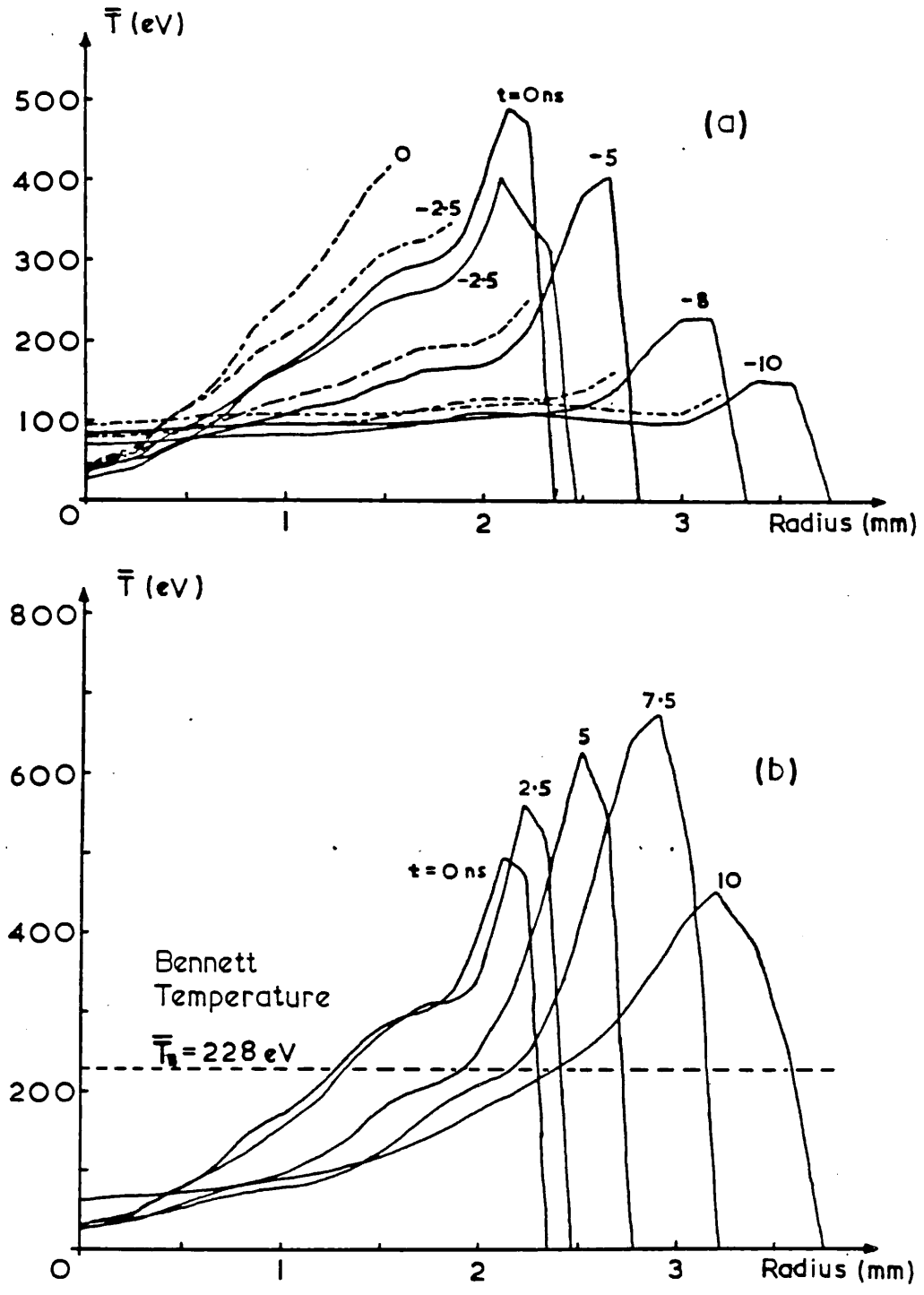

Figure 4.23

Average temperature profiles a) during the collapse phase assuming pressure balance (solid curve), and with sheath momentum included (dashed curve). b) Temperature profiles during the dense pinch phase assuming pressure balance.

$$\Delta p = 2n_e k_B \bar{T} + \frac{1}{2\mu_o} (B_\theta^2 - B_{\theta a}^2) \qquad (4.27)$$

and acts over an area per unit length of $2\pi(a-\delta)$. Setting the net outward force equal to the rate of change of momentum, we obtain the expression

$$\frac{d}{dt}(mv) = \Delta p . 2\pi(a-\delta) \qquad (4.28)$$

Application of this equation gives a more realistic temperature estimate than pressure balance. However, it is only applicable during the collapse phase when the sheath is well defined.

The temperature profiles predicted by this magnetic piston model are shown by the dashed curves of figure 4.23 a). At the time t = -10 ns, the curve is similar to that produced assuming pressure balance. This is because the sheath deceleration is small at this time. The difference becomes larger towards peak compression, where a temperature of 439 eV is calculated at the internal edge of the sheath. This is 143 eV higher than the equivalent temperature estimated using pressure balance. Again, low temperatures are evaluated for the axial region.

Ion Temperature

An estimate of the ion temperature can be made during the dense pinch phase by assuming that the observed expansion of the plasma column occurs at a rate given by the ion thermal velocity. This is a reasonable assumption if the plasma is confined by inertia. For the observed expansion velocity of 2.3×10^5 ms^{-1}, the equivalent ion temperature is 1.1 keV.

4.4.2 FIELD PENETRATION DEPTH

The average field penetration depth of 0.56 mm during the time period t = -10 ns to peak compression, is approximately half the width of the plasma sheath as observed interferometrically and described previously (cf section 4.2.4). It is known that the width of a collisionless shock wave is of the order of an ion Larmor radius [62]. Therefore, it will be instructive to compare the ion Larmor radius in the current sheath with the field penetration depth. The deuterium ion Larmor radius is given by

$$r_{Li} = 0.2 \sqrt{T_i}\ B_\theta^{-1} \text{ mm} \qquad (4.29)$$

where T_i is the ion temperature in units of electron volts. With the typical values of field strength and pressure balance temperature of 12 Tesla and 325 eV respectively, the ion Larmor radius is 0.3 mm. This is approximately half the observed penetration depth. Thus, the field penetration depth is approximately an ion Larmor diameter.

4.4.3 CLASSICAL RESISTIVITY

The classical electrical resistivity of a plasma parallel to the magnetic field, $\eta_{||}$, is given by [29]

$$\eta_{||} = \frac{1}{\gamma_E} \times 3.04 \times 10^{-5}\ Z T_e^{-3/2}\ \ell n\Lambda \text{ Ohm-m} \qquad (4.30)$$

where the temperature T_e is expressed in units of eV, and the factor γ_E is dependent upon the ionic charge Z and is tabulated by Spitzer [29]. For the case where Z = 1, $\gamma_E = 0.582$. The resistivity perpendicular to the magnetic field, $\eta_\perp$, is larger than $\eta_{||}$ by a factor 1.97.

For the Plasma Focus, the electrical current is perpendicular to the magnetic field, and so only $\eta_\perp$ will be considered. Taking the simplest case when Z = 1, this resistivity is given by

$$\eta_\perp = 1.03 \times 10^{-4} T_e^{-3/2} \ell n\Lambda \quad \text{Ohm-m} \qquad (4.31)$$

At peak compression, the electron density within the current carrying region is approximately $1.6\times10^{24}m^{-3}$, and from the pressure balance temperature calculations, assuming $T_e = T_i = \bar{T}$, $T_e \cong 500$ eV in the plasma skin. Therefore, with $\ln\Lambda \cong 12$, the electrical resistivity is 1.1×10^{-7}Ohm-m. This is larger than the resistivity of copper by a factor ~ 6. At time t = -10 ns, the resistivity is approximately 5 times larger than this due to the smaller electron temperature. Assuming that the temperature during the dense pinch phase remains constant, then the resistivity will also remain constant.

4.4.4 MAGNETIC FIELD DIFFUSION

A magnetic field will diffuse into a conductor within a time period τ_B given approximately by [62] $\tau_B \cong \mu_o L^2/\eta$ where η is the electrical resistivity, and L is a characteristic length. For the Plasma Focus, both the resistivity and a characteristic length - the plasma radius - are known, and so the field diffusion time can be estimated.

At the time t = -10 ns, the plasma radius is 3.76 mm, and the resistivity is 5.5×10^{-7} Ohm-m. Therefore, the field would diffuse to the axis in a time $\cong$ 32 micro-seconds. At peak compression, the diffusion time would be $\cong$ 63 micro-seconds. These times are very much larger than the nanosecond timescales of the plasma, and explain why the magnetic field is present only within the skin of the plasma. The field cannot diffuse ahead more rapidly than it is convected.

During the dense pinch phase, the magnetic field is observed to diffuse rapidly to the plasma axis in a 10 ns period commencing from peak compression. From the expression for the magnetic field penetration time, a perpendicular resistivity of 6.9×10^{-4} Ohm-m would be required to achieve this. This resistivity is consistent with an electron temperature of only 1.3 eV, which is smaller than the actual temperature by at least two orders of magnitude. Therefore, the plasma resistivity during this period is anomalous, and is larger by a factor approximately 6000 to that at peak compression. Thus, the electron-ion collision frequency is also anomalously high by this factor.

This value of anomalous resistivity is in close agreement with the results of Bernard et al [22], who estimated from magnetic probe measurements that the resistivity is larger by a factor 10^3 to 10^4 in comparison with the Spitzer value. Highly turbulent plasma was believed responsible.

4.4.5 CURRENT DENSITY DISTRIBUTION

The current density distribution, $J_z(r)$, can be determined from the observed magnetic field distributions by Ampere's law

$$J_z(r) = \frac{1}{\mu_o r} \frac{d}{dr}(rB_\theta) \tag{4.32}$$

This is evaluated at a radial point r_j with the following expression

$$J_z(r_j) = \{r_{j+1}B_\theta(r_{j+1}) - r_{j-1}B_\theta(r_{j-1})\}(2\mu_o r_j \Delta r)^{-1} \tag{4.33}$$

where Δr is the spatial separation of the points. The current density on axis, J_{zo}, assuming that the magnetic field varies linearly, is given by

$$J_{zo} = \frac{2}{\mu_o} \left[\frac{dB_\theta}{dr} \right]_{r=0} \qquad (4.34)$$

The current density distribution at the edge of the plasma is unknown beyond a radial point $r_j = 37a/40$. For convenience, it is assumed that the current density varies linearly between this point and the plasma radius, where it is zero.

From equation 4.33, the error in the current density, δJ_z, is given by

$$\delta J_z(r_j) = \{(r_{j+1}\delta B_\theta(r_{j+1}))^2 + (r_{j-i}\delta B_\theta(r_{j-1}))^2\}^{\frac{1}{2}}(2\mu_o r_j \Delta r)^{-1} \qquad (4.35)$$

where the magnetic field uncertainties at the neigbouring radial points are as given by equation 4.22. The error in the current density on axis, δJ_{zo}, is given by

$$\delta J_{zo} = \frac{2}{\mu_o} \frac{\delta B_\theta(r_1)}{r_1} \qquad (4.36)$$

where $r_1 = a/20$.

The current density profiles during the collapse phase are shown in figure 4.24. Included for comparison are the errors calculated with equation 4.35. All of the electrical current flows in the plasma skin, and the current density rises from $3.6\text{x}10^{10}$ Am^{-2} at time t = -10 ns, to $8.8\text{x}10^{10}$ Am^{-2} at peak compression. The uncertainties during this period range from 22% at t = -10 ns to 62% at t = 0 ns. Therefore, the profiles are more accurate the earlier the time.

The current density profiles during the dense pinch phase are shown in figure 4.25. The uncertainties in these calculations are also shown. These plots demonstrate more clearly the details of the rapid

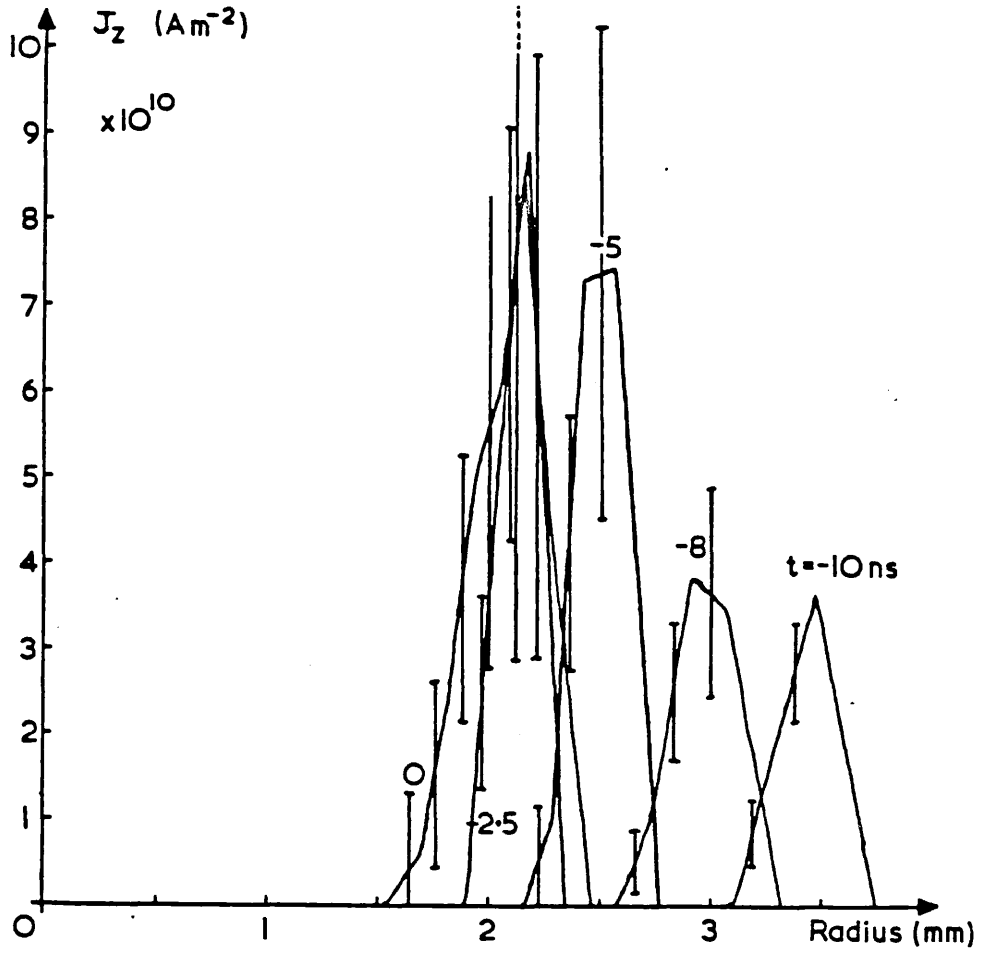

Figure 4.24

Axial current density distribution

during the collapse phase.

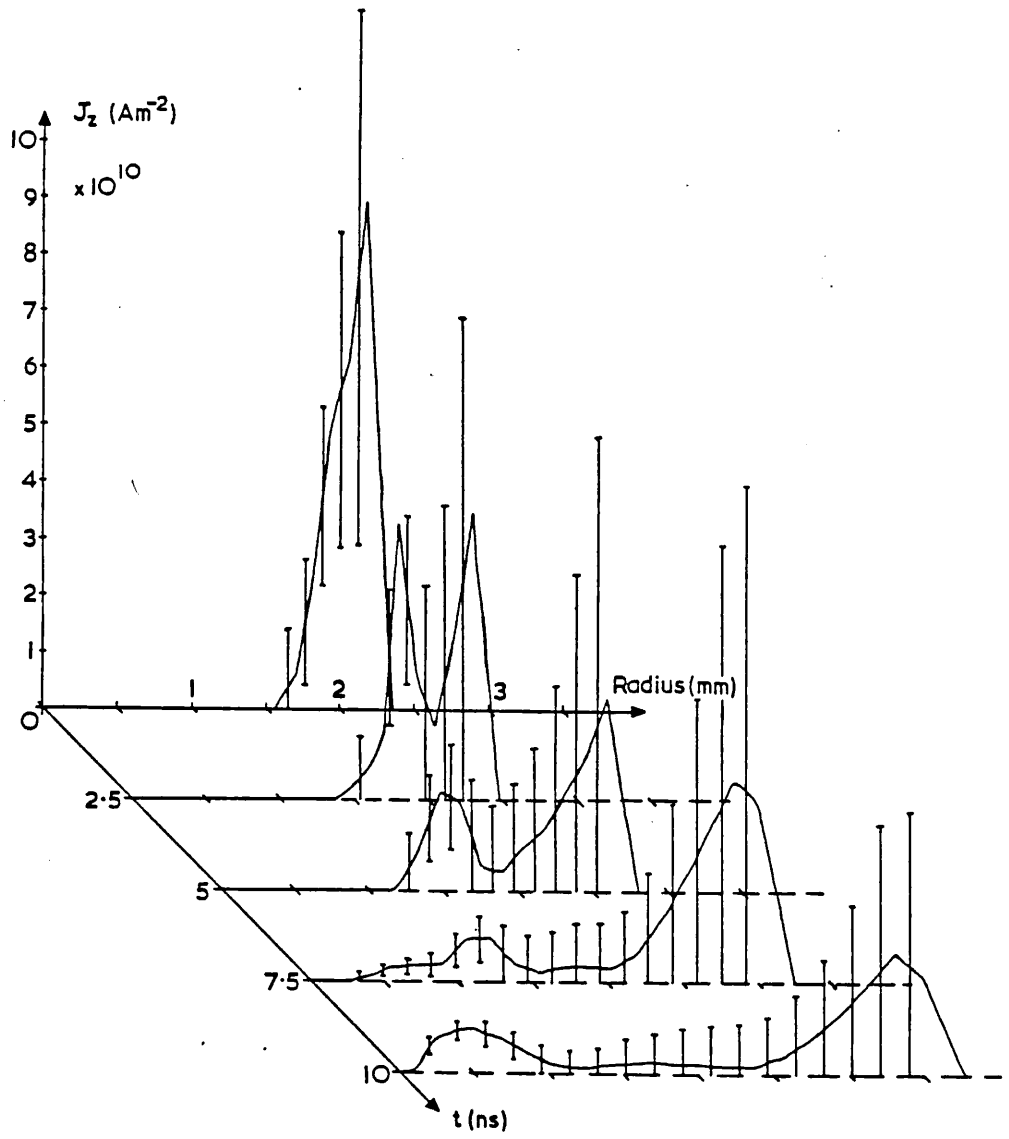

Figure 4.25

Axial current density distribution

during the dense pinch phase.

magnetic field diffusion. At time t = +2.5 ns, the current structure has divided into two peaked profiles. The relative error of the current density within the inner of these two profiles is approximately 50%, while within the division region and the outer profile it is greater than unity. Thus, it is not known whether the current density within the division is zero, or how the current is distributed within the outer profile. However, the total plasma current is a fixed quantity and is therefore an important constraint on the shape of the current density profile. At time t = +5 ns, the separation of the two current rings has increased, while the maximum currrent density of the inner ring has decreased from 4.8×10^{10} Am^{-2} at t = +2.5 ns to 1.74×10^{10} Am^{-2}. The error in the latter quantity is 55%. Again the details of the division region and outer profile are not accurately known. At time t = +7.5 ns, the two current structures are moving apart, one radially contracting, the other expanding with the plasma. The current density of the contracting current ring, 7.5×10^{9} Am^{-2}, has again fallen. Finally, at time t = +10 ns, the inner profile has almost reached the axis. The current density at this time is 7.8×10^{9} Am^{-2}, which is similar to that 2.5 ns earlier. The error in these two estimates are 30% and 50% respectively.

The electrical current flowing within the contracting current profile, can be obtained from the values of the magnetic field strength and radius at the point separating the two regions, via Ampere's law. At time t = +2.5 ns, the position of the current density minimum, between the two maxima, is approximately r = 2 mm. The magnetic field strength at this point is 12.2 Tesla. Therefore, the current flowing within a radius of 2 mm, is 125 kA, i.e. 37% of the total plasma current. At this time, the plasma radius is 2.47 mm, and so, most of the plasma current remains in the skin region. Later, at time

t = +5 ns, the radius of the separation point is approximately 1.9 mm, and the current flowing within the inner region is 68 kA, i.e. 20% of the total plasma current. At time t = +7.5 ns, the radius of the separation point is 2 mm, and the inner current flow 43 kA, i.e. 13% of the total. Finally, at time t = +10 ns, the radius value is 2.25 mm, with 36 kA, i.e. 11%, flowing in the plasma core. These observations indicate that the point of separation between the two current regions remains approximately constant with a radius value of 2 mm over the 7.5 ns period examined. In addition, the initially large fraction of current which diffuses radially inwards from the plasma skin, decays in time. This is despite the fact that the area of plasma carrying the current increases. The decay of the current may be a result of the anomalous resistivity within this region. As most of the plasma current remains in the plasma skin, then the resistivity of the plasma skin appears classical. Therefore, the region of anomalous resistivity is confined to the plasma core with a radius of 2 mm.

Axial Current Filaments

Figure 4.26 shows the current density distributions evaluated from the magnetic field profiles for the Faraday rotation data where 'spikes' were observed. The profiles are strongly peaked on axis, and are what would be observed with a single large axial current filament, or with many close packed axial filaments. The estimated value of current density for both times of +10 and +15 ns is approximately constant at 3.7×10^{11} Am^{-2}. This is larger than the maximum current density at peak compression of the pinch and the maximum current density of the radially contracted current ring at time t = +10 ns by factors 4 and 47 respectively. The error in the calculated value is 5 - 10%, which, because of the uncertainties involved in the original

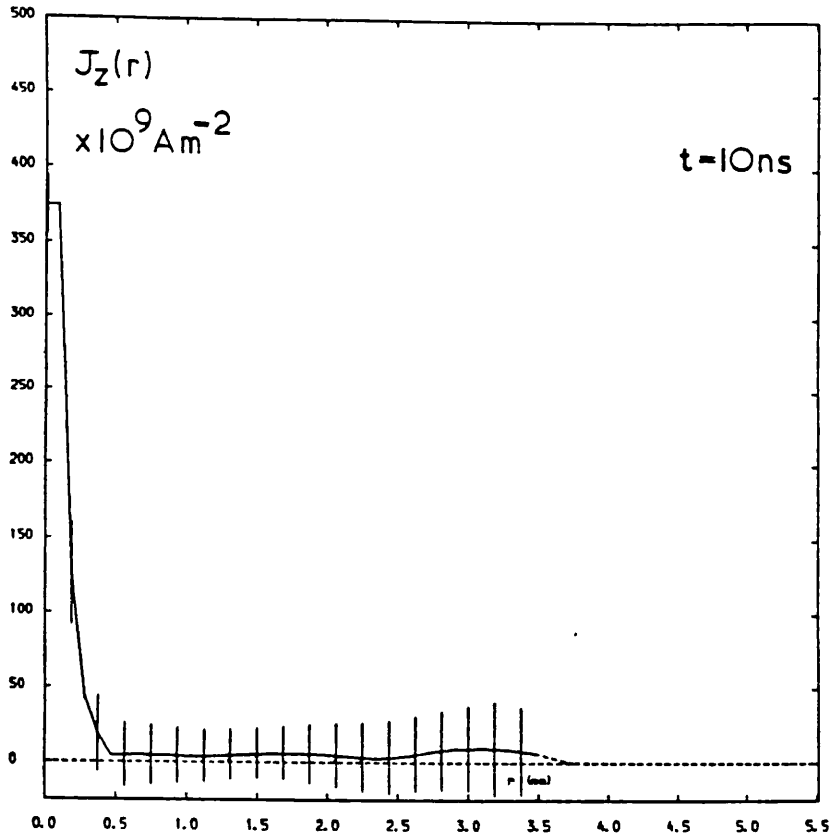

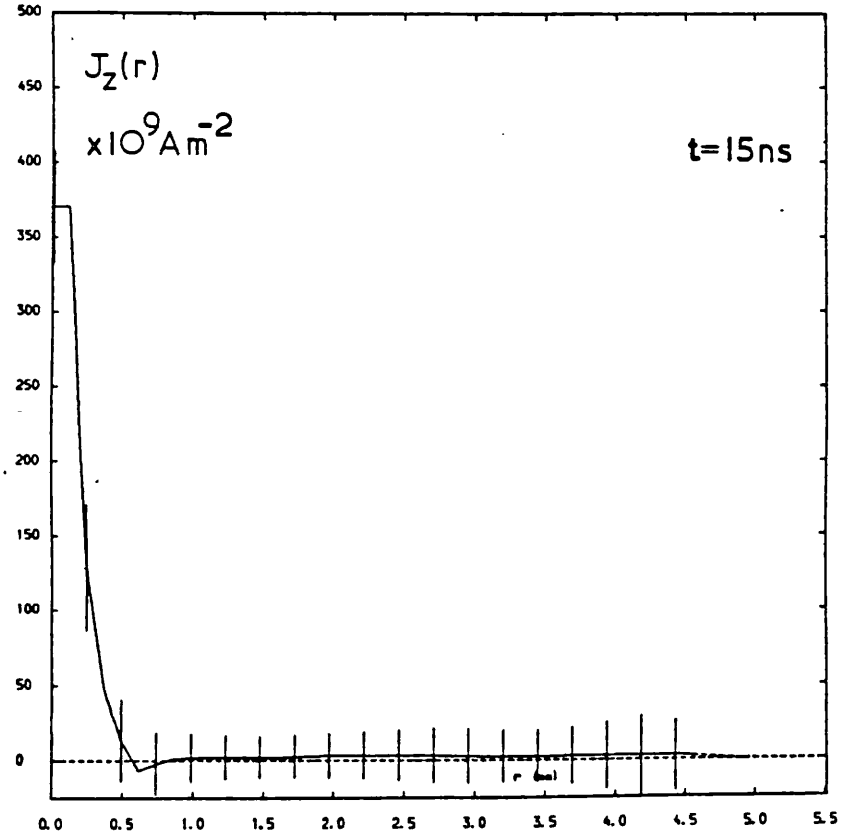

Figure 4.26

Current density distribution of plasma

with axial current filaments.

Faraday rotation profile, especially close to the axis, the finite spatial resolution of the Abel inversion scheme used, the finite size of the plasma chord viewed by the polarimeter, and the detection system bandwidth limitations, is too small an estimate. For the same reasons, the maximum current density calculated should be considered a lower limit. The current density distribution outside of the current filament is uncertain due to large errors.

From the magnetic field profiles for the current filaments, the maximum field strengths are between 44 and 57 Tesla at radii 0.19 and 0.25 mm for times t = +10 and +15 ns respectively. Therefore, from Ampere's law, the total electrical current flowing within the filaments is between 42 and 72 kA. These currents represent 12 and 21% of the total plasma current respectively. From the current density profiles, the half-maximum radii of the filaments is between 167 and 217 microns. Both the estimated values of peak field strength and filament current should, similarly to that of the current density, be treated as lower limits, while the values of filament radius should be considered as upper limits.

The values of current flow within these filaments are not significantly different to the values of current flow within the inner turbulent core of the plasma normally observed. The filaments also occur at times later than t = +10 ns, the time when current reaches the axis. Therefore, one possibility is that these filaments are the end result of a radial contraction of current density, in which the fraction of plasma current diffusing to the axis is larger than normal.

4.4.6 DRIFT VELOCITY

The electron drift velocity, v_d, can be determined from the current density calculations and electron density data using the expression

$$J_z = -en_e v_d \qquad (4.37)$$

The accuracy of the evaluation is given by the relative errors in both electron and current density

$$\frac{\delta v_d}{v_d} = \left\{ \left[\frac{\delta J_z}{J_z} \right]^2 + \left[\frac{\delta n_e}{n_e} \right]^2 \right\}^{\frac{1}{2}} \qquad (4.38)$$

The calculated radial profiles of the drift velocity during the collapse phase are shown in figure 4.27. During this period, t = -10 to 0 ns, the drift velocity increases by a factor of 4 from 1.2×10^5 ms^{-1} to 4.7×10^5 ms^{-1}, with errors 25 and 70% respectively. Also shown are those drift velocities corresponding to 5% of the thermal velocity of electrons with temperatures ranging from 100 eV to 1 keV. At peak compression, the pressure balance temperature in the skin is approximately 500 eV. Therefore, assuming this to be the electron temperature, the drift velocity at this time is approximately 5% of the thermal velocity. During the period shown, the drift parameter, $\zeta = v_d/v_e$, is constant at $\sim$ 5%.

Only the current density of the contracting current ring is known accurately during the dense pinch phase. Therefore, only the corresponding drift velocities will be certain. Figure 4.28 shows the maximum calculated drift velocities within this inner turbulent structure. Drawn througth the points is an exponentially decaying curve, with an e-folding time of 1.74 ns. It is apparent that the decrease by a factor 56 in the drift velocity, from 4.7×10^5 ms^{-1} to

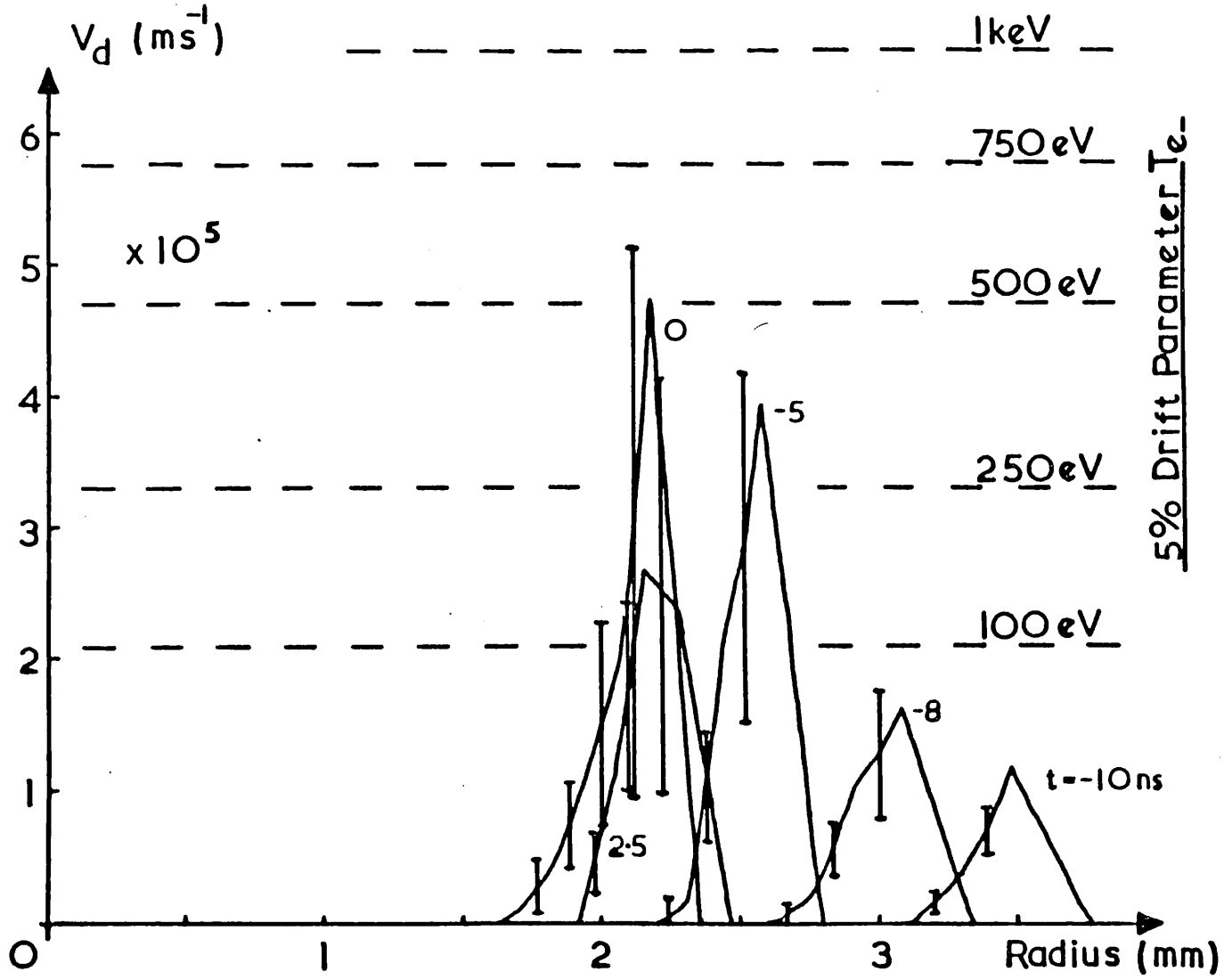

Figure 4.27

Electron drift velocity distribution

during the collapse phase.

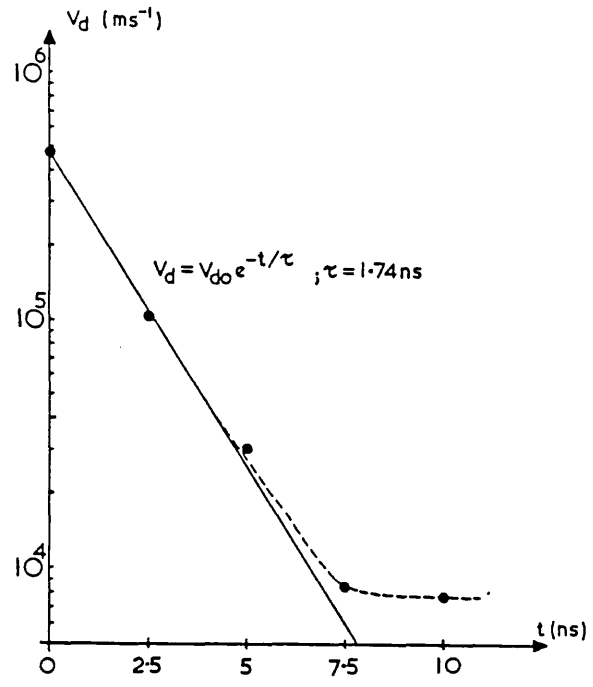

Figure 4.28

Maximum drift velocity within the inner current distribution during the dense pinch phase.

8.4×10^3 ms^{-1} in the time period t = 0 to +7.5 ns, is approximately exponential. The rapidity of this reduction is clearly expressed by the small 1.74 ns e-folding time. Similarly to the current density, the drift velocity between t = +7.5 and +10 ns is approximately constant. The accuracy of the drift velocity calculations during this phase is typically 50%.

In the absence of a potential difference across the plasma, the electron drift velocity would decay exponentially with an e-folding time given by the reciprocal of the electron-ion momentum transfer collision frequency. The observed rate of decay of the drift velocity, gives a collision frequency approximately a factor 10 times smaller than the classical value. Assuming that the resistivity is anomalous by a factor 10^3 during this period, the discrepancy between the actual collision frequency and the calculated frequency is 10^4. This large

factor suggests that current is being driven during this period. However, the level of turbulence does have a noticeable effect as the current flow during this period decays.

Current filaments

The minimum electron drift velocities in the current filaments are 3.3×10^5 ms^{-1} and 6.9×10^5 ms^{-1}, with errors 35% and 60%, at times t = +10 ns and +15 ns respectively. With an electron temperature at these times ≅ 1keV, the drift parameter is 2.5 - 5.2%, which may be the lower limit. This value of drift parameter is similar to that present in the plasma skin during the collapse phase and at peak compression.

Results from co-operative laser scattering [49] indicate that higher filament drift velocities occur (cf section 4.3.6), with the result that the filament may exist with very small dimensions. One estimate of the filament radius is obtained as follows: Assuming a drift parameter of unity, an electron temperature of 1 keV, and the observed electron densities of 7.1×10^{24} m^{-3} and 3.3×10^{24} m^{-3} at times t = +10 ns and +15 ns respectively, the corresponding axial current densities would be 1.5×10^{13} Am^{-2} and 7.0×10^{12} Am^{-2}. Assuming in addition the observed total filament currents of 42 kA and 72 kA at these times, the radii of the filaments would be 30 and 57 microns. Filaments with these radii and currents would have self magnetic fields of 280 and 253 Tesla respectively. These radii are similar to the values of ion Larmor radii that would exist. The electron Larmor radii would be approximately 0.5 microns.

This estimate of the filament radius assumes that all of the filament electrons conduct current and have a drift parameter of unity.

With the original dimensions, the fraction of electrons with drift parameter unity needed to carry the observed currents are 2.5% and 5.2% at times t = +10 ns and +15 ns respectively. Therefore, a small fraction of the available electrons, with large drift parameter, may be responsible for the observed filament characteristics.

4.4.7 HEATING MECHANISMS

Some estimates of the plasma heating due to Joule heating, magnetic compression, adiabatic compression, and shock heating, can be made during the time period of interest.

The location of the electrical current during the collape phase indicates that only the skin region obtains energy from Ohmic heating. The power input can be estimated from the calculated values of plasma resistivity and current density. During the time period t = -10 to 0 ns, the calculated value of classical resistivity decreased from 5.5×10^{-7} Ohm-m to 1.1×10^{-7} Ohm-m, while the current density rose from 3.6×10^{10} Am^{-2} to 8.8×10^{10} Am^{-2}. Therefore, the power dissipated per unit volume, $\eta_{\perp} J_z^2$, varies from 7.1×10^{14} to 8.5×10^{14} Wm^{-3}. The areas occupied by the current channel is $\cong 10^{-5} m^2$, and so the Joule heating per unit length is 7.7 GWm^{-1}, and is approximately constant during this period. Over the 10 ns time interval, the number of electrons per unit length within this area is constant, $\cong 1.5 \times 10^{19}$ m^{-1}, and so each electron will receive $\sim$ 32 eV of energy. If the resistivity were anomalous by a factor 100, the rate of magnetic field diffusion would still be slow ($\sim$500 ns) relative to the timescale of the observation and would not be seen from the magnetic field data. If the resistivity were anomalous by this factor, the Joule heating would be increased to 3.2 keV per electron.

Assuming an electron temperature of 500 eV during the dense pinch phase, the classical resistivity is 1.1×10^{-7} Ohm-m, and the total resistance per unit length of the plasma column is approximately 6.3 milli-Ohms per metre. Therefore, the power input per unit length is 740 MW. This heat input represents a heating of only 3 eV per particle in a 10 ns period. However, the plasma resistivity is anomalous during this period, having a value of 6.9×10^{-4} Ohm-m as derived from the magnetic field diffusion rate. This resistivity is found only within the central core of the plasma where the current density is low and the particle density high. In a 10 ns period, it can be calculated that the particle heating would be typically 1 kev. As the value of anomalous resistivity and current density vary throughout the pinch, there may be regions where significant heating (> 1 keV per particle) occurs.

When the current filament occurs, the Joule heating resulting from the high current density, assuming a classical resistivity of 1.1×10^{-7} Ohm-m, is approximately $1.5 \times 10^{16} \mathrm{Wm}^{-3}$. Therefore, during the 2.5 ns duration of the filament, heating of 37.5 MJm^{-3} occurs. The line density of electrons in the filament is approximately 5.5×10^{17} m^{-1}, and so, with a radius of 190 microns, the heating per particle is $\cong$ 25 eV. This low heating rate may be enhanced if the resistivity is anomalous. Assuming a resistivity of 6.9×10^{-4} Ohm-m, the plasma heating would be 125 keV per particle.

If the resistivity of the filament is anomalous, Joule heating will result in an increase in plasma kinetic pressure which is sufficiently larger than the filament magnetic pressure to cause break-up. From the magnetic field strengths and electron densities of the filaments, this would occur when the mean temperatures exceeded 340 eV and 1.2 keV for

times t = +10 and +15 ns respectively. These, although probably a lower limit, are not very large compared to the mean plasma temperature, and imply that the filaments are easily destroyed by internal Ohmic dissipation.

As the plasma column radius decreases from 3.76 to 2.35 mm at times t = -10 to 0 ns, the work done by the magnetic field per unit length is

$$W_B = \frac{\mu_o I_p^2}{4\pi} \ell n \left[\frac{r_2}{r_1} \right] = 5.5 \text{ kJm}^{-1} \qquad (4.39)$$

Taking the average particle line density of 2.2×10^{20} m^{-1} during this period, the energy gained per particle is 156 eV.

The average mass per unit length of the current carrying plasma sheath during the time interval t = -10 to 0 ns, is 5.1×10^{-8} Kgm^{-1}. With a sheath velocity of 2.35×10^5 ms^{-1}, the kinetic energy per unit length is 1.4 kJm^{-1}. This is carried mostly by the ions. Assuming that this is dissipated into thermal energy of all the plasma ions (ion viscosity scales as $T_i^{5/2}$), the heat gained by each ion would be 80 eV. If this energy were dissipated into thermal energy of only those ions in the plasma sheath, the heat gain would be 580 eV per ion. The total amount of kinetic energy avaiable to the ions is larger than 1.4 kJm^{-1}. The exact quantity is not known, but an estimate can be made as follows. The total mass per unit length of the plasma column is $3.7 \times 10^{-7} Kgm^{-1}$, and the mean square velocity is approximately half the square of the plasma-vacuum velocity. Therefore, the mean plasma kinetic energy is 5.1 kJm^{-1}. This estimate is larger than that of the sheath alone, and would give each plasma ion an energy gain of 290 eV.

During the late stages of the collapse phase, the plasma is compressed in a manner which may be assumed adiabatic. During the time

period t = -10 ns to t = 0 ns, the plasma velocities are less than the sound speed. Therefore, shock waves with their associated non-reversable changes of state, do not exist. The degree of Joule heating during this period is also minimal. However, one non-reversible process which occurs, is the reduction in the electron line density. This results in an outflux of heat from the system. Neglecting this, from the adiabatic compression equation PV^{γ} = constant, with volume proportional to radius squared, we obtain $\bar{T}r^{2(\gamma-1)}$ = constant. Assuming γ = 5/3, the increase in temperature due to the change in plasma radius from 3.76 mm to 2.35 mm at time t = -10 ns and t = 0 ns respectively, is approximately 1.9. This is not a large factor considering that the uncertainties in the estimate are large, especially since approximately 50% of the particles are lost to the system. During the time period t = 0 ns to t = +10 ns, the plasma expands by a similar amount. Therefore, adiabatic cooling will occur. However, because of anomalous Joule heating of electrons, together with viscous and turbulent heating of the ions, this cooling will probably not be observed.

4.4.8 THE ELECTRON DENSITY EXTERNAL TO THE PINCH COLUMN

An upper limit to the value of the electron density external to the pinched axial column and the return plasma sheath, can be determined from the observation that the Faraday rotation angle at large values of impact parameter drops to zero once the plasma radius is less than the value of impact parameter (see figure 4.15).

The following assumptions are made: The electron density outside the plasma column is radially constant, i.e. $n_e(r) = n_{ex}$. No current flows external to the pinch (i.e. the difference current between that

observed by Faraday rotation, and that measured by the Rogowskii coil, is the leakage current across the insulator). The magnetic field is given by the vacuum field of the plasma. The impact parameter is larger than the plasma column radius.

The Faraday rotation angle, from equation 1.53, is

$$\psi(h) = 5.05 \times 10^{-32} n_{ex} I_p \tan^{-1}\left\{\frac{1}{h}(a_r^2 - h^2)^{\frac{1}{2}}\right\} \qquad (4.40)$$

where a_r is the radius of the return current sheath. The upper limit to the electron density in the volume between the inner plasma column and the return current sheath is given when the Faraday rotation angle is set to the minimum measureable Faraday rotation angle. For the experiment, $\psi_{min} = 0.02$ degrees. Therefore, with a plasma current of 340 kA, an impact parameter of 10 mm (the largest used), and setting the radius of the return plasma sheath to that of the outer electrode, the upper limit to the electron density is $1.5 \times 10^{22} m^{-3}$, which is a factor 8.4 less than the filling gas electron density.

4.4.9 RAYLEIGH-TAYLOR INSTABILITY

In the time period around peak compression, the kinetic pressure of the plasma exceeds that of the magnetic field. This results in a deceleration of the plasma-vacuum boundary, which gives rise to Rayleigh-Taylor instabilities [62]. The rise time, or growth rate, is given by

$$w = (gk)^{\frac{1}{2}} \qquad (4.41)$$

where g is the acceleration, and k is the wavenumber of the instability.

The reconstructed hologram shown in figure 4.1 at time t = 0 ns,

was analysed for axial perturbations. The wavelength of the instability observed was 2.5 mm. The deceleration observed from the collection of interferograms was approximately $2 \times 10^{13} ms^{-2}$. Therefore, from equation 4.41, the e-folding time of the instability was 4.5 ns. Generally, the deceleration was smaller, and the wavelength larger, resulting in a longer rise time.

4.4.10 PLASMA AND GUN INDUCTANCE

The inductance of the plasma and the gun electrodes can be determined from the known geometry and magnetic field distribution.

Gun Inductance

The characteristic time frequency of the electrical circuit is approximately 100 kHz. At this frequency, the skin depth of copper - the electrode material - is approximately 200 microns. Therefore, the gun inductance per unit length, L_g, is given by [63]

$$L_g = \frac{1}{2\pi} \mu_o \ln \left[\frac{b}{a}\right] \qquad (4.42)$$

where a and b are the radii of the inner and outer electrodes respectively. The maximum value of gun inductance is 28 nH.

Plasma Inductance

The plasma inductance is defined by the ratio of magnetic flux external to the electrodes per unit plasma current. The amount of flux depends upon the plasma geometry, and the internal distribution of magnetic field. In calculating the magnetic flux, the following assumptions were made: The maximum axial extent of the plasma is as observed and shown in figure 4.12, and occurs at a radial position equal to the radius of the inner electrode. For smaller radii, the

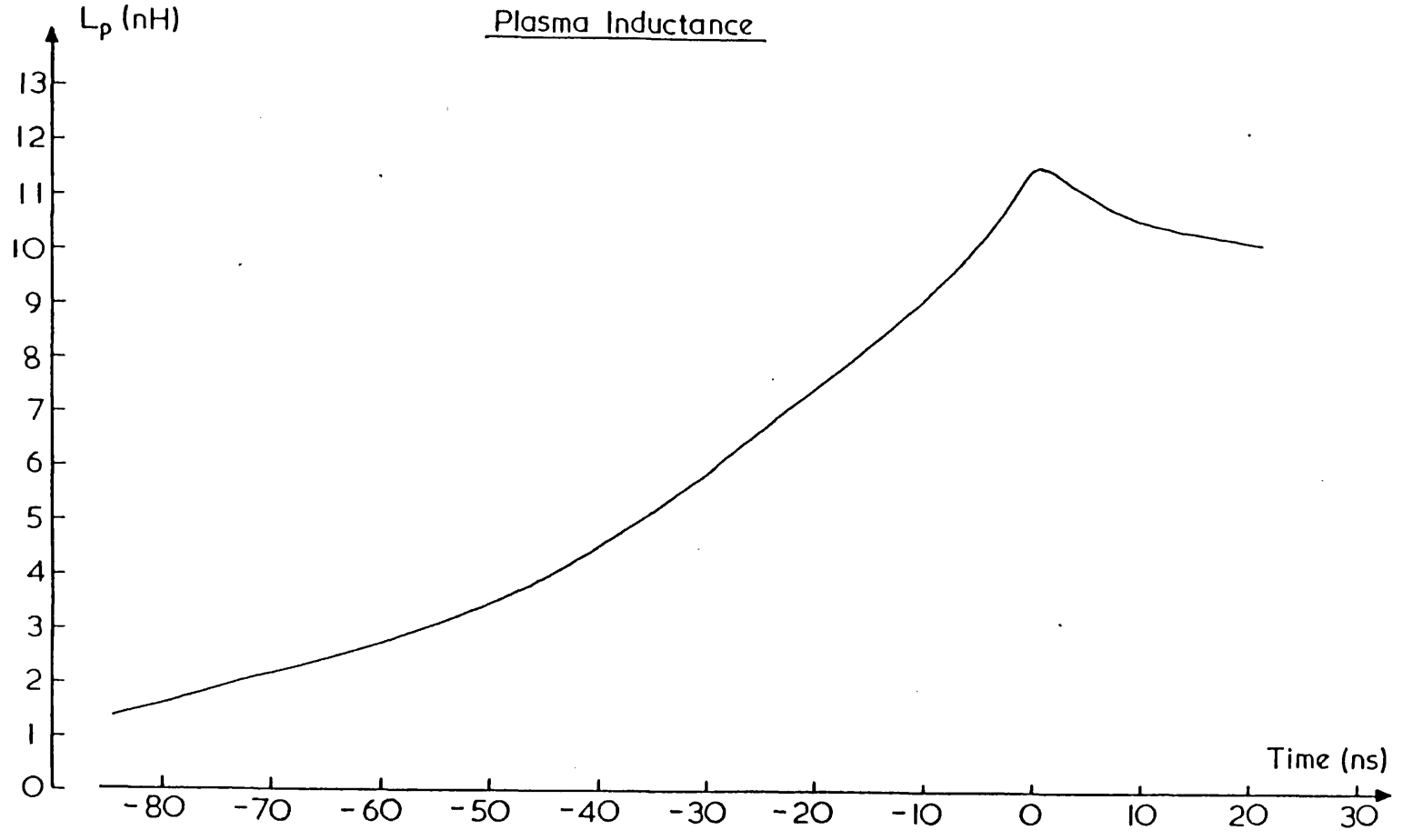

Figure 4.29

Plasma Inductance against time.

geometry of the plasma is as observed interferometrically. For larger radii, the geometry is parabolic. During the collapse phase, the magnetic field skin depth is 0.5 mm. During the dense pinch phase, the internal magnetic field distribution is linear.

With the above assumptions, the temporal behaviour of the calculated plasma inductance is as shown in figure 4.29. Maximum inductance occurs at peak compression of the pinch, and has a value of 11.5 nH. After peak compression, the inductance decreases slowly. This is because the decrease in inductance due to the radial expansion of the plasma column adjacent to the centre electrode, offsets the increase in inductance due to both the radial contraction at large axial position, and due to the increase in axial position of the return sheath.

The plasma column will be distorted by instabilities during the dense pinch phase. This will result in the true plasma inductance varying considerably in time, and explains the behaviour of the dI/dt Rogowskii coil signal observed after peak compression.

At peak compression of the pinch, the total inductance (plasma + gun) is 39.5 nH. Therefore, the energy stored in the source inductance is 4 kJ, and the energy stored in the plasma and gun is 2.3 kJ. Thus, the total stored magnetic energy at peak compression is 23% of the initial stored energy.

4.4.11 A TIME-DEPENDENT ELECTRIC CIRCUIT MODEL

A time-dependent model of the Plasma Focus electric circuit, was developed to examine the effects of insulator leakage, and current

arcing or short circuiting between and at the open end of the electrodes, on the current and voltage observed at the insulator. The aim was to compare the model with the waveforms normally observed with the Rogowskii coil and voltage stack, to determine whether or not insulator current leakage and shorting could be diagnosed.

The electric circuit of the model is shown in figure 4.30, where C is the capacity of the capacitor bank (93.85 micro-Farads); V_B is the bank voltage; R_s is the source resistance (2.25 milli-Ohms); L_s is the source inductance (33.7 nH); R_L is the insulator resistance; L_g is the gun inductance; R_A is the short circuit resistance; R_p is the plasma resistance; and L_p is the plasma inductance. The parameters I_T, I_L, I_A, and I_p, are the total, the leakage, the short-circuit, and the plasma currents respectively. The gun inductance is given by equation 4.42, and the position of the plasma is determined by a snow-plough model, discussed below. The plasma inductance is given by the curve shown in figure 4.29.

The axial position of the plasma was given by a simple snow-plough model [56], in which the axial velocity of the plasma is

$$v_z = \left\{ \frac{\mu_o}{8\pi^2 \varepsilon \rho a^2} \left[(I_A + I_p)^2 - \frac{8\pi^2 a^2 p_o}{\mu_o} \right] \right\}^{\frac{1}{2}} \qquad (4.43)$$

where a is the radius of the inner electrode; ρ is the filling gas density; p_o is the filling gas pressure; and ε is a factor describing the snow-plough efficiency. The model was run with the following initial conditions: The filling pressure was 1.7 torr of deuterium, and the bank voltage was 23 kV. In order to obtain a run-down time similar to that observed experimentally, approximately 2 micro-seconds, the snow-plough efficiency was fixed at 60%. The plasma resistance was

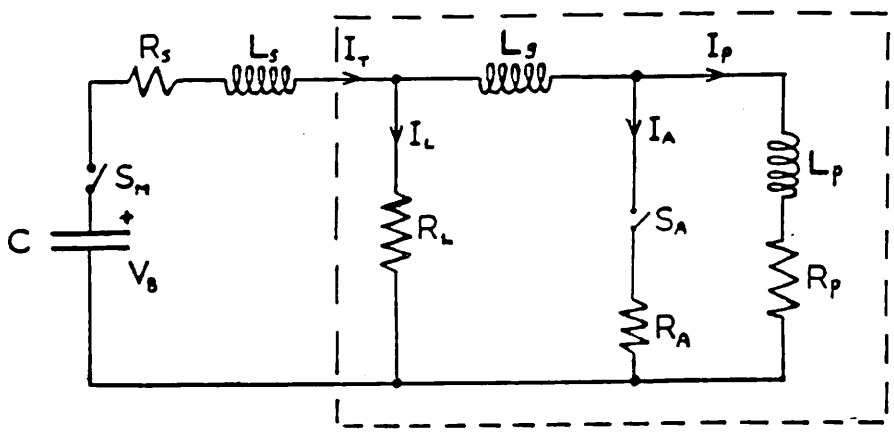

Figure 4.30

Equivalent Plasma Focus Discharge Circuit.

assumed constant at 2 milli-Ohms.

The rate of change of gun inductance was obtained by multiplying equation 4.42 by the snow-plough velocity. The rate of change of plasma inductance was obtained by differentiating the inductance-time plot of figure 4.29.

Three permutations of the model were examined:

a) No Leakage, No Short Circuit

The simplest model of the circuit is that in which there is no insulator loss, and no current arcing. Solution of the differential equations describing the circuit gives the results shown in figure 4.31. The current waveform, similar to that observed experimentally (see figure 2.2), peaks in excess of 500 kA after a

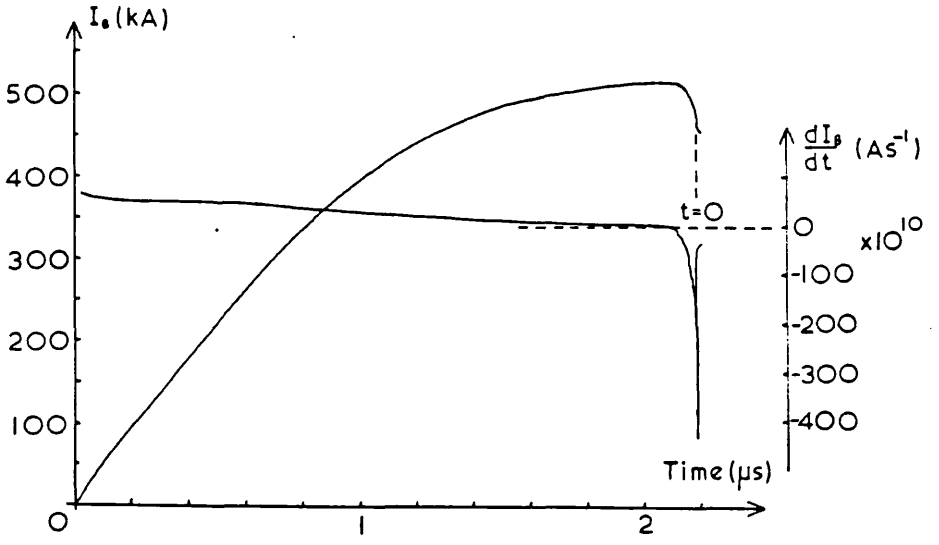

Figure 4.31

Current waveforms computed for the case when there is neither insulator leakage or current arcing.

run-down time of 2.2 micro-seconds. The rate of change of total current, also similar to that observed experimentally (see figure 2.3), is highly peaked at the time of peak compression. During the collapse phase, the current decreases from its peak value by 10%.

b) Leakage, No Short Circuit

For a circuit model in which insulator leakage occurs, but not current arcing, assuming an insulator resistance of 0.25 Ohms, the results are as shown in figure 4.32. The total current waveform is similar to that for case a), and has a 4% decrease from peak current during the collapse phase. Current leakage across the insulator occurs throughout the discharge, and only during the collapse phase does it begin to become large. This is because at this time, voltages in excess of 30 kV appear across the insulator, due to the rapid changes in plasma inductance that occur. The calculated value of current

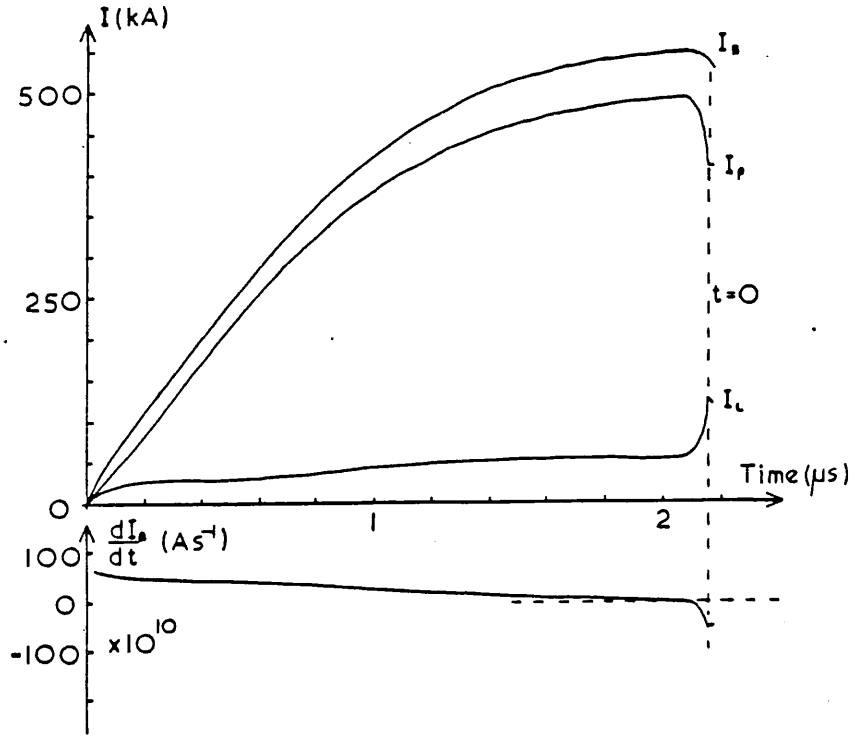

Figure 4.32

Current waveforms computed for the case when there is insulator leakage without current arcing.

leakage at peak compression is 120 kA. This is approximately the difference between the observed capacitor bank current and the current measured by Faraday rotation. The plasma current waveform shows a rapid drop as insulator leakage increases. This gives rise to a reduction in the plasma's axial velocity, as observed experimentally. At peak compression, the voltage appearing across the plasma, and between the open ends of the two electrodes, is in excess of 100 kV. This voltage is hidden from the insulator by the gun inductance, and may result in current arcing at the open end of the two electrodes. The rate of change of total current also peaks at the time of peak compression. It is smaller than case a) by a factor 8.

c) Leakage and Short Circuit

For this case, both insulator leakage and current arcing are considered. An insulator resistance of 0.25 Ohms and a short-circuit

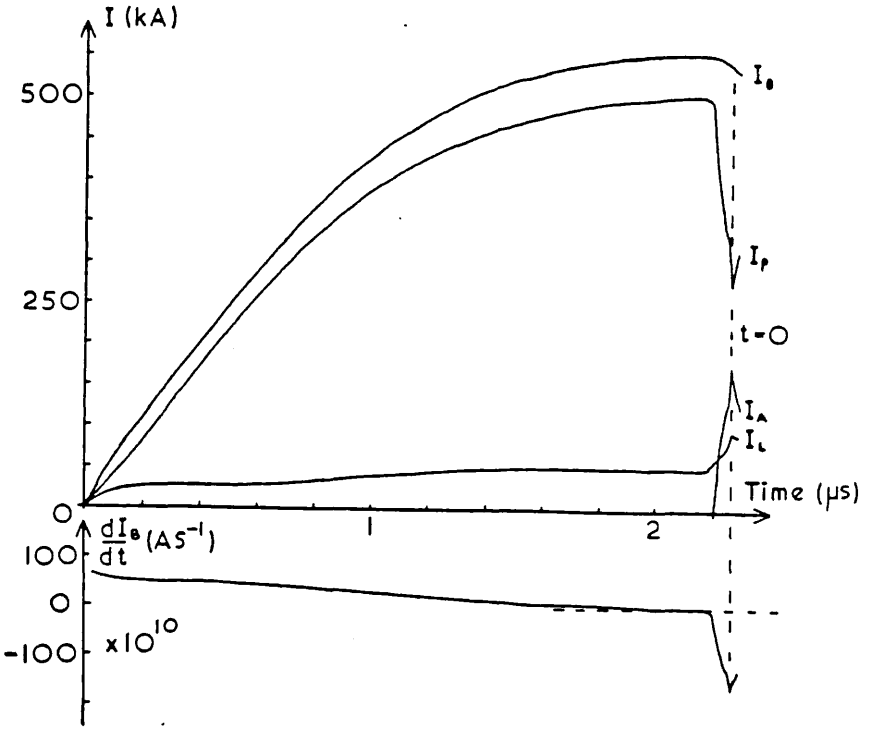

Figure 4.33

Current waveforms computed for the case when both insulator leakage and current arcing occur.

resistance of 0.25 Ohms, are assumed. Current arcing is assumed to occur once the plasma has spilled out of the ends of the electrodes. The results are shown in figure 4.33. Similarly to cases a) and b), the dI/dt waveform peaks at the time of peak compression, and is similar to that observed experimentally. The maximum value is smaller than case a) by a factor 2.6. The current waveforms are identical with case b) up until the short circuit occurs. Then, as the short circuit current rises, together with the rising insulator leakage, the plasma current falls very rapidly, to approximately 54% of its peak value. The maximum insulator and arc currents are 95 kA and 175 kA respectively. At peak compression of the pinch, the voltage across the plasma is approximately 110 kV.

Discussion

For the three model cases considered, no significant difference

between the total current and dI/dt waveforms exist. In case a), the very sharp dI/dt pulse may not be observed experimentally with a Rogowskii coil having a finite rise time. The calculated decreases in total current during the collapse phase from peak value to the value at peak compression, are very similar, and would not be distinguishable experimentally. The voltages appearing at the insulator, typically half the plasma voltage, are also very similar. Therefore, it is unlikely that either insulator current leakage or current arcing could be diagnosed with the electrical diagnostics.

As insulator leakage is known to exist in the Plasma Focus [57], case a) is too simple a model. Similarly, discharges in which current arcing was observed [64], gave neutron emissions which were lower than normal by several orders of magnitude. This is not surprising considering the dramatic decrease in plasma current shown in figure 4.33. Therefore, as with case a), case c) does not represent a typical Plasma Focus discharge. Based on the Faraday rotation measurements, and the observations of the axial return sheath position, case b) appears to best represent the Plasma Focus discharge circuit.

4.4.12 ELECTRON AND ION HALL TERMS

Many transport processes in plasmas [65] depend upon the degree to which the ions and electrons are tied to the magnetic field lines of force. Two parameters which quantify this are the electron and ion Hall terms. These are defined as $\omega_{ce}\tau_{ei}$ and $\omega_{ci}\tau_{ii}$ respectively, where ω_{ce} and ω_{ci} are the electron and ion Larmor frequencies, and τ_{ei} and τ_{ii} are the electron-ion and ion-ion momentum transfer collision times. When the Hall term is greater than unity, Larmor radius effects are important, and the particle is said to be collisionless. When the

Hall term is less than unity, the particle is collisional, and the Hall term in the transport coefficients can be neglected. The Hall term basically decribes the number of Larmor orbits a particle makes before losing momentum through collision.

The ratio of electron Hall term to ion Hall term, assuming equal particle temperatures, is approximately 60. Therefore, only one term need be determined. From this ratio value, it is clear that processes involving electrons may be affected by the magnetic field, while processes involving ions may not.

The electron-ion momentum transfer collision time τ_{ei} is given by the reciprocal of the effective momentum transfer collision frequency, discussed in section 1.4, and expressed by equation 1.35. For simplicity, assuming $\ln\Lambda = 12$, the collision time is approximately

$$\tau_{ei} = 2.87 \times 10^{10} T_e^{3/2} n_e^{-1} \text{ seconds} \qquad (4.44)$$

where the electron temperature is measured in electron volts.

During the collapse phase, the electron densities and pressure balance temperatures are typically $1.5 \times 10^{24} m^{-3}$ and 150 eV at time t = -10 ns, and are typically $2.0 \times 10^{24} m^{-3}$ and 500 eV at peak compression. These values occur where the magnetic field strengths are approximately half of their maximum values. From equation 4.44, the electron-ion collision time is 35 picoseconds and 160 picoseconds at these respective times.

The magnetic field strengths are typically 9 and 20 Tesla at times t = -10 ns and t = 0 ns respectively. Therefore, the electron Larmor frequencies are $1.58 \times 10^{12} rad\text{-}s^{-1}$ and $3.52 \times 10^{12} rad\text{-}s^{-1}$ respectively.

Combining these frequencies with the collision times, the electron Hall term varies from 55 at time t = -10 ns to 563 at time t = 0 ns. These are larger than unity, and therefore, the electrons are collisionless. The transport coefficients depend upon the square of the Hall term, and so changes in the values of the transport coefficients by a factor of 100 occur over the 10 ns time period considered.

The ion Hall term changes from approximately 0.9 to 9.4 during the time period t = -10 ns to peak compression. Therefore, during the time period considered, the initially collisional ions become collisionless.

During the dense pinch phase, the typical values of electron density, electron temperature (assumed to be the pressure balance temperature), and magnetic field strength, are not significantly different to those quoted above for the collapse phase. Therefore, on the basis of classical collisionality, the electron Hall term is of order 100, while the ion Hall term is of order unity. However, the resistivity of the plasma within a radius of 2 mm is anomalous by a factor of 6000 from the classical value. This is due to anomalous electron-ion collisionality. Therefore, the actual collision time is smaller by this factor of 6000. This results in an electron Hall term less than unity. Thus, the central core of the plasma is highly collisional, while outside of this core, the electrons are collisionless, and the ions are marginally collisionless.

4.4.13 COMMENTS ON NEUTRON PRODUCTION AND ION ACCELERATION

Two important processes which occur in the Plasma Focus are neutron production and ion acceleration. Perhaps the latter is the more important of the two as it may play a necessary role in the former.

However, neither is fully understood. In this final section, some comments on neutron production and ion acceleration are given in the light of the results from the Faraday rotation experiment. Firstly, brief reviews of neutron and deuteron emission characteristics are given, followed by some discussion on models and mechanisms proposed to explain the observations.

The neutron emission from a Plasma Focus, typically 10^9 to 10^{10} per discharge, originates from a small volume of a few cubic centimeters in front of the centre electrode [66]. The yield, proportional to the fourth power of the plasma current [67], is not correlated with the observed intensity of accelerated deuterons [68]. The emission is accompanied by anomalous resistivity [66], and the yield can be drastically reduced by application of a bias axial magnetic field [67]. The neutron emission occurs in two pulses. The first begins at peak compression, and the second at the onset of $m = 0$ instabilities [69] and peaks when the plasma has expanded to large radius and low density [67]. These pulses may be superposed depending when the instabilities occur. The neutron emission is anisotropic with a factor up to 3 times more neutrons emitted in the forward axial direction than in a direction perpendicular to the axis. The neutron energy spectrum shows a large axial energy shift of between 200 and 700 keV from the 2.45 MeV D-D reaction energy [70].

In addition to the neutron emission, the plasma emits beams of deuterons with energies up to 5 MeV [71]. The number of ions in the beam could be as large as 10^{15} [71], which would be larger than the neutron yield by a factor 10^5. The beam is highly directional, with typically 100 times more deuterons emitted in a forward axial direction compared with those emitted perpendicular to the axis [71]. The

deuterons are emitted in a single pulse of width $\cong$ 8 ns, or as a collection of $\sim$ 8 ns pulses covering a time period of 50 - 100 ns [72]. The ion beam can carry a significant amount of energy. Gullickson and Sahlin [71] estimate a conversion efficiency from initial stored energy to beam energy of 0.1%. This is smaller than the 3% value determined from measurements on the Limeil 340 kJ Plasma Focus [70].

Although no precise correlation between deuteron beam intensity and neutron yield has been established [68,72], it is probable that deuteron beams play an important role in the neutron production process. Therefore, an understanding of the mechanism behind ion acceleration will also give greater understanding of the neutron production process.

Two simple models which have been used in attempts to explain the observed neutron emission characteristics, are the beam-target and the moving boiler models, both reviewed in reference 66. In the former model, neutrons are assumed to be produced as the result of the interaction between a beam of deuterons, accelerated to energies of $\lesssim$ 0.25 MeV, with plasma ions and cold background filling gas. In the latter model, the neutron emission is assumed to come from a thermonuclear plasma of temperature $\sim$10 keV and with a centre of mass velocity of approximately 10^6 ms^{-1}. Neither of these models has so far been totally successful in describing the experimental observations. It is possible that many different processes are involved. However, there are some models which attempt to explain both deuteron acceleration and neutron production. These involve a single ion acceleration mechanism, and are discussed below.

In Bernstein's model [73], it is assumed that due to the onset of

anomalous resistivity during the dense pinch phase, there is a rapid radial contraction of the current distribution. The change in magnetic flux within the plasma generates an axial electric field via Faraday's induction law. Computations by Bernstein of the deuteron ion orbits in the crossed magnetic and electric fields revealed two classes of ion. The first class of ion occupied Larmor orbits which never crossed the magnetic axis. These gyrated in a radial gradient of axial electric field, and obtained substantial heating in a cyclotron process. The second class of ion occupied Larmor orbits which did cross the axis. In addition to the above heating mechanism, these ions also obtained a large relative axial drift. Bernstein found that up to 10% of the deuterons could be accelerated to energies of 600 keV. He concluded that the collisions between these accelerated ions and cold plasma ions would result in a neutron emission which satisfies the observed characteristics.

Extensions to Bernstein's model by Gary and Hohl [74], and Gary [75], examined the effect of an electric field on the pinch axis together with the contraction of current density due to anomalous resistivity, on the ion velocity distribution, initially assumed Maxwellian. Their computations found that, in addition to the cyclotron heating process, ions within a Larmor radius of the axis undergo very efficient axial acceleration.

In addition to the assumption of anomalous resistivity, the above models assumed that the ions were collisionless. If the ion Hall term was less than unity, both cyclotron heating and ion acceleration would be suppressed.

From the Faraday rotation measurements, it is found that anomalous

resistivity does occur during the dense pinch phase. Therefore, the models main assumption is correct, and deuteron acceleration would be expected. Particle acceleration certainly does occur after the observed contraction ends, as evidenced by the Faraday rotation spikes, with the acceleration region probably corresponding to a current contraction zone at a larger axial position.

For ions with classical collisionality, the ion Hall term is of order unity. This would satisfy the models second assumption, and so ion acceleration and heating would be possible. However, the ions are only marginally collisionless. Any increase in ion-ion scattering due to turbulence, as might be expected considering the anomalous electron-ion scattering, would reduce the ion Hall term to a value less than unity. This would be contrary to the models assumption, and would prevent both ion acceleration and heating. As no Faraday rotation spikes are observed during the current contraction period, it is more probable that the latter conclusion is correct. Therefore, during this period it is unlikely that neutron production arises from beam-target interactions.

During the contraction period, the ions do obtain considerable heating by Ohmic dissipation. This is localised to the region of anomalous resistivity. Therefore, it is possible that the first neutron pulse is by thermonuclear fusion. The pulse duration would last longer than the contraction period, as observed experimentally, if the contraction zone moved axially with the region of maximum plasma compression. The position of the neutron emission region would then follow behind the region of highest density, as observed [70].

Once the current contraction period has ended, Faraday rotation spikes are observed. This indicates that particle acceleration does occur, and that at this time neutron production via beam-target interactions are possible. It also indicates that the ions are collisionless. Therefore, the neutrons emitted from the plasma may come from thermonuclear reactions within the current contraction zone at large axial position and from beam-target interactions. Ion acceleration must occur in the plasma volume behind the current contraction zone. This volume is nearer to the centre electrode, which is the position where the plasma has experienced the greatest expansion. One model of ion acceleration which is applicable when the ions are collisionless, and when the plasma has low density, is that due to Potter and Haines [76], described below.

This numerical model simulates the interaction of 20,000 deuterons with the self-consistent electromagnetic field of an electron fluid. Initially, the ions are positioned uniformly within the plasma, and have a Maxwellian velocity distribution. It is found that when the ions are collisionless and the ion Larmor radius is smaller than the pinch radius, if a small axial electric field is applied, the ion distribution function obtains a singular component. Ions crossing the magnetic axis are rapidly accelerated to an energy of approximately 100 keV in a direction away from the centre electrode. The resulting neutron emission is anisotropic, and the neutron energy spectrum is consistent with a source moving with a centre of mass velocity of $1.2 \times 10^{6} ms^{-1}$.

The assumptions of this model are satisfied in the expanded plasma adjacent to the centre electrode. They are also satisfied after the onset of m = 0 instabilities when the plasma column has expanded

significantly. The second neutron pulse peaks after the onset of m = 0 instabilities [69]. Therefore, the second neutron pulse may arise from the effect of deuterons accelerated by the mechanism of Potter and Haines. The Faraday rotation spikes, and anisotropic neutron emission during the first neutron pulse, may also be due to this ion acceleration mechanism. Future studies of the correlation between the current contraction, the current filamentation, and the neutron and deuteron emissions, should lead to a better understanding of the neutron production and ion acceleration mechanisms in the Plasma Focus.

CHAPTER 5 CONCLUSIONS AND SUGGESTIONS FOR FUTURE WORK

5.1 DISCUSSION

The application of the Faraday rotation technique to the study of a Plasma Focus device has provided significant additions to our knowledge of this plasma.

With the highly sensitive purpose built polarimeter used in this study, the internal azimuthal magnetic field structure during the late collapse and early dense pinch phases of the discharge have been determined for the first time using a non-perturbing diagnostic technique. It follows therefore, that the axial current density and electron drift velocity profiles determined from the field distribution have also been resolved for the first time. This has enabled a variety of processes to be examined: current leakage across the insulator, plasma resistivity, Ohmic heating, and plasma collisionality. A new result from this study is the observation of rapid magnetic field diffusion during the dense pinch phase.

It has been possible to calculate an upper limit to the electron density external to the pinch column using the null result obtained in the experiment once the plasma radius is less than the viewed chord impact parameter. This is a new application of the technique.

A new observation made with this method, is that of the Faraday rotation 'spikes' due to current filamentation on axis. The filament

dimensions, associated magnetic field strengths, current density, and electron drift velocity, have been assessed.

The analysis and interpretation of the results from the holographic interferometry and Faraday rotation studies were the subject of chapter 4. Of these two studies, the former is by a standard diagnostic. However, differences between the results of the present study and those of an earlier study by Morgan [46] were obtained. This is probably because of the different initial conditions: bank voltage and filling gas. Since the results of the interferometry must be used in a full analysis of the Faraday rotation data, the Abel inversion technique and error analysis of the interferometric data has been described in detail.

It has previously been difficult to determine the accuracy of Abel inverted data. In the analysis of the Abel inverted electron density profiles, section 4.2.7, three new expressions were given which quantify the relative error in the electron density at the plasma edge, on the axis, and half way between the axis and the edge. In the analysis of the Abel inverted magnetic field profiles, section 4.3.8, a new expression was given for determining the absolute error, from the uncertainty in the Faraday rotation angle alone, at the plasma edge. This is used in conjunction with the errors in the plasma radius and electron density to give the total error. One conclusion was that the main source of error at the plasma edge was the 30 - 40% error in the electron density.

As no other Faraday rotation experiments on Plasma Focus devices have been successful, it has been difficult to compare the results of this study with the results of others. However, the results of Bernard

et al [22] on anomalous resistivity, the results of Neff et al [61] on electron beams, and the co-operative scattering results of Kirk [49], do support the two major new observations made with this technique: rapid field diffusion and current filamentation.

A summary of new results and conclusions from the investigation of the Plasma Focus is given in section 5.2. Following this section are suggestions for improving the experimental technique, and suggestions for future research. However, before the summary is given, the new work described in chapter 1 on polarisation effects and refraction, and in chapter 3 on the polarimeter and polarimetry, will be briefly discussed.

Polarisation Effects and Refraction: A theoretical review of Faraday rotation, birefringence, dichroism, and refraction, was given in chapter 1. A review detailing all of these effects has not been previously published. This review has examined the effects themselves, and, for the first time, the coupling between Faraday rotation and dichroism, and birefringence and dichroism. The coupling between Faraday rotation and birefringence has previously been analysed by others [37,38,39].

The effect of an axial magnetic field on the measurement of the azimuthal magnetic field by the Faraday rotation method, when the probe beam is misaligned from the r-θ plane, has been examined for the first time and shown to be important when $B_z > B_\theta$. It was demonstrated that for a Tokamak plasma, the misalignment angle must be smaller than 0.64 degrees.

In section 1.10, new analytic expressions for quantifying Faraday

rotation, and the effects of birefringence and dichroism, have been derived. These will be of considerable use to experimentalists planning future Faraday rotation studies of laboratory plasmas.

The previously known ray path differential equations which describe the trajectory of a refracted ray through a cylindrical plasma, at an arbitrary angle to the r-θ plane, have been determined using a new extension to the work of Schreiber et al [43]. This extension is the addition of a third dimension to the ray's path in the derivation which is based on Fermat's principle and uses the calculus of variations. This work is detailed in Appendix A.

The Polarimeter and Polarimetry: The polarimeter used in the investigation of the Plasma Focus was of a design which has not previously been used in Faraday rotation studies of laboratory plasmas. However, the differential half-shade method of polarimetry has been used before, as by Dougal et al [77], Falconer et al [78], and by Brown et al [79], on theta-pinch plasmas.

There are two main differences between the polarimeters used in these experiments and the polarimeter described in this thesis. The first is the half-shade angle: it was 2 degrees in this study, while for all these other experiments it was 45 degrees.

The second difference is that, whereas the half-shade angle was fixed in these experiments, the polarimeter used in this study was designed to have a variable half-shade angle, ranging from less than the 2 degrees used to greater than 45 degrees. This versatility was required for two reasons. Firstly, the magnitude of the Faraday rotation angle produced by the Plasma Focus at the wavelength of the

ruby laser probe beam was unknown, although it had been calculated from theory (cf section 1.10). The polarimeter was therefore required to have a high and variable sensitivity, so that it would be possible to detect a significantly smaller rotation than that predicted. The second reason was time resolution. A resolution of the order of 1 ns was needed, which ruled out the use of conventional difference amplifiers in determining the ratio of signal difference to signal sum. For simplicity, an oscilloscope was used. However, as the common mode rejection achievable in measuring signal differences from two oscilloscope traces on a Polaroid oscillograph is low, the observable effect on the detected signals due to Faraday rotation - sensitivity - needed to be as large as was feasible. This was not a constraint in the experiments of references 77,78, and 79.

It is interesting to compare the minimum observable Faraday rotation angles found in these experiments with that found in this study. Dougal et al achieved a resolution of 0.5 degrees, Falconer et al achieved a resolution of 0.017 degrees, and Brown et al obtained a resolution of 0.015 degrees. Both these latter two experiments had a similar resolution to that of this study, which was 0.02 degrees. Although the polarimeter of Dougal et al at first sight appears insensitive, it is useful to compare the minimum resolution with the maximum Faraday rotation observed. The ratio of maximum observed angle to mimimum resolution was 14 in the work of Dougal et al, it was 4.9 in the work of Falconer et al, and in this study, it was 18. It is not known in the work of Brown et al. Therefore, while the best resolutions are similar, the polarimeter used in this experiment was more accurate than those of references 77 and 78.

Two experimental techniques which have now been applied for the first time in Faraday rotation studies of plasmas, are the amplification of Faraday rotation by an orthogonal pair of dielectric beam-splitters, and the use of a single detector in a difference measurement scheme due to the use of different length fibre optics which cause an optical delay.

As the design of the polarimeter is new, the theoretical analysis of its optical properties is original. The predictions made with this theory have been fully confirmed experimentally. In addition, two new criteria were derived for determining the optimum sensitivity of a half-shade polarimeter when limited by polarisation ellipticity and analyser rejection ratio in the presence of strong plasma refraction of the probe beam. In Appendix B, the polarisation change caused by the surface curvature of lenses has been analysed.

5.2 SUMMARY OF NEW RESULTS AND CONCLUSIONS FROM THE PLASMA FOCUS STUDY

A summary of new results and conclusions from the investigation of the Plasma Focus by Faraday rotation polarimetry and holographic interferometry are given below.

Collapse Phase

During the collapse phase, at a Z-axis position 5 mm from the centre electrode, the plasma sheath contracts radially with a velocity of $2.35 \times 10^{5}\ ms^{-1}$ to a minimum plasma radius of 2.35 mm at time t = 0 ns. The axial sheath velocity decreases from the asymptotic value of $1.57 \times 10^{5}\ ms^{-1}$ at t = -25 ns by a factor of approximately 2 at time

t = 0 ns. This is because of the large increase in current leakage across the insulator at this time, due to the large inductive voltage generated by the pinching process. At peak compression, the axial electron density is $4.2 \times 10^{25} m^{-3} \pm 10\%$, which is 300 times the filling density, and the average density is $4.7 \times 10^{24} m^{-3}$. The electron line density drops by a factor 2.35 to $8.0 \times 10^{19} m^{-1}$ from time t = -20 ns to t = 0 ns. The mass per unit length of the plasma column at this latter time is 3.7×10^{-7} Kg m^{-1}. The line density at peak compression represents a focussing efficiency of 32% during the collapse phase only, and 1.4% when the run-down phase is included. The energy utilised in ionising the deuterium filling gas is 1.1% of the initial bank energy. The drop in line density represents an axial flow loss rate of $5.4 \times 10^{27} m^{-1} s^{-1}$.

The maximum Faraday rotation angle observed during this period is approximately 0.5 degrees at t = 0 ns. This is smaller by a factor $\cong$ 10 from that initially expected, and is due to the skin effect. The error in the Faraday rotation angle is approximately 0.05 degrees and arises from plasma irreproducibility and not measurement errors, e.g. the effect of refraction.

The null Faraday rotation result observed when the plasma radius is less than the value of impact parameter, gives a new estimate of the upper limit to the electron density in the volume between the focused plasma and the return current sheath. This estimate is $1.5 \times 10^{22} m^{-3}$, which is a factor 8.4 less than the filling density.

The magnetic field is confined to the plasma skin with a penetration depth of 0.56 mm, which corresponds to approximately one ion Larmor diameter and is approximately half the width of the plasma

sheath at times $t < -15$ ns. This is considerably less than the value of 7 mm computed by Potter [60] using a numerical fluid model. The magnetic field strength at the plasma edge, $\lesssim$ 28 Tesla, is consistent with a 340 $\pm$ 70 kA plasma, which is 70% of the capacitor bank current. The remaining 30% is lost due to insulator leakage. The magnetic field error is typically 40% at the edge, due mostly to 30% edge density errors, and is of magnitude 0.5 Tesla internally. The electron line density and mass per unit length of the plasma occupied by the magnetic field are 1.5×10^{19} m^{-1} and 5.1×10^{-8} Kg m^{-1} respectively.

Estimates of the average temperature using pressure balance gives $\bar{T}$ = 500 eV at peak compression. If sheath momentum is included, an increase in temperature by 143 eV is obtained. These are in reasonable agreement with the scattering results of Kirk [49]. The Bennett temperature of 228 eV is found to be too small, and indicates that the plasma is inertially confined with a plasma beta of approximately 2. The resistivity is 1.1×10^{-7} Ohm-m, which is six times larger than the resistivity of copper, and gives a magnetic field diffusion time of 63 microseconds. It is for this reason that the field is confined to the plasma skin, it cannot diffuse ahead more rapidly then it is convected. The maximum axial current density is $8.8 \times 10^{10} Am^{-2}$ $\pm$ 60%, and the electron drift velocity is $4.7 \times 10^{5} ms^{-1}$ $\pm$ 70%. The ratio of electron drift velocity to thermal velocity is approximately 5%, and is constant within the time period $t = -10$ ns to $t = 0$ ns.

The Joule heating in the sheath from time $t = -10$ ns to $t = 0$ ns, is approximately 32 eV per electron. During this time period, the magnetic work done is 156 eV per particle, and the kinetic energy of the pinching plasma is sufficient to heat the ions by 290 eV. Adiabatic heating by a factor 1.9 during this period is offset by a

reduction in line density by a similar amount.

The calculated plasma inductance peaks at 11.5 nH at time t = 0 ns. This gives an inductively stored energy in the plasma and gun of 8.5% of the initial stored energy. The total amount of energy stored inductively in the discharge circuit at this time is 23% of the initial energy. Numerical simulations of the discharge circuit with a snow-plough model of the plasma, show that the dI/dt singularity observed with the Rogowskii coil occurs at peak compression, in agreement with the results of holographic interferometry where peak compression is observed to occur simultaneously over an axial length $Z \lesssim 10$ mm. The numerical results show that it is possible for the 150 kA difference current between the observed plasma current and the 490 kA capacitor bank current to be lost due to insulator leakage. The value of insulator resistance necessary for this leakage is approximately 0.25 Ohms. Because of the inductance of the electrodes, the voltage across the plasma is approximately twice the voltage which appears across the insulator. If arcing were to occur across the open ends of the electrodes, the plasma current would drop very rapidly. This would result in a poor neutron yield as observed by Bernard et al [64].

During the time period t = -10 ns to t = 0 ns, the electron Hall term $\omega_{ce} \tau_{ei}$ increases from 55 to 563, and the ion Hall term $\omega_{ci} \tau_{ii}$ increases from 0.9 to 9.4 respectively. Therefore, the electrons are collisionless and the ions are marginally collisionless.

Dense Pinch Phase

During the dense pinch phase, the electron line density remains essentially constant at 8.0×10^{19} m^{-1}. This is in disagreement with

Morgan [46]. The average electron density decays approximately exponentially from the value $4.7 \times 10^{24} m^{-3}$ at time t = 0 ns with an e-folding time of 11.8 ns. This was not previously recognised and can be seen in Morgan's data. The plasma expands at a velocity of $\sim 2 \times 10^{5} ms^{-1}$, which is the free expansion velocity of 1.1 keV temperature ions.

During the time period t = 0 ns to +10 ns, the magnetic field diffuses to the axis. The internal magnetic field strength is low and falls from 15 to 3 Tesla during this period. Pressure balance temperatures give a maximum value of 680 eV at time t = +7.5 ns.

The magnetic field diffusion time of 10 ns is consistent with a resistivity of approximately 6.9×10^{-4} Ohm-m, which corresponds to an electron temperature of 1.3 eV. Therefore, the resistivity is anomalous by a factor $\sim$ 6000. This is in good agreement with the results of Bernard et al [22].

The current density profile peaks in the plasma skin, and has similar values to that during the collapse phase. During the time period t = 0 ns to +10 ns, the profile consists of two maxima. One is confined to the plasma skin and expands with the plasma. The other contracts radially. The plasma current flows mainly in the skin, where the resistivity is classical. The region of anomalous resistivity is confined to the plasma core with radius $\simeq$ 2 mm. The contracting current distribution has a maximum current density value of $4.8 \times 10^{10} Am^{-2}$ at time t = +2.5 ns, and falls to a value $7.5 \times 10^{9} Am^{-2}$ at time t = +7.5 ns. This latter value is similar to the peak current density at time t = +10 ns. The total current flowing within the core is 125 kA, i.e. 37% of I_p, at time t = +2.5 ns, and decreases to

43 kA, i.e. 13% of I_p, at time t = +7.5 ns. At time t = +10 ns, the current is 36 kA. The maximum drift velocity falls approximately exponentially from $4.7 \times 10^5 ms^{-1}$ at time t = 0 ns, by a factor 56 to $8.4 \times 10^3 ms^{-1} \pm 50\%$ at time t = +7.5 ns. The e-folding time is approximately 1.74 ns, which is larger than the anomalous electron-ion momentum transfer collision time by a factor 10^4. The electron drift velocities in the plasma skin are similar to those during the collapse phase. Joule heating in the region with anomalous resistivity is $\gtrsim$ 1 keV per particle in the time period t = 0 ns to +10 ns. It is insignificant in the plasma skin.

The electron Hall term in the plasma skin is of order 100 and the ion Hall term of order unity, similar to the values found during the collapse phase. The electron Hall term within the turbulent core $<<1$, and the ion Hall term, if the ion self collision time is anomalous, is also $<<1$. Therefore the plasma skin is collisionless, while the plasma core is collisional. Deuteron acceleration due to the mechanism of Bernstein [73] is suppressed at this time. Later, once the plasma has expanded, deuteron acceleration due to the mechanism of Potter et al [76] may occur and could explain the current filamentation.

Current Filaments

The Faraday rotation 'spikes' observed corresponded to Faraday rotation angles of 0.95 degrees. The measurements were bandwidth limited. The 'spikes' were observed to occur in the time period t = +10 ns to t = +15 ns. The duration of the 'spikes' was 2.5 ns. These results are interpreted as being due to axial current filamentation. These spikes may be similar to the observations of short lived electron beams by Neff et al [61], and have a strong time

correlation to the large enhancements in scattered light as observed by Kirk [49]. The duration of the current filaments is $\leq$ 2.5 ns. The associated magnetic field strengths are $\geq$ 44 Tesla and $\geq$ 57 Tesla, at radii 190 microns and 250 microns, at times t = +10 ns and +15 ns respectively. These radius values are similar to the resolution of the Abel inversion space mesh. The current density $\geq 3.7 \times 10^{11} Am^{-2}$ at both times, and the drift velocities $\geq 3.3 \times 10^{5} ms^{-1}$ and $\geq 6.9 \times 10^{5} ms^{-1}$ at times t = +10 and +15 ns respectively. These velocities correspond to drift parameters of $\geq$ 2.5% and $\geq$ 5.3% respectively. If only $\sim$ 4% of the available electrons carried the current, the drift parameter would be of order unity. The half current density maximum occurs at radii 167 microns and 217 microns respectively. The total currents carried by the filaments are 42 kA and 72 kA, i.e. 12% and 21% of the plasma current, at times t = +10 ns and +15 ns respectively. These currents are not significantly different to the current carried within the inner turbulent core at time t = +10 ns, and indicate that they may be related effects.

If the drift parameter is assumed to be of order unity, as indicated by the results of Kirk [49], it can be estimated that the filament radius would be approximately 50 microns, and the associated current density and magnetic field would be $\sim 10^{13} Am^{-2}$ and $\sim$ 250 Tesla respectively.

The electron line density of the filament is $5.5 \times 10^{17} m^{-1}$. Joule heating with classical resistivity gives 25 eV per particle for the lifetime of the filament. The heating will be greatly increased if the resistivity is anomalous. The temperature of the filament, estimated using pressure balance with the self-magnetic field, is 340 eV and 1.2 keV at times t = +10 ns and t = +15 ns respectively. Joule heating

to temperatures greater than these would cause the filament to break-up, and may be the reason for their short lifetime.

5.3 SUGGESTIONS FOR FUTURE IMPROVEMENTS

The results obtained from the Faraday rotation study were subject to a variety of limitations in the experimental method. These are discussed below, together with suggestions for future improvements.

a) The Faraday rotation measurements were built-up on a shot to shot basis. Similarly, electron density measurements were obtained from holographic interferograms of separate discharges. Because these measurements were not made simultaneously, the magnetic field measurements were subject to errors due to shot to shot plasma irreproducibility. The measurement technique would be considerably improved if both measurements were made simultaneously, with the polarimeter redesigned to view several different plasma chords. Interferometry of the plasma Z-plane being studied could be done continuously by using a streak-camera and Mach-Zehnder interferometer, as by Hirano et al [80]. The polarimeter image plane would easily accomodate several fibre optic pairs, and the light transmitted by the first beam-splitter in the polarimeter could be used as the scene beam in the interferometer.

b) The detection system of the polarimeter proved to have insufficient bandwidth to accurately resolve the current filamentation. Assuming a sub-nanosecond lifetime of the filament, similar to the 0.4 ns duration of the electron beam observed by Neff et al [61], a

bandwidth of 2 GHz would be required. This would also reduce any effects due to plasma motion.

There are two methods by which this bandwidth could be achieved. The first is to use a streak camera at the ends of equal length fibres. This would be capable of $\sim$ 100 picosecond resolution. The second method would be to use a fast photodiode, several are capable of 100 ps resolution, together with an analogue to digital converter. Whereas the best Tektronix waveform digitizer (7912AD) can sample at slightly better than 1 GHz, GaAs ADC's can sample at 8 GHz [81].

c) In the analysis of the Faraday rotation data, the main assumption made was that of cylindrical symmetry. On the basis of the plasma symmetry revealed by holographic interferometry, this may appear a reasonable assumption. However, this symmetry may not apply to the current density distribution, which may even not be continuous. Current filamentation may exist. In order to examine this aspect, Faraday rotation polarimetry based on the 'freeze' technique [9] should be attempted with simultaneous interferometry. Very high spatial resolution, $\sim$ 50 microns, can be achieved with common photographic materials. Also, high temporal resolution, $\sim$0.5 ns, can be achieved by using a single mode locked pulse from a suitable laser. These measurements, which would examine a full cross-section of the plasma, should be made simultaneously at a variety of θ positions around the plasma. A full tomographical analysis [82,83] of the data would then reveal filamentation on the dimensional scale of the measurement resolution.

5.4 SUGGESTIONS FOR FUTURE RESEARCH

In addition to the improvements discussed in the previous section, the following research topics are suggested for future investigation.

a) The existence of a self generated axial magnetic field in the Plasma Focus has long been suspected from indirect experimental observations [45]. It would therefore be of considerable importance to determine whether or not it does in fact exist. The Faraday rotation method would be ideal for this measurement. It would not be necessary for the field to be examined in detail, although this would be very useful. A demonstrable effect would be sufficient to establish the field's existence.

There are two ways in which this measurement could be achieved with the Culham Plasma Focus. The first would be to replace the solid centre electrode with a hollow electrode, and provide suitable entrance and exit optical windows. This would entail considerable re-engineering of the machine. An optical probe beam directed through the plasma parallel to the axis would then be used in a Faraday rotation experiment. The polarimeter described in this thesis would be suitable, although care would have to be taken as strong refraction, and perhaps birefingence, would occur because of the long optical path through the plasma in a direction perpendicular to large electron density gradients.

The second method, and perhaps the more practical, has already been discussed in sections 1.6.1 and 1.6.2 where the effect of an axial magnetic field on a probe beam which propagates through a cylindrical

plasma at an angle to the r - θ plane was described. Also discussed was the experimental method by which the effects of the azimuthal and axial fields could be separated. In the present context, the experiment would be to repeat the Faraday rotation experiment reported in this thesis simultaneously with an identical experiment which used a probe beam at an angle to the r - θ plane. The difference in the Faraday rotation angles observed would be due to an axial magnetic field alone. From section 1.10.1, it can be estimated that the rotation angles due to axial and azimuthal fields of equal magnitude would be similar if the probe beam were at an angle of 24 degrees from the r - θ plane. Therefore, it would be reasonable to expect a demonstrable effect if the experiment were conducted at an angle $\gtrsim$ 24 degrees.

b) It was demonstrated that the results obtained from the Faraday rotation 'spikes' observed, were affected by the measurement bandwidth limitation, the spatial resolution of the plasma chord viewed by the polarimeter, and the Abel inversion space mesh dimension. Assuming sufficient improvements in the experimental technique which avoid these problems, the following topics for investigation are suggested:

1) Using several fibre optic pairs, the spatial profile, at a constant axial position, of the Faraday rotation occuring with current filamentation would be observed. This would provide sufficient data to greatly improve the accuracy of the results discussed in this thesis. This experiment would also provide more accurate details of the current constriction process. The axial behaviour of both these phenomena should also be examined.

2) Using several fibre optic pairs aligned to view several axial

points at a constant impact parameter, the axial time dependence of the filamentation would be directly observable. Correlation with the time dependence of the current constriction to the axis would indicate whether or not these effects were coupled. Studies of the time correlation between the hard X-ray, neutron, and deuteron emission from the plasma, may shed new light on the mechanisms behind deuteron acceleration and neutron production.

APPENDIX A THE RAY PATH DERIVATIVES OF A REFRACTED RAY

The ray path derivatives which describe the trajectory of a ray through a refracting cylindrical plasma, can be derived from Fermat's principle using the calculus of variations. The problem is to determine the path L which minimises the optical path length, expressed mathematically as solving the extremum [34]

$$\delta \int_L \mu d\ell = 0 \qquad \text{A1}$$

Assuming cylindrical geometry, with the refractive index a function of radius only, i.e. $\mu=\mu(r)$, then with the path increment dl expressed in cylindrical co-ordinates

$$d\ell = (1 + r^2\theta_r^2 + Z_r^2)^{\frac{1}{2}} dr \qquad \text{A2}$$

where $\theta_r = d\theta/dr$, and $Z_r = dZ/dr$ are the ray path derivatives, the problem is now expressed as

$$\delta \int_L I dr = 0 \qquad \text{A3}$$

where the integrand I is

$$I = \mu(r)(1 + r^2\theta_r^2 + Z_r^2)^{\frac{1}{2}} \qquad \text{A4}$$

This integral has a minimum value when the path L satisfies the Euler-Lagrange equations [34]

$$\frac{d}{dr}\left(\frac{\partial I}{\partial \theta_r}\right) - \frac{\partial I}{\partial \theta} = 0 \qquad \text{A5}$$

$$\frac{d}{dr}\left(\frac{\partial I}{\partial Z_r}\right) - \frac{\partial I}{\partial Z} = 0 \qquad \text{A6}$$

Substituting the integrand I into equation A5 gives the result

$$\theta_r r^2 \mu (1 + r^2\theta_r^2 + Z_r^2)^{-\frac{1}{2}} = K_\theta = \text{constant} \qquad \text{A7}$$

Substituting the integrand into equation A6 gives the result

$$Z_r \mu (1 + r^2\theta_r^2 + Z_r^2)^{-\frac{1}{2}} = K_z = \text{constant} \qquad \text{A8}$$

Dividing equation A8 by A7 gives the relation between the ray path derivatives Z_r and θ_r, namely

$$Z_r = (K_z/K_\theta) r^2 \theta_r \qquad \text{A9}$$

Substituting this equation into equation A7 gives

$$\theta_r = \pm \frac{1}{r} K_\theta (\mu^2 r^2 - r^2 K_z^2 - K_\theta^2)^{-\frac{1}{2}} \qquad \text{A10}$$

and so

$$Z_r = \pm r K_z (\mu^2 r^2 - r^2 K_z^2 - K_\theta^2)^{-\frac{1}{2}} \qquad \text{A11}$$

These latter two equations are the ray path derivatives. The remaining part of the problem involves determining the constants K_θ and K_z.

As equations A10 and A11 are valid for all r, θ, Z, then by determining θ_r or Z_r explicitly outside the plasma, the constants K_θ and K_z can be derived. For a ray propagating at an angle Ω from the r-θ plane, in an orthogonal plane a distance h from the axis, it can be shown that the Z-position of a point on the ray's trajectory is related to the radius at the point by

$$Z^2 = \tan^2 \Omega \, (r^2 - h^2) \qquad \text{A12}$$

Differentiating with respect to r, gives

$$Z_r = \pm r \tan\Omega (r^2 - h^2)^{-\frac{1}{2}} \qquad \text{A13}$$

Comparison with equation A11 with $\mu(r) = 1$, gives on equating the coefficients

$$K_z = \sin \Omega \qquad \text{A14}$$

$$K_\theta = h \cos \Omega \qquad \text{A15}$$

Therefore, the equations for the ray path derivatives are

$$\theta_r = \pm \frac{1}{r} h \cos \Omega(\mu^2 r^2 - r^2 \sin^2\Omega - h^2 \cos^2\Omega)^{-\frac{1}{2}} \qquad \text{A16}$$

$$Z_r = \pm r \sin \Omega(\mu^2 r^2 - r^2 \sin^2\Omega - h^2 \cos^2\Omega)^{-\frac{1}{2}} \qquad \text{A17}$$

APPENDIX B LENS INDUCED POLARISATION CHANGE

Plane polarised light incident upon a lens will, in general, emerge with a different plane of polarisation. The change in polarisation is due to the variation in the reflection properties of the curved surfaces. The problem is analysed by applying Fresnel's reflection laws [34].

Consider a ray incident upon a dielectric. If it is plane polarised at an angle ϕ from the reflection plane, i.e. the p-plane, the transmitted ray will have a plane of polarisation at an angle θ_1, given by

$$\theta_1 = \tan^{-1}\{\alpha_1 \tan\phi\} \qquad \text{B1}$$

where $\alpha_1 = t_s/t_p$ and t_s and t_p are the amplitude transmittances for the s and p polarisations respectively. On transmission through a second surface, the plane of polarisation changes to θ_2, given by

$$\theta_2 = \tan^{-1}\{\alpha_1\alpha_2 \tan\phi\} \qquad \text{B2}$$

where α_2 is the transmittance ratio of the second surface. The ratio t_s/t_p, from Fresnel's laws, is

$$t_s/t_p = \alpha = \cos(\theta_i - \theta_r) \qquad \text{B3}$$

where θ_i is the angle of incidence, and θ_r is the angle of refraction. Therefore, the change in the plane of polarisation, ψ, is the difference between the angles θ_2 and ϕ, i.e.

$$\psi = \tan^{-1}\{\alpha_1\alpha_2 \tan\phi\} - \phi \qquad \text{B4}$$

From this expression, the polarisation change produced by a lens can be determined.

Consider the trajectory of a ray from a point source, O, imaged by a lens (see figure B1). The ray is incident upon the first surface at a height h_1 above the optic axis, a distance U from the source. The incidence angle is given by

$$\theta_{i1} = \tan^{-1} \frac{h_1}{U} + \sin^{-1} \frac{h_1}{R_1} \qquad \text{B5}$$

where R_1 is the radius of curvature of the first surface. The angle of refraction is given by Snell's law [34], and on substitution into equation B3, gives

$$\alpha_1 = \cos(\theta_{i1} - \sin^{-1}[\frac{1}{\mu} \sin \theta_{i1}]) \qquad \text{B6}$$

where μ is the refractive index.

Similarly, if I is the image position, an axial distance V from the point, a height h_2 above the axis, where the ray emerges from the lens, the angle of refraction is

$$\theta_{r2} = \tan^{-1} \frac{h_2}{V} + \sin^{-1} \frac{h_2}{R_2} \qquad \text{B7}$$

where R_2 is the radius of curvature of the second lens surface. From equation B3

$$\alpha_2 = \cos(\theta_{r2} - \sin^{-1}[\frac{1}{\mu} \sin\theta_{r2}]) \qquad \text{B8}$$

which, together with equation B6, gives the product $\alpha_1\alpha_2$.

The maximum change in polarisation angle occurs when the initial plane of polarisation is at an angle ϕ_m, given by

$$\phi_m = \cos^{-1}\left\{ \frac{\alpha_1\alpha_2(1-\alpha_1\alpha_2)}{1 - \alpha_1^2\,\alpha_2^2} \right\} \qquad \text{B9}$$

This angle is approximately 45 degrees, and is determined from equation B4 by differentiating with respect to ϕ, and setting to zero.

The maximum change in polarisation angle, ψ_m, is then given by

$$\psi_m = \tan^{-1}(\alpha_1\alpha_2 \tan \phi_m) - \phi_m \qquad \text{B10}$$

Example

Consider the maximum polarisation change caused by a plano-convex lens of focal length +650 mm. This lens is identical to the first imaging lens within the polarimeter described in chapter 3. If the point source (plasma) is at a distance U = 1 m, the resulting image distance V ≅ 2 m. Assuming a ray incident upon the plane surface of the lens at a height h_1 = 25 mm above the axis, the angle of incidence is 1.43 degrees. This results in a transmittance ratio of α_1 = 0.9999653. Assuming also that the ray emerges at a height h_2 = 25 mm, i.e. $h_1 = h_2$, the angle of refraction at the second convex surface is 5.13 degrees. This results in a transmittance ratio of α_2 = 0.9995537. Therefore, $\alpha_1\alpha_2$ = 0.999519, and from equations B9 and B10, the maximum polarisation change is -0.014 degrees.

The magnitude of the polarisation change actually caused by the first imaging lens in the polarimeter, was smaller than the above angle. This was because the initial plane of polarisation was approximately parallel to the p-plane of the lens, whatever the value of plasma impact parameter, or refraction angle. The effect is equally small for all the lenses used in the polarimeter, and as a result, the effect of lens induced polarisation change on the measurement of Faraday rotation can be neglected.

Generally, lens induced polarisation changes are important when the lens curvature is large. Lenses of this nature are often encountered in expansion telescopes. In the diagnosis of laser produced plasmas

where the 'freeze' method of polarimetery [9] is often used, because of strong refraction, the whole aperture of imaging optics must be used to form an image of the plasma. Therefore, the full effect of lens induced polarisation change can occur, and may be important when short focal length lenses are used.

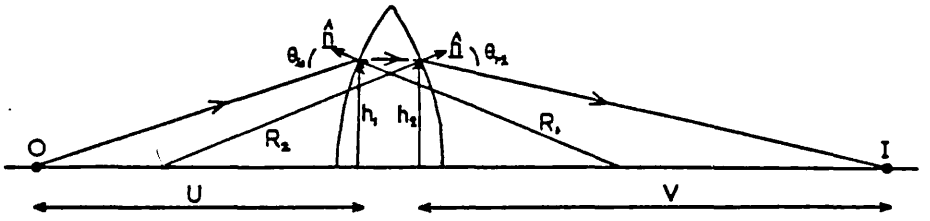

Figure B1

The trajectory of a ray through a lens.

REFERENCES

1. Evans D.E., Carolan P.G. : Phys. Rev. Lett. 25(1970) 1605

2. Forrest M.J., Carolan P.G., Peacock N.J. : Nature 271(1978) 718

3. Alladio F., Martone M. : Phys. Lett. 60A(1977) 39

4. McCormick M., Kick M., Olivain J. : Proc. 8th. European Conf. on Controlled Fusion and Plasma Physics, Prague, 1(1977) 140

5. West W.P. : Proc. 4th. APS Topical Conf. on High Temperature Plasma Diagnostics, Boston, 1(1982) paper F2

6. Peacock N.J. : Proc. Course Int. School of Plasma Physics, Varenna, (1978) 367

7. Equipe TFR : Nuclear Fusion 18(1978) 647

8. Stamper J.A., Ripin B.H. : Phys. Rev. Lett. 34(1975) 138

9. Raven A., Willi O., Rumsby P.T. : Rutherford Laboratory Report RL-78-036 (1978)

10. Kunz W., Equipe TFR. : Nuclear Fusion 18(1978) 1729

11. Soltwisch H., Equipe TFR. : Infrared Phys. 21(1981) 287

12. Hutchinson D.P., Ma C.H., Staats P.A., Vander Sluis K.L. Nuclear Fusion 21(1981) 1535

13. Mather J.W. : Phys. Fluids 8(1965) 366

14. Mather J.W. : Methods of Experimental Physics 9B(1971) 178

15. Peacock N.J., Speer R.J., Hobby M.J. : J. Phys. B 2(1969) 798

16. Kirk R.E., Muir D.G., Forrest M.J., Peacock N.J. : Proc. Int. Conf. on Plasma Physics, Goteborg(1982) 329

17. Notkin G.E., Filippov N.V., Shcheglov D.A. : Proc. 5th. European Conf. on Controlled Fusion and Plasma Physics, Grenoble, 1(1972) 69

18. Filippov N.V., Ivanov V.D., Moiseeva M.P., Stepanenko M.M., Sukhareva M.K. : Plasma Physics and Controlled Nuclear Fusion Research, Nuclear Fusion Suppl. (1975) 163, IAEA-CN-33/E6-4.

19. Kiagawa Y., Yamada Y., Tsuda I., Yokoyama M., Yamanaka C. : Phys. Rev. Lett. 43(1979) 1875

20. Peacock N.J., Norton B.A. : Phys. Rev. A 11(1975) 2142

21. Bernard A., Coudeville A., Garconnet J.P., Jolas A., De Mascureau J., Nazet C. : Proc. 6th. Int Conf. on Plasma Physics and Controlled Nuclear Fusion Research, Berchtesgaden, III(1976) 471

22. Bernard A., Coudeville A., Garconnet J.P., Jolas A., De Mascureau J., Nazet C. : Proc. 8th. European Conf. on Controlled Fusion and Plasma Physics, Prague, I(1977) 64

23. Dodel G., Kunz W. : Infrared Phys. 18(1978) 773

24. Kunz W., Dodel G. : Plasma Phys. 20(1978) 171

25. Falconer I.S., Ramsden S.A. : J. Appl. Phys. 39(1968) 3449

26. Culham Laboratory Progress Report CLM-PR23 (1981) B18

27. Clarke D., Grainger J.F. : 'Polarized Light and Optical Measurement', Int. Series of Monographs, Vol.35, Pergamon Press (1971).

28. Heald M.A., Wharton C.B. : 'Plasma Diagnostics with Microwaves', J.Wiley, New York (1965).

29. Spitzer L. : 'Physics of Fully Ionized Gases', Interscience Publishers, New York (1957).

30. Bekefi G. : 'Radiation Processes in Plasmas', J.Wiley, New York (1966).

31. Ginzburg V.L. : 'The Propagation of Electromagnetic Waves in Plasmas', Pergamon Press, Oxford (1964).

32. Muir D.G., Carolan P.G. : Proc. 14th. Int. Conf. on Phenomena in Ionized Gases, Grenoble, Vol.I Contributed Papers, Journal de Physique, Colloque 7 (1979) C7-833

33. Evans D.E. : 'Optical Methods of Plasma Diagnostics', Culham Plasma Physics Summer School (1974).

34. Born M., Wolf E. : 'Principles of Optics', Pergamon Press, Oxford, Third Edition (1964).

35. Lehmberg R.H., Stamper J.A. : NRL Memorandum Report 3703 (1978)

36. Heald M.A. : Plasma Phys. 6(1964) 617

37. De Marco F., Segre S.E. : Plasma Phys. 14(1972) 245

38. Craig A.D. : Plasma Phys. 18(1976) 777

39. Segre S.E. : Plasma Phys. 20(1978) 295

40. Shurcliff W.A. : 'Polarized Light', Harvard University Press 1962

41. Ramachandran G.N., Ramaseshan S. : 'Crystal Optics', Encyclopedia of Physics, Vol.25/1, Springer, Berlin (1961).

42. Wort D.J.H. : Culham Report CLM-R27 (1963)

43. Schreiber P.W., Hunter A.M. II, and Smith D.R. Jr. : Plasma Physics, 15(1973) 635

44. Heald M.A. : Culham Report CLM-R34 (1964)

45. Sestero A., Robouch B.V., Podda S. : Plasma Phys. 22(1980) 1039

46. Morgan P.D. : Ph.D. Thesis, University of London (1974)

47. Mather J.W., Bottoms P.J. : Phys. Fluids 11(1968) 611

48. Evans D.E., Katzenstein J. : Rep. Prog. Phys. 32(1969) 207

49. Kirk R.E. : Ph.D. Thesis (to be published), University of London 1983.

50. Jahoda F.C., Siemon R.E. : Los Alamos Report LA-5058-MS (1972)

51. Faw R.E., Dullforce T.A. : Culham Report CLM-RR/S2/19 (1977)

52. Collier R.J., Burckhardt C.B., and Lin L.H. : 'Optical Holography' Academic Press, New York (1971).

53. Jarboe T.R. : J. Appl. Phys. 48(1977) 557

54. Veron D. : Report EUR-CEA-FC-980 (1978)

55. Bockasten K. : J. Opt. Soc. Am. 51(1961) 943

56. Butler T.D., Henins I., Jahoda F.C., Marshall J., Morse R.L. : Phys. Fluids 12(1969) 1904

57. Gourlan C., Kroegler H., Maisonnier Ch., Rager J.P., Robouch B.V., Gentilini A. : Proc. 7th. Int. Conf. on Plasma Physics and Controlled Nuclear Fusion Research, Innsbruck, II(1978) 123

58. Bernard A., Garconnet J.P., Jolas A., Le Breton J.P., De Masureau J. : Proc. 7th. Int. Conf. on Plasma Physics and Controlled Nuclear Fusion Research, Innsbruck, II(1978) 159

59. Gorenflo R. : Report IPP/6/19 (1964)

60. Potter D.E. : Phys. Fluids 14(1971) 1911

61. Neff W., Krompholz H., Ruhl F., Schonbach K., Herziger G. : Phys. Lett. 79A(1980) 165

62. Boyd T.J.M., Sanderson J.J. : 'Plasma Dynamics', Thomas Nelson and Sons Ltd., London (1969).

63. Lorrain P., Corson D.R. : 'Electromagnetic Fields and Waves', W.H. Freeman and Company, San Francisco (1962), 2nd. Edition.

64. Bernard A., Coudeville A., Watteau J.P. : Phys. Lett. 33A(1970)477

65. Braginskii S.I. : Reviews of Plasma Physics, Vol 1, Consultants Bureau, New York, 1965.

66. Gentilini A., Maisonnier Ch., Rager J.P. : Report CNEN 79.7/p (1979)

67. Decker G., Herold H., Kaeppeler H.J., Kies W., Maysenholder W., Nahrath B., Oppenlander T., Pross G., Ruckle B., Sauerbrunn A., Schilling P., Schmidt H., Shakhatre M., Trunk M. : Proc. 7th. Int. Conf. on Controlled Nuclear Fusion Research, Innsbruck, II(1978) 135 part A.

68. Morgan P.D., Peacock N.J., Cloth P., Conrads H., Maisonnier Ch., Pecorell F., Rager J.P., Samuelli M. : Proc. 6th. Eur. Conf. on Controlled Fusion and Plasma Physics, Moscow, vol 1(1973) 359

69. Herold H., Bertalot R., Deutsch R., Grauf W., Jager U., Kaeppeler H.J., Lepper F., Oppenlander T., Schmidt H., Schmidt R., Schwarz J., Schworer K., Shakhatre M., Hayd A., Maurer M., and Meinke P. : Report IPF-82-12 (1982).

70. Schmidt H. : Atomkernenergie Kerntechnik 36(1980) 161

71. Gullickson R.L., Sahlin H.L. : J. Appl. Phys. 49(1978) 1099

72. Bertalot L., Deutsch R., Herold H., Jager U., Mozer A., Sadowski M., Schmidt H. : Report IPF-81-9 (1981)

73. Bernstein M.J. : Phys. Fluids 13(1970) 2858

74. Gary S.P., Hohl F. : Phys. Fluids 16(1973) 997

75. Gary S.P. : Phys. Fluids 17(1974) 2135

76. Potter D.E., Haines M.G. : Proc. 4th. Int. Conf. on Plasma Physics and Controlled Nuclear Fusion Research, Madison, vol I(1971) 611

77. Dougal A.A., Craig J.P., Gribble R.F. : Phys. Rev. Lett. 13(1964) 156

78. Falconer I.S., Benesch R., Ramsden S.A. : Phys. Lett. 14(1965) 38

79. Brown R., Deuchars W.M., Illingworth R., Irving J. : J. Phys. D 10(1977) 1575

80. Hirano K., Schimoda K., Emori S. : Rev. Sci. Inst. 50(1976) 1236

81. Waller L. : Electronics, March 1979, p43

82. Swindell W., Barrett H.H. : Physics Today, December 1977, p32

83. Schivell J. : IEEE Trans. Plasma Sci. PS-8(1980) 226

PUBLICATIONS

JOURNAL DE PHYSIQUE Colloque C7, supplément au n°7, Tome 40, Juillet 1979, page C7- 833

FARADAY ROTATION APPLIED TO A REVERSE FIELD PINCH

D.G. Muir* and P.G. Carolan.

Culham Laboratory, Abingdon, Oxon, OX14 3DB, UK (EURATOM/UKAEA Fusion Association).

INTRODUCTION

There are now a variety of techniques for measuring internal magnetic fields in tokamaks, that have been successfully developed, e.g. light scattering,[1][2] Zeeman splitting[3] and Faraday rotation[4]. The poloidal field, B_θ, was the quantity of interest since its distribution determines the plasma equilibrium and stability properties (the toroidal field distribution, $B_z(r)$ differs only slightly from that produced externally). In reversed field pinch plasmas, both the $B_z(r)$ and $B_\theta(r)$ field distributions are mainly generated internally and play and equal role in the plasma stability. Therefore, both B_θ and B_z are the quantities of interest.

The Faraday rotation method give a continuous integral measurement of the internal poloidal magnetic field alone when the beam is in the vertical plane, but otherwise gives a continuous integral measurement of both internal magnetic fields. The integral is over a straight path and the measurement of the Faraday rotation angle is done by simple polarimetry external to the machine. It is proposed to use the Faraday rotation technique, employing an HCN/DCN laser (λ = 337/190 µm) to measure both distributions in the HBTXIA plasma.

The HBTXIA machine is a reversed field pinch (RFP) under construction at Culham. It has a major radius of 0.8m and minor radius of 0.26m. The expected plasma parameters are: $T_e \sim 50$-150eV; $n_e \sim 1.5\times10^{20}$-$4\times10^{20}$ m^{-3}; current ~ 400kA; $\langle B \rangle \sim 0.5$T.

THE CHOICE OF WAVELENGTH AND SOURCE

The choice of a suitable wavelength for Faraday rotation is governed essentially by considering what sources are available, and whether this source has sufficient power for an accurate measurement of the Faraday rotation angle obtained at the source wavelength. Other important effects which have to be considered are refraction, loss of transmitted power due to turbulence[5] and degradation of the beam polarisation due to the perpendicular component of magnetic field[6][7].

We have found that because of the low toroidal magnetic field in RFP plasmas, the depolarisation effect is negligible. This is in contrast to tokamak plasmas where because of the large toroidal field, the depolarisation effect becomes important when the Faraday rotation angle exceeds some 10°. The rotation angle, ψ, is described by the relation:

$$\psi \propto \lambda^2 \int_L n_e \vec{B}.d\vec{l}$$

where λ is the laser wavelength; n_e and $\vec{B}$ are the electron density and magnetic field respectively; and L is the path length. This relation is not valid when depolarisation is present.

If the plasma can be considered to be a horizontal cylinder, of radius a, with cylindrical symmetry, then for a beam of wavelength λ propagating through the plasma with an impact parameter, h, and at an angle, Ω, from the vertical plane, then the Faraday rotation angle, ψ, is found to be given by:

$$\psi = 2A\lambda^2\left\{\int_h^a n_e B_\theta \frac{h\,dr}{\sqrt{r^2-h^2}} + \tan\Omega \int_h^a n_e B_z \frac{r\,dr}{\sqrt{r^2-h^2}}\right\}$$

$$= \psi_\theta + \psi_z \qquad (1)$$

where B_θ and B_z are the poloidal and longitudinal magnetic fields respectively; $A = 2.62 \times 10^{-13}$ rad $tesla^{-1}$; and ψ_θ and ψ_z are the rotation angles due to the individual magnetic fields B_θ and B_z respectively, and are given by the integral incorporating the appropriate magnetic field.

The Faraday rotation angle, therefore scales as λ^2, as does refraction. Numerical calculations of the expected angle of rotation, and refractive deviation for various source wavelengths are given in Table I. The axial electron density used was 1.5×10^{20} m^{-3} and the plasma current 400kA. The ratio of axial to critical electron density, n_e/n_c, is a measure of transmission of the beam. A ratio greater than 0.2 could indicate very high attenuation due to turbulence and a ratio less than 0.02 would be desirable[5]. From Table I the wavelength giving rise to the largest Faraday rotation angle with an n_e/n_c ratio of less than 0.02 and with a tolerable beam deflection is 337µm produced by an HCN laser. At this wavelength the rotation expected is typically 10° with a beam deviation less than 5mm. The minimum measurable angle at this wavelength determined by detector and amplifier noise is about 0.1° verified experimentally at Fontenay-aux-Roses[4]. At a higher axial electron density of 4×10^{20} m^{-3} the DCN laser wavelength of 190µm would also give a Faraday rotation angle of typically 10° and a beam deviation less than 5mm. The source producing rad-

iation at these wavelengths also has sufficient power for a multichannel Faraday rotation diagnostic.

DATA INVERSION

From equation (1) the Faraday rotation angle, ψ, for a beam propagating at an angle, Ω, from the vertical plane, is the sum of two rotations, ψ_θ and ψ_z, arising from the two magnetic fields B_θ and B_z. The poloidal field rotation, ψ_θ, can be measured alone when $\Omega=0$. The toroidal field rotation, ψ_z, can also be measured when $\Omega \neq 0$, but this requires that the appropriate ψ_θ be known. Therefore, for measuring the two rotation angles, we must have two beams propagating through the plasma simultaneously, at the same impact parameter, and one beam having $\Omega=0$. It is by this method that the internal magnetic fields of HBTXIA will be measured. To obtain the field profiles the diagnostic must be a multichannel one. The pitch profile can be determined without any knowledge of the electron density, since by Abel inversion of ψ_θ and ψ_z:

$$2A\lambda^2 \tan\Omega\, n_e B_z = -\frac{1}{\pi}\int_r^a \left(\frac{d\psi_z}{dh}\right)\frac{dh}{\sqrt{h^2-r^2}}$$

$$\frac{2A\lambda^2 n_e B_\theta}{r} = -\frac{1}{\pi}\int_r^a \left\{\frac{d}{dh}\left(\frac{\psi_\theta}{h}\right)\right\}\frac{dh}{\sqrt{h^2-r^2}}$$

and from the definition of the pitch, $P = rB_z/B_\theta$ and the above equations:

$$P = \frac{\int_r^a \left(\frac{d\psi_z}{dh}\right)\frac{dh}{\sqrt{h^2-r^2}}}{\tan\Omega \int_r^a \left\{\frac{d}{dh}\left(\frac{\psi_\theta}{h}\right)\right\}\frac{dh}{\sqrt{h^2-r^2}}}$$

which does not involve the electron density. The safety factor profile is also given since $q = P/R$ where R is the plasma major radius.

CONCLUSIONS

We have concluded that a Faraday rotation diagnostic using an HCN/DCN laser is a practical diagnostic method for measuring the internal magnetic fields of a RFP and in particular the HBTXIA plasma. With the wavelengths available with this laser system, 337μm or 190μm, and the expected range of electron density (1.5×10^{20} - 4×10^{20} m^{-3}), Faraday rotation angles of typically 10^o will be observed with negligible refraction, depolarisation, or loss of transmitted power.

REFERENCES

[1] FORREST M J, CAROLAN P G, PEACOCK N J: Nature 271 5647 (1978) 718

[2] ALLADIO F, MARTONE M: Phys Lett, 60A, 1 (1977) 39

[3] McCORMICK K, KIRK M, OLIVAIN J: Proc 8th Eur Conf on Controlled Fusion and Plasma Physics, Prague, 1 (1977) 140

[4] KUNZ W: Equipe TFR, Nuc Fus, 18, 12 (1978) 1729

[5] WORT D J H: Plasma Phys, 8 (1966) 79

[6] CRAIG AD: Plasma Phys., 18 (1976) 777

[7] SEGRE S E: Plasma Phys., 20 (1978) 295

TABLE I

SOURCE OF WAVELENGTHS, ROTATION AND DEFLECTION ANGLE FOR HBTXIA

SOURCE		n_e/n_c	ψ	α
1mm	μ-wave	0.13	88^o	20^o
CH_3F	496μm	0.032	22^o	5^o
HCN	337μm	0.015	10^o	2^o
DCN	190μm	0.005	3^o	1^o
Methanol	118μ	0.002	1^o	0.3^o
CO_2	10.6μm	5×10^{-5}	0.01^o	0.002^o

$n_e = 1.5 \times 10^{20} m^{-3}$; ψ = typical Faraday rotation angle; α = maximum deflection angle.

*Attached from Royal Holloway College, University of London

Proc. Int. Conf. on Plasma Physics, Goteborg(1982) 329

NEW EVIDENCE FOR NON-THERMAL FLUCTUATIONS IN THE PLASMA FOCUS USING IMPROVED LIGHT SCATTERING TECHNIQUES

R E Kirk*, D G Muir*, M J Forrest, N J Peacock
Culham Laboratory, Abingdon, Oxon, OX14 3DB
(Euratom/UKAEA Fusion Association)

*On attachment from Royal Holloway College, University of London

ABSTRACT

Refined optical laser scattering techniques have been used to investigate the dynamics of the plasma focus device. Holographic interferometry, Faraday rotation and co-operative laser light scattering have provided detailed temporal evolution of the plasma parameters. Of these, three are believed to be unique measurements in this device, namely, the radial magnetic and current density profiles and three simultaneous scattered ion spectra.

The physical understanding of the plasma focus device [1] has been hitherto restricted by the difficulties in diagnosing such complex transient plasmas. Here, we report the application of three complementary optical diagnostics techniques to investigate the collapse and dense-pinch phases of a focus described previously [2,3] with a stored energy of 25 kJ at 23 kV and with a filling pressure of 1.8 torr of deuterium. Holographic interferometry, Faraday rotation and co-operative laser light scattering from a multiple beam output Q-switched ruby laser producing pulses of 15-300 MW and 1.5-30 ns FWHM provide comprehensive temporal information on the plasma parameters. These include the radial electron density profile $n_e(r)$, the azimuthal magnetic field $B_\theta(r)$, the current density distribution $J_z(r)$ and three ion fluctuation spectra $S_i(\underline{k},\omega)$.

The Faraday rotation (FR) technique [4] is based on the differential half-shade method [5] with a viewed plasma chord diameter of 250 μm and has a temporal resolution of 2.5 ns and an angular rotation resolution of 0.4 mrad. The detailed temporal evolution of the FR observed at a given chord impact parameter is built-up over several plasma shots, using a 30 ns 20 MW laser pulse, while the spatial variation is obtained by repeating the measurement over several impact parameters. By combining the FR measurements with electron density distributions obtained using 1.5 ns exposure holographic interferometry, the magnetic field structure is obtained by Abel inversion [6]. The current density is then obtained with Ampere's law.

The ion feature of the Thomson scattered light spectrum has been measured synchronously for three differential scattering vectors $\underline{k}$ and two values of the scattering parameter $\alpha = (k\lambda_D)^{-1}$. Three sets of collection optics [7] view essentially identical scattering volumes situated at a position on the pinch $\underline{z}$-axis 10 mm below the centre electrode, with the laser incident, $\underline{k}_{inc}$ normal to this axis. Two scattering angles of 10 and 45 degrees (and thus two different α values) having differential scattering vectors $\underline{k}$ with no component parallel to the $\underline{z}$-axis (i.e. no current driven effects) yield thermal levels of the scattered light. This has enabled the effects of the radial velocity component [8] and plasma impurities [9] on the ion spectrum to be measured by cross correlating the effects for both α values for a single shot. A second 10 degree scattering direction is in the plane defined by $\underline{z}$ & $\underline{k}_{inc}$ and permits the additional effects on the scattered light spectrum due to a relative electron-ion drift velocity [10] parallel to the $\underline{z}$-axis to be measured. The temporal evolution of the ion features for these three $\underline{k}$ vectors has been built up over a large number of shots from t = -50 ns to +80 ns relative to the peak compression of the pinch.

The FR measurements obtained at a z position = 5 mm indicate that the maximum rotation, observed at peak compression of the pinch (t = 0 ns), was 0.475 degrees. Abel inverted magnetic field profiles are shown in Fig. 1. At times t = -8 ns and t = 0 ns, the field and hence current is confined to the plasma skin with penetration depths 0.5 and 0.7 mm respectively. During these times, the plasma current is 340 kA $\pm$ 30%, which is 70% of the load current. Figure 2 shows the scattered data obtained from a shot at t = -5 ns. For times before peak compression it is observed that the 10 degree $\underline{k}$ parallel to $\underline{z}$ spectrum is enhanced with respect to the thermal spectrum by 20% at t = -40 ns rising to 100% at t = 0 ns. The enhanced spectrum is characterised by being asymmetric with its peak blue shifted with respect to the ruby wavelength. This is interpreted as being due to an electron-ion drift

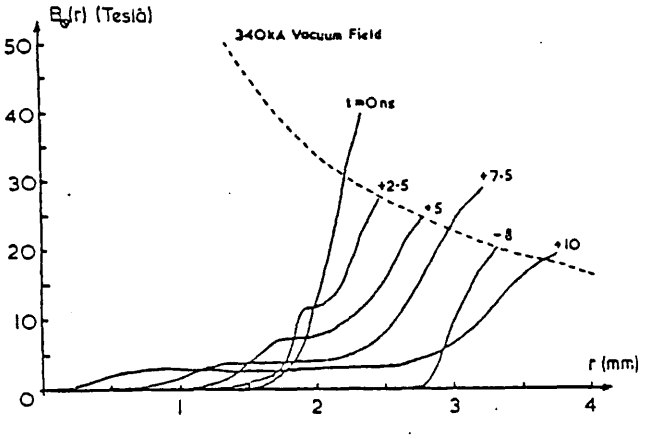

Fig. 1

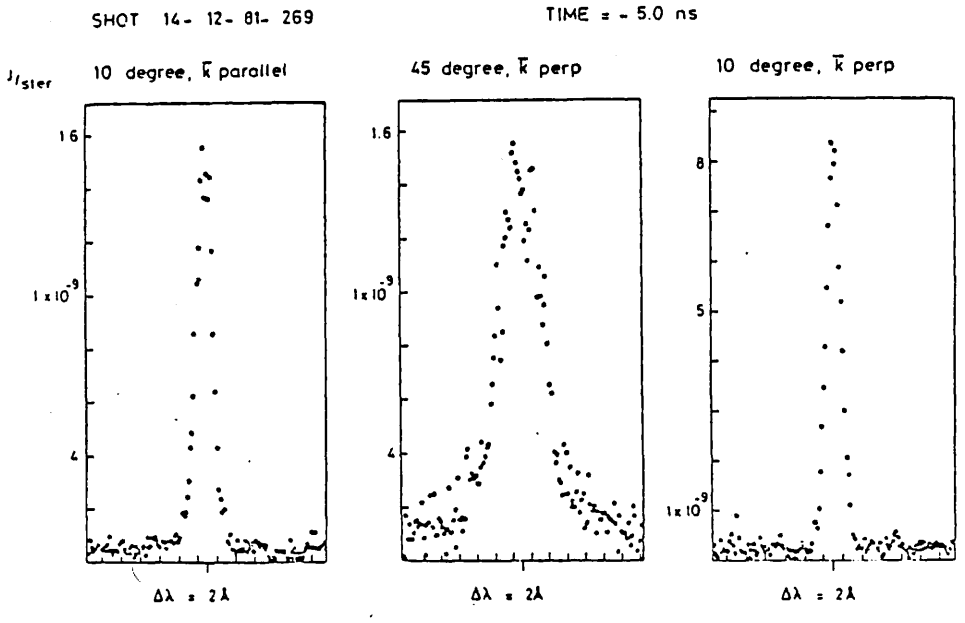

Fig. 2. Scattered data from optical multichannel analyser

velocity, v_d, with a $v_d/v_{th} \sim 0.1$-0.8 which is in agreement with the plasma current being carried in the skin. During this period profile fitting of the two thermal level spectra indicates that allowing for radial velocity effects the average parameters across the plasma diameter are Ti $\sim$ 400 eV, Te $\sim$ 800 eV and a radial velocity of $\sim 2.0 \times 10^5$ m/s which is in agreement with the radial velocities observed from the holographic interferometry. Pressure balance calculations from the magnetic field profiles indicate that with a Te/Ti $\sim$ 2 the plasma edge temperatures are Ti $\sim$ 600 eV and Te $\sim$ 1200 eV from which the $\underline{B}$ penetration depth is $\sim$ 2-3 ion Larmour radii and $\omega_{ce}\tau_{ei} \sim 10^2$.

The important feature of the FR results is the observation of a rapid diffusion of the magnetic field after peak compression towards the axis (penetration time $\sim$ 10 ns). The current density profiles shown in Fig. 3 clearly illustrates this diffusion. At t = +2.5 ns, the current structure has divided into two annular rings. At times t = +5 ns and t = +7.5 ns it is seen that one ring is radially contracting, while the other is expanding. At t = +10 ns, the current has all but reached the axis. This rapid field diffusion could be explained as being due to an enhancement of the resistivity to $\sim 10^4$ Spitzer due to the Hall term $[1 + (\omega_{ce}\tau_{ei})^2]$. The rapid collapse of the current density distribution as observed, has been proposed as a possible ion acceleration mechanism for neutron production in the plasma focus [11].

During some plasma shots, relatively large rotations $\sim$ 1 degree were observed at times between +10 ns and +15 ns with duration of $\leq$ 2.5 ns. At a slightly later time interval of +15 to +20 ns (due to the difference in z-axis observation positions) very large enhancements are observed in the k parallel to z scattered spectrum which are typically five to ten times the thermal level.

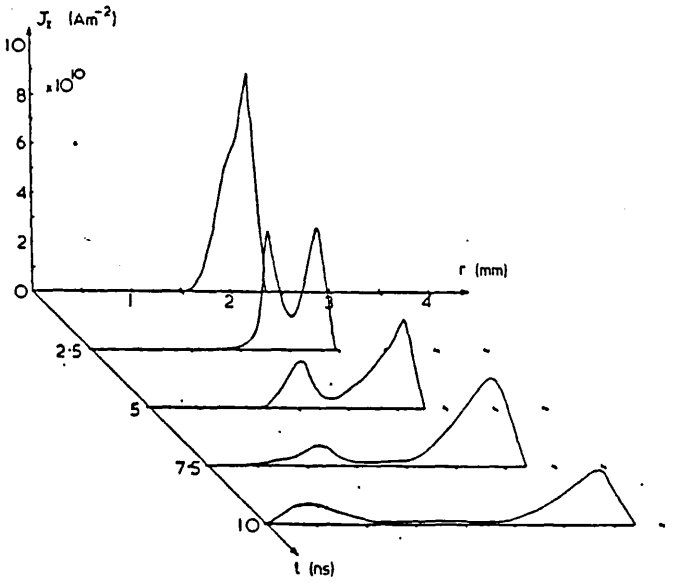

Fig. 3

Enhancements of up to 30 times have been observed. The indication is that during this period v_d/v_{th} becomes greater than unity. Abel inversion of the FR profiles has revealed the existence at these times of beam currents on the axis carrying $\geq$ 60 kA, i.e. $\geq$ 20% of the plasma current. In conclusion we report the first detailed FR and scattering observations of the plasma focus giving firm evidence for the existence of current redistribution and the resultant production of axial beam currents during the dense pinch phase.

REFERENCES

[1] Mather, J.W., Phys. Fluids, 8 336, (1965).

[2] Peacock, N.J., Speer, R.J. & Hobby, M.J., J. Phys. B. 2, 798 (1969).

[3] Peacock, N.J., Hobby, M.G. & Morgan, P.D., Plasma Physics and Controlled Fusion Research, IAEA, Vienna, 1, 537 (1971).

[4] Muir, D.G. et al, to be published.

[5] Falconer, I.S. & Ramsden, S.A., J. Appl. Phys., 39, 7, 3449 (1966).

[6] Bockasten, K., J. Opt. Soc. Am., 51, 9, 943, (1961).

[7] Kirk, R.E. et al, to be published.

[8] Downing, J.N. & Eisner, M., Phys. Fluids (USA), 18, 8, 991, (1975).

[9] Evans, D.E., Plasma Physics, 12, 573, (1970).

[10] Evans, D.E. & Katzenstein, J., Rep. Prog. Phys., 32, 207, (1969).

[11] Bernstein, M.J., Phys. Fluids, 13, 11 2858, (1970).